FERMILAB-CONF-17-664-PPD

LES HOUCHES 2017: PHYSICS AT TEV COLLIDERS NEW PHYSICS WORKING GROUP REPORT

G. Brooijmans[1], **M. Dolan**[2], **S. Gori**[3], **F. Maltoni**[4], **M. McCullough**[5], **P. Musella**[6], **L. Perrozzi**[6], **P. Richardson**[5,7] **and F. Riva**[5,8], **(convenors)**
A. Angelescu[9], S. Banerjee[7,10], D. Barducci[11], G. Bélanger[10], B. Bhattacherjee[12], M. Borsato[13], A. Buckley[14], J. M. Butterworth[15], G. Cacciapaglia[16], H. Cai[16], A. Carvalho[17], A. Chakraborty[18], G. Cottin[19], A. Deandrea[16,20], J. de Blas[21,22], N. Desai[23], M. Endo[18], N. Ezroura[24], G. Facini[15], S. Fichet[25], L. Finco[16], T. Flacke [26], B. Fuks[20,27], P. Gardner[24], S. Gascon-Shotkin[16], A. Goudelis[27,28], P. Gras[29], D. Grellscheid[7], R. Gröber[7], D. Guadagnoli[10], U. Haisch[5,30], J. Harz[27,28], J. Heisig[31], B. Herrmann[10], J. Hewett[32], T. Hryn'ova[33], J. F. Kamenik[34,35], S. Kraml[36], U. Laa[37,38], K. Lane[39], A. Lessa[40], S. Liebler[41], K. Lohwasser[42], D. M. Lombardo[8], D. Majumder[43], A. Malinauskas[30], O. Mattelaer[4], K. Mimasu[4], G. Moreau[44], M. Mühlleitner[41], A. E. Nelson[45], J. M. No[46], M. M. Nojiri[18,47], P. Pani[48], L. Panizzi[49,50], M. Park[45], G. Polesello[51], W. Porod[52], L. Pritchett[39], H. B. Prosper[53], A. Pukhov[54], J. Quevillon[36], T. Rizzo[32], P. Roloff[48], H. Rzehak[55], S. Sekmen[56], D. Sengupta[57], M. Spira[58], C. Vernieri[59], D. G. E. Walker[24], D. Yallup[15], B. Zaldivar[10], S. Zhang[16,60], J. Zurita[61,62]

Abstract

We present the activities of the 'New Physics' working group for the 'Physics at TeV Colliders' workshop (Les Houches, France, 5–23 June, 2017). Our report includes new physics studies connected with the Higgs boson and its properties, direct search strategies, reinterpretation of the LHC results in the building of viable models and new computational tool developments.

Acknowledgements

We would like to heartily thank all funding bodies, the organisers (N. Berger, F. Boudjema, C. Delaunay, M. Delmastro, S. Gascon, P. Gras, J.P. Guillet, B. Herrmann, S. Kraml, G. Moreau, E. Re, P. Slavich and D. Zerwas), the staff and all participants of the Les Houches workshop for providing a stimulating and lively atmosphere in which to work.

[1] Physics Department, Columbia University, New York, NY 10027, USA
[2] ARC Centre of Excellence for Particle Physics at the Terascale, School of Physics, The University of Melbourne, Victoria 3010, Australia
[3] Department of Physics, University of Cincinnati, Cincinnati, Ohio 45221, USA
[4] Centre for Cosmology, Particle Physics and Phenomenology (CP3), Université catholique de Louvain, Chemin du Cyclotron, 2, B-1348 Louvain-la-Neuve, Belgium
[5] Theoretical Physics Department, CERN, Geneva, Switzerland
[6] ETH Zurich - Institute for Particle Physics and Astrophysics (IPA), Zurich, Switzerland
[7] Institute for Particle Physics Phenomenology, Department of Physics, Durham University, DH1 3LE, Durham, UK
[8] Département de Physique Théorique, Université de Genève, 24 quai E. Ansermet, CH-1211 Geneva, Switzerland
[9] Department of Physics and Astronomy, University of Nebraska-Lincoln, Lincoln, NE, 68588, USA
[10] Univ. Grenoble Alpes, CNRS, USMB, LAPTh, 74000 Annecy, France
[11] SISSA and INFN, Sezione di Trieste, via Bonomea 265, 34136 Trieste, Italy
[12] Centre for High Energy Physics, Indian Institute of Science, Bangalore 560012, India
[13] Universidade de Santiago de Compostela, Santiago de Compostela, Spain
[14] SUPA, School of Physics and Astronomy, University of Glasgow, Glasgow G12 8QQ, UK
[15] Department of Physics & Astronomy, UCL, London, UK
[16] Univ. Lyon, Université Claude Bernard Lyon 1, CNRS/IN2P3, IPNL, 69622 Villeurbanne, France
[17] National Institute for Chemical Physics and Biophysics, Akadeemia tee, 10143 Tallinn, Estonia
[18] Theory Center, Institute of Particle and Nuclear Studies, KEK, 1-1 Oho, Tsukuba, Ibaraki 305-0801, Japan
[19] Department of Physics, National Taiwan University, Taipei 10617, Taiwan
[20] Institut Universitaire de France, 103 boulevard Saint-Michel, 75005 Paris, France
[21] Dipartimento di Fisica e Astronomia "Galileo Galilei", Università di Padova, I-35131 Padova, Italy
[22] INFN, Sezione di Padova, I-35131 Padova, Italy
[23] Laboratoire Univers et Particules de Montpellier, CNRS-Université de Montpellier, 34095 Montpellier, France
[24] Department of Physics and Astronomy, Dartmouth College, Hanover, NH 03755, USA
[25] ICTP-SAIFR & IFT-UNESP, R. Dr. Bento Teobaldo Ferraz 271, São Paulo, Brazil
[26] Center for Theoretical Physics of the Universe, Institute for Basic Science (IBS), Daejeon, 34126, Korea
[27] Sorbonne Université, CNRS, Laboratoire de Physique Théorique et Hautes Énergies, LPTHE, F-75005 Paris, France
[28] Sorbonne Université, Institut Lagrange de Paris (ILP), 75014 Paris, France
[29] IRFU, CEA, Université Paris-Saclay, Gif-sur-Yvette, France
[30] Rudolf Peierls Centre for Theoretical Physics, University of Oxford, OX1 3PN Oxford, United Kingdom
[31] Institute for Theoretical Particle Physics and Cosmology, RWTH Aachen University, 52056 Aachen, Germany
[32] SLAC National Accelerator Laboratory, 2575 Sand Hill Rd., Menlo Park, CA, 94025, USA
[33] Univ. Grenoble Alpes, Univ. Savoie Mont Blanc, CNRS, LAPP, 74000 Annecy, France
[34] Jožef Stefan Institute, Jamova 39, 1000 Ljubljana, Slovenia
[35] Faculty of Mathematics and Physics, University of Ljubljana, Jadranska 19, 1000 Ljubljana, Slovenia
[36] Univ. Grenoble Alpes, CNRS, Grenoble INP, LPSC-IN2P3, 38000 Grenoble, France
[37] School of Physics and Astronomy, Monash University, Clayton, VIC 3800, Australia
[38] Department of Econometrics and Business Statistics, Monash University, Clayton, VIC 3800, Australia
[39] Department of Physics, Boston University, Boston, MA 02215, USA
[40] Centro de Ciências Naturais e Humanas, Universidade Federal do ABC, Santo André, 09210-580 SP, Brazil
[41] Institute for Theoretical Physics, Karlsruhe Institute of Technology, 76131 Karlsruhe, Germany
[42] Department of Physics & Astronomy, Sheffield University, UK
[43] The University of Kansas, Lawrence, KS, USA

[44] Laboratoire de Physique Théorique, Bât. 210, CNRS, Univ. Paris Sud, Université Paris-Saclay, F-91405 Orsay Cedex, France
[45] Department of Physics, Box 1560, University of Washington, Seattle, WA 98195-1560 USA
[46] Department of Physics, King's College London, Strand, WC2R 2LS London, UK
[47] Kavli IPMU (WPI), University of Tokyo, Kashiwa, Chiba 277-8583, Japan
[48] CERN, Experimental Physics Department, CH-1211 Geneva 23, Switzerland
[49] Dipartimento di Fisica, Università di Genova and INFN, Sezione di Genova, 16146 Genova, Italy
[50] School of Physics and Astronomy, University of Southampton, Highfield, Southampton SO17 1BJ, UK
[51] INFN, Sezione di Pavia, Via Bassi 6, 27100 Pavia, Italy
[52] Institut für Theoretische Physik und Astrophysik, Uni. Würzburg, 97070 Würzburg, Germany
[53] Department of Physics, Florida State University, Tallahassee, Florida 32306, USA
[54] Skobeltsyn Institute of Nuclear Physics, Moscow State University, Moscow 119991, Russia
[55] CP3-Origins, University of Southern Denmark, Odense, Denmark
[56] Kyungpook National University, Physics Dept., Daegu, South Korea
[57] Department of Physics and Astronomy, Michigan State University, East Lansing, Michigan-48824, USA
[58] Paul Scherrer Institut, CH–5232 Villigen PSI, Switzerland
[59] Fermi National Accelerator Laboratory, Batavia, IL, 60510, USA
[60] Institute of High Energy Physics/University of the Chinese Academy of Sciences, Shijingshan District, Beijing, China 100049
[61] Institute for Theoretical Particle Physics (TTP), Karlsruhe Institute of Technology, 76128 Karlsruhe, Germany
[62] Institute for Nuclear Physics (IKP), KIT Karlsruhe Institute of Technology, D-76344 Eggenstein-Leopoldshafen, Germany

Contents

Introduction

G. Brooijmans, M. Dolan, S. Gori, F. Maltoni, M. McCullough, P. Musella, L. Perrozzi, P. Richardson, F. Riva

This document is the report of the New Physics session of the 2017 Les Houches Workshop 'Physics at TeV Colliders'. The workshop brought together theorists and experimenters who discussed a significant number of novel ideas related to Higgs and beyond the Standard Model physics. New computational methods and techniques were considered, with the aim of improving the technology available for theoretical, phenomenological and experimental new physics studies.

More precisely, one set of studies undertaken during the workshop concerns investigations associated with specific new physics models either constructed from a top-down approach or built following a bottom-up path. A second set of studies is connected to the Higgs boson discovered a few years ago. Its properties are now measured with increasing accuracy at the LHC, constraining the construction of any realistic new physics theory correspondingly. Finally, recasting techniques are the subject of a third series of contributions, including suggestions on the way experimental information could be presented.

In the first section searches for new physics beyond the Standard Model are presented, covering diverse frontiers in the hunt for new states, from new two-body resonances to new particles with macroscopic lifetimes. A first contribution reviews two-body resonance searches at the LHC, highlighting a few cases that are not currently covered. Many models contain vector-like quarks, for which single production can significantly enhance the search range. In direct single production, next-to-leading order effects, studied in a second contribution, can have significant effects on distributions used to separate the signal from the Standard Model background. The third contribution explores another way to produce single vector-like quarks: the production of new heavy spin-0 or spin-1 bosons that decay to a vector-like quark and a Standard Model fermion, which again leads to changes in distributions used to discriminate against the backgrounds. Three contributions tackle macroscopic lifetimes. The first reveals the connection between searches for long-lived particles (LLPs) and a compelling paradigm for dark matter production, known as "freeze-in". This connection relates the dark matter abundance in freeze-in models to the lifetime of the LLP produced at the LHC, making the lifetime determination a key target for such models. A complementary study determines the accuracy with which one could hope to answer this question, revealing how detector effects or analysis cuts could influence the accuracy with which the LLP lifetime could be determined. A related study in the tools sections exposes how attempts to recast current LHC LLP searches may be hampered by the format in which analysis details are presented. Consequentially, this contribution makes recommendations on the presentation of analysis details to maximise the impact of LHC searches in recasting for alternative scenarios.

In the top sector, two studies have been performed. One explores the "mono-top" signature of dark matter production, and a second flavour-violating top squark decays, showing the limitations of simplied models in quantifying LHC sensitivity to new physics. This is followed by an examination of the sensitivity of the LHC to intermediate mass (pseudo-)scalars produced in association with heavy flavor quark partners, indicating that with some optimization the LHC could cover the relevant areas in parameter space.

Another area in which the face of new physics may be already partially revealed is flavour physics, particularly concerning b-quarks, where a number of mild anomalies in individual measurements of different b-meson decay final states may be consistently pointing towards evidence of violation of lepton-flavour universality. The status of these anomalies and potential theories of new physics that may coherently explain the measurements through the existence of new particles is reviewed.

The second section includes contributions related to the physics of the Higgs boson and the electroweak symmetry breaking sector. Some contributions focus on effective field theories (EFTs) for Higgs physics, some on models with new light Higgs bosons, and some on models with additional heavy Higgs bosons. In particular, in the context of EFTs, one study compares different ways of experimentally accessing Beyond the Standard Model (BSM) physics via EFTs: either via a direct search dedicated to these effects, or via Simplified Template Cross Sections (STXS). Another study discusses, instead, the EFT reach at linear colliders (using CLIC as benchmark) in diboson processes, and designs a dedicated search to maximise it. Another study compares different EFT bases numerically and identifies the higher order effects that differ between them. Finally, the last study investigates the potential of the measured Higgs fiducial cross sections for deriving constraints on BSM Higgs production. In the context of models with new light Higgs bosons, one contribution investigates the bounds on models containing new scalars addressing the $Z \to b\bar{b}$ ALEPH anomaly, using Contur. A study of collider bounds on light pseudoscalars with a mass below 50 GeV is also presented, focusing on the mass regions [3, 5] GeV and [9, 11] GeV, where the mixing of the pseudoscalar with QCD bound states has to be included. A last project analyses the LHC prospects to discover a light scalar with mass below 65 GeV produced in association with a Z boson. Finally, in the context of models with new heavy Higgs bosons, a study presents the full NLO corrections to Higgs gluon fusion in SUSY QCD, within the framework of the MSSM including the full mass dependence of the particles running in the loop. We also report the first sensitivity study of the channel: $H_1 \to H_2 H_2 \to b\bar{b}b\bar{b}$, with both H_1 and H_2 states beyond the Standard Model, and we discuss the importance of interference effects in the search for heavy Higgs bosons decaying into hh and Zh.

Finally, the third section presents progress specific to software tools and methods that are crucial for any new physics investigation. Four contributions are included. The first focuses on the sensitivity of SM LHC measurements to new particles simulated through simplified models, using pairs of photons in the final state. The exercise shows that the generic light scalar models considered imply significant contributions to differential cross sections involving weak bosons and/or isolated photons which have already been measured at the LHC and shown to be consistent with the Standard Model, posing stringent constraints on the new physics parameter space. The second contribution proposes a first benchmark comparison assessing the performance of different public recasting tools in reproducing ATLAS and CMS searches with Monte Carlo simulation. The analyses considered show good agreement between the different frameworks and detector simulation techniques. The proposed method can be further applied to assess the reliability of the recasting methods in, e.g. extreme regions of phase space and/or for very different signal hypotheses than the one the analyses have been designed for. The third deals with the recasting of Long-Lived Particles Searches. In fact, extrapolating LHC search limits to other scenarios often proves to be a difficult task outside the experimental collaborations. The study proves that without detailed object reconstruction and selection efficiencies a satisfactory recasting can not be performed, and provides recommendations to the experimental collabo-

rations to include cut-flow tables and limits for at least two models or topologies as a sanity check. The last contribution investigates the usage of an analysis description language for LHC result reinterpretations, to be employed to describe in an unambiguous and concise manner a data analysis including all the details needed for recasting.

The meeting in Les Houches has fostered a large number of discussions between theorists and experimenters. In-depth studies could however only be completed for several of the generated ideas on the required timescale. It is clear that even those that could not converge to a written contribution have paid off through the breadth of searches conducted by experimenters and the understanding of the challenges placed on an experiment by the ever-changing theoretical landscape. We expect that many more future results will benefit from the discussions held at the workshop.

New physics

Contribution 1

Overview of two-body resonant searches at LHC

G. Brooijmans, G. Facini, J. Hewett, T. Hryn'ova, T. Rizzo

This contribution presents a novel approach to categorizing the existing two-body resonant searches at LHC and is aimed to identify some potential search channels that have been so far overlooked. This work is inspired by Ref. [1].

A typical resonance search looks for a bump on top of a smooth background. Some searches are intrinsically model independent (e.g. the inclusive, opposite-sign dilepton searches [2]). Other searches are more fine-tuned to a specific new physics model, such as the same-sign dilepton search which looks in particular for the pair-production of the doubly charged Higgs bosons [3] so that an additional invariant mass requirement is added to the more general search criteria. Here we will specifically highlight these general searches in our categorization in order to make it as model-independent at possible:

- Existing two body resonant searches are summarized in Table 1.
- Existing two body resonant searches which have additional particle or double-production requirements are summarized in Table 2.
- If no search is performed in either of the above categories, the corresponding channel is marked with "0", the channels covered only in one of two tables are marked by "*".
- The neutrino (ν) category in this table experimentally corresponds to a missing transverse momentum requirement. Typical searches (except in the $l\nu$ channel) assume not a Standard Model neutrino as the MET source, but some yet to be discovered stable or long-living neutral particle.

The tables show the most recently available results from the ATLAS or CMS collaborations with highest available integrated luminosity for the largest possible center-of-mass energy.

Some single production searches, e.g. $l\nu$ (W'), will not cover the pair-production of similar resonances ($l\nu l\nu$), because this search is performed employing the transverse mass variable and assumes that all of the missing transverse energy comes from a single particle. It also does not cover associated production (e.g. $ll\nu$) because it has a second lepton veto [4]. We note the cases where the final state *is* covered, but the search was not done using the corresponding mass distribution, which might reduce its sensitivity to find a resonance. For example, in Ref. [5] (Zt channel) a single bin analysis is performed for the pair production search for vector-like-quarks in the one lepton, jets, plus missing transverse momentum channel. In Ref. [6] (Wt channel) both a cut-based analysis and a boosted-decision-tree approach are used. The latter might not be easily reinterpretable for other models.

The following channels are identified as completely uncovered by present searches, although they would be interesting to pursue in the context of certain models as indicated below:

- be, te, $b\mu$, $t\mu$ - leptoquarks

Table 1: Existing two-body exclusive final state resonance searches performed by ATLAS or CMS. Only highest luminosity and largest center-of-mass energy publication is shown, the default being the full 2015+2016 dataset. References in *italic* employ only the 2015 or partial 2015-2016 datasets. Underlined references use Run 1 data. Note that $e/\mu + MET$ had extra lepton veto applied.

	e	μ	τ	ν	j	b	t	γ	Z	W	h
e	$\pm\mp$ [2],$\pm\pm$ [3]	$\pm\pm$ [3]	*[8]*	[4]	[9]	0	0	*	[10]	*	*
μ	-	$\pm\mp$ [2],$\pm\pm$ [3]	*[8]*	[4]	[9]	0	0	*	[10]	*	*
τ	-	-	[11]	[12], [13]	*	*	*	0	*	*	*
ν	-	-	-	* (?)	*	*	*	[14]	*	*	*
j	-	-	-	-	[15]	*[16]*	0	[17]	[18]	[18]	0
b	-	-	-	-	-	*[16]*	[19]	0	*	*	*
t	-	-	-	-	-	-	*[20, 21]*	0	[22]	*	*
γ	-	-	-	-	-	-	-	[23]	*[24]*	[25]	0
Z	-	-	-	-	-	-	-	-	[18]	[18]	[26]
W	-	-	-	-	-	-	-	-	-	[18]	[26]
h	-	-	-	-	-	-	-	-	-	-	[27, 28]

– $\tau\gamma$, $b\gamma$, $t\gamma$ - excited leptons and quarks

– tj - vector-like top quark

– hj - vector-like light flavour quark

– $h\gamma$ - Kaluza-Klein excitation of Higgs

Some of the channels not covered by the dedicated searches above (be, $b\mu$, $b\gamma$) are instead covered in the so-called general search [7], in which various combinations and multiplicities of electrons, muons, photons, jets, b-jets and missing transverse momentum are scanned for deviations from the Standard Model Monte Carlo prediction in the distributions of the effective mass and the total visible invariant mass of the reconstructed objetcs.

We believe it might be interesting for the ATLAS and CMS collaborations to adopt this approach in the presentation of summaries of the two-body resonant search results in addition to their current summary tables. Furthermore, this analysis should be extended to three-body resonance searches, as in many new physics models the largest production cross-sections are not for the lightest new particles, and heavier particles are naturally strongly coupled to lighter ones.

Table 2: Existing two-body exclusive final state resonance searches (with extra particle or double production requirement) by ATLAS or CMS. Only highest luminosity and largest center-of-mass energy publication is shown, the default is the full 2015+2016 dataset. References in *italic* use only the 2015 or partial 2015-2016 datasets. Underlined references use Run 1 data. * means that this state is covered exclusively in Table 1. x denotes double production requirement. The channels shown in red are those in which analyses might be not optimal for a resonant search or reinterpretation tricky because of the use of a multi-variate technique.

	e	μ	τ	ν	j	b	t	γ	Z	W	h
e	x $\pm\pm$ [3]	x $\pm\pm$ [3]	*	*	e [29], x *[30]* [31]	0	0	e [32]	e [32],$\nu/lV/h$ [33]	$\nu/lV/h$ [33]	$\nu/lV/h$
μ	-	x $\pm\pm$ [3]	*	*	μ [29], x *[30]* [31]	0	0	μ [32]	μ [32],$\nu/lV/h$ [33]	$\nu/lV/h$ [33]	$\nu/lV/h$
τ	-	-	*	*	x *[34]*	x [35]	x [36]	0	$\nu/lV/h$ [33]	$\nu/lV/h$ [33]	$\nu/lV/h$
ν	-	-	-	j [37,38], γ [39], H [40] W [38], Z [38,43,44]	ej, μj [31]	x [41], [42]	x [42]	*	$\nu/lV/h$ [33]	$\nu/lV/h$ [33]	$\nu/lV/h$
j	-	-	-	-	j [45]	*	0	*	*	*	0
b	-	-	-	-	-	*	*	0	bj;V/H+b [46]	x [47,48]	b [49];V/H+
t	-	-	-	-	-	-	*	0	x [5]	V/H+b/t [6]	*V/H+b/t*
γ	-	-	-	-	-	-	-	γ/x [52]	*	*	0
Z	-	-	-	-	-	-	-	-	*	*	*
W	-	-	-	-	-	-	-	-	-	*	*
h	-	-	-	-	-	-	-	-	-	-	*

Contribution 2

Exotic decays of heavy boson into SM quarks and vector-like quarks

D. Barducci, H. Cai, T. Flacke, B. Fuks, R. Gröber, W. Porod, T. Rizzo

Abstract
We identify the quantum numbers of heavy scalar or vector resonances that can be singly produced via proton-proton scattering at the LHC. We then classify the quantum numbers of heavy vector-like quarks into which the heavy bosons can decay in association with a Standard Model quark. We subsequently briefly discuss the phenomenology of these non-standard signatures at the LHC.

1 INTRODUCTION

Searches for the on-shell production of heavy resonances are among the priorities of the Large Hadron Collider (LHC) physics program and a powerful tool to probe various new physics (NP) scenarios. In fact many beyond the Standard Model (BSM) realizations formulated to address the shortcomings of the Standard Model (SM) predict the presence of unstable spin-0 or spin-1 states which can promptly decay into a pair of SM particles. The latter can generally be reconstructed within the LHC detectors and consequently provide sensitivity to the possible presence of such BSM states. The most simple examples of this program are the searches for peaks in, *e.g.*, the $\gamma\gamma$, jj and $\ell^+\ell^-$ invariant-mass distributions. Final state consisting of a pair of unstable SM states, such as $t\bar{t}$, ZZ and W^+W^-, can also be exploited, thanks to the generally good reconstruction efficiency for such objects.

On general grounds, in order to have a significant number of signal events, the heavy resonance should decay copiously into the chosen SM final state with the event rate (within the narrow width approximation) being determined by the product of the on-shell resonance production cross section and the corresponding branching fraction into the specific final state of interest. However, in many NP models there exist additional decay channels for such heavy states that are open and so decays into non-SM final states can become the dominant ones. This happens, for example, in Composite Higgs Models (CHMs), where new spin-1 resonances can have a sizeable branching fractions into a pair of vector-like quarks (VLQs) or a VLQ and a SM quark [53–55] or of supersymmetric models with extended gauge symmetries, where the heavy Z' and W' can directly decay predominantly into non-SM states [56–58]. The "depletion" of the heavy resonances branching ratios into SM states can reduce the reach of the NP searches performed at the LHC and relax the constraints that can be enforced on the masses of such objects.[1] In order to be sensitive to the maximum number of NP configurations possible, recently the experimental collaborations have started to pursue analyses targeting possible non-minimal decays of heavy resonances. This is, for example, the case of the CMS search of Ref. [60],

[1] Note however that by reinterpreting non-dedicated analyses these bounds can be recovered [59].

wherein a heavy spin-1 resonance is looked for in a final state containing a top quark and a VLQ with an electric charge equal to 2/3.

Motivated by this analysis, we categorize in this note the possible final state configurations arising from the decay of a heavy spin-0 or spin-1 particle that can be resonantly produced in the s-channel via proton-proton collisions, and that can decay into a SM quark and a VLQ. We identify the SM quantum numbers of such bosonic resonances as well as the quantum numbers of the VLQs that can be present in their decays. We then discuss the associated phenomenology highlighting which channels could be experimentally covered by the reinterpretation of existing experimental analyses and which ones require a new dedicated search strategy.

2 HEAVY RESONANCES PRODUCTION

In order for a bosonic resonances to be produced via the s-channel in proton-proton collisions, they should couple to SM quarks and/or gluons whose quantum number under $\mathcal{G}_{SM} = SU(3)_c \times SU(2)_L \times U(1)_Y$ are provided for the sake of clarity in the following Table [2],

Field	q_L	u_R	d_R	g
$\mathcal{G}_{SM}$	(**3**, **2**, 1/6)	(**3**, **1**, 2/3)	(**3**, **1**, -1/3)	(**8**, **1**, 0)

In the case of a vector resonance, the interaction structure with the SM quarks is of the form $\bar{q}^c_L\gamma^\mu u_R$, $\bar{q}^c_L\gamma^\mu d_R$, $\bar{q}_L\gamma^\mu q_L$, $\bar{u}_R\gamma^\mu u_R$, $\bar{d}_R\gamma^\mu d_R$, $\bar{u}_R\gamma^\mu d_R$, while it is of the form $\bar{q}_L u_R$, $\bar{q}_L d_R$, $\bar{q}_L q^c_L$, $\bar{u}^c_R u_R$, $\bar{u}^c_R d_R$ or $\bar{d}^c_R d_R$ in the case of a scalar resonance. Here we have defined $\psi^c_L = (\psi_L)^c = C\gamma_0\psi^*_L$, with ψ^c_L transforming like a right-handed field and ψ^c_R like a left-handed field and with $C = i\gamma^2\gamma^0$ in Dirac notation. We then provide in Tab. 1 the quantum number under $\mathcal{G}_{SM} = SU(3)_c \times SU(2)_L \times U(1)_Y$ of the new resonances that can be singly produced via proton-proton collisions, together with their electric charges and the schematic form of their interaction with the proton constituents; more information is also available in Refs. [61,62]. We however do not account in for the case where an interaction between a new scalar and the SM fermions arises due to mixing, as this would be for example the case for a $(\mathbf{1}, \mathbf{1}, 0)$ scalar that acquires a vacuum expectation value and its interactions to the SM fermions would then stem from a mixing with the SM Higgs boson.

From a model building point of view new vectors usually arise either in strongly-interacting theories (similar to the ρ meson in QCD) or in weakly-interacting theories as part of extended gauge groups. This usually implies that there is a whole new plethora of particles which may participate in the vector decays. While in the former case the theory can be regarded as an effective field theory valid up to some cut-off scale and hence it can be described by a non-renormalizable theory, in the latter case, on which we focus on here, it would be desirable to restore renormalizablity. This in turns implies that certain constraints on the possible interactions between the various states must be fulfilled if the model is to be ultraviolet (UV) complete, *e.g.* that the interactions are built up from gauge-covariant quantities. Conversely, for spin-0 resonances the situation is more straightforward and the SM can be simply extended by a new scalar multiplet.[3] Moreover, since the purpose of this study is to categorize the possible SM

[2] We adopt the convention $Q_{\rm em} = T^3_L + Y$.

[3] If BSM scalar fields participate in electroweak symmetry breaking they can mix with the SM Higgs, and the mass mixing affects production and decay of the new scalar resonances (as well as of the Higgs boson). In this analysis we focus on heavy new states for which we expect scalar mass mixing effects and the effects from electroweak symmetry breaking in interactions to be suppressed by $\mathcal{O}(v/M_\phi)$, with M_ϕ being the scalar mass.

Vectors			Scalars		
$\mathcal{G}_{\mathcal{SM}}$	Q_{em}	Interaction	$\mathcal{G}_{\mathcal{SM}}$	Q_{em}	Interaction
$(\mathbf{1}\oplus\mathbf{8},\mathbf{1},0)$	0	$\bar{u}u,\bar{d}d,\bar{q}q,(gg)$	$(\mathbf{1},\mathbf{2},1/2)$	$0,1$	$\bar{q}u,\bar{q}d$
$(\mathbf{1}\oplus\mathbf{8},\mathbf{1},1)$	1	$u\bar{d}$	$(\mathbf{8},\mathbf{2},1/2)$	$0,1$	$\bar{q}u,\bar{q}d$
$(\mathbf{1},\mathbf{3},0)$	1,0,-1	$\bar{q}q$	$(\mathbf{3}\oplus\bar{\mathbf{6}},\mathbf{1},-4/3)$	-4/3	$\bar{u}^c u$
$(\mathbf{3}\oplus\bar{\mathbf{6}},\mathbf{2},1/6)$	2/3,-1/3	$\bar{q}^c d$	$(\mathbf{3}\oplus\bar{\mathbf{6}},\mathbf{1},-1/3)$	-1/3	$\bar{q}^c q,\bar{d}^c u$
$(\mathbf{3}\oplus\bar{\mathbf{6}},\mathbf{2},-5/6)$	-1/3,-4/3	$\bar{q}^c u$	$(\mathbf{3}\oplus\bar{\mathbf{6}},\mathbf{1},2/3)$	$2/3$	$\bar{d}^c d$
$(\mathbf{8},\mathbf{3},0)$	1,0,-1	$\bar{q}q$	$(\mathbf{3}\oplus\bar{\mathbf{6}},\mathbf{3},-1/3)$	2/3,-1/3,-4/3	$\bar{q}^c q$

Table 1: The new bosons quantum numbers under the SM gauge group together with their electric charge and schematic interaction structure with the SM quarks and gluons, for both cases of vector (left) and scalar (right) resonances. The chirality of the SM quarks is implicit from the interaction structure. In the vector case we moreover do not explicitly write the γ^μ factor.

quantum numbers of the resonances that can be produced on-shell at the LHC and that can decay into a SM quark and a VLQ, we do not consider any other possible interaction among the heavy vectors and scalars with the SM fields except the ones responsible for these production and decay mechanisms. Restricting then to just gauge invariant and renormalizable interactions, the generic Lagrangians for the production of the resonances of Tab. 1 are given in Eq. (1) and Eq. (2) for the vector case and in Eq. (3) and Eq. (4) for the scalar case, where σ^a are the Pauli matrices acting in the $SU(2)_L$ space, T^A are the $SU(3)_c$ generators in the fundamental representation with A=1,...,8, λ,κ are generic coupling parameters and the subscripts on V^μ vector resonances and S scalar resonances indicate their quantum numbers under $\mathcal{G}_{SM}$.[4]

$$\begin{aligned}\mathcal{L}_{1\oplus 8} = {}& \kappa_{1R}\overline{u_R}\gamma_\mu d_R V^\mu_{\mathbf{1},\mathbf{1},1} + \kappa_{8R}\overline{u_R}\gamma_\mu T^A d_R V^{\mu,A}_{\mathbf{8},\mathbf{1},1} \\ & + \left(\kappa_{qL}\overline{q_L}\gamma_\mu T^A q_L + \kappa_{uR}\overline{u_R}\gamma_\mu T^A u_R + \kappa_{dR}\overline{d_R}\gamma_\mu T^A d_R\right) V^{\mu,A}_{\mathbf{8},\mathbf{1},0} \\ & + \left(\kappa'_{qL}\overline{q_L}\gamma_\mu q_L + \kappa'_{uR}\overline{u_R}\gamma_\mu u_R + \kappa'_{dR}\overline{d_R}\gamma_\mu d_R\right) V^\mu_{\mathbf{1},\mathbf{1},0} \\ & + \kappa_{3L}\overline{q_L}\sigma^a\gamma_\mu T^A q_L V^{\mu,A,a}_{\mathbf{8},\mathbf{3},0} + \kappa'_{3L}\overline{q_L}\sigma^a\gamma_\mu q_L V^{\mu,a}_{\mathbf{1},\mathbf{3},0} + \text{h.c.}\,.\end{aligned} \tag{1}$$

$$\mathcal{L}_{3\oplus\bar{6}} = \kappa_2\overline{q_L^c}i\sigma_2\gamma_\mu d_R V^\mu_{\mathbf{3}\oplus\bar{\mathbf{6}},\mathbf{2},1/6} + \kappa'_2\overline{q_L^c}i\sigma_2\gamma_\mu u_R V^\mu_{\mathbf{3}\oplus\bar{\mathbf{6}},\mathbf{2},-5/6} + \text{h.c.}\,, \tag{2}$$

$$\mathcal{L}_{1\oplus 8} = \lambda_u\overline{q_L}T^A i\sigma_2\, u_R S^{A*}_{\mathbf{8},\mathbf{2},1/2} + \lambda'_u\overline{q_L}i\sigma_2\, u_R S^*_{\mathbf{1},\mathbf{2},1/2} + \lambda_d\overline{q_L}T^A d_R S^A_{\mathbf{8},\mathbf{2},1/2} + \lambda'_d\overline{q_L}d_R S_{\mathbf{1},\mathbf{2},1/2} \tag{3}$$

$$\begin{aligned}\mathcal{L}_{3\oplus\bar{6}} = {}& \left(\lambda_{qL}\overline{q_L^c}i\sigma_2 q_L + \lambda_R^{1/3}\overline{u_R^c}d_R\right) S_{\mathbf{3}\oplus\bar{\mathbf{6}},\mathbf{1},-1/3} + \lambda_R^{2/3}\overline{d_R^c}d_R S_{\mathbf{3}\oplus\bar{\mathbf{6}},\mathbf{1},2/3} \\ & + \lambda_R^{4/3}\overline{u_R^c}u_R S_{\mathbf{3}\oplus\bar{\mathbf{6}},\mathbf{1},-4/3} + \lambda_{3L}\overline{q_L^c}i\sigma_2\,\sigma^a\, q_L\, S^a_{\mathbf{3}\oplus\bar{\mathbf{6}},\mathbf{3},-1/3} + \text{h.c.}\end{aligned} \tag{4}$$

[4] In Tab. 1, we indicate a possible production from gluon fusion of a color octet vector which is allowed by virtue of the conservation of all quantum numbers, but does not follow from Eq. (3). Such an interaction is absent at tree-level but is not forbidden by the Landau Yang theorem [63] and could be induced at higher order.

$\psi_{\rm VLQ} = (\mathbf{3}, \mathbf{1}, Y)$				$\psi_{\rm VLQ} = (\mathbf{3}, \mathbf{2}, Y)$			
$\psi_{\rm SM}$	vector	$\psi_{\rm VLQ}$	$Q_{\rm VLQ}$	$\psi_{\rm SM}$	vector	$\psi_{\rm VLQ}$	$Q_{\rm VLQ}$
u_R	(**1** $\oplus$ **8**,**1**,0)	(**3**,**1**,2/3)	2/3	q_L	(**1**$\oplus$ **8**,**1**,0)	(**3**,**2**,1/6)	(2/3,-1/3)
	(**1**$\oplus$ **8**,**1**, $\pm$1)	(**3**,**1**,-1/3)	-1/3		(**1**$\oplus$ **8**,**1**,$\pm$1)	(**3**,**2**,7/6)	(5/3,2/3)
		(**3**,**1**,5/3)	5/3			(**3**,**2**,-5/6)	(-1/3,-4/3)
d_R	(**1**$\oplus$ **8**,**1**,0)	(**3**,**1**,-1/3)	-1/3		(**1**$\oplus$ **8**,**3**,0)	(**3**,**2**,1/6)	(2/3,-1/3)
	(**1**$\oplus$ **8**,**1**, $\pm$1)	(**3**,**1**,2/3)	2/3				
		(**3**,**1**,-4/3)	-4/3				

$\psi_{\rm VLQ} = (\mathbf{3}, \mathbf{3}, Y)$				$\psi_{\rm VLQ} = (\mathbf{3}, \mathbf{4}, Y)$			
$\psi_{\rm SM}$	vector	$\psi_{\rm VLQ}$	$Q_{\rm VLQ}$	$\psi_{\rm SM}$	vector	$\psi_{\rm VLQ}$	$Q_{\rm VLQ}$
u_R	(**1**$\oplus$ **8**,**3**,0)	(**3**,**3**,2/3)	(5/3,2/3,-1/3)	q_L	(**1**$\oplus$ **8**,**3**,0)	(**3**,**3**,1/6)	(5/3,2/3,-1/3,-4/3)
d_R	(**1**$\oplus$ **8**,**3**,0)	(**3**,**3**,-1/3)	(2/3,-1/3,-4/3)				

Table 2: Quantum numbers of the VLQs into which a color singlet or octet vector resonance can decay together with the indicated SM quark for the case of a VLQ lying in the singlet (upper left), double (upper right), triplet (lower left) and fourplet (lower right) representations of $SU(2)_L$.

3 HEAVY RESONANCE DECAY

Having classified the possible resonances that can be singly produced on-shell at the LHC, we identify in this Section the quantum numbers of the VLQs, *i*.e. the fermions lying in the fundamental representation (**3**) of $SU(3)_c$, into which the heavy resonance can decay in association with with a SM quark, thus assuming this process to be kinematically allowed. We discuss separately the cases of vector and scalar resonances, and categorize the VLQs according to the representation of $SU(2)_L$ in which the corresponding field lies. By matching the VLQ hypercharge in order to have gauge invariant interactions we can identify the electric charge of the various components of the VLQ multiplets.

3.1 Vectors

If the new vectors lie in the singlet or octet representation of $SU(3)_c$ then gauge invariant and renormalizable interactions with a VLQ and a SM quark can be written only for VLQ with weak isospin up to 3/2, while the maximum allowed weak isospin is 1 in the case where the new vectors lie in the triplet or anti-sextet representation of $SU(3)_c$.

3.1.1 Case of $1 \oplus 8$

The categorization of the allowed VLQ quantum numbers in cases where the vector resonance lies in the singlet or octet representation of $SU(3)_c$ is given in Tab. 2, assuming decays into either the SM quark weak doublet q_L or the weak singlets u_R and d_R. We observe that most of the VLQs lying in the singlet, doublet and triplet representation of $SU(2)_L$ are "standard" VLQ representations that generally arise in CHM, *i.e.* representations for which it is possible to write gauge invariant, renormalizable Yukawa type interactions that mix the SM quarks and the VLQs once electroweak symmetry is broken. Through this mass mixing these VLQ can

$\psi_{\rm VLQ} = (\mathbf{3}, \mathbf{1}, Y)$				$\psi_{\rm VLQ} = (\mathbf{3}, \mathbf{2}, Y)$			
$\psi_{\rm SM}$	vector	$\psi_{\rm VLQ}$	$Q_{\rm VLQ}$	$\psi_{\rm SM}$	vector	$\psi_{\rm VLQ}$	$Q_{\rm VLQ}$
q_L	($\mathbf{3} \oplus \bar{\mathbf{6}}$, **2**,-5/6)	(**3**,**1**,2/3)	2/3	u_R	($\mathbf{3} \oplus \bar{\mathbf{6}}$, **2**,-5/6)	(**3**,**2**,1/6)	(2/3,-1/3)
	($\mathbf{3} \oplus \bar{\mathbf{6}}$, **2**, 1/6)	(**3**,**1**,-1/3)	-1/3		($\mathbf{3} \oplus \bar{\mathbf{6}}$ **2**, 1/6)	(**3**,**2**,-5/6)	(-1/3,-4/3)
				d_R	($\mathbf{3} \oplus \bar{\mathbf{6}}$, **2**,- 5/6)	(**3**,**2**,7/6)	(5/3,2/3)
					($\mathbf{3} \oplus \bar{\mathbf{6}}$, **2**, 1/6)	(**3**,**2**,1/6)	(2/3,-1/3)

$\psi_{\rm VLQ} = (\mathbf{3}, \mathbf{3}, Y)$			
$\psi_{\rm SM}$	vector	$\psi_{\rm VLQ}$	$Q_{\rm VLQ}$
q_L	($\mathbf{3} \oplus \bar{\mathbf{6}}$, **2**,-5/6)	(**3**,**3**,2/3)	(5/3,2/3,-1/3)
	($\mathbf{3} \oplus \bar{\mathbf{6}}$, **2**,1/6)	(**3**,**3**,-1/3)	(2/3,-1/3,-4/3)

Table 3: Quantum numbers of the VLQs into which a color triplet or anti-sextet vector resonance can decay itogether with the indicated SM quark for the case of a VLQ lying in the singlet (upper left), doublet (upper right) or triplet (lower) representations of $SU(2)_L$.

decay into a SM boson (W, Z or h) and a SM quark, and these decay channels have been largely explored at the LHC in conventional VLQ searches (see *e.g.* in Refs. [5, 47, 48, 64]), albeit with the assumption that the branching fractions for these three final states sum to unity. However, for the special assignments $(\mathbf{3}, \mathbf{1}, 5/3)$ and $(\mathbf{3}, \mathbf{1}, -4/3)$ these types of interactions are not possible. The same is true for the $SU(2)_L$ quadruplet, for which a dimension-4 Yukawa type interaction with the SM Higgs is forbidden, (see *e*.g in Ref. [65]). Consequently these VLQs will decay back into a SM quark and the new resonance through which they were produced which will, however, be off-shell and will itself subsequently decay into a pair of SM quarks or gluons. This process gives thus rise to a $qqqq$ or $ggqq$ final state, where q could be a light quark, a b quark or a top quark. While these "backward decays" are possible also in the case where Yukawa type interactions are allowed, they will generically be suppressed with respect to the $VLQ \to SM\ SM$ decay pattern, being the former a three- instead than a two-body decay proceeding through an off-shell state. We thus expect that these decay patterns do not affect the reach of conventional VLQ experimental searches, as long as the couplings to the SM states are not strongly suppressed compared to the ones to the new vector.

3.1.2 Case of $\mathbf{3} \oplus \bar{\mathbf{6}}$

In the case of vectors lying in the triplet or the anti-sextet representation of $SU(3)_c$, the allowed quantum numbers for the VLQ are given in Tab. 3. Only standard quantum numbers for the VLQs, *i.e.* quantum numbers that allow for Yukawa type interactions with the SM fields are found in these cases.

3.2 Scalars

In this Section we perform the same classification as in Sec. 3.1 above for the case of the scalar resonances reported in Tab. 1. Again, the new scalar is still assumed to decay into a SM-fermion plus a new vector-like quark as before although with a different chirality structure.

$\psi_{\rm VLQ} = (\mathbf{3}, \mathbf{1}, Y)$				$\psi_{\rm VLQ} = (\mathbf{3}, \mathbf{2}, Y)$			
$\psi_{\rm SM}$	scalar	$\psi_{\rm VLQ}$	$Q_{\rm VLQ}$	$\psi_{\rm SM}$	scalar	$\psi_{\rm VLQ}$	$Q_{\rm VLQ}$
q_L	(**1**$\oplus$ **8**,**2**,1/2)	(**3**,**1**,2/3)	2/3	t_R	(**1**$\oplus$ **8**,2,1/2)	(**3**,**2**,1/6)	(2/3,-1/3)
		(**3**,**1**,-1/3)	-1/3			(**3**,**2**,7/6)	(5/3,4/3)
				b_R	(**1**$\oplus$ **8**,**2**,1/2)	(**3**,**2**,1/6)	(2/3,-1/3)
						(**3**,**2**,-5/6)	(-2/3,-4/3)

$\psi_{\rm VLQ} = (\mathbf{3}, \mathbf{3}, Y)$			
$\psi_{\rm SM}$	scalar	$\psi_{\rm VLQ}$	$Q_{\rm VLQ}$
q_L	(**1**$\oplus$ **8**,**2**,1/2)	(**3**,**3**,2/3)	(5/3, 2/3, -1/3)
		(**3**,**3**,-1/3)	(2/3,-1/3,-4/3)

Table 4: Quantum numbers of the VLQs into which a color singlet or octet scalar resonance can decay together with the indicated SM quark for the case of a VLQ lying in the singlet (upper left), doublet (upper right) and triplet (lower) representations of $SU(2)_L$.

3.2.1 Case of $1 \oplus 8$

The quantum numbers and charges of the possible vector-like quarks ψ_{VLQ} in cases where the scalar resonance lies in the trivial or adjoint representation of $SU(3)_c$ can be found in Tab. 4. Also in this case we see that only standard quantum numbers for the VLQs, *i.e.* are found.

3.2.2 Case of $3 \oplus \bar{6}$

The same classification can be made for a scalar resonance lying in the triplet or sextet $(3 \oplus \bar{6})$ representation of the strong gauge group. The results are reported in Tab. 5. As in the vector $1 \oplus 8$ cases above we now observe the appearance of non-standard VLQ quantum numbers.

4 PHENOMENOLOGY

Having identified all the possible quantum numbers of VLQs arising from the decay of an on-shell vector or scalar resonance singly produced at the LHC and decaying into a SM quark and a VLQ, we now give an overview of the phenomenology which is expected from these production and decay patterns[5].

– **Prompt decay into a VLQ and a SM quark:** If the new VLQs have the same color and electric charge quantum numbers as do the SM fermions we can write down a mixing term generated by a coupling to the SM Higgs boson. This would hence lead to decays of the new vector-like quarks into either a Higgs boson and a SM fermion, a Z-boson and a SM fermion or a W-boson and a SM fermion, see e.g. [67]. Searches for such modes have been recently performed by the CMS collaboration [60].

[5]Some of the scalars and vectors could be leptoquarks, e.g. couple to leptons and quarks. We assume here that the corresponding couplings are zero as these are heavily constraint by the non-observation of proton decay [66].

$\psi_{\rm VLQ} = (\mathbf{3}, \mathbf{1}, Y)$				$\psi_{\rm VLQ} = (\mathbf{3}, \mathbf{2}, Y)$			
$\psi_{\rm SM}$	scalar	$\psi_{\rm VLQ}$	$Q_{\rm VLQ}$	$\psi_{\rm SM}$	scalar	$\psi_{\rm VLQ}$	$Q_{\rm VLQ}$
u_R	($\mathbf{3} \oplus \bar{\mathbf{6}}$,**1**,-4/3)	(**3**,**1**,2/3)	2/3	q_L	($\mathbf{3} \oplus \bar{\mathbf{6}}$,**1**,-4/3)	(**3**,**2**, 7/6)	(2/3,5/3)
	($\mathbf{3} \oplus \bar{\mathbf{6}}$,**1**,2/3)	(**3**,**1**,-4/3)	-4/3		($\mathbf{3} \oplus \bar{\mathbf{6}}$,**1**,2/3)	(**3**,**2**,-5/6)	(-1/3,-4/3)
	($\mathbf{3} \oplus \bar{\mathbf{6}}$,**1**,-1/3)	(**3**,**1**,-1/3)	-1/3		($\mathbf{3} \oplus \bar{\mathbf{6}}$,**1**,-1/3)	(**3**,**2**,1/6)	(2/3,-1/3)
d_R	($\mathbf{3} \oplus \bar{\mathbf{6}}$,**1**,-4/3)	(**3**,**1**,5/3)	5/3				
	($\mathbf{3} \oplus \bar{\mathbf{6}}$,**1**,2/3)	(**3**,**1**,-1/3)	-1/3				
	($\mathbf{3} \oplus \bar{\mathbf{6}}$,**1**,-1/3)	(**3**,**1**,2/3)	2/3				

$\psi_{\rm VLQ} = (\mathbf{3}, \mathbf{3}, Y)$				$\psi_{\rm VLQ} = (\mathbf{3}, \mathbf{4}, Y)$			
$\psi_{\rm SM}$	scalar	$\psi_{\rm VLQ}$	$Q_{\rm VLQ}$	$\psi_{\rm SM}$	scalar	$\psi_{\rm VLQ}$	$Q_{\rm VLQ}$
u_R	($\mathbf{3} \oplus \bar{\mathbf{6}}$,**3**,-1/3)	(**3**,**3**,-1/3)	(2/3,-1/3,-4/3)	q_L	($\mathbf{3} \oplus \bar{\mathbf{6}}$,**3**,-1/3)	(**3**,**4**,1/6)	(5/3,2/3,-1/3,-4/3)
d_R	($\mathbf{3} \oplus \bar{\mathbf{6}}$,**3**,-1/3)	(**3**,**3**,2/3)	(5/3,2/3,-1/3)				

Table 5: Quantum numbers of the VLQs into which a color triplet or anti-sextet scalar resonance can decay together with the indicated SM quark for the case of a VLQ lying in the singlet (upper left), doublet (upper right), triplet (lower left) and fourplet (lower right) representations of $SU(2)_L$.

– **Displaced vertices:** Conversely, if the new fermion has exotic quantum numbers, such mixing terms are not allowed. In these cases the VLQ will decay back into an off-shell heavy boson which will then decay back to the SM. Depending on the lifetime of the VLQ, both prompt multijet final states, with the potential presence of top quarks, or signatures exhibiting a displaced vertex will be possible.

– **R hadron:** For long enough lifetimes the VLQ will hadronize before decaying, allowing in this way for the formation of new exotic and heavy bounds states [68, 69].

– **Associated production of new scalars:** Producing the new scalars in $q\bar{q}$ annihilation together with quarks of the first and/or second generation could be strongly constrained by flavour observables. However, one can produce the scalar in association with a $b\bar{b}$ or a $t\bar{t}$ pair. The allowed quantum numbers for the scalar remain the same of Tab. 1.

– **Reversed mass hierarchy:** While throughout our discussion we have assumed a mass hierarchy such as the new boson can decay into a VLQ and a SM quark, the opposite hierarchy can also give rise to an interesting phenomenology. In that case the VLQ will undergo a decay into a heavy boson and a SM quark. This configuration has recently received some attention, also due to the possibility that bounds on the mass of the VLQs could be relaxed [70–73].[6]

[6]Note that exclusion bounds for VLQs with decays into new particles can also be strengthened, for instance in the case where they decay into a stable scalar, such that stop searches can be reinterpreted [74]. This is typically the case in non-minimal Composite Higgs Models [75].

5 CONCLUSIONS

New bosons of spin-0 and/or spin-1 are common in many extensions of the Standard Model, in particular in composite Higgs models or extra-dimensional models. We have classified all spin-0 and spin-1 states that can be produced at the LHC through initial state quarks by an s-channel exchange. Several existing LHC searches set bounds on such resonances when they decay into SM states. Less explored is the possibility that the s-channel resonance decays into non-SM states, as predicted in many new physics models. In such a case dedicated searches should be performed. We have concentrated here on the case where the new resonance decays into a VLQ and a SM fermion and identified all the possible quantum numbers of the VLQ; our list contains VLQs with charges of $5/3$, $2/3$, $-1/3$ and $-4/3$. We have also commented on the phenomenology of these new states. While for some specific quantum numbers the VLQs can mix with the SM quarks through a Yukawa type interaction and hence decay into SM states, for some of the cases we have observed that this was not possible. The VLQs can then decay only via "backwards" decay, meaning via the (off-shell) heavy boson through which they were produced. Depending on the coupling strength between these states, the VLQ might be long-lived giving rise to a peculiar phenomenology which deserves a deeper investigation.

ACKNOWLEDGEMENTS

The authors would like to thank the organizers of the Les Houches workshop where this work was initiated. RG is supported by a European Union COFUND/Durham Junior Research Fellowship under the EU grant number 609412. TF is supported by IBS under the project code IBS-R018-D1. TR was supported by the Department of Energy, Contract DE-AC02-76SF00515, and BF has been partly supported by French state funds managed by the Agence Nationale de la Recherche (ANR), in the context of the LABEX ILP (ANR-11-IDEX-0004-02, ANR-10-LABX-63). WP is supported by the DFG, project nr. PO 1337-7/1.

Contribution 3

Precision predictions for the single production of third generation vector-like quarks

G. Cacciapaglia, A. Carvalho, A. Deandrea, T. Flacke, B. Fuks, D. Majumder, L. Panizzi

Abstract

We study the effects of next-to-leading-order corrections in QCD on the single production of third generation vector-like quarks, assuming standard couplings of the extra quarks to the weak gauge and Higgs bosons so that they could decay into one of these bosons and a Standard Model quark.

1 INTRODUCTION

Vector-like quarks (VLQs), *i.e.* coloured heavy fermions that have non-chiral couplings to the Standard Model (SM) gauge interactions, are a common ingredient of many models of new physics. In particular, when they couple to the third generation of SM quarks, they often play a role in the fine-tuning problematics of the Higgs-boson mass. In addition, they also appear in models with extra space dimensions. These reasons, together with the fact that they can be copiously produced at hadron colliders, make them an ideal target to be searched for at the LHC and at future hadron colliders.

Many searches targeting VLQs coupled to third generation quarks are performed by both the ATLAS and CMS collaborations [22, 76–79], although specific searches complementarily focus on VLQs coupling to light quarks [80, 81]. In the third generation case, the considered final state contains one third generation quark (top or bottom) and one SM weak or Higgs boson (W-boson, Z-boson or a Higgs boson). The corresponding branching ratios in each channel depend on the details of the model, and in particular on the dimension of the $\mathrm{SU}(2)_L$ multiplet the VLQ belongs to and on the electroweak symmetry breaking pattern. In a previous Les Houches workshop [82], some of the authors of this contribution worked out a model-independent strategy to study the most general decay pattern relying on a parameterisation of the couplings in terms of the physical branching ratios [83–85]. However, non-standard decay modes may still be allowed in specific models, for which a full classification can be found in Ref. [72] and dedicated analyses in Refs [70, 71, 86–89].

In this project, we focus on the standard channels, but we aim at studying in detail effects that arise from next-to-leading order (NLO) corrections in QCD. While such effects are well studied for the QCD production of a pair of VLQs, which is analogous to top-antitop pair production, no such studies exist for VLQ single production. In Ref. [90], some of us published a FeynRules [91] implementation of a general VLQ model that includes full NLO effects in QCD. This model was developed as part of a previous Les Houches project [72], and applied first to the study of di-Higgs final states originating from the decays of on-shell VLQs that couple to first generation quarks [92]. We now use this implementation to study the kinematic distributions of jets produced in association with a single VLQ of third generation, the most

well-known examples of such a new physics state being top partners, *i.e.* VLQs with the same SM quantum numbers as the top quark.

2 THE MODEL AT NLO

There are four types of VLQs that can decay directly into a SM quark plus a boson, and they are distinguished by their electromagnetic charge: two have the same charge e_Q as the top and bottom quarks respectively, and we call them T ($e_T = 2/3$) and B ($e_B = -1/3$), and two exhibit exotic charges that differ by one unit from the standard ones, X ($e_X = 5/3$) and Y ($e_Y = -4/3$). The leading order Lagrangian that we have implemented reads [90]

$$\begin{aligned}\mathcal{L}_{\rm LO} = i\bar{Q}\not{D}Q - m_Q\bar{Q}Q - h\left[\bar{B}\left(\hat{\kappa}_L^B P_L + \hat{\kappa}_R^B P_R\right) B + \bar{T}\left(\hat{\kappa}_L^T P_L + \hat{\kappa}_R^T P_R\right) T + \text{h.c.}\right] \\ + \tfrac{g}{2c_W}\left[\bar{B}\not{Z}\left(\tilde{\kappa}_L^B P_L + \tilde{\kappa}_R^B P_R\right) b + \bar{T}\not{Z}\left(\tilde{\kappa}_L^T P_L + \tilde{\kappa}_R^T P_R\right) t + \text{h.c.}\right] \\ + \tfrac{g}{\sqrt{2}}\left[\bar{B}\not{W}^-\left(\kappa_L^B P_L + \kappa_R^B P_R\right) t + \bar{T}\not{W}^+\left(\kappa_L^T P_L + \kappa_R^T P_R\right) b + \text{h.c.}\right] \\ + \tfrac{g}{\sqrt{2}}\left[\bar{X}\not{W}^+\left(\kappa_L^X P_L + \kappa_R^X P_R\right) t + \bar{Y}\not{W}^-\left(\kappa_L^Y P_L + \kappa_R^Y P_R\right) b + \text{h.c.}\right], \end{aligned} \tag{1}$$

where $Q = X, T, B, Y$. The covariant derivative only contains gauge interactions from QCD and QED, the couplings of a pair of VLQs to W-bosons and Z-bosons being omitted as they are very model dependent and give minor contributions to the production cross sections [83]. This model differs slightly from the parameterisation proposed in Ref. [83] in the mass dependence of the couplings that has been removed. The reason behind this choice is to render the NLO implementation easier, as the couplings can be renormalised independently of the masses. There is however a qualitative (and quantitative) difference between the VLQ coupling to the Higgs-boson h and that to the gauge bosons. The former corresponds to a Yukawa coupling while the latter to a mixing angle, and the relation between the two is a factor v/m_Q where v is the vacuum expectation value of the SM Higgs field [85].

Our simulations for the LHC make use of an NLO model file encoded in the UFO format [93] that has been generated with the FEYNRULES [91] and NLOCT [94] packages. The resulting UFO library contains tree-level vertices as well as ingredients necessary for the evaluation of one-loop diagrams in MADGRAPH5_aMC@NLO [95]. For more details on the validation of our implementation we refer to Ref. [90]. We then use the MADGRAPH5_aMC@NLO platform for generating events both at the LO and NLO accuracy in QCD. We have used the NNPDF2.3 (LO QCD + LO QED) [96] for the LO processes, while for the NLO processes we have used the NNPDF3.0 (NLO) set. The simulation of the QCD environment (parton showering and hadronisation) has been achieved with PYTHIA 8.2 [97], while the jet reconstruction has been made by using using the anti-k$_T$ algorithm [98] with radius 0.4 and b-jet tagging with distance ΔR=0.5, implemented in FASTJET 3.2.1 [99].

2.1 Simulation results

One of the main impacts of the QCD corrections to the single production of a VLQ is to modify the corresponding production cross-section. We focus in this work on single VLQ production in association with a jet, as illustrated by the representative Feynman diagrams of Fig. 1 for single T production. At tree-level, such a process occurs through VLQ couplings to the W-boson (*i.e.* the $\kappa_{L/R}^T$ interactions), while for single B production it occurs through the VLQ coupling to the Z-boson (*i.e.* the $\tilde{\kappa}_{L/R}^B$ couplings). Total rate results given as a function of the mass of the T and

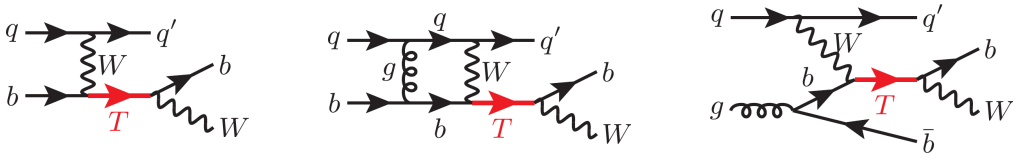

Figure 1: Subset of topologies for single T production at the LHC. Left panel: Tj production at LO in the 5FNS; central panel: NLO QCD contribution to the Tj process in the 5FNS; right panel: real emission for the Tj process in the 5FNS and LO topology for the Tjb process in the 4FNS.

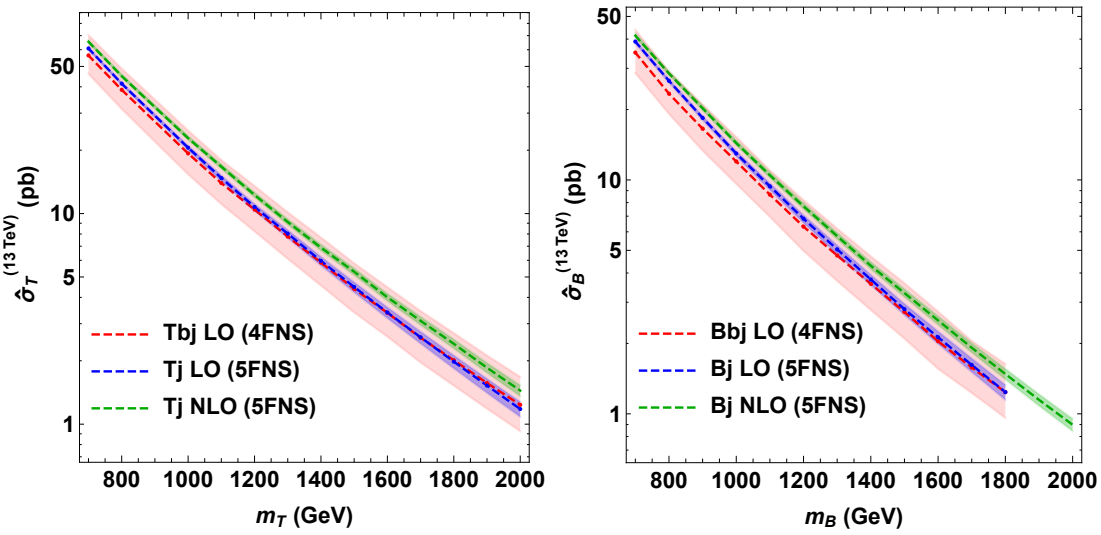

Figure 2: Production cross section of a single VLQ in association with jets for LHC collisions at a centre-of-mass energy of 13 TeV. We present results in the case of a T (left) and B (right) quark, and show their dependence on the VLQ mass. The cross sections are normalised to $\kappa^T = \tilde{\kappa}^B = 1$.

B quark, and for LHC collisions at a centre-of-mass energy of 13 TeV, are shown in Fig. 2. We compare predictions in the 5-flavour-number scheme (5FNS) with predictions in the 4-flavour-number scheme (4FNS). In the 5FNS, bottom quark contributions to the parton densities of the proton are included, while in 4FNS, initial bottom quarks originate from gluon splitting. The results are normalised to κ parameter values equals to 1, and include contributions from both VLQ and anti-VLQ production. While calculations in the 5FNS are easier and hence allows to include higher-order corrections, 4FNS results are known to better describe the shapes of the kinematic distributions.

The global effect of the NLO corrections is to increase the cross-section value and to generally reduce the scale uncertainties, although new subprocesses may appear at NLO and contribute significantly enough to spoil the reduction of the uncertainties. Results in the 4FNS and 5FNS agree, after accounting for the uncertainties. Significant NLO effects are however expected when considering more exclusive observables like those related to the final-state jet properties. For instance, the kinematics of the b-jet produced in association with the VLQ is crucial. While such a jet already appears at tree-level in the 4FNS, as this consists in a $2 \to 3$ process (see Fig. 1), NLO corrections are required in the 5FNS as b-jets arise at the lowest order through radiative contributions. To ascertain which strategy better characterises the kinematic properties of the event, we compare below distributions obtained by the three calculations, *i.e.*

in the 4FNS (at LO, $2 \to 3$ process) and in the 5FNS (at LO and NLO). NLO corrections to the 4FNS results are left to future work.

To this end, in the remaining of this contribution we consider single-T quark production where the extra quark decays with a 100% branching fraction into a Wb system. In Fig. 3, we compare the (normalised) distributions of the transverse momentum (p_T) and pseudorapidity (η) of the leading (top row) and sub-leading (bottom row) reconstructed b-jets, for a T mass set to $M_T = 1200$ GeV, and after applying cuts on the b-jet $p_T > 20$ GeV and $|\eta| < 5$. The markedly central pseudorapidity distribution of the leading b-jet and the steep fall of the p_T distribution for p_T values larger than $M_T/2 = 600$ GeV show that this jet can clearly be associated with the bottom quark originating from the T-quark decay, independently on the scheme in which the calculation has been made. Furthermore, as the decay of the T-quark is computed at the LO accuracy in all cases, the leading b-jet distributions do not exhibit clear differences between the LO and NLO results, except for a slight tendency towards softer p_T values at NLO as shown by the reduction of events with p_T larger than $M_T/2 = 600$ GeV. The sub-leading b-jet distributions shows as well a slightly different behaviour. The soft p_T spectrum is in agreement with the fact that this jet originates from radiation, as it is the case for all the events in the 5FNS-LO. The pseudorapidity shows a slight difference between the two LO results and the NLO one, the latter exhibiting a tendency to more forward distribution of b-jets. A more thorough investigation of these results is needed to draw definite conclusions. Our preliminary results show, nevertheless, that properly accounted NLO effects are crucial for an accurate description of the kinematic distributions of the additional jets accompanying the singly produced VLQ.

For completeness, in Fig. 4 we show the transverse momentum and pseudorapidity distributions for the leading (non-b) jet. In this case, we observe that the NLO results showcase more forward jets, together with a population of jets which are more markedly central. Note that we selected only events featuring a leptonic decay of the W-boson, so that the jet distributions do not include the ones from hadronic W decays (which tend to have higher transverse momentum and be central). Further investigation of the features of these results, together with NLO distributions in the 4FNS, are under way.

CONCLUSIONS

We have studied the single production of third generation VLQs, which can decay into a SM quark plus a SM boson, at NLO in QCD. While the total single production cross-section is only slightly affected by the corrections (as the main production diagrams are of electroweak origin), we have shown that the detailed distributions are in contrast significantly impacted.

ACKNOWLEDGEMENTS

We would like to thank the organisers of the 2017 Les Houches workshop on TeV colliders for the hospitality and the nice atmosphere offered during which some of the work contained herein was performed. TF is supported by IBS under the project code IBS-R018-D1, and BF is partly supported by French state funds managed by the Agence Nationale de la Recherche (ANR), in the context of the LABEX ILP (ANR-11-IDEX-0004-02, ANR-10-LABX-63). GC and AD acknowledge partial support from the Labex-LIO (Lyon Institute of Origins) under grant ANR-10-LABX-66 and FRAMA (FR3127, Fédération de Recherche “André Marie Ampère”).

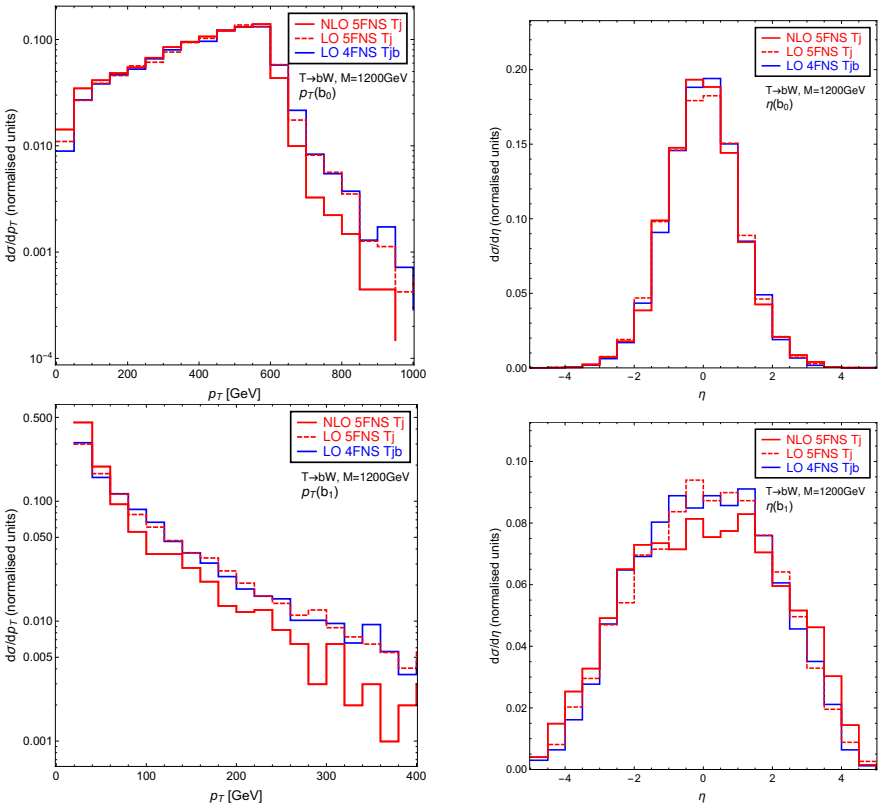

Figure 3: Normalised distributions of the transverse momentum and pseudorapidity of the leading (top row) and sub-leading (bottom row) reconstructed b-jets for single T production, *i.e.* $pp \to Tj$ in the 5FNS at LO and NLO and $pp \to Tbj$ in the 4FNS at LO after including a subsequent $T \to bW$ decay for M_T=1200 GeV.

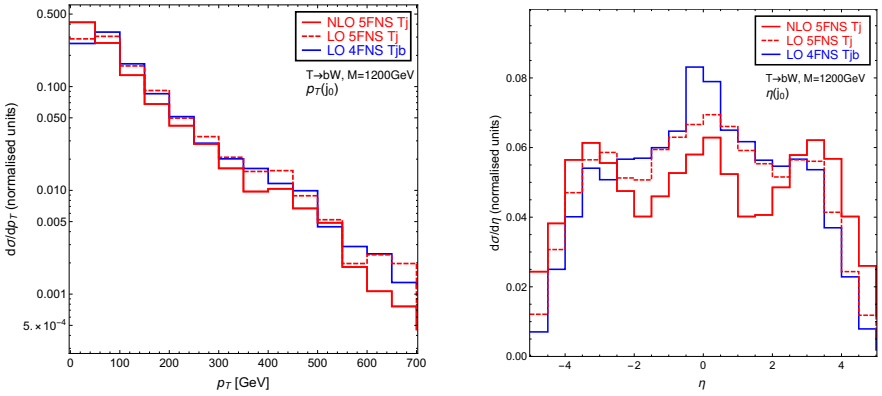

Figure 4: Normalised distributions of the transverse momentum and pseudorapidity of the leading jets (non-b) for the processes $PP \to Tj$ (5FNS at LO and NLO) and $PP \to Tbj$ (4FNS at LO) with subsequent $T \to bW$ decay for M_T=1200 GeV. We select leptonic decays for the W.

Contribution 4

Long-lived particles at the LHC and freeze-in dark matter

G. Bélanger, H. Cai, N. Desai, A. Goudelis, J. Harz, A. Lessa, J. M. No, A. Pukhov, S. Sekmen, D. Sengupta, B. Zaldivar and J. Zurita

Abstract

Long-lived particles appearing in models in which dark matter is produced via the freeze-in mechanism can be probed at the LHC. This is illustrated for the case of a long-lived charged fermion which decays into dark matter and a lepton (electron or muon), using a search for heavy stable charged particles and a displaced lepton search by the CMS collaboration.

1 INTRODUCTION

The search for long-lived particles (LLPs) at the Large Hadron Collider (LHC) has recently gained momentum in the high-energy physics community. One obvious reason for this tendency is the lack of evidence for physics Beyond the Standard Model (BSM) in more traditional searches involving, for example, several jets along with missing transverse momentum. Thus, other –more exotic– analyses should be invoked in order to make the most of the present experimental capabilities.

From an experimental standpoint, an LLP is a BSM state with a macroscopic lifetime, typically longer than a few hundreds of ps. From the theory side, there are essentially two ways in which a particle produced at the LHC can decay slowly enough to be considered an LLP: 1) the decay is kinematically suppressed because the particle is part of a new sector characterised by a compressed enough mass spectrum, or 2) the decay is suppressed due to small (effective) couplings to the "daughter" particles. The latter can arise in several ways (mass suppression, breaking of symmetries, fine-tuning, etc) , and we are ultimately agnostic about its origin. The case of kinematic suppression has so far been the most studied one, for example in the context of Supersymmetry [100–106]. In this work we will instead focus on the case in which long particle lifetimes are due to coupling suppression.

At the same time, the search for dark matter (DM)[1] at the LHC is currently one of the most active topics of research. Typically, DM searches are interpreted in the framework of WIMPs (Weakly Interacting Massive Particles). These DM candidates are characterised by couplings to the SM of the order of the electroweak interactions, and thus, they could be copiously produced at the LHC. However, as mentioned before, no evidence of WIMPs has appeared so far, which motivates the consideration of other types of DM candidates. For example, DM could be made up of particles whose interactions with the SM are extremely suppressed such that, contrary to WIMPs, their production in the early universe would be out of thermal equilibrium with the SM (or, more generally, the visible) sector. Such types of DM candidates have been dubbed FIMPs

[1] As usual, note that the LHC itself cannot determine whether a particle escaping the detectors is (at least) part of the observed DM in the universe, since it requires complementary information from other DM-related experiments.

(Feebly Interacting Massive Particles), and they can be produced through the so-called freeze-in mechanism [107, 108]. The purpose of this work is to establish a link between the search for LLPs at the LHC and the freeze-in production of FIMP dark matter.

Indeed, the process through which a particle produced at the LHC decays into DM far away from the collision point could also be the one responsible for the DM production in the early universe. To the best of our knowledge, there are just a few examples in the literature which have studied this connection see, *e.g.* [109–111]. Here, we study the connection between LLPs and FIMPs in one of the simplest freeze-in DM models that could give rise to observable signals at the LHC. We consider the case in which an electrically charged mother particle decays into a neutral one (a DM candidate) along with a lepton. The lifetime of the mother particle is such that the corresponding signature consists of a Heavy Stable Charged Particle (HSCP) producing a heavily ionised track or a displaced vertex.

In this model, there is a one-loop contribution to $\mu \to e, \gamma$. However, for the values of the couplings under consideration, this constribution is much below the current sensitivity [112].

2 THE MODEL

We consider an extension of the Standard Model by an additional real scalar field s that transforms trivially under $SU(3)_c \times SU(2)_L \times U(1)_Y$ as well as an additional vector-like charged lepton E transforming as $(\mathbf{1}, \mathbf{1}, -\mathbf{1})$ [2] . Both particles are taken to be odd under a discrete $\mathcal{Z}_2$ symmetry, whereas all Standard Model fields are taken to be even. Under these assumptions, the Lagrangian of the model reads

$$\begin{aligned}\mathcal{L} = \mathcal{L}_{\rm SM} + (\partial_\mu s)(\partial^\mu s) - \frac{\mu_s^2}{2}s^2 - \frac{\lambda_s}{4}s^4 - \lambda_{sh}s^2\left(H^\dagger H\right) \\ + i\left(\bar{E}_L \not{D} E_L + \bar{E}_R \not{D} E_R\right) - \left(m_E \bar{E}_L E_R + y_e s \bar{E}_L e_R + y_\mu s \bar{E}_L \mu_R + \text{h.c.}\right),\end{aligned} \tag{1}$$

where $E_{L,R}$ and e_R, μ_R are the left- and right-handed components of the heavy lepton and the right-handed component of the Standard Model electron and muon, respectively. For simplicity we have neglected couplings to the third generation leptons. The model is described by six free parameters, namely

$$\mu_s,\ \lambda_s,\ \lambda_{sh},\ m_E,\ y_e,\ y_\mu \tag{2}$$

out of which λ_s is irrelevant for our purposes whereas μ_s can be traded for the physical mass of s through $\mu_s^2 = m_s^2 + \lambda_{sh}v^2$, where v is the Higgs vacuum expectation value. For simplicity, we will also take the coupling λ_{sh} to be identically zero. These choices leave us with only four free parameters

$$m_s,\ m_E,\ y_e,\ y_\mu. \tag{3}$$

Due to its electric charge, the heavy lepton E is kept in thermal equilibrium with the SM thermal bath in the early Universe. For $m_s < m_E$, the scalar s becomes stable and can play the role of a dark matter candidate.

Note that the model described by Lagrangian (1) can, for light enough values of m_E, lead to substantial contributions to the SM Z boson decay width. Throughout the following, we will always place ourselves in the situation $m_E > m_Z/2$.

[2] The vector-like nature of E ensures that the model is anomaly-free.

3 FREEZE-IN PRODUCTION

The dominant processes contributing to DM production are $E \to es$ and $E \to \mu s$. Additional contributions can come from scattering processes, which we have found to be subleading for our choices of parameter values. The Boltzmann equation for DM can be written as:

$$\begin{aligned} \dot{n}_s + 3Hn_s &= \sum_i \int \frac{d^3p_E}{(2\pi)^3 2E_E} \frac{d^3p_i}{(2\pi)^3 2E_i} \frac{d^3p_s}{(2\pi)^3 2E_s} (2\pi)^4 \delta^{(4)}(P_E - P_i - P_s) |\mathcal{M}_i|^2 \\ &\times \left[f_E(1-f_i)(1+f_s) - f_i f_s (1-f_E) \right] , \end{aligned} \tag{4}$$

where the sum runs over the two processes with $i = e, \mu$. Besides, n_s is the DM number density, H the Hubble parameter, $P_k = (E_k, p_k)$ the four-momentum of particle k with distribution function f_k. $\mathcal{M}$ denotes the amplitude of the process.

Simplifying assumptions. The standard freeze-in computation relies on the following assumptions: 1) the initial density of DM particles is zero such that (for small enough couplings) the annihilation term can be neglected, 2) DM production occurs during the radiation dominated era, and 3) Maxwell-Boltzmann distribution functions are assumed for all bath particles (i.e. no difference between bosons and fermions)[3].

By adopting these simplifications the comoving DM number density (or yield Y_s) is given by the following expression:

$$Y_s \approx \frac{45 \xi M_{\rm Pl}}{8\pi^4 \cdot 1.66} \frac{g_E}{m_E^2} \Gamma \int_{m_E/T_R}^{m_E/T_0} dx\, x^3 \frac{K_1(x)}{g_*^s(x)\sqrt{g_*(x)}}, \tag{5}$$

where $\xi = 2$ since the decaying particle E is not self-conjugate (otherwise $\xi = 1$), g_E are the internal degrees of freedom of E and Γ the sum of all partial decay widths into DM: $\Gamma = \Gamma_e + \Gamma_\mu$. $M_{\rm Pl} = 1.2 \times 10^{19}$ GeV is the Planck mass, T_R the reheating temperature of the universe (an input for freeze-in calculations), T_0 is the temperature today, $K_1(x)$ is the modified Bessel function of the second kind of degree 1, and g_*, g_*^s the effective degrees of freedom for the energy and entropy densities, respectively. The relation between today's relic abundance and yield of DM is [108]:

$$\Omega_s h^2 \approx \frac{m_s Y_s}{3.6 \times 10^{-9} \text{GeV}} . \tag{6}$$

Most of the details of the model in Eq. (5) are encoded in the expression for the decay width Γ, which leads to the lifetime

$$c\tau \sim 10^3 \text{ cm} \left(\frac{10^{-9}}{y_e^2 + y_\mu^2} \right) \left(\frac{\text{TeV}}{m_E} \right) . \tag{7}$$

Consequently, by assuming that freeze-in via decay of the LLP is the dominant mechanism responsible for DM abundance, we can make a fairly model-independent connection between the lifetime of the LLP and the LLP and DM masses by requiring the correct DM abundance via freeze-in:

$$c\tau \approx 4.5 \text{ m } \xi g_E \left(\frac{0.12}{\Omega_s h^2} \right) \left(\frac{m_s}{100 \text{keV}} \right) \left(\frac{200 \text{GeV}}{m_E} \right)^2 \left[\frac{\int_{m_E/T_R}^{m_E/T_0} dx\, x^3 K_1(x)}{3\pi/2} \right] , \tag{8}$$

[3] See [113] and [114] for a more detailed discussion on the distribution functions of the bath particles.

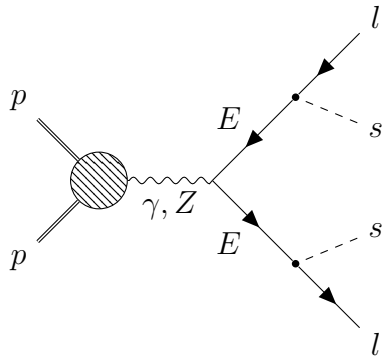

Figure 1: *Diagram for the main production and decay process of E at the LHC.*

where we have evaluated $g_*(x), g_*^s(x)$ on $x = 3$ [4]. Note the large hierarchy of masses between the DM and the mother particle, needed in order to obtain the observed relic abundance while having a sufficiently long lifetime for the LLP, provided $m_E \ll T_R$.[5] Alternatively, a freeze-in solution for DM masses $m_s \gg$ MeV could be obtained by decreasing the reheating temperature, such that $m_E \gtrsim T_R$. This means essentially that the DM production history is shorter, relying only on the Boltzmann tail of the mother particle. In this work we will adopt the former regime.

We have solved numerically the Boltzmann equation (4) with the `micrOMEGAs 5.0` code [113] under the assumptions discussed above. The results are in good agreement with the analytical approximation (8) shown in Fig.3.

4 LHC CONSTRAINTS

As illustrated in Fig. 3, in order for the scenario described in Sec. 2 to produce the observed dark matter relic abundance, the vector-like lepton (E) lifetime has to be larger than $\simeq 0.01$ ns (corresponding to $c\tau \sim 0.1$ m). Consequently, if E is produced at the LHC with moderate to high velocities, it will cross a macroscopic distance in the detector. Searches for long lived particles (LLPs) can then be used to constrain this scenario. In our model, E will always be pair-produced via a Drell-Yan process at the LHC and will then decay via the $s - E - e/\mu$ coupling, as shown in Fig. 1. The LLP signature associated with the production of E's strongly depends on their lifetime. For $\tau \lesssim 10$ ns, the decay occurs mostly inside the tracker, leading to a displaced lepton or tracks with kinks. If E is sufficiently long lived to decay outside the detector ($\tau \gtrsim 100$ ns) or outside the tracker ($\tau \gtrsim 10$ ns), it will appear as a heavy stable charged particle (HSCP). Below we will discuss how the LHC searches for displaced leptons and HSCPs constrain the parameter space of the model.

4.1 HSCP Searches

If the vector-like lepton (E) has a $c\tau$ of the order of a few meters, it will deposit a considerable fraction of its energy in the tracker. Due to its large mass, the long-lived particle will be produced in the non-ultrarelativistic regime, thus leading to a highly ionized track, which can be

[4] This turns out to be a good approximation since for this model, most of the production occurs around the freeze-in temperature $T \approx m_E/3$.

[5] For $T_0 \ll m_E \ll T_R$, the ratio in squared brackets in Eq. (8) will approach to 1.

distinguished from the ultrarelativistic tracks produced by long-lived Standard Model particles. Furthermore, if the LLP traverses the muon chambers, it will produce a non-ultrarelativistic track with a larger (or anomalous) *time-of-flight* (TOF) than the one expected from muons, since $\beta_{\text{HSCP}} < 1$. This anomalous TOF can also be used when searching for HSCPs. Both ATLAS and CMS have performed HSCP searches at 7, 8 and 13 TeV [115–120]. Because of their small background, these searches are highly sensitive to charged LLPs and model independent, since no special veto (except for some basic HSCP isolation) is imposed on the signal. Here we will consider the results obtained by the CMS 8 TeV search [117], as it provides all the detailed information required for re-interpretation of the HSCP limits. The 8 TeV search presents limits for charged LLPs using only tracker data as well as tracker plus muon chamber (or time-of-flight) data. As mentioned above, the former is more sensitive to lifetimes satisfying $3\text{ m} \lesssim c\tau \lesssim 10\text{ m}$, while the latter is more sensitive for $c\tau \gtrsim 10$ m. Since the E lifetime can vary in a wide range of values (*cf Sec. 2*), we will consider both the tracker-only and the tracker plus time-of-flight constraints. In order to compute the constraints on our model, we use MADGRAPH5_AMC@NLO [95] and PYTHIA 8.2 [97] to simulate events for the pair production of E's.

Using the full recasting of the tracker plus time-of-flight analysis discussed in Appendix A, we computed the expected number of signal events for the FIMP scenario described in Sec. 2. The signal yield, along with the number of observed and expected background events provided by CMS [121], allows us to constrain the model parameter space. The red region in Fig. 2 shows the region in the $c\tau$ vs m_E plane excluded at 95% C.L. by the tracker plus TOF data. For very large lifetimes we obtain a constraint $m_E > 550$ GeV. It is important to point out that due to its vector-like and fermionic nature, the cross-section for E pair production is significantly higher than the corresponding cross-section for charged scalars. For this reason the constraints on m_E are stronger than the ones obtained by CMS for pair production of staus [117]. Once the vector-like lepton is no longer stable at detector scales, the limits on its mass become increasingly weaker. In particular, for $c\tau \simeq 2$ m, we have $m_E \gtrsim 200$ GeV.

Although the limits obtained using the tracker plus TOF data become weaker once $c\tau \lesssim 5$ m, if the LLP decay occurs outside the tracker volume, it is still possible to constrain our scenario using the tracker-only data. In Ref. [117] CMS has provided cross-section upper limits (as a function of the LLP mass) for the tracker-only analysis. However, the corresponding trigger and selection efficiencies are not publicly available, hence a full recasting of the tracker only search is not feasible. Nonetheless, since the Drell-Yan process for production of the vector-like leptons E shown in Fig. 1 is kinematically similar to pair production of staus, it is still possible to re-interpret the CMS limits for long-lived staus and use them to constrain the FIMP scenario. The CMS limits from Ref. [117] are given for the total production cross-section of staus as a function of its mass under the assumption that the staus are stable at detector scales ($c\tau \gg 10$ m). Therefore we can not directly apply the limits to the E production cross-section, $\sigma(EE)$, if the vector-like lepton has a finite lifetime. In order to account for the finite lifetime – induced – suppression of the limits, we compute an effective production cross section using:

$$\sigma_{eff}(EE) = \sigma(EE) \times f_L \tag{9}$$

where f_L represents the effective fraction of HSCPs which have decayed at a distance L from the primary vertex. This fraction depends on the LLP lifetime and the size of the tracker, which we assume to be 3 m, since it approximately corresponds to the maximum tracker radius in CMS. For the specific details on the calculation of f_L, see Appendix A.

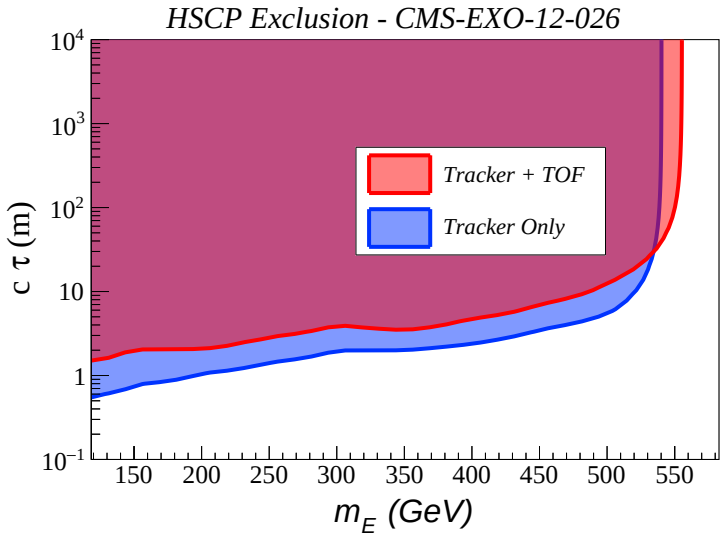

Figure 2: *LHC contraints on the LLP vector-like lepton model. The red area corresponds to the region of the FIMP parameter space excluded by the 8 TeV CMS search for HSCPs [121] using the tracker plus time-of-flight data. The red region shows the corresponding bounds using the tracker-only data. See text for more details.*

Once the effective cross-section is computed for each value of m_E and τ, we can directly compare it to the corresponding cross-section upper limit (σ_{UL}) presented by CMS in Ref. [117]. If $\sigma_{eff}(EE) > \sigma_{UL}$ we consider the point in parameter space to be excluded by the CMS 8 TeV search. The results are shown by the blue region in Fig. 2. As expected, for small lifetimes ($c\tau \lesssim 30$ m) the constraints are more severe than the ones obtained previously, while for large lifetimes, the tracker-only limits are slightly weaker than the tracker plus TOF ones, resulting in $m_E > 540$ GeV instead.

4.2 Displaced Lepton Searches: $e\mu$

For LLP decay lengths in the range $c\tau \sim 0.1 - 100$ mm, the LLP can decay at a sizable distance from the interaction point. If the decay products are charged, this leads to tracks with a non-zero impact parameter (which can further be used to reconstruct displaced vertices). The simplest of such searches is the CMS search for events with oppositely charged, displaced electrons and muons, conducted at both 8 TeV [122] and 13 TeV [123] runs. This search is potentially sensitive to our model if E decays with similar branching fractions to electrons and muons ($y_e \simeq y_\mu$).

Here we analyze the bounds from the 13 TeV CMS search with 2.6 fb^{-1} [123]. The discriminating variable is the transverse impact parameter d_0, defined as the closest distance between the beam axis and the track in the transverse plane. For our study, we use generator-level information to calculate the transverse impact parameter of the lepton as:

$$d_0^\ell = \frac{\left| p_x^\ell L_y - p_y^\ell L_x \right|}{p_T^\ell} \tag{10}$$

where $L_{x,y}$ the distance in x, y travelled by the LLP before decaying, p_T^ℓ the transverse momentum of the lepton and $p_{x,y}^\ell$ the x, y components of the lepton and LLP 3-momenta.

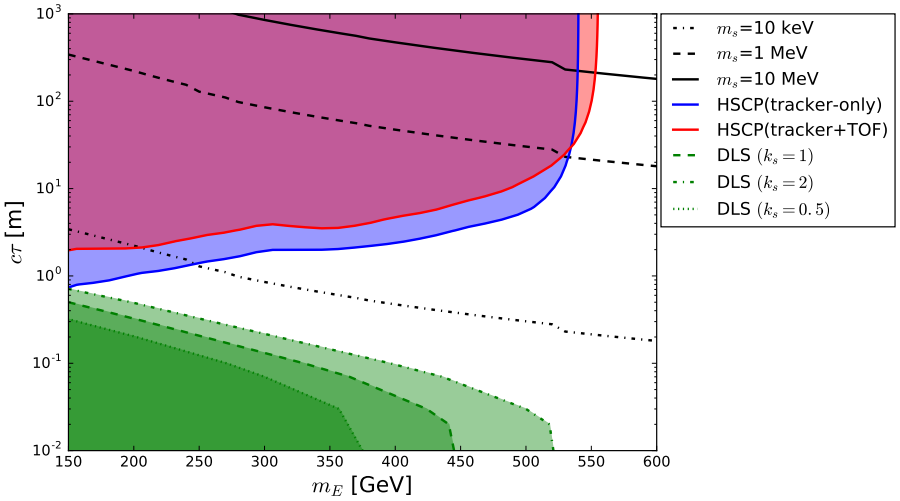

Figure 3: *Summary plot of this work. Iso-contours of the DM relic abundance $\Omega_s h^2 = 0.12$ are shown for three different masses: m_s =10 MeV (black solid), 1 MeV (black dashed) and 10 keV (black dot dashed), according to the freeze-in calculation, where the reheating temperature is taken as $T_R = 10^{10}$ GeV. Red and blue regions are excluded by the HSCP searches, wheres green regions are excluded by the displaced lepton searches. See text for more details.*

The displaced-$e\mu$ CMS search selects events with exactly one electron and one muon with $|\eta_\ell| < 2.4$ and $p_T^\ell > 42$ (40) GeV for electrons (muons), in addition to $\Delta R_{e\mu} > 0.5$ and further isolation criteria for both leptons[6]. The search then defines three non-overlapping signal regions (SR):

- SR III: Both d_0^e and $d_0^\mu \in [1, 100]$ mm.
- SR II: Both d_0^e and $d_0^\mu > 0.5$ mm but one or both leptons fail SR III.
- SR I: Both d_0^e and $d_0^\mu > 0.2$ mm but one or both leptons fail SR III and SR II.

We use MADGRAPH5_AMC@NLO [95] to simulate E^+E^- production from Drell-Yan, with the vector-like leptons Es decaying to electrons and muons with equal branching fractions. We include a flat NLO κ-factor for Drell-Yan E^+E^- production, $\kappa \sim 1.2$ [124]. We use identification efficiencies for electrons and muons as a function of p_T^ℓ and d_0^ℓ publicly provided in the displaced-$e\mu$ 8 TeV CMS analysis [122]. Since it has been shown that using this parametrisation leads to a factor of two mismatch when extrapolating to 13 TeV[7], we show all limits with a rescaling of the signal s_i (i = I, II, III) by $\kappa_s = 2,\ 1,\ 1/2$.

Once we obtain the number of expected signal events in SR I, II, III, $s_i(c\tau, m_{\rm LLP})$, we perform a likelihood analysis to obtain the 95 % C.L. exclusion limit from the 13 TeV displaced-$e\mu$ CMS search in the $(c\tau, m_{\rm LLP})$ plane. Our likelihood function is built as a product of Poisson

[6] A lepton is considered "isolated" if the sum of the p_T of *all other* particles in a cone of radius R around it, normalized to its own p_T, is below a cut-off value ϵ. For electrons in the barrel, electrons in the endcap and muons we have $(R, \epsilon) = (0.3, 3.5\%), (0.3, 6.5\%)$ and $(0.4, 15\%)$ respectively.

[7] For validation of the displaced-$e\mu$ 13 TeV CMS analysis using these efficiencies, see Cottin et al. in the same proceedings volume.

probabilities for the three SR

$$L^{\ell}(s_i, \kappa_s) = \prod_{i=\mathrm{I,II,III}} e^{-(\kappa_s s_i + b_i)} \, \frac{(\kappa_s s_i + b_i)^{n_i}}{n_i!} \,, \tag{11}$$

with b_i the number of predicted background events in SR I, II, III, being respectively < 3.2, < 0.50, < 0.020 (for the present analysis, we assume these inequalities are saturated), and n_i the number of observed events in SR I, II, III, being respectively 1, 0, 0. The significance is estimated via the test statistic $Q^{\ell}_{\kappa_s}$,

$$Q^{\ell}_{\kappa_s} \equiv -2 \, \mathrm{Log} \left[\frac{L^{\ell}(s_i, \kappa_s)}{L^{\ell}(0)} \right] \,, \tag{12}$$

and the 95 % C.L. exclusion limit is given by $Q^{\ell}_{\kappa_s}(s_i(c\tau, m_{\mathrm{LLP}})) = 3.84$. We show the respective limits for $\kappa_s = 2,\, 1,\, 1/2$ in Fig. 3. These limits are highly complementary to those from HSCP searches discussed in section 4.1, ruling out $c\tau < 30$ cm for $m_E = 200$ GeV (for $\kappa_s = 1$). For LLP decays $c\tau \sim 1$ cm, the bounds go as far as imposing $m_E > 440$ GeV. The effect of a possible higher efficiency in moving from 8 TeV to 13 TeV, $\kappa_s = 2$, is also apparent from Fig. 3, extending the limits to rule out $m_E < 520$ GeV for $c\tau = 1$ cm and $c\tau < 50$ cm for $m_E = 200$ GeV. In such a case the combination of the 13 TeV displaced $e - \mu$ CMS search and HSCP searches can rule out $m_E < 150$ GeV through the entire freeze-in parameter space of the model.

In any case, we need to stress again that the bounds from the 13 TeV displaced-$e\mu$ CMS search shown in Fig. 3 apply in the limit $y_e = y_\mu$, but as soon as one departs from this scenario and one of the $E \to \ell s$ ($\ell = e,\, \mu$) branching fraction dominates over the other, the bounds are correspondingly weaker as the signal is proportional to the product of the two branching ratios.

CONCLUSIONS

Dark matter is undoubtedly a driver for the construction of Standard Model extensions. Here we have studied the connection between the freeze-in mechanism and the LHC searches for long-lived particles. An alternative scenario to the vanilla thermal paradigm, freeze-in drives out-of-equilibrium dark matter production via tiny $\mathcal{O}(10^{-10})$ couplings which guarantee macroscopic lifetimes irrespectively of the mass splittings between the new states. Employing a simplified model featuring a scalar dark matter particle and a long-lived charged fermion, we have used two out of the ample LHC LLP searches, namely the Heavy Stable Charged Particles (HSCP) and the high-impact displaced lepton ones, to show that LLP masses up to about 550 GeV can be probed by the current LHC.

The case of a very light dark matter (below the MeV scale) which is associated with a shorter lifetime of the new heavy charged lepton is the most challenging to probe. Nevertheless, a combination of these two searches can rule out masses of the new charged lepton up to 150 GeV for the full parameter space compatible with the freeze-in scenario within the assumption that the heavy lepton decays with the same branching fraction into electrons and muons. We further expect the constraints from HSCP searches to improve with the use of 13 TeV data. early results show that the gain in sensitivity in the case of stable staus reaches about 200GeV with early 13 TeV data [125]. Cosmologically viable scenarios involving heavier dark matter and shorter heavy lepton lifetimes are likely to require a modification of the thermal history of the Universe and will be studied in future work.

ACKNOWLEDGEMENTS

The work of G.B., A.P. and B.Z. was supported in part by the French ANR, Project DMAstro-LHC ANR-12-BS05-0006, by the *Investissements d'avenir*, Labex ENIGMASS, and by the Research Executive Agency (REA) of the European Union under the Grant Agreement PITN-GA2012-316704 ("HiggsTools"). A.P. also acknowledges support from MESRI, France (progamme ACCES). J.M.N. is supported by the European Research Council under the European Union's Horizon 2020 program (ERC Grant Agreement no.648680 DARKHORIZONS). The work of A.L. was supported by the São Paulo Research Foundation (FAPESP), projects 2015/20570-1 and 2016/50338-6. N.D. acknowledges the support of the OCEVU Labex (ANR-11-LABX-0060) and the A*MIDEX project (ANR-11-IDEX-0001-02) funded by the "Investissements d'Avenir" French government program managed by the ANR. J. H. and A.G. were supported by the Labex ILP (reference ANR-10-LABX-63) part of the Idex SUPER, and received financial state aid managed by the Agence Nationale de la Recherche, as part of the programme Investissements davenir under the reference ANR-11-IDEX-0004-02.

Appendix

A Details of the CMS HSCP analysis recast

Here we briefly elucidate the procedure employed to recast the CMS HSCP analysis for constraints from the tracker plus TOF scenario. In Ref. [121], CMS has provided efficiencies for the trigger and event selection of HSCPs for the tracker plus TOF search.[8] The CMS efficiencies are given as a function of the HSCP truth level kinematics, $\vec{k} = (p_T, \eta, \beta)$ such that no detector simulator is required. Since the signal selection requires at least one HSCP in each event, the total trigger (or selection) efficiency for an event containing two isolated HSCPs (such as pair production of vector-like leptons) is given by:

$$\epsilon_T^a = \epsilon_1^a \times (1 - \epsilon_2^a) + \epsilon_2^a \times (1 - \epsilon_1^a) + \epsilon_1^a \times \epsilon_2^a \,, \tag{A.1}$$

where a = trigger or selection, ϵ_i^a represents the efficiency for the i-th HSCP and ϵ_T^a the combined efficiency. The first two terms in Eq. (A.1) correspond to the probability of at least one HSCP passing the trigger or selection, while the last term corresponds to the probability of both particles being selected. With the above definitions, the final event efficiency is simply given by:

$$\epsilon_{\text{event}} = \epsilon_T^{trigger} \times \epsilon_T^{selection}. \tag{A.2}$$

Finally, to compute the total signal efficiency, one must sum over the efficiencies of all events:

$$\epsilon_{signal} = \frac{1}{N} \sum_{events} \epsilon_{event} \,, \tag{A.3}$$

where N is the total number of events generated.

All the above efficiencies correpond to (detector) stable LLPs. However, if the long lived particle has a finite lifetime, the event efficiency must be rescaled by the fraction of LLPs which cross the detector without decaying. Eq. (A.2) must then be modified if τ is finite:

$$\epsilon_{event} = \epsilon_T^{trigger} \times \epsilon_T^{selection} \times f_L \,, \tag{A.4}$$

[8] For more details on the recasting procedure see Ref. [126].

where f_L is the effective fraction of HSCPs which cross a distance L of the detector without decaying. For events with a single LLP the rescaling is trivial and f_L is simply given by

$$f_L = F \equiv e^{-mL/(c\tau|\vec{p}|)} \tag{A.5}$$

In the above expression L is the detector radius, m is the LLP mass, τ its proper lifetime and $\vec{p}$ its 3-momentum in the event. For the full CMS detector we take $L = 9$ m, 10 m or 11 m for a pseudo-rapity $|\eta| < 0.8$, 1.1 or 2.5. However, for events with two LLPs, the effective fraction of LLPs is given by:

$$\begin{aligned} f_L = F_1 \times F_2 \;\; &+ \;\; F_1\,(1-F_2) \times \left(\epsilon_1^{trigger}\epsilon_1^{selection}\right) / \left(\epsilon_T^{trigger} \times \epsilon_T^{selection}\right) \\ &+ \;\; F_2\,(1-F_1) \times \left(\epsilon_2^{trigger}\epsilon_2^{selection}\right) / \left(\epsilon_T^{trigger} \times \epsilon_T^{selection}\right) \;\; , \end{aligned} \tag{A.6}$$

where F_i is the fraction in Eq. (A.5) computed for the i-th LLP in the event. The first term corresponds to both LLPs decaying outside the detector, while the last two terms correspond to only one LLP crossing the detector without decaying. Eqs. (A.6), (A.4) and (A.3) can then be used to compute the total signal efficiency for a given model with finite lifetime. Finally, we point out that we expect the signal efficiencies of the tracker-only and the tracker plus TOF analyses to rescale equally with lifetime. Therefore, although the values of f_L are computed explicitly using the trigger and selection efficiencies for the tracker plus TOF analysis, we use the same values when rescaling the results for the tracker only analysis. The only difference is that for the tracker only analysis we take L to be the size of the CMS tracker ($L \simeq 3$ m).

Contribution 5

Towards determining the lifetime of long-lived particles at the LHC

S. Banerjee, D. Barducci, B. Bhattacherjee, A. Goudelis, B. Herrmann, D. Sengupta

Abstract

We address the question of measuring the lifetime of a long-lived particle (LLP), assuming evidence for a displaced vertex at the Large Hadron Collider. In particular, we analyse to which precision it will be possible to access the lifetime experimentally. Based on a simplified framework, we investigate the dependence of the lifetime estimation on several factors, *viz.*, the mass of the LLP, its momentum distribution, the experimental cuts imposed and the final statistics. We also discuss the potential impact of smearing effects, on the lifetime estimation.

1 Introduction

The Large Hadron Collider (LHC) is currently operating in its Run-2 phase and pursues the quest for New Physics. Up to now, no direct or indirect signal of new particles has been observed in the existing search channels. Consequently, it is important to also consider alternative possibilities going beyond the standard assumptions adopted in traditional searches for physics beyond the Standard Model (SM). One such possibility is that some of the produced particles are long-lived, *i.e.* that the secondary vertices through which they decay are macroscopically displaced with respect to the primary interaction point. While some relevant studies are already being pursued at at the LHC, see *e.g.* [125, 127–130], most new physics searches are targeting scenarios where beyond the SM states undergo a prompt decay.

Typically, long-lived particles (LLPs) are states with a proper lifetime τ greater than ~ 100 ps. Such lifetimes can be induced either by very small couplings or in specific kinematic configurations involving small mass splittings and/or large propagator masses. They appear in a large variety of New Physics frameworks such as supersymmetry [131–135], Twin Higgs models [136], dark matter [108–110, 137], Hidden Valley models [138–140] or baryogenesis [141] and they can be either neutral or charged, see also [142] and references therein. Charged long-lived particles typically lead to disappearing or kinked tracks, while neutral ones to displaced vertices.

Regardless of the underlying model, LLPs introduce an additional complication for experimental searches, related to the particle's lifetime. For instance, from a theorist's standpoint, an electron is a universally-defined entity. However, experimentally, an electron that appears within the tracker is a completely different object than an electron which appears, *e.g.*, in the electromagnetic calorimeter. This implies that an experimental search for neutral particles decaying into a pair of visible objects at different parts of the LHC detectors could necessitate radically different analyses which can be more or less challenging. In this work we will focus

on the case in which a – larger or smaller – fraction of LLPs decay into pairs of charged particles within the tracker detector. The associated displaced vertex signature consists a pair of "emergent" tracks accompanied by signals in (some of the) other parts of the detector.

Our goal is not to study the discovery potential of the LHC for such scenarios, but to place ourselves in the situation in which a signal is observed and investigate the capacity of the LHC to reconstruct the lifetime of the decaying particle. To the best of our knowledge, only a handful of such studies have been performed in the literature, focusing on different LLP decay channels [143, 144]. Although our study will be performed within a toy framework, the method is fairly generic, leaving more concrete realisations of this scenario in terms of models for future work. We will explore various models elucidating the efficacy of this method in a future work.

2 Long-lived particle lifetime reconstruction

Measured in the laboratory frame, the decay length of a particle is given by

$$d \;=\; \beta\gamma c\tau\,, \tag{1}$$

where τ is the proper decay time of the decaying particle, *i.e.* the time interval until the particle decays as measured in its own rest frame, $\gamma = E/m = (1-\beta^2)^{-1/2}$ is the relativistic factor with $\beta = v/c = |\vec{p}|/E$, v is the velocity of the decaying particle and c denotes the speed of light. In the LHC setting, if we consider the production of a number N_0 of such unstable particles with proper decay times τ_i and mean (proper) lifetime τ, the expected number of decay events as a function of τ_i is given by the usual exponentially decreasing distribution

$$N_i \;=\; N_0\, e^{-\tau_i/\tau}\,. \tag{2}$$

By measuring the decay length d_i of each event, together with the corresponding kinematical factor β_i, we can compute the proper decay time associated to the event. Ideally then, it is possible to infer the values of N_0 and τ by performing an exponential fit of the sample data, provided that enough statistics is available.

Here we will consider the production of a neutral long-lived particle, hereafter denoted by X, decaying into a pair of leptons. As already mentioned in the Introduction, the part of the LHC detectors in which a decay event occurs drastically alters the amount of information that can be extracted for this event. Here we study the case in which the particle X decays inside the tracker. As a first approximation, let us assume that the momenta of the decay products as well as the position of the secondary vertex can be reconstructed with infinite precision. These are, of course, simplifying assumptions, which will not hold in a real experimental analysis. In the following we will relax the former condition, whereas the impact of vertex position measurement uncertainties is a heavily experiment-dependent issue which is difficult to address without a fair amount of knowledge on technical aspects of the LHC detectors. Note also that we neglect the effects of initial or final state radiation, which can provide additional information on the reconstructed events.

In order to study this ideal situation we have have used `Pythia 6` [145] to generate data samples of 10000 events each, assuming different lifetimes and masses for the particle X. For the ideal case where we assume the four momenta of the long-lived particles to be precisely reconstructed it is sufficient to generate parton-level events, $qq \to XX$. However, we must mention here that the $\beta\gamma$ spectra of the LLPs will vary depending on their production mode.

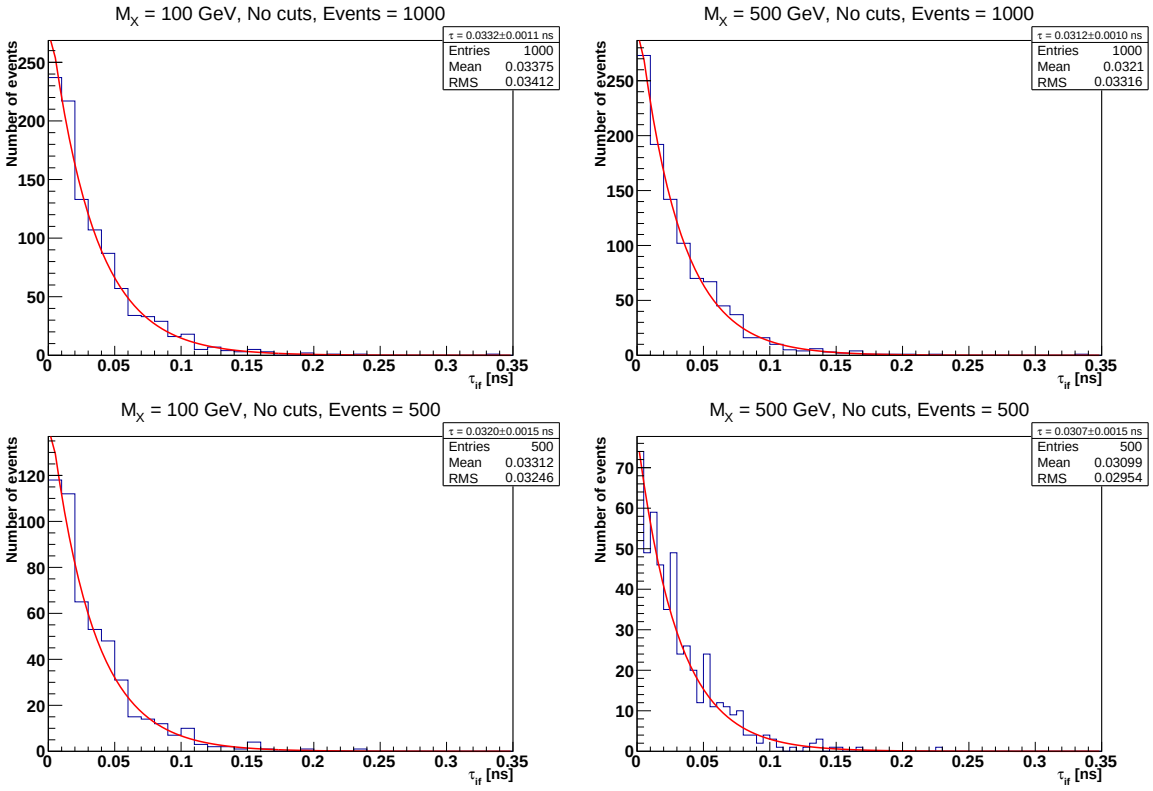

Figure 1: Lifetime determination using an exponential fit for two LLP masses (100 and 500 GeV, left and right columns) for samples containing 1000 and 500 events (top and bottom rows respectively).

In Fig. 1 we show the results of a simple exponential fit as performed using the `TF1` class integrated in the `ROOT` [146] environment, to a randomly selected subset of our samples for two LLP masses (100 and 500 GeV, left and right columns respectively) assuming two different numbers of observed events (1000 and 500, top and bottom rows) and a lifetime of 0.033 ns, without imposing any kinematic cuts on the events contained in the samples. Naturally, we see that in this idealised case the lifetime of the parent particle can be reconstructed with an excellent precision of $\sim 3\%$ assuming 1000 events and of 5% assuming 500 events for $m_X = 100$ GeV.

For the sake of a realistic study, experimental cuts must be imposed. A basic set of requirements consists of demanding a pseudorapidity $|\eta| < 2.4$ and a transverse momentum $p_T > 5$ GeV. Samples satisfying only these two conditions will be hereafter referred to as BCA (Basic Cuts Applied). In addition to the BCA cuts, given the increasing difficulty in reconstructing the secondary vertex as the latter approaches the outer surface of the tracker, we will study event samples satisfying an additional condition on the displacement of the secondary vertex with respect to the interaction point, $\beta_i\gamma_i c\tau_i$. Concretely, we consider three such extra cuts (EC), $\beta_i\gamma_i c\tau_i < 20$ mm (EC1), 50 mm (EC2) and 100 mm (EC3) [1]. The strongest constraint on $\beta_i\gamma_i c\tau_i$ is inspired from the 8 TeV CMS study pertaining to the reconstruction of leptons as functions of the transverse impact parameter (d_0), in supersymmetric scenarios involving displaced vertices [148].

[1] Note that current ATLAS and CMS searches are sensitive to displaced vertices between 10 mm to $\sim$ 300 mm with a peak sensitivity at around 100 mm. [129, 147]

The imposition of the EC cuts, however, introduces an important subtlety: by rejecting large values of $\beta_i\gamma_i c\tau_i$ we are inevitably biasing our event samples in favour of events characterised by smaller proper decay times. This implies that the expected exponential distribution is skewed and our estimate for the reconstructed lifetime will also be biased towards smaller values. In other words, provided enough statistics is available, every lifetime reconstruction based on samples with EC cuts tends to underestimate the true LLP lifetime. This effect is exemplified in Tab. 1, where we present the fitting procedure results for three different combinations of LLP masses and lifetimes assuming the four sets of cuts, BCA and BCA+EC.

Events	M_X	l (mm)	$\tau_{\rm BCA}$ (ns)	$\tau_{\rm EC1}$ (ns)	$\tau_{\rm EC2}$ (ns)	$\tau_{\rm EC3}$ (ns)
1000	200	10	$0.0338 \pm 11 \times 10^{-4}$	$0.0196 \pm 8 \times 10^{-4}$	$0.0258 \pm 9 \times 10^{-4}$	$0.0309 \pm 10 \times 1$
1000	200	5	$0.0170 \pm 6 \times 10^{-4}$	$0.0196 \pm 8 \times 10^{-4}$	$0.0127 \pm 5 \times 10^{-4}$	$0.0164 \pm 5 \times 1$
1000	2500	10	$0.0326 \pm 9 \times 10^{-4}$	$0.0304 \pm 9 \times 10^{-4}$	$0.0325 \pm 9 \times 10^{-4}$	$0.0326 \pm 9 \times 1$

Table 1: (mis-)Reconstructed lifetimes. M_X is given in GeV. In all cases, we start with 1000 Monte Carlo events which are reduced upon imposing each cut.

We can, indeed, clearly see that when cutting harder (EC1) on $\beta_i\gamma_i c\tau_i$, we obtain an estimate of the LLP lifetime which, although seemingly accurate, can be false. The effect is more pronounced for larger lifetimes, as can be seen by comparing the first with the second row of Tab. 1 since, all other quantities kept constant, a smaller lifetime implies overall smaller values of $c\tau_i$ and, hence, that a greater number of events is concentrated in a smaller area of $\beta_i\gamma_i c\tau_i$. Similarly, by comparing the first and the third rows of Tab. 1, we can see that the bias induced by the EC cuts is larger for smaller LLP masses. This is due to the fact that heavy LLPs are globally characterised by smaller $\beta_i\gamma_i$ values, hence, the impact of the EC cuts on the selected proper decay times is milder.

These comments are further illustrated in Fig. 2, where we show the number of events as a function of $\beta\gamma$ for the three benchmarks of Tab. 1 after the successive imposition of the BCA and EC cuts.

In light of these observations, we need to devise a method in order to reconstruct the LLP lifetime without biasing the signal. The crucial observation is that, as long as a sufficient number of events with large τ_i values is kept in the sample, the estimate tends asymptotically towards the true LLP lifetime from below as the considered τ_i region becomes larger. Then, given an EC cut, we can successively compute lifetime estimates based on an increasing number of events with large proper decay times which can, in turn, be achieved simply by restricting the $\beta_i\gamma_i$ region to smaller and smaller values. If, below a certain value of $\beta_i\gamma_i$, the estimate saturates, this means that we have included a sufficient number of events with large τ_i values and the estimate for the true LLP lifetime, along with its associated uncertainty, can be trusted. If, on the other hand, the estimate does not saturate, it can only be viewed as a lower bound on the true LLP lifetime.

The results obtained with this method are shown in Fig. 3 for two examples assuming an LLP mass $M_X = 200$ GeV and two different decay lengths (lifetimes) of 10 mm (left) and 5 mm (right). In the former case, we can clearly observe the saturation of the estimated LLP lifetime once an upper bound of about 0.6 is imposed on $\beta_i\gamma_i$. In the latter case, although perhaps less visible graphically, a similar situation occurs around $\beta_i\gamma_i < 1$ whereas, as expected, the estimated lifetime globally varies in a much narrower range. Besides, in both cases, we observe

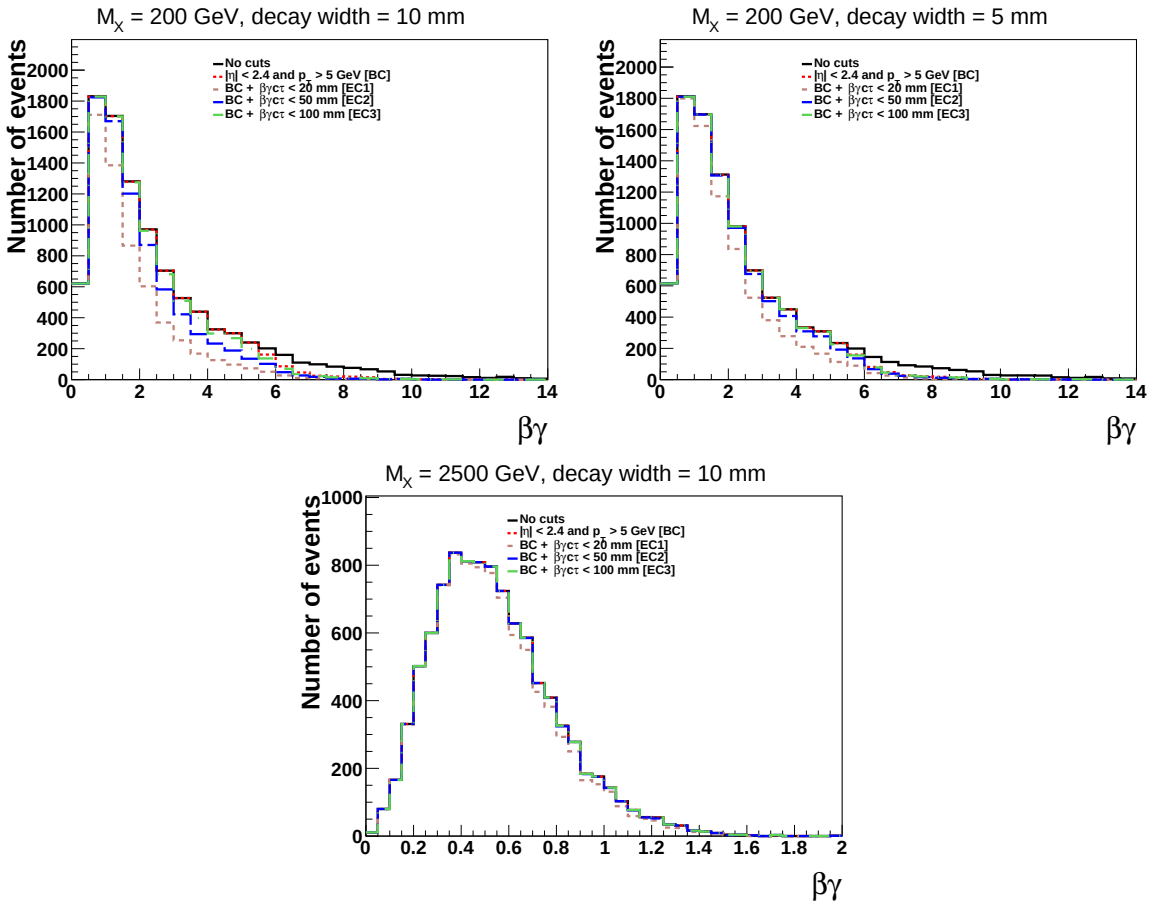

Figure 2: Number of events as a function of $\beta\gamma$ for the three mass and lifetime combinations of Tab. 1.

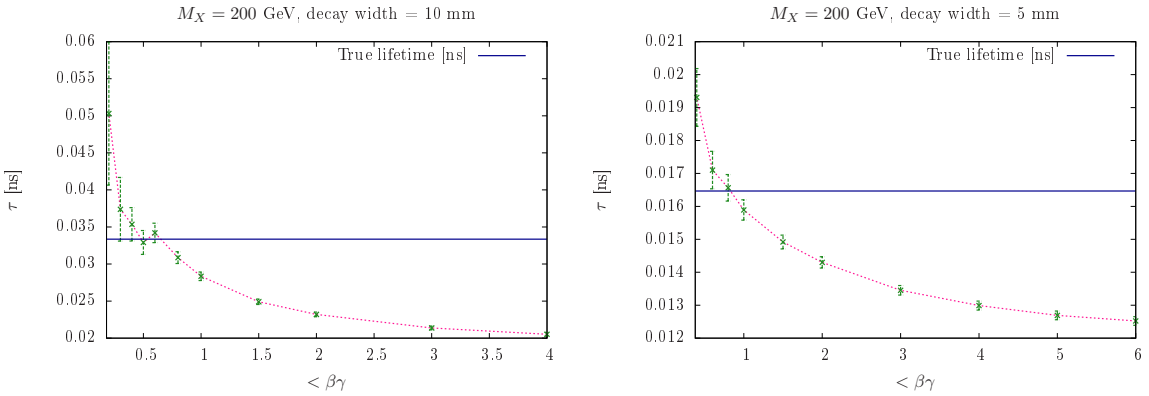

Figure 3: Reconstructed LLP lifetime along with its associated uncertainty as a function of the highest $\beta\gamma$ considered, for $M_X = 200$ GeV and two different true lifetime values.

that restricting $\beta_i\gamma_i$ to extremely small values leads to an overestimate of the LLP lifetime. This simply reflects the fact that below a certain threshold for $\beta_i\gamma_i$ there is not enough statistics to obtain an accurate estimate. Still, the true value of the lifetime lies within 2σ to 3σ from the estimated one.

So far, we have made the assumption that the lepton momenta can be reconstructed with infinite precision. In order to study the impact of the associated uncertainties, we consider a more generic process where the LLP decays into three very light daughter particles [2]. Using the standard smearing algorithm of `Pythia 6`, we parametrise the shift in the transverse momentum (p_T) measurement of each daughter particle as $\Delta p_T = a\sqrt{p_T}$, where a denotes the smearing parameter and is assumed to be the same for all the daughter particles. Hence, we obtain $\frac{\Delta p_T}{p_T} = \frac{a}{\sqrt{p_T}}$. We generate random Gaussian numbers for each daughter particle, smear their p_T and, using standard kinematic relations, obtain their smeared four-momenta. For this study, we focus on a simple scenario where a massive LLP decays to very light final state particles. These daughter particles, in turn, will be highly boosted, rendering $\frac{\Delta p_T}{p_T}$ negligible. Upon choosing two benchmark values of $a = 1$ and 1.5 (which correspond to 10% and 15% smearing on each particle), we do not obtain any observable effect on the lifetime fit. However, we must stress that a scenario involving one or more heavy daughter particles or the parent LLP being much lighter, will amount to the daughter particles being less boosted and, consequently, the smearing effects may play an important role in the lifetime fit. Lastly, we must mention here that in actual experiments, the uncertainties on measuring the secondary vertex may be dependent on the p_T measurements of the tracks used to reconstruct them, which in turn will depend on the particle smearings. In this study, we test the effect of smearing on the benchmark $M_X = 200$ GeV, decay length 10 mm, decaying to very light daughter particles.

3 Conclusions and perspectives

In this note, we examined the capacity of the LHC to reconstruct the mean lifetime of long-lived particles. At first, we investigated an ideal situation in which an LLP decays inside the tracker into an all-visible final state and its four momenta, as well as the position of the secondary vertex, can be precisely measured. We highlighted the fact that the experimental cuts on the displacement of the secondary vertex introduce a bias in the reconstructed LLP lifetime and proposed a method to overcome it. We saw that, under these idealised conditions, following this method it is indeed possible to measure, or at least to put a lower limit on, the lifetime of the LLP to a good degree.

As a second step, we studied a scenario involving decays of an LLP into an all-visible final state and introduced p_T smearing on the daughter particles. We found that for highly boosted final state particles, the effects of smearing are negligible on the lifetime measurement. However, for less boosted final states, momentum smearing will have a more severe impact on the measurement.

There are several layers of complication that can, and *should*, be added to this first study. In particular, having computed τ_i from the ratio between $\beta_i\gamma_i c\tau_i$ and $\beta_i\gamma_i c$, it is important to properly consider the error propagation corresponding to this ratio. Moreover, in several New Physics scenarios involving long-lived particles, at least one of the LLPs can have invisible decay products along with –at least – two visible ones (the minimum number of visible de-

[2] The motivation for studying three- rather than two-body decays lies with the fact that the greater the number of daughter particles, the more important the smearing effect will be on the reconstructed mother LLP.

cay products required to reconstruct the secondary vertex is two). In such cases, the LHC experiments can reconstruct the secondary vertex (our $\beta_i\gamma_i c\tau_i$) for each event, but not the exact four-momenta ($\beta_i\gamma_i$) of the LLPs. In such scenarios, some observables like M_{T2} may provide handles on the mass of the LLP, making it possible to extract its four-momenta as well. Besides, here we have not considered effects related to the initial state particles. The shape of the $\beta\gamma$ spectra will be different depending on whether the process is gluon-gluon, quark-anti-quark or quark-gluon initiated. Such effects may affect the lifetime measurement in a substantial manner.

Acknowledgements

We would like to thank the organizers of the 2017 "Les Houches – Physics at TeV colliders" workshop where this work was initiated. S.B. thanks Shilpi Jain for helpful discussions regarding fitting in `ROOT`. The work of B.H. and S.B. are partially supported by Investissements d'avenir, Labex ENIGMASS, contrat ANR-11-LABX-0012. The works of S.B. and B.B. are partially supported by the CNRS LIA-THEP (Theoretical High Energy Physics) and the INFRE-HEPNET (IndoFrench Network on High Energy Physics) of CEFIPRA/IFCPAR (Indo-French Centre for the Promotion of Advanced Research). The work of S.B. is also partially supported by a Durham Junior Research Fellowship COFUNDed between Durham University and the European Union under grant agreement number 609412. The work of B.B. is also supported by the Department of Science and Technology, Government of India, under the Grant Agreement number IFA13-PH-75 (INSPIRE Faculty Award). A.G. was supported by the Labex ILP (reference ANR-10-LABX-63) part of the Idex SUPER, and received financial state aid managed by the Agence Nationale de la Recherche, as part of the programme Investissements d'avenir under the reference ANR-11-IDEX-0004-02. The work of D.S. is supported by the National Science Foundation under Grant No. 1519045.

Contribution 6

Associated production of a single top with dark matter in a two-Higgs-doublet plus pseudoscalar mediator model

G. Bélanger, B. Fuks, F. Maltoni, J. M. No, P. Pani, G. Polesello, B. Zaldivar

Abstract

This proceeding aims to extend the studies already available in literature on the associated production of a single top quark and dark matter in a model with two Higgs doublets and a pseudoscalar mediator. We put the model into a broader context of astrophysical quantities and measurements and we extend the interpretation in terms of selections and parameter space.

1 Introduction

The sensitivity of the LHC experiments to the associated production of dark matter (DM) with a single top has been recently studied [149] in the framework of an extension of the standard model featuring two Higgs doublets and an additional pseudo-scalar mediator [150, 151] (2HDM+a). The study in Ref. [149] and the one of this contribution extend the results previously available in the literature [152–154], that show the importance of final states involving a single top quark and DM (DMt) by means of a simplified model. Like single top production within the Standard Model (SM), the DMt signature in the 2HDM+a model receives three different types of contributions at leading order (LO) in QCD. These are t-channel production, s-channel production and associated production together with a W boson (tW). The presence of an extended Higgs sector, contrary to the case of a singlet mediator, ensures perturbative unitarity of the $pp \to t\chi\bar{\chi} + X$ class of processes where χ denotes the DM particle. Moreover, the fact that $tW\chi\chi$ final states can be produced with sizeable cross sections in diagrams involving the on-shell production of intermediate charged Higgs bosons renders the phenomenology of this model particularly interesting. In this contribution to the Les Houches proceedings, we aim to extend the study of Ref. [149] by broadening the interpretation of the model in terms of collider searches. Furthermore, we include the estimation of the sensitivity of direct dark matter experiments on the parameter space and we propose new selection strategies for analyses targeting events with a single lepton in the final states and assess the parameter-space coverage of these new selections assuming an integrated luminosity of 300 fb^{-1} of proton-proton collisions at a centre-of-mass energy of 14 TeV.

2 Cosmological constraints

The model in question contains a fermionic DM candidate χ that is assumed to be a Weakly Interacting Massive Particle (WIMP). The DM particle communicates with the SM via exchanges with a pseudo-scalar mediator that mixes with the Higgs sector and it thus couples to all SM particles. Then, depending on the spectrum and the mixing angles, the relic abundance of DM

will be dominated by DM annihilation into pairs of b-quarks, top quark pairs or pairs of mediators a, as well as in final states comprised of a ah or aZ system, h and Z respectively denoting the SM Higgs boson and Z-boson. The latter channels represent the most important difference between this model and the corresponding simplified-model implementation, which only couples the mediator to the fermionic sector of the SM. Consequently, the prediction of the relic abundance will be very different from one model to another, in the relevant region of the parameter space where those new channels dominate. This region is defined by the condition $2m_\chi \gtrsim (m_a + m_{h,Z})$. For more details on the relic density predictions of the model, we refer the reader to Ref. [155].

On the other hand DM indirect detection constraints are potentially very important. For a pseudo-scalar mediator, DM annihilation into a fermion pair consists in an s-wave process and there is thus no velocity suppression of the cross section at present time. On the other hand, the $\chi\bar{\chi} \to aa$ annihilation channel is p-wave suppressed, but the $\chi\bar{\chi} \to ah$ and aZ ones are not and the relative importance of the latter on the cosmological consequences for the model have not been addressed. For the region of parameter space where the fermionic channels dominate, predictions for the DM annihilation cross section at present times coincide with those estimated in the simplified model context. We therefore refer the reader to Ref. [156] for a detailed analysis of the indirect detection constraints in the 2HDM<+a framework.

On different lines, DM direct detection searches are not relevant since the strongest constraints from that front come from the presence of spin-independent interactions in the theory that our model does not feature at tree level. As in contrast, the featured DM spin-dependent interactions lead to a velocity suppression allowing to evade any direct detection bound.

3 Dedicated LHC analysis for 300 fb^{-1}

A detailed analysis explicitly optimised for the signature depicted above, and targeting the full projected statistics of the LHC Run 3 of 300 fb^{-1} is described in Ref. [149]. We briefly summarise in the following the methods and the results of this analysis, and we extend it by projecting the results on additional slices of the parameter space. We moreover include signatures that are relevant and that have been neglected before.

3.1 Summary of the available LHC projection

We base the simulation of the DM signal and the SM background following the strategy introduced in Ref. [149]. We simulate a full set of SM processes leading to the presence of one or two final-state leptons (e, μ) originating from the decay of a W-boson, a Z-boson or a τ lepton. Events are generated within either the `POWHEG BOX` framework [157] or the `MadGraph5_aMC@NLO` platform [95], and the simulation of the QCD environment (parton showering and hadronisation) has been performed with `PYTHIA 8` [97]. Hard-scattering signal events have been produced with `MadGraph5_aMC@NLO` on the basis of the UFO model [93] provided together with Ref. [151], and parton showering and hadronisation have been again simulated with `PYTHIA 8`. We finally include detector effects by smearing the properties of the final-state physics objects (*i.e.* electrons, muons, jets and E_T^{miss}) in a way reproducing the measured performance of the ATLAS detector.

We specifically focus on a final state comprised of two W-bosons, a jet issued from the fragmentation of a b-quark (*i.e.* a b-jet), and missing transverse momentum associated with the presence of the two undetected DM particles. Two analyses have been developed, requiring

either one or two leptons in the final state, corresponding to the the cases where only one or both of the two W bosons decays into leptons respectively. The selection criteria are based on constraints imposed on a set of dimensionful transverse variables, such as the transverse mass $m_{\rm T}^{\ell}$ [158], $m_{\rm T2}$ [159, 160], and $am_{\rm T2}$ [161, 162]. All those variables exhibit a kinematic endpoint in the SM context, when all the missing energy arises from the neutrinos originating from W-boson decays. In the signal case, the presence of additional E_T^{miss} induced by the DM particles violates these bounds, and provides a handle for the separation of the signal from the background. Prior studies (see Fig. 8 of Ref. [149]) have determined the regions of the parameter space (presented in the $(m(H^{\pm}), \tan\beta)$ plane) that can be excluded at the 95% confidence level (CL), for an integrated luminosity of $300\,\text{fb}^{-1}$ of proton-proton collisions at a centre-of-mass energy of $14\,\text{TeV}$ LHC. The results are given for a fixed mediator mass of $m(a) = 150$ GeV. The two-lepton signature, which has lower signal statistics but allows for a softer kinematic selection, dominates for lower $m(H^{\pm})$ masses, whereas the single-lepton signature allows to get sensitivity to charged-Higgs masses above $m(H^{\pm}) = 600$ GeV.

3.2 Reinterpretation of the LHC reach

The analysis in Ref. [149] concentrated on assessing the dependence of the LHC reach on the main model parameters $m(H^{\pm})$, $\tan\beta$ and $m(a)$. It is however interesting to compare the parameter space which can be covered by different analyses, as it can help prioritising the search strategy at the LHC. A rather complete survey is provided in Ref. [151], in which the coverage expected from the analysis of different signatures is presented in the $(m(a), \tan\beta)$ plane for four different model configurations. Whilst for maximal mixing of the singlet and doublet pseudo-scalars (*i.e.* $\sin\theta \sim 0.7$) the dominant model signature consists of the production of a single Higgs boson recoiling against a pair of DM particles, mono-Z-boson probes become predominant for cases in which the a boson is mostly doublet-like ($\sin\theta \sim 0.35$). We recast in Figure 1 the reach of the di-lepton analysis described in Ref. [149] and present it in the $(m(a), \tan\beta)$ plane, for $m(A) = m(H^{\pm}) = m(H) = 500$ GeV and for the two mixing scenarios discussed above. By comparing these results with the sensitivity projections for the same integrated luminosity shown in Ref. [151], we find out that the associated production of a single top and a charged Higgs boson $H^{\pm}$ covers a region of parameter space comparable to the one for which the mono-Z and mono-h probes are sensitive to.

3.3 Additional handles on the model

A limitation of the analysis described in Ref. [149] lies in the fact that the selections for the single-lepton analysis are focused on a situation where the lepton is produced in the decay chain of the charged Higgs boson $H^{\pm}$, which implies a hadronically-decaying top quark recoiling against a lepton-E_T^{miss} system that is very hard. The selection cuts explicitly exploit this situation, killing in this way both the topology where the lepton originates from the top quark decay and the t-channel contribution, which becomes relevant at high $H^{\pm}$ masses. In order to increase the LHC sensitivity to the model, we develop a new selection strategy, focusing on the situation where the lepton arises from the decay of the top quark. Two non-overlapping signal selections are defined, respectively targeting the $H^{\pm} \to \ell\nu\chi\chi$ and $H^{\pm} \to jj\chi\chi$ decays. They will be referred to in the following as leptonic-$H^{\pm}$ and hadronic-$H^{\pm}$ selections, respectively. In the leptonic-$H^{\pm}$ selection, we require that the system comprised of the lepton and the leading b-jet has a large invariant mass, $m(b1, \ell) > 150$ GeV, and that the system comprised of the leading light jet and leading b-jet has a small invariant mass, $m(b1, j1) < 150$ GeV. In the

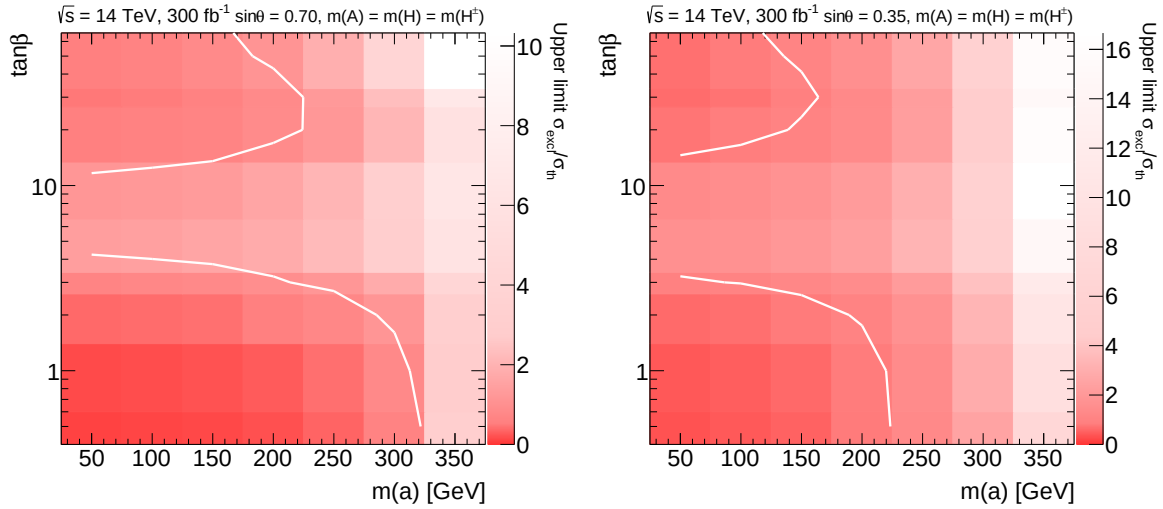

Figure 1: Regions in the $(m(a), \tan\beta)$ planes which can be excluded at the 95% CL through single-lepton and di-lepton searches. In the left panel, the singlet-doublet pseudo-scalar mixing is maximal ($\sin\theta \sim 0.7$) whilst in the right panel it is smaller ($\sin\theta \sim 0.35$). The z-axis palette shows the ratio between the excluded cross section and the theoretical one. For both cases, we have fixed $m(A) = m(H^{\pm}) = m(H) = 500$ GeV and the results assume $300\,\text{fb}^{-1}$ of 14 TeV LHC data and a systematic uncertainty of 20% on the SM background and of 5% on the signal.

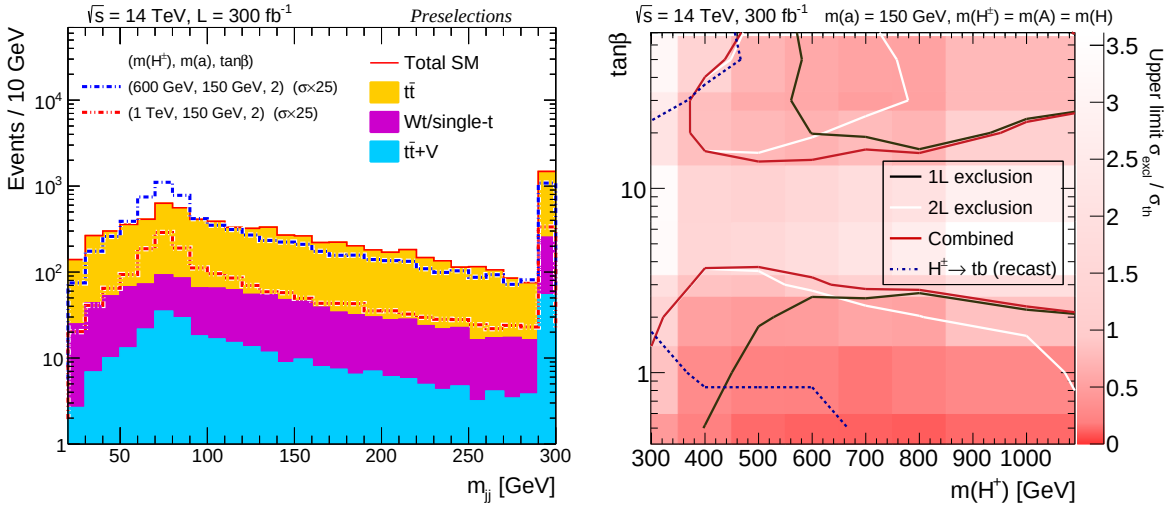

Figure 2: (Left) Distribution of the hadronic W-boson mass for a relaxed version of the analysis selections. (Right) 95% CL exclusion limits for the combination of the two one-lepton regions described in the text and the two-lepton selections of Ref. [149]. We assumes $300\,\text{fb}^{-1}$ of 14 TeV LHC data and a systematic uncertainty of 20% (5%) on the SM background (signal).

hadronic-$H^\pm$ selections, we in contrast require that $m(b1,\ell) < 150$ GeV and $m(b1,j1) > 130$ GeV, where the former cut ensure the orthogonality between the regions. We moreover improve the background rejection by requesting that the invariant mass of the system comprised to the two leading light jets lies between 60 and 105 GeV. This requirement, applied in both selections, is extremely efficient in separating the signal from the background, as shown in the left panel of Fig. 2.

We impose that all reconstructed jets with a transverse momentum $p_{\mathrm{T}}^{j} > 25$ GeV and a pseudorapidity satisfying $|\eta_j| < 2.5$ are well separated from the missing momentum, requiring that the jet that is the closest to the $\vec{p}_{\mathrm{T}}^{\,\mathrm{miss}}$ in azimuth satisfies $|\Delta\phi_{\mathrm{min}}| > 1.0$. At least one jet is required to be b-tagged and events with a second b-tagged jet with $p_{\mathrm{T}} > 50$ GeV are rejected. The asymmetric stransverse mass, am_{T2}, is required to be at least of 230 (200) GeV in the leptonic-$H^\pm$ (hadronic-$H^\pm$) selection. The rest of the selections is designed to exploit in the signal the fact that the boost of the charged Higgs is either propagated to the leptonic or to the hadronic part of the event.

In the leptonic-$H^\pm$ selection, we additionally require three jets of relatively low transverse momenta ($p_{\mathrm{T}} > 50, 50, 20$ GeV) and exactly one isolated lepton (e or μ) with $p_{\mathrm{T}} > 120$ GeV, $|\eta_\ell| < 2.5$. The missing energy is imposed to be larger than 250 GeV and the lepton-E_T^{miss} system transverse mass has to satisfy $m_{\mathrm{T}}^{\ell} > 300$ GeV. In addition, we impose that $E_T^{miss} + 0.4 \cdot m_{\mathrm{T}}^{\ell} > 375$ GeV.

For the hadronic-$H^\pm$ selection we instead require the presence of three relatively hard jets ($p_{\mathrm{T}} > 100, 50, 40$ GeV) and exactly one isolated lepton with low transverse momentum $p_{\mathrm{T}} > 25$ GeV. The requirement on m_{T}^{ℓ} is kept at the minimum value needed to suppress the background contributions of semi-leptonic $t\bar{t}$ decays, $m_{\mathrm{T}}^{\ell} > 120$ GeV. Finally the events are selected if $E_T^{miss} > 400$ GeV. As in this topology the E_T^{miss} and the hadronically decaying W-boson come from the decay of the same particle, it is convenient to define a proxy for the $H^\pm$ transverse mass as the invariant mass on the transverse plane of the hadronic W-boson, constructed from the two leading light jets, and the E_T^{miss}. This variable is required to be of at least 680 GeV, in order to enhance the sensitivity of this selection to charged Higgs bosons of about 1 TeV.

The total background in the leptonic-$H^\pm$ selection amounts for approximately 4 events, dominantly arising from $tt + V$ and tZ production. For charged Higgs masses ranging from 500 GeV to 1 TeV the signal acceptance is of $[0.12, 0.35]\%$ ($[0.12, 0.31]\%$) for $m(a) = 150$ GeV and $\tan\beta = 1\,(20)$. In the hadronic-$H^\pm$ selection, the total background is expected to be approximately 2 events, also dominantly arising from $tt + V$ and tZ production. For charged-Higgs masses ranging again from 500 GeV to 1 TeV the signal acceptance is found to be $[9 \cdot 10^{-5}, 0.17]\%$ ($[9 \cdot 10^{-5}, 0.16]\%$) for $m(a) = 150$ GeV and $\tan\beta = 1\,(20)$. The corresponding exclusion limits are presented in the right panel of Fig. 2 and compared with the di-lepton selection from Ref. [149]. We observe that the new selection extends the reach of the analysis towards high $H^\pm$ masses. However, the improvement is tamed by the strong kinematic similarity of the hadronic-$H^\pm$ signal to the background, which can only be suppressed by very aggressive selection requirements that are characterised by a low signal efficiency.

4 Conclusions

The prospects of future LHC runs for probing interactions between a DM particle and top quarks via the $t + E_T^{miss}$ signature have been studied. We observed that the sensitivity of the single top

signal is complementary to the one of the mono-Higgs and mono-Z-boson probes, once we include searches targetting a single-leptonic and di-leptonic final state. In particular, thanks to a dedicated optimisation of the analysis focusing on the single-lepton final state, we have shown that the LHC is in principle sensitive to charged Higgs bosons of about 1 TeV, for a large range of $\tan\beta$ values and assuming an integrated luminosity of 300fb^{-1}.

Contribution 7

Probing flavour-violating decays of squarks at the LHC

A. Chakraborty, M. Endo, B. Fuks, B. Herrmann, M. M. Nojiri, P. Pani and G. Polesello

Abstract

We study squark decays beyond minimally flavour-violating supersymmetry at the LHC. Considering second and third generation squark mixings, we consider a simplified model with two active squark flavours and evaluate the sensitivity of current squarks searches at the Run-1 and Run-2 of the LHC. We moreover investigate the gain in sensitivity of a dedicated search strategy involving leptons, jets and missing transverse energy at the high luminosity run of LHC.

1 Introduction

Despite the absence of any experimental evidence at the Large Hadron Collider (LHC), from a theoretical and phenomenological point of view supersymmetry (SUSY) remains an attractive extension of the Standard Model (SM) of particle physics. Whereas current experimental searches are unfruitful, supersymmetry can still be viable either after introducing heavy superpartners, or by considering non-minimal realisations of the theory. While the former explanation is rather unattractive from the phenomenological point of view, the latter one calls for studies of supersymmetric frameworks beyond the "usual" Minimal Supersymmetric Standard Model (MSSM).

Without adding extra fields or extending the gauge symmetry groups, going beyond the "standard" MSSM can be achieved by considering additional mixing between the states of the model. More precisely, in addition to the helicity mixing between "left-handed" and "right-handed" states, the model symmetries allow for inter-generational mixing of the scalar partners beyond the commonly assumed Cabibbo-Kobayashi-Maskawa (CKM)- and Pontecorvo-Maki-Nakagawa-Sakata (PMNS)-induced terms. In the following, we consider this non-minimally flavour-violating (NMFV) framework and assume additional mixing between the second and third generation of squarks. The latter is indeed allowed to be sizeable, in contrast to any mixing involving the first generation that is largely constrained by flavour data. In particular, at that stage of our study, we focus on mixing between charm and top flavours in the squark sector.

From the model-building point of view, non-minimal flavour violation can be motivated from Grand Unified Theories, possibly in combination with certain flavour symmetries at the high scale (see, *e.g.* Refs. [163, 164]). In the present study, however, we introduce the corresponding terms directly at the TeV scale. More precisely, we consider the generation-mixing entries of the sfermion mass matrices as free parameters, in the same way as the diagonal entries in such a phenomenological TeV-scale setup. Although there are stringent constraints on the flavour-violating neutral currents induced by these additional generation-mixing entries, a considerable part of the resulting parameter space is in agreement with theoretical constraints and current experimental measurements [165]. Moreover, the additional charm-stop mixing

leads to characteristical signatures at the LHC [166–172]. A particular feature is that, if the lightest up-type squark is a mixture of charm and top flavour, its decays into charm and top quarks, together with a neutralino, may be simultaneously open [168].

Experimental ATLAS and CMS searches have led to stringent limits on the production cross sections of charmed and top squarks [37, 173–179]. However, these searches are mainly based on simplified models assuming no generation-mixing entries in the squark mass matrices. As adding such entries may altern the decay pattern of the squarks, it is an interesting question to evaluate their impact on the present mass limits and evaluate the sensitivity of new dedicated searches at the LHC. This is the goal of the present work. Within an *ad-hoc* simplified model containing two squark flavours, we recast mass limits from previous ATLAS and CMS analyses. We then estimate the sensitivity of dedicated searches at the LHC with a centre-of-mass energy of $\sqrt{s} = 14$ TeV and assuming 300 fb^{-1} of integrated luminosity.

2 Model setup and existing LHC limits

In this section, we present the general setup of our study. We first introduce the simplified model which we base our analysis on. We then discuss the adopted search strategy and recast recent squark searches at the LHC.

2.1 A simplified model for squark flavour violation

While in the general MSSM, each squark eigenstate is an admixture of the six flavours eigenstates (see Ref. [165]), the present analysis is based on a simplified model capturing the essential features of non-minimal flavour violation in the squark sector once existing bounds are accounted for. In our setup, the squark sector consists of two active flavours, namely a right-handed stop and a right-handed scharm, and their mixing leads to two physical eigenstates $\tilde{u}_1$ and $\tilde{u}_2$ defined by

$$\begin{pmatrix} \tilde{u}_1 \\ \tilde{u}_2 \end{pmatrix} = \begin{pmatrix} \cos\theta_{tc} & \sin\theta_{tc} \\ -\sin\theta_{tc} & \cos\theta_{tc} \end{pmatrix} \begin{pmatrix} \tilde{c}_R \\ \tilde{t}_R \end{pmatrix} . \tag{1}$$

Here, $\tilde{u}_1$ is assumed to be the lighter of the two squark mass eigenstates. In addition, we include one neutralino $\tilde{\chi}_1^0$ whose mass is fixed to $m_{\chi_1^0} = 50$ GeV and composition taken bino-like[1]. The rest of the spectrum is assumed to be decoupled and ignored in the following. Our simplified setup is thus governed by three parameters: the masses $m_{\tilde{u}_1}$ and $m_{\tilde{u}_2}$ of the squarks together with the squark mixing angle θ_{tc}. This choice of a mixing between the "right-handed" squark flavours allows for more flexibility, as less affected by constraints originating from B-physics, contrary to a mixing between "left-handed" states.

Being an admixture of $\tilde{t}_R$ and $\tilde{c}_R$ eigenstates, each physical squark may decay either into a top or a charm quark,

$$\tilde{u}_i \to t\tilde{\chi}_1^0 , \qquad \tilde{u}_i \to c\tilde{\chi}_1^0 \qquad \text{with } i = 1, 2 . \tag{2}$$

Once pair-produced at the LHC, the pair-produced squarks hence give rise to two final-state neutralinos manifesting themselves as missing transverse energy (E_T^{miss}). Assuming squark-antisquark production at the LHC, typical existing search strategies focus on the processes

$$pp \to t\bar{t} + E_T^{miss} \qquad \text{and} \qquad pp \to c\bar{c} + E_T^{miss} . \tag{3}$$

[1]These assumptions do not have a significant impact on the analysis, the main ingredient being the considered branching fractions of the squarks into quarks and the neutralino.

However, after considering additional flavour mixing as introduced above, another process may be relevant,

$$pp \to tc + E_T^{miss} \to \ell bc + E_T^{miss}\,, \tag{4}$$

where one squark decays into a top and the other into a charm quark [168] and the final step assumes leptonic top decay. We hence propose to target a final state comprised of one isolated lepton, one b-tagged jet, one c-tagged jet, and a large amount of missing transverse energy.

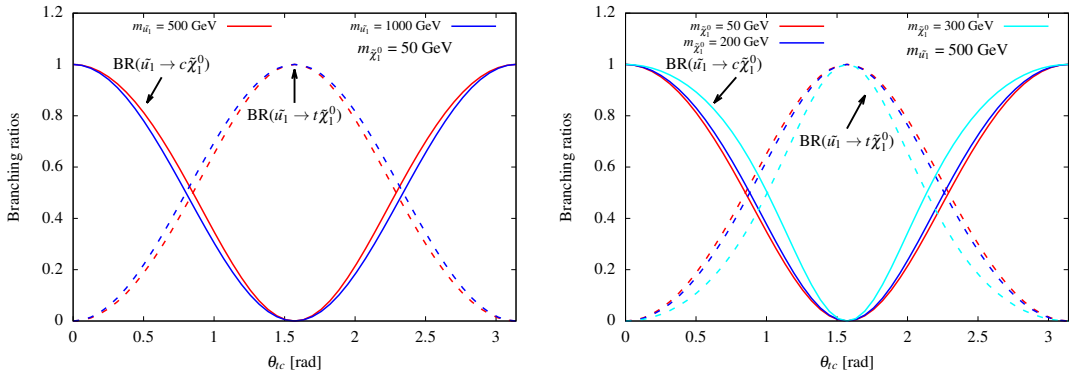

Figure 1: Branching ratios of the $\tilde{u}_1 \to t\tilde{\chi}_1^0$ (dashed line) and $\tilde{u}_1 \to c\tilde{\chi}_1^0$ (solid line) decays, shown as functions of the mixing angle θ_{tc}. In the Left figure, the red and blue curves correspond to squark masses of $m_{\tilde{u}_1} = 500$ GeV and $m_{\tilde{u}_1} = 1000$ GeV, respectively with a fixed $m_{\chi_1^0} = 50$ GeV. In the right plot, we fix $m_{\tilde{u}_1}$ to 500 GeV and vary $m_{\chi_1^0}$ for three different values 50 GeV (red), 200 GeV (blue) and 300 GeV (cyan).

We present the two relevant branching ratios as function of the generation mixing in Fig. 1. The branching fractions are found to vary significantly as a function of the value of the mixing angle θ_{tc}. In particular, we can obtain a situation where both decay modes have comparable rates. There exists another key parameter which controls these branching ratios which is the mass difference between the squark and the neutralino. In the right panel of Fig. 1 we show the dependence of the branching ratios on the mass of the neutralino by setting $m_{\chi_1^0}$ to three different values 50 GeV (red), 200 GeV (blue) and 300 GeV (cyan) for a fixed $m_{\tilde{u}_1}$ = 500 GeV. We observe that, even though the impact on the squark mass itself is marginal, the branching ratios can vary significantly with the the mixing angle as soon as the mass difference between the squark and neutralino becomes close to the top mass threshold. In the rest of our analysis, the neutralino mass is held fixed at 50 GeV.

2.2 Recasting LHC limits

Dedicated searches for scalar top quarks decaying into a $t\bar{t} + E_T^{miss}$ system or scalar charm quarks decaying into a $c\bar{c} + E_T^{miss}$ system have been performed by both the ATLAS and CMS collaborations at the LHC [37, 173–179]. The observed exclusion limits in case of light neutralino masses are of the order of the TeV for top squarks and of about 500 GeV for charmed squarks[2]. As a comparison, the present limits for flavour-agnostic squark searches, summed over left and right squarks and over four flavours are around 1.5 TeV [180, 181]

Using the available information provided by the ATLAS collaboration for the search for top squarks in the single lepton final state [174], we recast their observed limits in terms of

[2]The charm squark analysis is published only for a centre-of-mass energy of 8 TeV.

the three-dimensional parameter space of our model ($m_{\tilde{u}_1}$, $m_{\tilde{u}_2}$ and θ_{tc}), as shown in Fig. 2. The acceptances and efficiencies for each of the "discovery tN_med" and "discovery tN_high" regions have been used to estimate the signal yield ($N_{\rm sig}$) in these regions, considering the appropriate decay branching ratios for each parameter choice. These two signal regions are optimized specifically looking at moderate and higher stop masses respectively.

The signal yields were then compared to the model-independent upper limit ($N_{\rm non-SM}^{\rm obs\ limit}$) provided in Ref. [174] for each of the regions. When the ratio of these two yields exceeds one, the signal point is considered to be excluded. For the final exclusion limit estimation, the ATLAS analysis does not consider the "discovery regions" as they are, but exploits a multi-bin fit in the most sensitive distribution. As the reinterpretation performed in this paper cannot exploit the full multi-bin information, due to the lack of details in the reference, the exclusion contour presented in Fig. 2 can be considered as a conservative limit. The official observed limit of Ref. [174] is therefore shown as a star on the right panel of Fig. 2 in order to provide a comparative assessment of the multi-bin effects. It is interesting to mention that the star corresponds to the case in which the lightest squark dominantly (almost 100%) decays into the top and neutralino system, while the charm mode is negligible. Consequently, a non-negligible mixing angle yields a significant production of charm quarks in the decays (see Fig. 1), that importantly impacts the current exclusion limits.

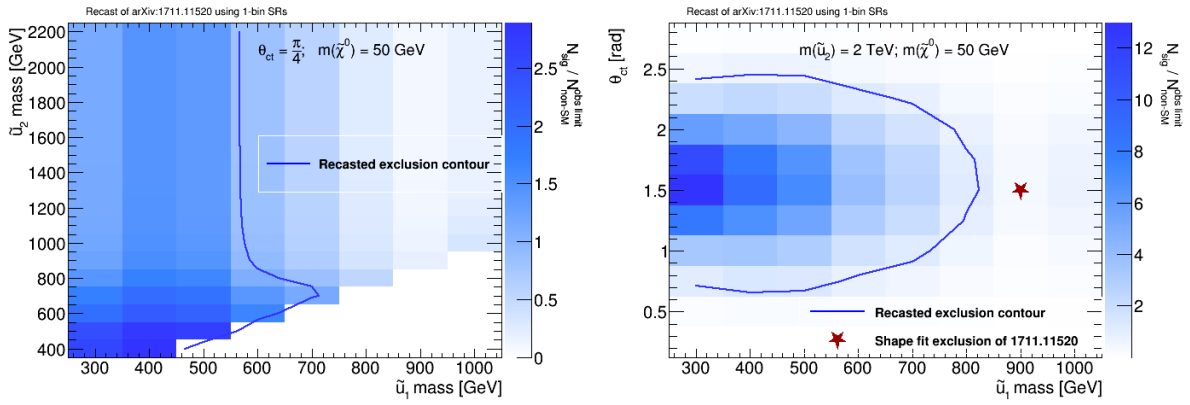

Figure 2: Reinterpretation of the ATLAS search for top squarks in the single lepton final state [174] in the $(m_{\tilde{u}_1}, m_{\tilde{u}_2})$ (left) and $(m_{\tilde{u}_1}, \theta_{tc})$ (right) planes.

3 Collider projections for the reach of the tc channel

In this section, we describe a dedicated analysis aimed at evaluating the reach for the signature under consideration for the full LHC statistics and for the HL-LHC. We first provide a brief outline of the Monte-Carlo (MC) simulations used to generate signal and background events. The reconstruction of the final-state leptons, jets and missing transverse momentum ($\vec{p}_{\rm T}^{\,\rm miss}$) along with some handy kinematic variables is also discussed. In order to optimise the signal selection together with the rejection of the SM backgrounds, we impose several kinematic requirements on the final state, that we provide below together with our findings.

3.1 Monte Carlo simulation

Signal events originating from squark pair-production were produced using `MadGraph5_aMC@NLO` [95], the hard-scattering matrix elements being convoluted with the `NNPDF3.0` parton distribution

functions [96]. We use Feynrules 2.0 [91] to obtain the model files incorporating the mixing between the charm and top squarks. The mass of the squark with a dominant stop component (denoted stop hereafter) was scanned in steps of 100 GeV in the [600 GeV, 1.4 TeV] mass window. The lightest neutralino mass was kept fixed to 50 GeV, as discussed in Sec. 2.1, and the squark mixing angle was set to $\theta_{tc} = \pi/4$. The generated events were passed to PYTHIA 8.2 [97] for parton showering and hadronisation and the events have been reweighted to a production cross-section at the NLO+NLL accuracy [182]. In the results presented below, we consider LHC proton-proton collisions at a centre-of-mass energy of 14 TeV.

For the backgrounds, we focus on SM processes with one or two final-state leptons originating from the decay of either a vector boson, or of a tau lepton, and that precisely consists in $t\bar{t}$, Wt, t-channel single top, $t\bar{t}W$, $t\bar{t}Z$, tWZ, tZ, W+jets, Z+jets, WW, WZ and ZZ production. $t\bar{t}$ and single top events are simulated at the next-to-leading (NLO) order accuracy within the POWHEG BOX framework [157], while the W+jets, Z+jets and tWZ samples are generated at leading order (LO) with MadGraph5_aMC@NLO, merging samples containing up to four additional jets at the level of the matrix element matched with the CKKW prescription as implemented in PYTHIA8 [183]. $t\bar{t}W$ and $t\bar{t}Z$ production has been achieved at the LO accuracy, matrix elements containing up to two extra jets having been merged this time, with the W-boson being forced to decay leptonically and the Z-boson invisibly. All these background samples have been normalised to the next-to-next-to-leading order (NNLO) cross-sections, if available, or to the NLO cross section otherwise. For details on the background simulation and the normalization technique, we refer the reader to Ref. [149].

In order to perform a realistic analysis, we need to consider the detector effects on the various reconstructed objects, namely leptons (e and μ), jets and E_T^{miss}. Jets are reconstructed based on the MC truth particles using FASTJET [99], relying on the anti-k_T algorithm [98] with a radius parameter $R = 0.4$, whereas the missing transverse energy is defined as the vector sum of the transverse momenta of all the invisible particles. We then make use of smearing functions tuned to mimic the performance of the ATLAS detector [184, 185], as described in Ref. [149]. We have validated our results by comparing with a reduced statistical sample in which the simulation of the detector is performed within the publicly available code Delphes [186].

3.2 Variable definition and event selection

Several variables exploiting the kinematic difference between the signal and the backgrounds are used in our analysis. The construction of these discriminating variables is based on the assumption that the events are selected with exactly one lepton (electron or muon) and one and only one b-tagged jet. The final state is further allowed to contain extra jets, and missing transverse energy. More precisely, we preselect events containing exactly one electron or one muon with a transverse momentum and pseudorapidity fulfilling $p_{\mathrm{T}} > 25$ GeV and $|\eta| < 2.5$, and exactly one b-tagged jet with $p_{\mathrm{T}} > 30$ GeV within $|\eta| < 2.5$. The chosen b-tagging working point corresponds to an average tagging efficiency of 77% and is based on the parameterisations given in Ref. [187]. We moreover demand the presence of at least one additional jet with a transverse momentum $p_{\mathrm{T}} > 100$ GeV and $|\eta| < 2.5$ failing the b-tagging algorithm.

The dominant background for the present analysis arises from $t\bar{t}$ production, and the main handles for reducing this background consist of a set of kinematic variables in the transverse plane with respect to the LHC beams that are bounded from above by the fact that the invisible particles are always neutrinos issued from W-boson decays in the SM.

– Transverse mass of lepton and E_T^{miss} (m_{T}^{lep}): This variable, defined as

$$m_{\mathrm{T}}^{lep} \equiv \sqrt{2\,|\vec{p}_{\mathrm{T}}^{\,\ell}|\,|\vec{p}_{\mathrm{T}}^{\,\mathrm{miss}}|\,(1-\cos\Delta\phi_{\vec{p}_{\mathrm{T}}^{\,\ell}\vec{p}_{\mathrm{T}}^{\,\mathrm{miss}}})}\,, \tag{5}$$

is built from the lepton transverse momentum ($\vec{p}_{\mathrm{T}}^{\,\ell}$) and the vector sum of the transverse momenta of the invisible particles ($\vec{p}_{\mathrm{T}}^{\,\mathrm{miss}}$). For all processes where the lepton and the missing transverse energy are issued from the decay of a single W-boson, this variable has a kinematic end-point at 80 GeV, whilst it is allowed to reach much larger values for the signal. Imposing a lower bound on this variable therefore strongly suppresses the $t\bar{t}$ background, killing events where only one leg decays leptonically, as well as the W+jets background. We impose $m_{\mathrm{T}}^{lep} > 160$ GeV.

– Asymmetric m_{T2} (am_{T2}): After the m_{T}^{lep} requirement, the background is still dominated by $t\bar{t}$ events that decay into two leptons, but with one of the two leptons that is not identified in the detector. The variable am_{T2} [161, 162] was developed to tame this kind of background, and consists in a generalisation of the m_{T2} variable [159, 160]. It is built by considering the production of two particles that each decay into visible objects and missing energy, forming hence two legs. For the first leg, the visible momentum is defined as the vector sum of the momenta of the b-tagged jet and the lepton, whilst a vanishing test mass is introduced to kinematically derive the missing momentum. For the second leg, the visible momentum is fixed to that of the additional jet, that is most likely to be a b-jet, and the invisible transverse vector is derived from a test mass set to 80 GeV. In real experimental conditions, the jet employed for the second leg is the second hardest b-tagged jet, or, if there isn't any, the light jet with the highest weight returned by the b-tagging algorithm. Since this information not available within our parametric detector simulation, we use the information at truth level. We identify as the second leg either the hardest non-b-tagged b-jet or the hardest c-jet or the hardest light jet. For top quark pairs decaying into two leptons where one lepton is lost, this variable has an end-point at around 150 GeV, which provides a handle to suppress background contamination. We require $am_{\mathrm{T2}} > 200$ GeV.

– $m_{b\ell}$: The invariant mass of the system made of the b-tagged jet and lepton provides a good discriminant against backgrounds not including a top quark, since if the b-jet and the lepton originate from the decay of a single top quark, the corresponding distribution exhibits an endpoint at ~ 160 GeV; we impose $m_{bl} < 160$ GeV.

– $\Delta\phi_{\mathrm{min}}$: The minimum azimuthal angle between any jet and the missing transverse momentum $\vec{p}_{\mathrm{T}}^{\,\mathrm{miss}}$ can be used to increase the background rejection. In the extreme configurations stemming from the selections on the various m_{T2}-like variables, the backgrounds tend to exhibit missing transverse energy aligned with a hard jet, whereas there is no correlation for the signal. We therefore require that $|\Delta\phi_{\mathrm{min}}| > 0.6$.

– $\Delta R_{b\ell}$: The distance in the transverse plane between the lepton and the leading b-tagged jet is used as an additional discriminant, and we demand that $\Delta R_{b\ell} < 1.75$.

– $m_{\mathrm{T2}_{blj}}$: We compute the m_{T2} variable as usual by using two legs with a visible and invisible component. The first leg is defined as above, whilst the second leg takes as visible momentum the momentum of the hardest non-b-tagged jet. Both test masses are

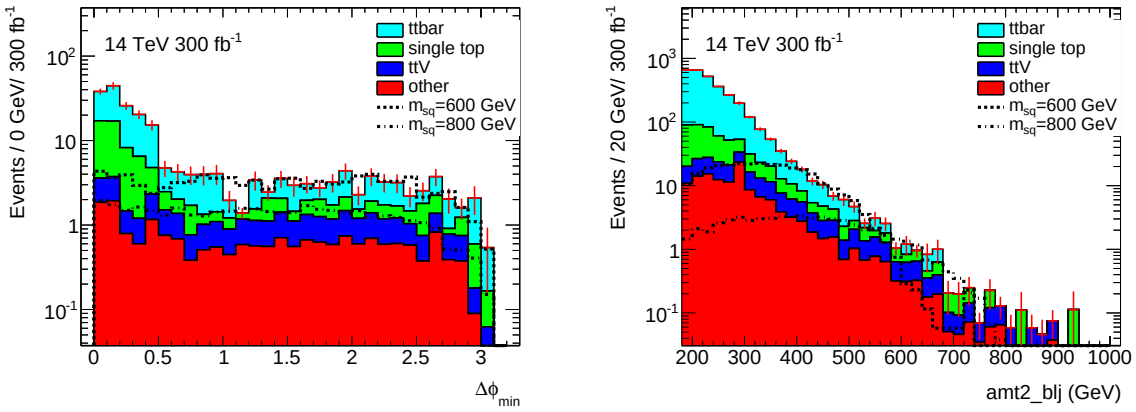

Figure 3: Distributions in the $|\Delta\phi_{\rm min}|$ (left) and $m_{\rm T2_{blj}}$ (right) variables after imposing all cuts of our analysis, excepted the one on the represented variable. We present results for the different background contributions and for two representative signal scenarios. The $|\Delta\phi_{\rm min}|$ results include a selection on the $m_{\rm T2_{blj}}$ variable that is imposed to be larger than 400 GeV.

put to zero. This variable is dependent on the mass difference of the squark and the lightest neutralino, as it tries, from the definition of the second leg, to approximate the Jacobian of the squark into charm and $\tilde{\chi}_1^0$ decay. This is therefore the final discriminant used in the analysis, and different selections are imposed optimising the sensitivity for each targeted squark mass. As can be seen in the right panel of Figure 3, the minimal cut to reduce the $t\bar{t}$ background to the same level as the signal for the minimum squark mass considered in the analysis is approximately 400 GeV, and a cut at $\sim$ 550 GeV mostly removes the $t\bar{t}$ background.

In Fig. 3 we present the distributions in $|\Delta\phi_{\rm min}|$ and $m_{\rm T2_{blj}}$, obtained after imposing all selection cuts but the one that is shown, for the different background contributions and two representative signal benchmarks. The $|\Delta\phi_{\rm min}|$ results include a $m_{\rm T2_{blj}} > 400$ GeV selection.

3.3 Results

We now estimate the sensitivity of our analysis to the presence of mixed stop states and present our results in Tables 1 and 2 for integrated luminosities of 300 and 3000 fb^{-1} respectively (without modifying the detector performance). We consider multiple signal scenarios for which we introduce different selections on the $m_{\rm T2_{blj}}$ variable, the threshold being obtained by maximising the sensitivity with a scan in steps of 50 GeV.

A profile likelihood test statistic is then used to evaluate the upper limit on the ratio of the signal yield to the one predicted in the context of the considered simplified model, and we use the CLs method [188] to derive exclusion limits at the 95% confidence level (CL). The statistical analysis has been performed by employing the `RooStat` toolkit [189] and the discovery/exclusion reaches assume systematic uncertainties of 20% (5%) for the SM background (signal), as well as a 3% uncertainty on the luminosity. We observe that mixed stop scenarios with a squark mass up to about 1 TeV would yield a 2σ excess already with an integrated luminosity of 300 fb^{-1}, this range being extended to 1.3 TeV for the high-luminosity LHC run. It is thus crucial to extend the current LHC search program and include analyses dedicated to the pair-production of top partners decaying into a single top quark and a lighter jet.

$m_{\tilde{u}_1}$ (GeV)	$m_{\tilde{\chi}_1^0}$ (GeV)	$m_{\mathrm{T2}_{blj}}$ cut (GeV)	N_s	N_b	$\sigma^{\mathrm{excl}}/\sigma^{\mathrm{SUSY}}$
600	50	400	124.9	63.0	0.23
700	50	450	55.6	31.5	0.30
800	50	500	25.8	15.3	0.41
900	50	500	17.0	15.3	0.63
1000	50	550	8.3	7.6	0.89
1100	50	600	4.0	4.4	1.41

Table 1: Number of background (N_b) and signal (N_s) events surviving our selection, for different benchmark models and optimised selections on the $m_{\mathrm{T2}_{blj}}$ variable. We present the results under the form of upper limits, at the 95% CL, on the ratio of the signal yield to the corresponding benchmark predictions. We assume an integrated luminosity of $300\,\mathrm{fb}^{-1}$ of proton-proton collisions at 14 TeV, and systematic uncertainties of 20% (5%) on the SM background (signal).

$m_{\tilde{u}_1}$ (GeV)	$m_{\tilde{\chi}_1^0}$ (GeV)	$m_{\mathrm{T2}_{blj}}$ cut (GeV)	N_s	N_b	$\sigma^{\mathrm{excl}}/\sigma^{\mathrm{SUSY}}$
600	50	400	1249	630	0.18
700	50	500	321.5	152.6	0.19
800	50	550	161.1	76.4	0.21
900	50	550	117.8	76.4	0.28
1000	50	700	26.7	11.1	0.33
1100	50	700	22.5	11.1	0.44
1200	50	700	15.2	11.1	0.59
1300	50	700	10.2	11.1	0.87
1400	50	750	5.1	6.8	1.38

Table 2: Same as Table 1 but for a luminosity of $3000\,\mathrm{fb}^{-1}$.

4 Outlook

In the analysis presented above, we have targeted a supersymmetric scenario where right-handed charm and top squarks mix and where squark pair-production could yield a signature made of charm jets, top quarks or both. In principle, mixing between the first and third generation could be allowed, although the situation is severely constrained by flavour data. It might be nevertheless interesting to design a strategy that may effectively discriminate these two possibilities at the LHC. This requires the ability to tag jets originating from the fragmentation of c-quarks, as opposed to jets arising from the fragmentation of light quarks or b-quarks. Charm tagging is currently being addressed by both LHC collaborations, as described *e.g.* by ATLAS [190]. We have however ignored charm tagging in our analysis, relying only on b-tagging, as there is currently no public information on the correlations between the b-tagging

and c-tagging algorithms. The latter are indeed necessary for a meaningful study. An alternative interesting possibility to discriminate the actual squark mixing could be to study the dependence of the results on the b-tagging working point, as the amount of light, c-jet (mis)identification varies significantly. Comparisons could indeed yield indications on the fraction of c-jets that is selected. An excellent control of the variations of the background composition with the b-tagging working point should however be necessary for this exercise, and robust predictions therefore require dedicated investigations.

Acknowledgements

The authors would like to thank Michihisa Takeuchi for many useful discussions and comments. This work has been partially supported by French state funds managed by the Agence Nationale de la Recherche (ANR) in the context of the Investissements d'avenir Labex ENIGMASS (ANR-11-LABX-0012) and Labex ILP (ANR-11-IDEX-0004-02, ANR-10-LABX-63), and by the Grant-in-Aid for Scientific Research on Scientific Research B (No.16H03991) and Innovative Areas (16H06492).

Contribution 8

Phenomenological Aspects of Intermediate Higgs (or Natural Composite Higgs) Models

N. Ezroura, P. Gardner, A. E. Nelson, M. Park and D. G. E. Walker

Abstract

Intermediate Higgs Models [191] (IH), rechristened in the literature as natural composite Higgs models, have a large region of parameter space yet to be constrained by the Large Hadron Collider (LHC). We explore the parameter space of these models by exploring the possibility of resolving low-mass boosted objects produced in association with colored partners of the top and bottom quark. For a simple model with an approximate $SU(4)/Sp(4)$ coset space, we consider unconstrained benchmark points that are consistent with precision electroweak data. We find that extending current searches for boosted objects to very low invariant masses (~ 25 GeV) provides an improved sensitivity to this theory relative to standard searches for top and bottom partners. Although we focus on a simple IH model, our analysis is useful in any scenario with new colored partners with approximate global symmetries, as are common for natural solutions to the hierarchy problem. The full analysis appears in [192].

1 INTRODUCTION

In this summary, we explore some phenomenological consequences of Intermediate Higgs model [191] at the Large Hadron Collider (LHC). IH models, rechristened in the literature as natural composite Higgs models, allow for a light Higgs boson where all of the new physics appears at a new scale which is naturally larger than the Higgs mass by a loop factor. This scenario is largely consistent with current measurements at the LHC. Given the lack of new physics beyond the Standard Model (SM), this loop factor has become insufficient. If naturalness arguments are relevant for the weak scale, new physics associated with compositeness must be at a much larger scale. IH scenarios allow for this by adding new top partners which cancel to corrections to the Higgs mass from the top loop. Here we study a simple IH model based on an $SU(4)/Sp(4)$ coset space. This $SU(4)/Sp(4)$ extension yields five new pNGB degrees of freedom, one of which is a new pseudo-scalar, with couplings to SM quarks through a new Yukawa sector (heavy top and bottom partners). The pseudo-scalar and top partners feature exotic LHC signatures at hadron collider scales.

2 THE MODEL

We use a nonlinear sigma model with a antisymmetric unitary matrix Σ that transforms under *SU(4)* as:

$$\Sigma \to V \Sigma V^\dagger \tag{1}$$

where V are $SU(4)$ representations. Σ is defined as:

$$\Sigma(x) = e^{2i\Pi/f}\Sigma_0 \tag{2}$$

where f is a decay constant, Σ_0 is a background field invariant under *Sp(4)*, and Π represents the fluctuations of the Nambu-Goldstone bosons about Σ_0 in the direction of the broken generators:

$$\Sigma_0 = \begin{pmatrix} i\sigma_2 & \\ & i\sigma_2 \end{pmatrix} \qquad \Pi = \pi^a X^a \tag{3}$$

The Higgs bosons are in the coset space Π which is defined as:

$$\Pi = \frac{1}{2\sqrt{2}} \begin{pmatrix} A & H \\ H^\dagger & -A \end{pmatrix} \tag{4}$$

Here A and H are matrices such that:

$$A = \begin{pmatrix} a & \\ & a \end{pmatrix} \qquad H = \begin{pmatrix} h^0 + ih_3 & ih^2 + h_2 \\ ih_1 - h_2 & h^0 - ih_3 \end{pmatrix}. \tag{5}$$

Here a is the electroweak singlet. H must satisfy $\sigma_2 H - H^*\sigma_2 = 0$ and h_i are real.

The new physics for a low energy effective Higgs theory with an $SU(4)/Sp(4)$ coset space is the existence of a single additional pseudo-scalar particle a. Such a particle would be produced with electroweak couplings and decay hadronically. This particle would also be generically lighter than the Higgs boson, making it one the worst case scenarios at a hadron collider like the LHC, as a leptophobic timid pseudo-scalar [193].

Addressing the hierarchy problem requires the addition of a colored multiplet of vector-like fermionic partner states $\Psi = (Q_T,\, Q_B,\, T,\, B)$ and $\overline{\Psi}$ that mix with the Standard Model top and bottom quarks $q = (q_T,\, q_B)$, $\bar{t}_3$ and $\bar{b}_3$. The extended theory introduces a new vector-like doublet $(Q', \overline{Q}')$, and has the following gauge invariant Yukawa sector.

$$\mathcal{L}_{\text{yukawa}} \supset -i\lambda_1 f\, \Psi\, \Sigma\, \overline{\Psi} + \lambda_2 f\, q\, \overline{Q} + \lambda_3 f\, T\, \bar{t}_3 + \lambda_4 f\, B\, \bar{b}_3 + \text{h.c.} \tag{6}$$

$$+ \; M'\, Q'\, \overline{Q}' + \tilde{\lambda}_1 f\, \overline{Q}'\, (q_3 + Q) + \tilde{\lambda}_2 f\, Q'\, \overline{Q} + \text{h.c.} \tag{7}$$

The addition of the extra doublet alleviates tension with precision electroweak data by allowing for small mixings between the SM doublet and the lightest partner states, while SM top and bottom mass ratio is still determined largely by the ratio $m_{\text{top}}/m_{\text{bottom}} \sim \lambda_3/\lambda_4$. We choose two benchmark points from this extension that are within the bounds of precision electroweak data. We then develop search strategies for resolving the pseudo-scalar in its low mass regime through its production in association with the top and bottom partners via the decays such as $Q \to a\, b$.

2.1 Simulation results

For our study of the process at the LHC (pp collisions at the $\sqrt{s} = 13$ TeV), we have chosen two benchmark points to demonstrate the analysis. The minimal Yukawa sector couplings are set to a common value $\lambda_1 = 2$, $\lambda_2 = 0.2$, $\lambda_3 = 2.9$, $\lambda_4 = 0.04$, the mass of the additional doublets is set to $M' = 1000$ GeV, and the pseudo-scalar mass is fixed at $m_a = 25$ GeV. With these

values there is a parameter subspace that interpolates between regions with low pseudo-scalar production rates due to large mass splittings of the partner states ($\tilde{\lambda}_1 > \tilde{\lambda}_2$) and one where their masses are fairly degenerate ($\tilde{\lambda}_1 < \tilde{\lambda}_2$). The chiral symmetry breaking scale f raises the partner masses uniformly and is chosen to fix the lightest partner (which is always the bottom quark) at the mass of its current LHC limit $m \sim 750$ GeV [194].

– Signal Benchmark A: $\tilde{\lambda}_1 = 2.9$, $\tilde{\lambda}_2 = 0.81$ $f = 500$ GeV

– Signal Benchmark B: $\tilde{\lambda}_1 = 0.79$, $\tilde{\lambda}_2 = 2.8$, $f = 650$ GeV

Event generation for all signal and background processes was performed using `MadGraph v2.6.0`, with parton showering by `Pythia8` and detector simulations using `Delphes3`. Signal benchmarks A and B were simulated using model files created in `UFO` format with `FeynCalc` with the full spectrum of tree level decays. Our study closely resembles the lepton + jets analysis performed recently by CMS [64]. The requirements of a high-p_T isolated lepton (> 50 GeV) and sizable $\not{E}_T$ in this channel are used to minimize the contribution from QCD multijets, while the dominant remaining backgrounds come from $t\bar{t}$+jets, W/Z+jets, diboson, and single-top production in association with W bosons and b jets. Hadronically decaying boosted objects are resolved by defining "fat jets" with large radii $\Delta R = 0.8$ which are divided into exclusive categories as either "H-tagged" or "V-tagged", based on the number of b-tagged subjects and their invariant mass which is required to be in the range $[60, 160]$. H-tagged fat jet are then divided into two categories H_1 and H_2 based on the number of subjets that pass the b-tag requirement.

With these cuts, events are divided into exclusive categories based on the number of tagged

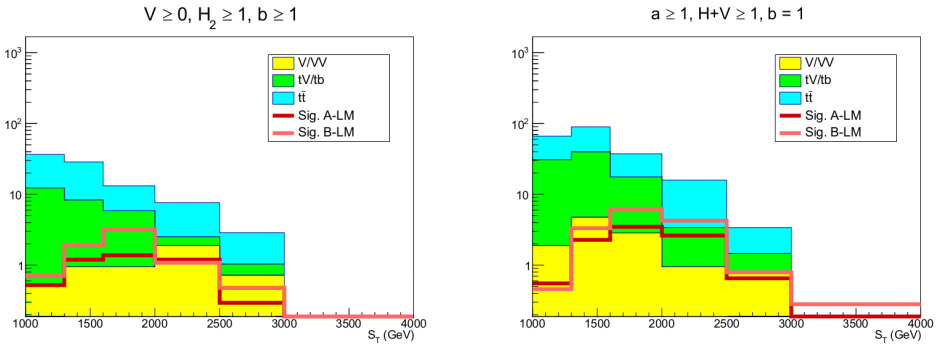

Figure 1: S_T distributions for two of the proposed search categories with the highest signal efficiency.

Signal Region Selection Efficiencies		
Final State	H-tag Channel Signal A/B	a-tag Channel Signal A/B
$V \geq 1, H \geq 1, a = 0$	2.6% / 3.0%	2.6% / 3.4%
$V \geq 1, H = 0, a \geq 1$	4.1% / 2.9%	5.3% / 5.0%
$V = 0, H \geq 1, a \geq 1$	0.06% / 0.14%	1.1% / 0.3%
$V \geq 1, H \geq 1, a \geq 1$	5.3% / 5.2%	5.3% / 5.4%

Table 1: Signal efficiencies in the proposed search categories. These efficiencies are comparable to those used to set the current strongest limits. [64]

boosted H_1, H_2 and V bosons, and binned by the total momentum scale of the event S_T. Additional categories focused on selecting boosted objects with low invariant masses, in the range of 10 - 40 GeV are then studied. This new category targets a low mass (25 GeV) pseudo-scalar a decaying predominantly to $b\bar{b}$ pairs, aimed at probing theory spaces beyond the simplified limit. We thus define an object to be "a-tagged" if it lies in the invariant mass window $[10, 40]$ GeV, has $p_T > 70$ GeV, and massdrop variable $\mu < 0.8$, and has at least one b-tagged subjet. We find that binning events in these new categories by their S_T provides signal-to-background ratios comparable to the signal categories in the CMS search [64]. The selection efficiencies for the signal region by various final states is given in Table [1], and S_T distributions for the two best categories are Figure [1].

CONCLUSIONS

The existence of a low mass pseudo-scalar particle, that is produced with electroweak cross sections but decays with dominantly hadronic branching fractions, presents a surmountable challenge for the Large Hadron Collider. In a forthcoming publication we demonstrate the effectiveness of boosted object taggers at low invariant masses in identifying these objects, if they are produced in association with other heavy states.

Contribution 9

Review of flavour anomalies

M. Borsato, D. Guadagnoli

Introduction – A whole range of $b \to s$ data involving a $\mu^+\mu^-$ pair display a consistent pattern, with experimental data below the respective Standard-Model (SM) prediction, for di-lepton invariant masses below the charmonium threshold. This is true for the $B^0 \to K^0\mu^+\mu^-$, the $B^+ \to K^+\mu^+\mu^-$ and the $B^+ \to K^{*+}\mu^+\mu^-$ decays [195], for the $B_s^0 \to \phi\mu^+\mu^-$ decay [196] and, very recently, even in hyperon channels for the $\Lambda_b \to \Lambda\mu^+\mu^-$ decay [197, 198]. With these data alone, however, it is presently impossible to establish beyond-SM effects, as branching-ratio measurements suffer in general from sizable theoretical uncertainties due to hadronic form factors. On the other hand, such problems are basically absent if one considers suitable ratios of branching ratios to different lepton channels. Dedicated measurements exist on such ratios, and actually constitute the most alluring set of anomalies. In the $b \to s$ case these measurements are [199, 200]

$$\begin{aligned} R_K([1,6]\text{GeV}^2) \equiv \tfrac{\mathcal{B}(B^+\to K^+\mu^+\mu^-)}{\mathcal{B}(B^+\to K^+e^+e^-)}|_{q^2\in[1,6]\text{GeV}^2} &= 0.745^{+0.090}_{-0.074}\,(\text{stat}) \pm 0.036\,(\text{syst})\,, \\ R_{K^{*0}}([0.045, 1.1]\,\text{GeV}^2) &= 0.660^{+0.110}_{-0.070} \pm 0.024\,, \\ R_{K^{*0}}([1.1, 6]\,\text{GeV}^2) &= 0.685^{+0.113}_{-0.069} \pm 0.047\,, \end{aligned} \tag{1}$$

where we have omitted the definition of $R_{K^{*0}}$, analogous to the R_K one, and where q^2 denotes the invariant mass squared of the di-lepton pair. All of the above measurements are predicted to be unity (first and third of them) and respectively close to it (second one) within the SM, with a few-percent accuracy [201] (see also [202–204]). Therefore, the R_K and $R_{K^{*0}}$ measurements each imply a discrepancy between 2 and 2.6σ [199, 200], at face value signalling lepton-universality violation (LUV) beyond the SM.

The electron-channel measurement would be an obvious culprit for the discrepancies, because of bremsstrahlung and lower statistics. However, the measurement agrees with the SM. It is instead in the muon channel that experiment tends to depart from the SM [195, 205, 206], with data *below* predictions. Note that such a pattern is coherent with R_K being below unity. Besides, muons are among the most reliable objects within LHCb, and this would disfavour (although of course not exclude) systematic effects as an explanation. These arguments provide circumstantial support to the overall coherence of the experimental picture, that suggests a violation of lepton universality, with effects in muons, and not in electrons.

Importantly, the emerging picture can be established from ratios alone, but it is supported by the other measurements, whose theory error is more debated. Some comments are deserved in particular for the $B \to K^*\mu\mu$ angular analysis [207–212], exhibiting a discrepancy in one combination of the angular-expansion coefficients, known as P_5'. The theory error on this observable is a matter of debate because, while it is designed to minimize f.f. dependence [213], what cancels is the dependence on the infinite-m_b form factors. The crucial issue is how important departures from the infinite-m_b limit are as the di-lepton invariant mass squared q^2 approaches the charmonium threshold $4m_c^2$ – in particular, departures due to $c\bar{c}$-loop contributions, that at present are still incalculable. Such contributions are formally power suppressed

in a $1/m_b$ expansion, but also come with a factor of $1/(q^2 - 4m_c^2)$ [214], that becomes larger and larger as q^2 approaches the charmonium threshold. On the different approaches towards assigning a significance to the P_5' discrepancy, see in particular [215–218]. Nonetheless, this observable again supports, even quantitatively, the picture emerging from ratios alone.

Equally interesting results come from measurements of the ratios $R(D^{(*)}) \equiv \mathcal{B}(B \to D^{(*)}\tau\nu)/\mathcal{B}(B \to D^{(*)}\ell\nu)$ [219–222]. Here the theory error is less intuitive, as the τ mass is not negligible with respect to m_B, and f.f. (form factor) dependence does not quite cancel in these ratios. However, they can be constrained thanks to accurate LQCD determinations (in the case of R_D) [223,224] or to other experimental measurements (R_{D^*}) [225,226]. Accordingly, a simultaneous fit to all these $R(D)$ and $R(D^*)$ measurements yields a discrepancy with respect to the SM predictions with a significance of about 4σ [227], comparable to the global significance of $b \to s$ anomalies. Note also that $b \to c$ anomalies come jointly from several experiments: B factories and LHCb.

Theory considerations – The above-mentioned discrepancies are intriguing for at least the following reasons: *(a)* they concern two sets of observables ($b \to s$ and $b \to c$) related by the SM $SU(2)_L$ symmetry [228]; *(b)* both $b \to s$ and $b \to c$ measurements suggest dynamics that distinguishes between the different species of leptons, i.e. beyond-SM Lepton-Universality Violation" (LUV); *(c)* discrepancies appear to obey a pattern, i.e. data are always on a given side with respect to the SM predictions; *(d)* this pattern finds a straightforward interpretation within what is called an effective-field-theory (EFT) framework, to be expanded upon next.

Let us consider the following Hamiltonian, which is part of the full $\bar{b} \to \bar{s}\ell\ell$ one

$$\mathcal{H}_{\rm SM+NP}(\bar{b} \to \bar{s}\ell^+\ell^-) = -\frac{4G_F}{\sqrt{2}} V_{tb}^* V_{ts} \frac{\alpha_{em}(m_b)}{4\pi} \times \left[\bar{b}_L \gamma^\lambda s_L \, \bar{\ell}\left(C_9^{(\ell)}\gamma_\lambda + C_{10}^{(\ell)}\gamma_\lambda\gamma_5\right)\ell\right] + \text{H.c.}\,, \tag{2}$$

where the index (ℓ) on the Wilson coefficients $C_{9,10}$ denotes that the corresponding new-physics shift distinguishes between lepton flavours, whereas the SM contribution doesn't, as well known. The SM contributions are such that $C_9 \simeq -C_{10}$ at the m_b scale, yielding (accidentally) an approximate $(V-A)\times(V-A)$ structure. Advocating likewise $C_{9,\rm NP}^{(\mu)} = -C_{10,\rm NP}^{(\mu)}$ for the new-physics shifts (note, in the μ-channel only) turns out to account at one stroke for all $b \to s$ discrepancies [229, 230]. Further global fits by different groups consistently show that the most favourite solutions are either a negative new-physics (NP) contribution to C_9, with $C_{9,\rm NP}^{(\mu)} \sim -30\%\, C_{9,\rm SM}$, or NP in the mentioned SU(2)$_L$-invariant direction $C_{9,\rm NP}^{(\mu)} = -C_{10,\rm NP}^{(\mu)} \simeq -12\%\, |C_{9,\rm SM}|$. Note that such a solution is approximately RGE-stable.

The latter solution is especially interesting from a UV point of view, because it amounts to a $(V-A)_{\rm quark} \times (V-A)_{\rm lepton}$ operator (see eq. (2)), that can in turn be promoted to an $SU(2)_L$-invariant, which is what one would expect of interactions arising above the EWSB scale. Let us then focus on this solution: $C_9^{(\ell)} \approx -C_{10}^{(\ell)}$ and $|C_{9,\rm NP}^{(\mu)}| \gg |C_{9,\rm NP}^{(e)}|$. Such a pattern, with effects much larger for muons than for electrons, can be generated from a purely third-generation interaction [231]

$$\mathcal{H}_{\rm NP} = G\,(\bar{b}'_L\gamma^\lambda b'_L)\,(\bar{\tau}'_L\gamma_\lambda\tau'_L)\,, \tag{3}$$

with $G = 1/\Lambda_{\rm NP}^2$ a new Fermi-like coupling, corresponding to a NP scale $\Lambda_{\rm NP}$ in the TeV ballpark. The interaction in eq. (3) is expected, e.g., in partial-compositeness frameworks [232].

The prime on the fields indicates that they are in the "gauge" basis, i.e. that below the EWSB scale they need to be rotated to the mass eigenbasis by usual chiral unitary transformations of the form

$$b'_L \equiv (d'_L)_3 = (U^d_L)_{3i}(d_L)_i \,, \qquad \tau'_L \equiv (\ell'_L)_3 = (U^\ell_L)_{3i}(\ell_L)_i \,, \tag{4}$$

whereby the r.h.s. fields represent the mass eigenbasis. In the absence of further assumptions on the structure of the rotation matrices, they will in general induce LUV *and* Lepton-Flavor Violation (LFV) effects alike [231]. This is also a general expectation in a 'top-bottom' approach: consider a new, LUV interaction introduced to explain R_K, and defined above the electroweak symmetry breaking (EWSB) scale. Such interaction may be of the kind $\bar{\ell} Z' \ell$, with Z' a new vector boson, or $\bar{\ell}\phi q$, with ϕ a leptoquark. The question arises, in what basis are quarks and leptons in the above interaction. Generically, it is not the mass eigenbasis – this basis does not yet even exist, as we are above the EWSB scale. Rotation to the mass eigenbasis generates LFV effects, although the initial interaction was introduced to produce only LUV ones.

With the above ingredients we can straightforwardly explain $b \to s$ data. In particular, neglecting the negligible phase-space difference between the electron and the muon channels, one finds

$$R_K \approx \frac{|C^{(\mu)}_9|^2 + |C^{(\mu)}_{10}|^2}{|C^{(e)}_9|^2 + |C^{(e)}_{10}|^2} \simeq \frac{2|C_{10,\mathrm{SM}} + C^{(\mu)}_{10,\mathrm{NP}}|^2}{2|C_{10,\mathrm{SM}}|^2} \,, \tag{5}$$

where the factors of 2 on the r.h.s. are due to the contributions from $|C_9|$ and $|C_{10}|$ being equal by assumption. Note as well that

$$0.77 \pm 0.20 = \frac{\mathcal{B}(B_s \to \mu\mu)_{\mathrm{exp}}}{\mathcal{B}(B_s \to \mu\mu)_{\mathrm{SM}}} = \frac{\mathcal{B}(B_s \to \mu\mu)_{\mathrm{SM+NP}}}{\mathcal{B}(B_s \to \mu\mu)_{\mathrm{SM}}} = \frac{|C_{10,\mathrm{SM}} + C^{(\mu)}_{10,\mathrm{NP}}|^2}{|C_{10,\mathrm{SM}}|^2} \,, \tag{6}$$

implying, within the model in ref. [231], the correlations (see also [229])

$$\frac{\mathcal{B}(B_s \to \mu\mu)_{\mathrm{exp}}}{\mathcal{B}(B_s \to \mu\mu)_{\mathrm{SM}}} \simeq R_K \simeq \frac{\mathcal{B}(B^+ \to K^+\mu\mu)_{\mathrm{exp}}}{\mathcal{B}(B^+ \to K^+\mu\mu)_{\mathrm{SM}}} \,. \tag{7}$$

This relation states that the measurement-over-SM ratio for $\mathcal{B}(B_s \to \mu\mu)$ provides a proxy for R_K. This is one more good reason to pursue accuracy in the $\mathcal{B}(B_s \to \mu\mu)$ measurement. To the extent that the central value on the l.h.s. of eq. (6) remains low, this test will be a sensitive one already by the end of Run 2, because the $\mathcal{B}(B_s \to \mu\mu)$ total error (dominated by the experimental component) is anticipated to be around 10% [233, 234].

Concerning the expected LFV, the crucial question of course is whether it is experimentally accessible. The interaction (3), plus the measured amount of LUV pointed to by R_K, provide a general argument [231, 235] on the LFV rates to expect. In fact, R_K yields the ratio

$$\rho_{\mathrm{NP}} = -0.159^{+0.060}_{-0.070} \tag{8}$$

between the NP and the SM+NP contribution to $C^{(\mu)}_9$. Then, for *any* decay of the kind $B \to K\ell^\pm_i\ell^\mp_j$, where $i \neq j$ amounts to LFV, one can write

$$\frac{\mathcal{B}(B \to K\ell^\pm_i\ell^\mp_j)}{\mathcal{B}(B^+ \to K^+\mu^+\mu^-)} \simeq 2\rho^2_{\mathrm{NP}} \frac{|(U^\ell_L)_{3i}|^2|(U^\ell_L)_{3j}|^2}{|(U^\ell_L)_{32}|^4} \,, \tag{9}$$

where we used the U-matrix transformations (4), and normalised to the well-measured $\mathcal{B}(B^+ \to K^+\mu^+\mu^-) \simeq 4.3 \times 10^{-7}$ [195]. One thereby obtains

$$\mathcal{B}(B \to K\ell_i^\pm \ell_j^\mp) \simeq 5\% \cdot \mathcal{B}(B^+ \to K^+\mu^+\mu^-) \cdot \frac{|(U_L^\ell)_{3i}|^2 |(U_L^\ell)_{3j}|^2}{|(U_L^\ell)_{32}|^4} \simeq$$
$$\simeq 2.2 \times 10^{-8} \cdot \frac{|(U_L^\ell)_{3i}|^2 |(U_L^\ell)_{3j}|^2}{|(U_L^\ell)_{32}|^4} \,. \tag{10}$$

Eq. (10) neglects all terms proportional to lepton masses, which in the case of τ leptons produce corrections of several tens of percent. Such effects are unimportant in the context of the present argument, whose aim is to produce order-of-magnitude estimates. Eq. (10) tells us that LFV $B \to K$ decays are expected to be of order 10^{-8} times an *unknown factor* involving U_L^ℓ matrix entries. Then, the argument about the expected size of LFV effects boils down to an argument about such factor.

In the $\ell_i\ell_j = e\mu$ case, this ratio reads $|(U_L^\ell)_{31}/(U_L^\ell)_{32}| \lesssim 3.7$ [231], implying that the $B \to K\mu e$ rate may be around 10^{-8}, or much less if $|(U_L^\ell)_{31}/(U_L^\ell)_{32}| \ll 1$. The latter possibility would suggest U_L^ℓ entries that decrease in magnitude with the distance from the diagonal. But then one may expect the ratio $|(U_L^\ell)_{33}/(U_L^\ell)_{32}| > 1$, implying a $B \to K\mu\tau$ rate of O(10^{-8}) or above! In short, assuming the interaction (3), one can expect just because of the overall unitarity of the U_L^ℓ matrix that at least one LFV $B \to K$ decay rate be in the ballpark of 10^{-8} [231], which happens to be within reach at LHCb's Run 2.[1] An entirely analogous reasoning applies for the purely leptonic modes $B_s \to \ell_i^\pm \ell_j^\mp$.[2]

Being defined above the EWSB scale, the operator in eq. (3) can, and should be promoted to a full $SU(2)_L$ invariant [239], as mentioned above. This operation yields interactions of the kind $(\bar{Q}_L'^i \gamma^\lambda Q_L'^i)\,(\bar{L}_L'^j \gamma_\lambda L_L'^j)$ and $(\bar{Q}_L'^i \gamma^\lambda Q_L'^j)\,(\bar{L}_L'^j \gamma_\lambda L_L'^i)$, with i, j SU(2)$_L$ indices and Q_L', L_L' the SM quark and lepton doublets in the gauge basis. The second interaction yields in turn charged currents like $(\bar{t}_L' \gamma^\lambda b_L')(\bar{\tau}_L' \gamma_\lambda \nu_{\tau L}')$. After rotation to the mass eigenbasis, the last structure contributes to $\Gamma(b \to c\tau\nu_\tau)$ [228], thereby allowing to explain the LHCb and B-factories deviations on $R(D^{(*)})$.

While the above scenario is very attractive, it has to withstand non-trivial constraints, in particular from $B \to K\bar{\nu}\nu$ (see also [240]), from LEP-measured $Z \to \ell\ell$ couplings, and, most importantly, from LUV effects in $\tau \to \ell\nu\nu$ decays [241]. The latter constraints are especially dangerous, as they are tested to per mil accuracy, and they turn out to "strongly disfavor an explanation of the $R(D^{(*)})$ anomaly model-independently" [241]. The same argument shows that also LFV decays of leptons are generated, and that they provide probes well competitive with the ones pointed out above, in particular $\mathcal{B}(\tau \to 3\mu)$, $\mathcal{B}(\tau \to \mu\rho) \sim 5 \times 10^{-8}$ [241].

Model-building considerations – Up to now we have restricted ourselves to EFT considerations. Needless to say, we would expect the EFT picture to be the result of some new UV dynamics. Progress in this respect has to face a few challenging obstacles. The first one is the fact that, in the SM, $B \to D^{(*)}\tau\nu$ and $B \to K^{(*)}\ell\ell$ decays arise respectively at tree and loop level, whereas the NP corrections hinted at by data are in either case of O(15-25%). This issue is relevant if we seek a common explanation of $b \to c\tau\nu$ and $b \to s\ell\ell$ discrepancies.

[1] For more quantitative studies, see e.g. [236–238].

[2] We should keep in mind that at Run 2 the LHCb is expected [234] to provide a first measurement of $\mathcal{B}(B_d \to \mu^+\mu^-)$, which in the SM is as small as $1 \cdot 10^{-10}$.

A second obstacle is inherent in the fact that the needed NP is of the kind $J_{\rm q} \times J_\ell$, i.e. the product of a quark and a lepton current. In most UV setups, such operators are typically accompanied by $J_{\rm q} \times J_{\rm q}$ and $J_\ell \times J_\ell$ structures, that are severely constrained by data, respectively from B_s-mixing observables, and from purely leptonic LFV or LUV decays.

Finally, a third obstacle emerges from the observation that most model-building attempts advocate new charged, and possibly colored, states, with masses not larger than O(tens of TeV) and with significant couplings to 3$^{\rm rd}$-generation SM fermions. These conditions make constraints from direct searches, in particular of resonances decaying to $\tau\tau$ pairs, especially relevant, see [242, 243].

With the above qualifications, many proposals of plausible UV models for the anomalies have been made, typically involving a new Lorentz scalar or vector, with any[3] of the following transformation properties under the SM gauge group: a singlet or a triplet under SU(3)$_c$ (the latter case is known as leptoquark); a singlet or a doublet or a triplet under SU(2)$_L$.

It follows a very short review of the models proposed to account simultaneously for the $b \to s$ and the $b \to c$ anomalies. This review is far from exhaustive, in particular it limits itself to work published at the time of this workshop (summer 2017). Our aim is primarily to expose the non-trivial challenges that such simultaneous explanation poses in the face of all the existing constraints.

Explicit Models – A first natural possibility among those mentioned before is that of a color-singlet, weak-triplet vector field, i.e. a heavier replica of the $W^\pm, Z^0$ bosons [242, 244]. Ref. [242] discusses in detail the bounds imposed by $\tau \to \ell\nu\nu$, B_s-mixing, and direct searches. The minimal model turns out to be ruled out by searches of resonance-produced τ pairs. Non-minimal versions of the model can avoid this constraint at the price of a larger parameter space. Ref. [244] aims at a general discussion of gauge extensions with LUV, and concludes that within these models universality violation is most likely a signature of Yukawa couplings between the SM fermions and new vector-like fermions. The other color-neutral possibilities (weak triplet of scalars, and weak doublets or singlets) either amount to extended Higgs sectors, that in general have a tree-level FCNC problem, or else fail to fulfil gauge invariance.

Let us now turn to color-triplet scalars or vectors. Color triplets are usually referred to as leptoquarks (LQ) [245], i.e. states coupled to a quark and a lepton. By definition they thus avoid tree-level contributions to meson mixings and purely leptonic LUV/LFV decays. Besides, vector LQs are ubiquitous in grand-unified theory (GUT) scenarios. Ref. [246] proposes an $SU(2)_L$-singlet Lorentz-scalar LQ able to explain both $R_{K^{(*)}}$ and $R(D^{(*)})$ with loop corrections to the former and tree corrections to the latter. While such dynamics is rather appealing, in that it reproduces the same suppression pattern as the SM, the model produces too large corrections to the measured ratio $\mathcal{B}(B \to D\mu\nu)/\mathcal{B}(B \to De\nu)$ [247]. Ref. [248] proposes a weak-triplet Lorentz-vector with completely general flavour couplings g_{ij} to a $\bar{Q}^i_L L^j_L$ bilinear, i, j denoting flavour indices. This scenario generalises [240], where the LQ is assumed to couple only to the third-generation fermions in the weak basis. From a fit to data, one obtains $g^*_{b\mu} g_{s\mu} \sim 10^{-3} \cdot (M_U/\text{TeV})^2$ and $|g_{b\tau}| \gtrsim 2$ from $b \to s$ and respectively $b \to c$ anomalies, with M_U the mass of the LQ. One may argue that this hierarchy introduces another flavour problem. One further problem, actually common to all cases involving *vector* LQs, will be emphasized below.

Ref. [249] interprets the patterns of corrections required by the anomalies as the result of a broken flavour symmetry. Specifically, the authors note that $b \to c\tau\nu$ anomalies involve the

[3] Compatibly with gauge invariance.

$3^{\rm rd}$ generation of leptons, whereas $b \to s\ell\ell$ ones concern light generations of leptons only. They then invoke a flavour group G_F and a tree-level LQ exchange such that, in the limit of exact G_F, the LQ couples only to the $3^{\rm rd}$ generation of SM fermions, and the needed NP effects arise from the G_F breaking. This implies singly suppressed corrections to $b \to c\tau\nu$ and three times suppressed effects in $b \to s\ell\ell$. Ref. [249] encompasses the cases of a weak-singlet vector, and of a weak-singlet scalar or vector LQ. While the mechanism is very plausible, the generated EFT operators do not escape, in general, the argument in ref. [241], because the only G_F-invariant SM fermions are the left-handed doublets. Among the merits of ref. [249] is also the fact that it exposes a problem that is common to all models with *massive vector* LQs, and already signalled at the end of the previous paragraph. It is the problem of *power-like* sensitivity to the UV cutoff. This sensitivity manifests itself in the power-like divergence of 2-, 3-point functions, and box diagrams. This issue, on the one hand *de facto* reintroduces at one loop the constraints from, e.g., B-meson mixings, that for LQs is, as mentioned above, absent at tree level; on the other hand, it prevents a reliable assessment of such constraints. This is problematic in the same way it was to allow for $M_{W,Z} \neq 0$ before the introduction of the Higgs mechanism and the discovery of its renormalizability. In short, such cutoff sensitivity in the words of ref. [249] "cries out for an explicit UV completion", if only for the sake of calculability. An attempt (as of the present writing) in this direction is ref. [250], although a separate challenge is represented by the detailed verification that this UV completion does withstand all the existing constraints.

Finally, ref. [251] advocates a weak-doublet scalar LQ coupled to the bilinears $\bar{d}_R L_L$ and $\bar{Q}_L \nu_R$ through Y_L and Y_R Yukawa couplings, whereby the right-handed ν field is required to have negligibly small mass. By virtue of the $(V+A)_{\rm quark} \times (V-A)_{\rm lepton}$ current invoked, this setup is not affected by the constraint in ref. [241], but predicts $R_{K^*} > 1$, in tension with the recent measurement [200].

Further tests – The above discussion highlights that the UV aspects of the dynamics responsible for the anomalies are not quite as established as the EFT picture. Of course, if anomalies are here to stay, the correct UV picture will eventually emerge, guided from data. Further tests that can help consolidating the picture may be classified into three broad categories:

- Measurements of additional LUV ratios;
- Extraction of long-distance effects from *data*;
- Definition and measurement of new observables sensitive to C_9 and C_{10}.

The first direction is rather evident. Other planned measurements include R_ϕ, $R_{K_0(1430)}$, R_{f_0}, and the inclusive R_{X_s}. An interesting test [252] is to define the double ratios

$$X_H \equiv \frac{R_H}{R_K} \,, \tag{11}$$

with $H = K^*$, ϕ, $K_0(1430)$, f_0 or X_s. Deviations from unity in X_H can only come from right-handed quark currents.

As concerns the second item, it should be recalled that, especially in $b \to s\ell\ell$ modes an important obstacle towards a robust comparison of data with theory is the presence of long-distance (LD) effects due to $c\bar{c}$ loops. (I reiterate, however, that while this may be an issue for branching ratios, it is not for ratios such as R_K.) Encouraging is the fact that, in many cases,

this matter seems amenable to be sorted out experimentally, by measuring the $m_{\mu^+\mu^-}$ spectrum, including the $c\bar{c}$ resonances, and fitting it to suitable parameterizations such as [216, 253, 254]. An application of this approach to the $B^+ \to K^+\mu^+\mu^-$ case was recently presented in ref. [255]. Interestingly, the measurement yields a result compatible with previous measurements [195] and, again, *below* the SM prediction [256].

Finally, the third item above suggests to pursue measurements of new observables, independently sensitive to C_9 and C_{10}. One example is the $B_s \to \mu^+\mu^-\gamma$ decay [257, 258], whose spectrum is, for low q^2, sensitive to electromagnetic-dipole operators, and, in the whole q^2 range, to interactions in eq. (2) as well as to their right-handed counterparts. Besides, its total branching ratio is one order of magnitude above the $B_s \to \mu^+\mu^-$ one, since the chiral suppression in the latter decay is replaced by an $\alpha_{\rm em}/\pi$ factor [257]. (For this very reason, the radiative decay is promising even for lepton-flavor-violating searches [235, 238].) However, a measurement of the $B_s \to \mu^+\mu^-\gamma$ decay by direct detection of the photon poses a major challenge at hadron colliders, because photons are also the typical signature of the ubiquitous π^0, and because photons leave only (if at all) calorimetric information. Ref. [259] points out that, for large q^2, $B_s \to \mu^+\mu^-\gamma$ events may actually be searched for in the very same event sample selected for the $\mathcal{B}(B_s \to \mu^+\mu^-)$ measurement, by enlarging the q^2 signal window beneath the peak region $q^2 \simeq m^2_{B_s}$. Hence this method combines the advantage of a large and ever increasing $B_s \to \mu^+\mu^-$ event sample with the advantage of $B_s \to \mu^+\mu^-\gamma$, that probes the interactions hinted at by the anomalies more thoroughly than $B_s \to \mu^+\mu^-$. From an experimental point of view, this method may be the only one practicable at hadron colliders, for the reasons already stated at the beginning of this paragraph. We also note that this method would provide the first experimental determination (ever) of $\mathcal{B}(B_s \to \mu^+\mu^-\gamma)$, because the PDG does not even quote a bound on this mode.

The Higgs Boson

Contribution 10

Simplified Template Cross Sections: sensitivity to dimension-6 interactions at the LHC

J. de Blas, K. Lohwasser, P. Musella, and K. Mimasu

Abstract

We perform a sensitivity study of the simplified template cross section (STXS) measurements to dimension-6 interactions within the Standard Model Effective Field Theory framework. We focus on energy dependent effects in Higgs production in association with a Z-boson, $pp \to ZH \to \ell^+\ell^- b\bar{b}$. Several benchmark points are considered, with different values of a representative Wilson coefficient, alongside the Standard Model prediction as well as the dominant $Zb\bar{b}$ background. We contrast the expected sensitivity obtained by the STXS to an analysis exploiting multivariate techniques via a boosted decision tree classifier. The aim of this exercise is to estimate the amount information retained in the STXS binning, and therefore the power of the framework for model-independent hypothesis testing in Higgs physics. We observe that the final performance of the BDT analysis does not differ significantly from the differential information in Z-boson p_T offered by the STXS, with one notable exception. This would suggest that, once the sensitivity of the STXS measurements is saturated, moving towards optimised multivariate methods remains well-motivated.

1 Introduction

The Standard Model Effective Field Theory (SMEFT) is, by now, a well established framework for parametrising new physics effects in the interactions of Standard Model (SM) particles in a model independent way. It has been and continues to be a key part of the LHC programme, complementary to direct searches for new physics. The framework employs an operator expansion in canonical dimension suppressed by a generic cutoff scale, Λ, assumed to be much larger than the electroweak (EW) scale. The leading new physics contributions supplement the SM Lagrangian with dimension 6 operators[1],

$$\mathcal{L} = \mathcal{L}_{SM} + \sum_i \frac{C_i}{\Lambda^2} \mathcal{O}^i_{D=6} + \cdots . \tag{1}$$

New physics effects are then always suppressed by q^2/Λ^2, where $q < \Lambda$ is a given mass scale, e.g. $q = v$ the Higgs vacuum expectation value, or $q = E$ the typical energy scale of a physical process.

[1]There is also one dimension-5 operator, the Weinberg operator, which generates neutrino masses.

One of the main strengths of the LHC in this respect is its ability to probe the high energy regime, in which it is expected that the sensitivity to the E^2/Λ^2 effects will be maximised. Furthermore, the discovery of the Higgs boson in 2012 [260, 261] has opened a brand new avenue in constraining the SMEFT parameter space consisting of the various operators involving Higgs fields. Measurements of Higgs production and decay modes have already provided new constraints on many operators and have also helped to constrain some blind directions in existing fits to low-energy data such as precision electroweak measurements at LEP.

In the first run of the LHC, a very successful programme of signal strength measurements took place, in which information from many searches was combined into a global fit to overall coupling modifiers between the Higgs and the rest of the SM particles [262]. The natural evolution of these measurements for Run 2 is to subdivide the phase space and work towards differential observables in Higgs production and decay. To this end, a staged approach termed Simplified Template Cross Sections (STXS) is being developed [263], consisting of an increasingly fine-grained binning of kinematic observables, separated by production and decay mode. The aim is to provide measurements in mutually exclusive regions of phase space, performed in simplified fiducial volumes and unfolded to remove detector and acceptance effects.

Being one of the main elements of LHC searches for non-SM physics, it is of great interest to evaluate the sensitivity of the STXS measurements to SMEFT effects in Higgs boson interactions, particularly since they will be able to access these high energy tails of kinematic distributions. In particular, one would like to know how the information provided by a generic framework such as the STXS would compare to an optimised, dedicated search for SMEFT effects. Naively, one may expect some loss of information given, *e.g.*, the finite binning of the distributions. In this study, we aim to quantify this difference by comparing and contrasting the ability to constrain SMEFT effects in Higgs production between the STXS measurements and an optimised analysis making use of multivariate methods to extract the maximum classification power of the SMEFT signals. We consider the concrete scenario of the (ZH) production of a Higgs boson decaying into a pair of b-quarks in association with a Z-boson decaying to a pair of leptons, in the presence of a single EFT operator. We simulate several benchmark values for the operator Wilson coefficient consistent with current constraints, along with the dominant reducible SM background, and evaluate the statistical discriminating power of a hypothesis test using the STXS measurements versus a multivariate Boosted Decision Tree (BDT) classifier.

The paper is organised as follows. We first outline the Monte Carlo event generation procedure for the SM and EFT benchmarks in Section 2, then in Section 3 we describe the fiducial selection employed, the training and analysis implemented using the BDT classifier and the STXS binning used for ZH. In Section 4, we summarise the results of the selections and binning, and perform a statistical hypothesis test to quantify the relative strengths of the two methods. We conclude by laying out the avenues for further investigation in Section 5.

2 Generated Models

The production of a Higgs boson in association with an EW gauge boson can be considered one of the canonical LHC processes sensitive to SMEFT effects. Evidence for this process involving the $b\bar{b}$ decay mode of the Higgs and leptonic vector boson decays was finally observed in 2017 [264, 265]. Some of the operators which modify the Higgs coupling to these gauge bosons introduce E^2/Λ^2 effects in the production rate, enhancing it at high energies. The associated production process can naturally access this region of phase space since the Higgs is produced

recoiling against the associated vector, meaning that the p_T of the Higgs or vector boson are a faithful proxy for the energy flowing through the EFT vertex. Of the many dimension-6 operators that can contribute to this process, we consider

$$\mathcal{O}_{HW} = \frac{ig}{2\Lambda^2}\left[D^\mu\varphi^\dagger\sigma_k D^\nu\varphi\right]W^k_{\mu\nu}, \tag{2}$$

an operator from the so called strongly interacting light Higgs (SILH) basis [266, 267]. Here, σ_k refers to the Pauli matrices and the covariant derivative, D_μ, for the Higgs field is defined as

$$D_\mu\varphi = \partial_\mu\varphi - ig\frac{\sigma_k}{2}W^k_\mu\varphi - \frac{1}{2}ig'B_\mu\varphi, \tag{3}$$

with g and g' the weak and hypercharge gauge couplings respectively.

A global fit [268] combining information from precision measurements at LEP and LHC Run 1 data constrains the Wilson coefficient, C_{HW}, to lie in the range

$$\frac{m_W^2}{\Lambda^2}C_{HW} \in [-0.07,\ 0.03] \text{ at } 95\% \text{ C.L.} \tag{4}$$

A sensitivity estimate for LHC Run 2 was also performed in Ref. [269] by projecting an 8 TeV ZH analysis [270] to 13 TeV. The results of the study indicated that the previous bound could be improved by an order of magnitude. This indicates that the STXS measurements are likely to provide even greater sensitivity to this parameter.

Motivated by the limits from the global fit, we select the following benchmark values for $c_{HW} \equiv C_{HW}\, m_W^2/\Lambda^2$:

$$c_{HW} = \pm 0.03 \text{ and } \pm 0.01. \tag{5}$$

The first value roughly saturates the positive end of the limit, and has been shown to yield drastic effects in the kinematic tails of distributions [269]. The second corresponds to a smaller, yet potentially accessible value of the parameter that may better test the relative discriminating power of relatively small effects between the two methods we investigate. We simulate our Monte Carlo samples at leading order using MADGRAPH5_AMC@NLO [95] with the public HELATNLO [269, 271] FEYNRULES [91] model, exploiting reweighting methods to simulate multiple parameter space points (including the SM) simultaneously. We also include the dominant irreducible background contribution from $Zb\bar{b}$ production with the Z-boson decaying leptonically. Showering and hadronisation, as well as the Higgs boson decay to $b\bar{b}$ are performed with PYTHIA8 [97] and the events are reconstructed from hadron level with MADANALYSIS5 [272] which makes use of FASTJET [99].

3 Analysis

3.1 Fiducial selection

We first perform a simple fiducial selection on the event samples, to emulate a typical LHC selection that would be performed for the ZH process. To this end, we also implement a p_T and $|\eta|$ dependent smearing function on the b-jet momenta to approximate finite detector resolution effects following the parametrised functions determined by the CMS particle-flow performance analysis [273].

Jets are clustered with the anti-k_T algorithm with a radius parameter of 0.4 and required to have $p_T > 20$ GeV. Events are required to have two leptons satisfying $p_T > 25$ GeV and $|\eta| < 2.5$. Exactly two b-jets, as identified using truth-level information by MADANALYSIS5, are required satisfying $p_T > 20$ GeV and $|\eta| < 2.5$. We assume a flat b-tagging efficiency of 70%, corresponding to the DeepCSV medium working point defined in Ref. [274]. Additionally, Z- and Higgs-boson mass windows are imposed on the invariant masses of the lepton and b-jet pairs such that $75 < M_{\ell\ell} < 105$ GeV and $60 < M_{bb} < 140$ GeV. This defines our fiducial volume on which both the BDT training and STXS binning are performed. Table 1 summarises the cross sections obtained after the fiducial selection for the Monte Carlo samples generated. The $H \to b\bar{b}$ branching fraction is computed in the SM and the SMEFT benchmark points using the eHDECAY [275] interface of ROSETTA [276] and folded into the cross section results. Clearly,

$pp \to b\,\bar{b}\,\ell^+\,\ell^-$	$\sigma_{\text{fid.}}[fb]$
ZH SM	2.72
ZH $c_{HW} = 0.03$	3.64
ZH $c_{HW} = -0.03$	2.21
ZH $c_{HW} = 0.01$	3.38
ZH $c_{HW} = -0.01$	2.50
$Zb\bar{b}$ SM	291.3

Table 1: Cross sections obtained at LO after imposing the fiducial selection cuts described in Section 3.

the $Zb\bar{b}$ background is overwhelmingly large even after the Higgs mass window selection. A realistic analysis will employ multivariate analyses techniques to reduce this background. As explained in the next section, we mimic this aspect of the experimental analyses by training a BDT discriminant to optimally reject this background in favour of the SM ZH process.

3.2 Kinematic discriminants

We built a set of gradient BDT classifiers to efficiently discriminate between the different classes of event hypotheses involved in the analysis, namely $Zb\bar{b}$, SM ZH, and BSM ZH production. The classifiers receive kinematic variables related to the event as inputs and approximate the likelihood for each event to belong to any of the three classes. The likelihoods are parameterised as

$$p_i(\vec{x}) = \frac{e^{\beta_i(\vec{x})}}{\sum_j e^{\beta_j(\vec{x})}}, \tag{6}$$

where $\vec{x}$ represents all the input variables to the discriminant, that are shown in Table 2, and $\beta_i(\vec{x})$ are non-linear functions of these variables.

These kind of algorithms are regularly used by the experimental analyses and often provide a comparable performance to those of more sophisticated techniques such as matrix element methods.

Five sets of discriminants were trained:

1. A binary discriminant to separate $Zb\bar{b}$ production from the SM ZH production.

Variable name	Variable definition
$p_T(l_1)$	leading lepton p_T
$p_T(l_2)$	sub-leading lepton p_T
$p_T(b_1)$	leading b-jet p_T
$p_T(b_2)$	sub-leading b-jet p_T
$\eta(l_1)$	leading lepton pseudo-rapidity
$\eta(l_2)$	sub-leading lepton pseudo-rapidity
$\eta(b_1)$	leading b-jet pseudo-rapidity
$\eta(b_2)$	sub-leading b-jet pseudo-rapidity
$y(Z)$	Z-candidate rapidity
$y(H)$	H-candidate rapidity
$p_T(Z)$	Z-candidate p_T
m_{bb}	H-candidate invariant mass
m_{ZH}	HZ invariant mass

Table 2: Input variables used by the kinematic BDT discriminants.

Parameter	Value
number of trees	600
maximum depth	5
bagging fraction	0.8
learning rate	0.05
L_2 regularisation strength	1

Table 3: Optimized BDT training hyperparameters.

2. Four sets of three-class discriminants (one for each of the c_{HW} benchmarks) to discriminate between $Zb\bar{b}$, SM ZH and BSM ZH production.

The first discriminant was used to reduce the $Zb\bar{b}$ background in the template cross section analysis, in such a way to mimic the experimental analyses. The last four discriminants were used to first reduce the $Zb\bar{b}$ background and then to further classify the selected events to discriminate between the SM and BSM hypotheses.

The BDTs were trained using the scikit-learn [277] and xgboost packages [278]. To this end, the events were split into two statistically independent samples, with a ratio of 3:1, used respectively for training and application of the discriminants. We used the categorical cross-entropy loss function, and the algorithm hyperparameters were optimised on the training sample using stochastic grid search and the mean k-fold cross-validation loss as figure of merit, with $k = 5$. The optimized hyperparameters are shown in Table 3.

After training, the $p(Zb\bar{b})$ ($\equiv p_{Zb\bar{b}}(\vec{x})$) variables were used to define selection criteria for the events to be considered for analysis. The maximum allowed value for $p(Zb\bar{b})$ was

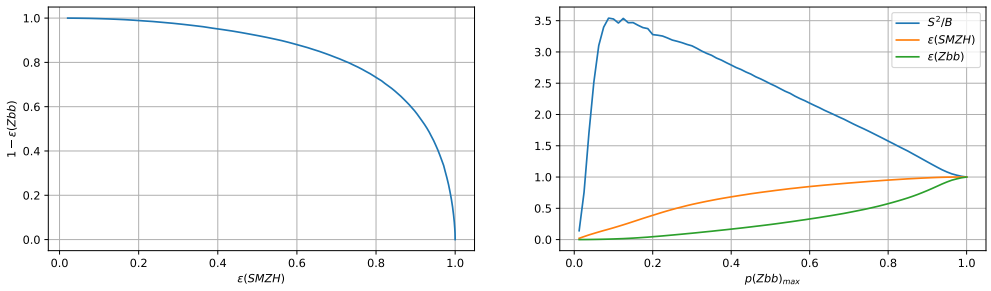

Figure 1: Optimisation analysis to determine the maximum value of $p(Zb\bar{b})$ for events considered in the analysis. (left) *ROC* curve for $Zb\bar{b}$ vs SM ZH separation. (right) Regularised $\varepsilon^2(SMZH)/\varepsilon(Zb\bar{b})$ as a function of the $p(Zb\bar{b})_{max}$.

determined in order to maximise the quantity $\varepsilon^2(SMZH)/\varepsilon(Zb\bar{b})$, where ε is the selection efficiency of a given sample. Such a figure of merit is, in the Gaussian limit, proportional to the squared median expected discovery significance to observe the standard model production of of ZH. The choice was made again to mimic the experimental analyses, for which the observation of the SM Higgs signal will be the primary goal.

In order to ensure a smooth behaviour, the figure $\varepsilon^2(SMZH)/\varepsilon(Zb\bar{b})$ was regularised by replacing $\varepsilon(Zb\bar{b})$ with $\varepsilon(Zb\bar{b}) \oplus \varepsilon_0$ where $\oplus$ denotes the sum in quadrature and $\varepsilon_0 = 0.03$. Figure 1 shows, as an example, the result of the optimisation scan for the discriminant trained to separate $Zb\bar{b}$ production from the SM ZH production. The analysis was repeated separately for each of the 5 discriminants and similar results were obtained in all cases.

For this exploratory study, we only considered four BSM benchmarks, varying c_{HW} and testing the sensitivity to each of these benchmarks using a dedicated set of kinematic discriminants. While the design of an optimal discriminant that continuously depends on the BSM parameters is beyond the scope of this work, we investigated the degree of correlation between the BSM discriminants for each of the scenarios. Figure 2 shows the linear correlation coefficient between $p(BSM)$ for each of the four scenarios, evaluated on SM ZH production events. The $p(BSM)$ BDT outputs estimate the likelihood for an event to come from each of the considered BSM scenarios. As can be seen, the linear correlation varies between 0.3 and 0.96, and it increases as the distance between the benchmark points decreases. This suggests that the information used to discriminate the different benchmarks is similar, but that optimal results are obtained when a specific benchmark is targeted.

3.3 STXS binning

For the STXS sensitivity analysis, the generated samples for all signal benchmarks as well as the backgrounds (SM $pp \to ZH, H \to b\bar{b}$ and $pp \to Zb\bar{b}$) are categorized according to the STXS proposal for the VH channel in Ref. [263]. Within this framework, different regions of the phase space – referred to as "bins" for simplicity – are defined, with the purpose of optimizing the sensitivity of the measurements while at the same time minimizing their dependence on theory assumptions. The different STXS bins are defined specifically for each Higgs production mode. For our process of interest ($pp \to ZH \to \ell^+\ell^- b\bar{b}$) the different stages of the categorization and the resulting bins can be summarized as follows (see [263] for details):

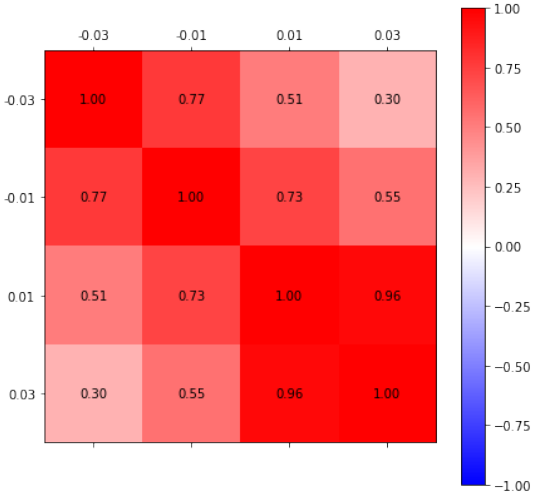

Figure 2: Linear correlation coefficient between $p(BSM)$ for each of the four scenarios, evaluated on SM ZH production events. Rows and columns are labelled by the value of c_{HW}.

– **Stage 0:** Events with $|y_H| < 2.5$ are selected.

– **Stage 1:** ZH production is split into $q\bar{q}$ and gg initial states (our process sample was generated at LO and therefore only contains $q\bar{q} \to ZH$ events). Events are subsequently classified according to the value of p_T^Z and number of extra jets in the event as follows:

$$\underline{\mathbf{q\bar{q} \to ZH}}$$

$$\begin{aligned} p_T^Z \in &\quad [0, 150]\ \text{GeV}, \\ p_T^Z \in &\quad [150, 250]\ \text{GeV} \quad (0\text{-j}), \\ p_T^Z \in &\quad [150, 250]\ \text{GeV} \quad (\geq 1\text{-j}), \\ p_T^Z > &\quad 250\ \text{GeV}. \end{aligned} \tag{7}$$

– **Stage 2:** In this last stage the low p_T^Z bins are further separated according to the number of extra jets, while the high-p_T^Z region is split at 400 GeV. The final set of STXS bins that apply in our case are the following six:

$$\underline{\mathbf{q\bar{q} \to ZH}}$$

$$\begin{aligned} p_T^Z \in &\quad [0, 150]\ \text{GeV} \quad (0\text{-j}), \\ p_T^Z \in &\quad [0, 150]\ \text{GeV} \quad (\geq 1\text{-j}), \\ p_T^Z \in &\quad [150, 250]\ \text{GeV} \quad (0\text{-j}), \\ p_T^Z \in &\quad [150, 250]\ \text{GeV} \quad (\geq 1\text{-j}), \\ p_T^Z \in &\quad [250, 400]\ \text{GeV}, \\ p_T^Z > &\quad 400\ \text{GeV}. \end{aligned} \tag{8}$$

In order to profit from the maximum amount of available information, we use the stage 2 categorisation to compare with the multivariate analysis. Additionally, we use the BDT discriminant, $p(Zb\bar{b})$, trained to reject the $Zb\bar{b}$ background in favour of SM ZH, described in Section 3.2 to purify our event sample. Our STXS yields are computed after cutting on this discriminant with 18.6% efficiency for SM ZH and $> 99\%$ rejection for $Zb\bar{b}$. No extra information or discriminant to enhance sensitivity to new physics is used, consistently with the STXS hypotheses. Figure 3 shows the predicted cross sections for the various samples in the STXS bins. The $Zb\bar{b}$ contribution has clearly been brought under control by the BDT discriminant. In the bins that have been split by jet multiplicity, this contribution appears to have a larger relative increase when going from zero to one or more jets, probably owing to the dominant gg-initiated contribution to this process increasing the radiation probability. We see that the EFT contributions diverge from the SM prediction with increasing p_T, as expected, and the $Zb\bar{b}$ background also becomes less and less important.

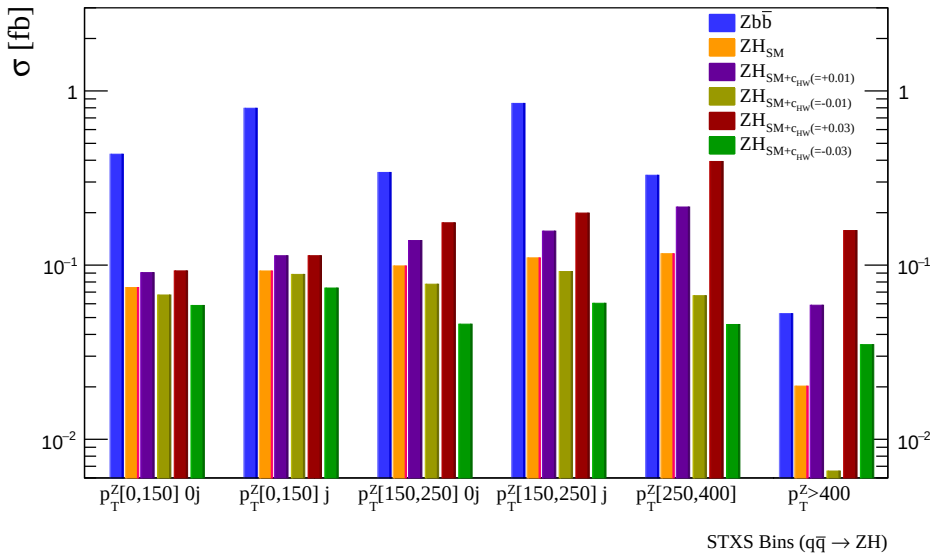

Figure 3: Predicted cross sections in the stage 2, ZH STXS bins for SM ZH production as well as our four EFT benchmarks and the $Zb\bar{b}$ background. The cross sections correspond to events passing the basic fiducial selection of Section 3.1, accounting for b-tagging efficiencies and after applying a cut on the $Zb\bar{b}$ BDT discriminant as described in the text.

4 Statistical Hypothesis testing

A statistical analysis is carried out to estimate the sensitivity to SMEFT effects in Higgs boson interactions using the STXS measurements of Section 3.3. We compare that sensitivity to the one obtained from a dedicated analysis using the multivariate classifier described in Section 3.2. To this effect, a simple significance analysis is used based on the ROOSTATS framework [189] which determines the expected significance using an asymptotic calculator with nominal Asimov data sets and a one-sided profile likelihood.

A few approximations have been made. No systematic uncertainties have been considered, even if the generated events have been smeared to reflect the limited resolution and corrected for the finite efficiencies of b-tagging. The measurement in the STXS bins requires an

extrapolation from the measured phase space, which includes those selections applied specifically to reject backgrounds, in this case from the $Zb\bar{b}$ process. In the present analysis this is achieved using a BDT specifically trained to select $H \to b\bar{b}$ over $Zb\bar{b}$ events. For the STXS analysis, a BDT cut is applied, retaining 18.6% of all SM Higgs events but less than 1% of the $Zb\bar{b}$ background. For the BDT analysis targeting EFT operators, two settings are explored: using the same BDT requirement as in the STXS analysis and additionally using a selection requirement of the BDT that leads to similar acceptances as in the STXS case.

In general, the sensitivity to any non-SM contribution to a measured cross section can only come from the events recorded in the fiducial volume, prior to any model-dependent extrapolations. Therefore, we do not use such extrapolations in this analysis. We perform our study directly in the region of the phase space selected by the BDT cuts. In a real-life analysis, however, some degree of extrapolation is always performed. Different acceptances of SM and BSM can therefore play a role in BSM searches, if in the latter the events selected at detector level are extrapolated assuming SM acceptances alone. Nevertheless, if one models the acceptances of the BDT-selection properly for both cases, this kind of effects can be accounted for. The information on acceptances is, however, not always reported in the experimental analyses.

The acceptances of our BDT-selection for both SM and BSM events with $c_{HW} \neq 0$ are summarized in Table 4. The acceptance for the SM Higgs can (depending on the BDT cut) be very similar for both STXS BDT (i.e. the BDT used to reject $Zb\bar{b}$) and EFT optimized-BDT (around 19%). The acceptance for events with a Wilson coefficient $c_{HW} = 0.03$ is larger than that by about a factor of 1.5 whilst it is smaller by the 25% for $c_{HW} = -0.03$. For the samples produced with a smaller Wilson coefficient, $c_{HW} = \pm 0.01$, the acceptances are slightly closer to the SM Higgs scenario, which is expected since for $c_{HW} \to 0$ the SM is restored. The smaller the Wilson coefficients, the smaller the issues from acceptance effects.

Sample	STXS: Acceptance (BDT_{SM}) [%]	BDT: Acceptance (BDT_{SM}, same as STXS SM-acceptance) [%]	BDT: Acceptance (BDT_{SM}, same cut as STXS-BDT) [%]
Higgs (BDT for $c_{HW} = +0.03$)	18.6	18.5	29.6
Higgs (BDT for $c_{HW} = -0.03$)	18.6	18.3	33.1
Higgs (BDT for $c_{HW} = +0.01$)	18.6	18.6	33.4
Higgs (BDT for $c_{HW} = -0.01$)	18.6	19.8	34.2
$c_{HW} = 0.03$	31.1	31.8	42.7
$c_{HW} = -0.03$	14.4	13.4	28.2
$c_{HW} = 0.01$	22.9	23.0	37.9
$c_{HW} = -0.01$	15.9	17.2	31.7
$Zb\bar{b}$	< 1.0	$\sim$1.0	$\sim$3.0

Table 4: Acceptances (in %) of the first BDT selection, meant to separate $H \to b\bar{b}$ from $Zb\bar{b}$ production.

After application of the BDT requirements to reject $Zb\bar{b}$, either the STXS binning or the distribution of the other BDT classifiers are used to estimate the sensitivity to new physics $c_{HW} \neq 0$. Three different luminosity scenarios are investigated: the full LHC Run-2 results, corresponding to 150 fb^{-1}, the integrated luminosity projected for LHC Run-3 (300 fb^{-1}) and the expected data collected at the High-Luminosity LHC (3000 fb^{-1}). The significance is determined simultaneously in the 6 STXS bins (see Section 3.3) and in the BDT discriminant distributed in 10 equal bins. (We checked that a finner binning did not significantly change the

significance.) For both, STXS and BDT discriminant, no uncertainties on the shapes of these distributions are assumed. Figure 4 depicts the distributions used as inputs in the STXS (left) and the BDT (right) case for 300 fb^{-1}. The SM hypothesis ($Zb\bar{b}$ + ZH) is shown as blue line, whereas the BSM signal with $c_{HW} = 0.03$ is shown as red line. They are added in the signal+background hypothesis which is depicted as dashed black line. A simple significance test for the signal+background hypothesis is carried out using the ROOSTATS framework [189] for these binned distributions.

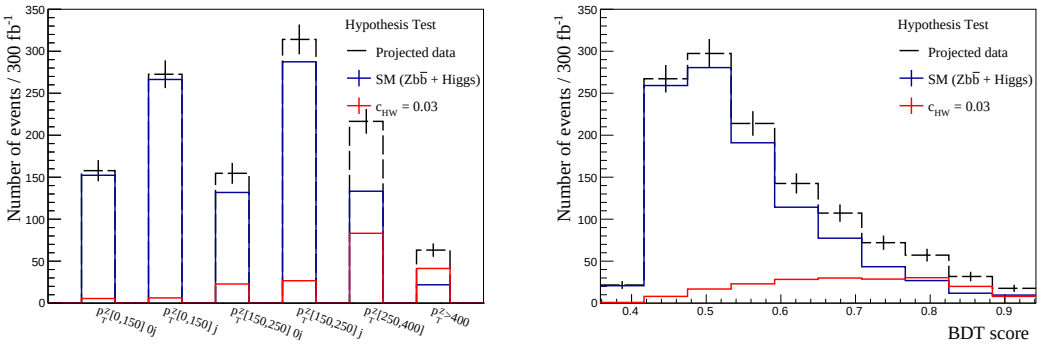

Figure 4: Predicted number of events selected for 300 fb^{-1}. Since the acceptance extrapolation into the STXS phase space does not change the available data statistics, it it not applied here, i.e. the distributions are shown after the first cut on the BDT classifier to reject the $Zb\bar{b}$ background.

To get a feeling of how realistic the scenario considered here is, the significance of a Higgs discovery in the STXS scenario is also investigated, in addition to the BSM sensitivity. The expected significances for the 2-lepton channel we studied here are 1.9 for ATLAS [264] and 1.8 for CMS [265] for ∼36 fb^{-1}. This is about what is expected from the simplified studies herein, which do not account for systematic uncertainties (which make up to half the total uncertainty in the measurements) but are not optimized for a Higgs observation. The expected significance of a Higgs signal compared to a background-only (i.e. $Zb\bar{b}$) sample is shown in Table 5.

Table 5 also summarizes the significances found for the three luminosity scenarios for the hypothesis tests for the STXS and the BDT approach for Wilson coefficients of $c_{HW} = \pm 0.03$ and $c_{HW} = \pm 0.01$. In the case of the BDT approach and $c_{HW} = \pm 0.03$, three alternatives were tested. For these, either the first BDT selection with the same STXS SM-acceptance or the same BDT cut as STXS are investigated. In addition, an alternative non-optimal BDT discriminant is used. This was trained not on the targeted Wilson coefficient (e.g. $c_{HW} = +0.03$), but on the one with opposite sign (-0.03).

5 Conclusions

We have performed an exploratory study comparing the sensitivity to higher dimensional operators of the proposed STXS measurements in ZH production to an optimised analysis exploiting multivariate methods. We considered four benchmark scenarios in which the $\mathcal{O}_{HW}$ operator coefficient is set to values $c_{HW} = \pm 0.03$ and $c_{HW} = \pm 0.01$. The former case corresponds to saturating existing limits from a global fit to LHC Run 1 data and precision electroweak measurements, while the latter case intends to showcase a scenario with smaller deviations from SM expectations. The sensitivity was quantified by the expected statistical significance against

Hypothesis test	Full Run-2 (150 fb^{-1})	LHC Run-3 (300 fb^{-1})	HL-LHC (3000 fb^{-1})
STXS: Higgs discovery	3.01	3.70	8.06
STXS: $c_{HW} = 0.03$	6.44	8.82	26.46
STXS: $c_{HW} = -0.03$	1.66	2.24	6.44
BDT: $c_{HW} = 0.03$ (STXS SM-acceptance)	6.29	8.58	25.61
BDT: $c_{HW} = -0.03$ (STXS SM-acceptance)	1.80	2.44	7.24
BDT: $c_{HW} = 0.03$ (same BDT cut as STXS)	6.17	8.64	27.03
BDT: $c_{HW} = -0.03$ (same BDT cut as STXS)	1.74	2.08	7.50
BDT: $c_{HW} = 0.03$ (alt BDT cut)	4.40	6.15	19.18
BDT: $c_{HW} = -0.03$ (alt BDT cut)	1.44	2.41	6.69
STXS: $c_{HW} = 0.01$	2.26	3.04	8.78
STXS: $c_{HW} = -0.01$	1.08	1.46	4.30
BDT: $c_{HW} = 0.01$	2.62	3.07	8.90
BDT: $c_{HW} = -0.01$	1.44	1.99	6.10

Table 5: Expected significances for the different scenarios.

the SM hypothesis obtainable after a collected integrated luminosity of 150, 300 and 3000 fb^{-1}, taking into account the presence of the dominant SM background of $Zb\bar{b}$ production. The contribution of this background is efficiently mitigated by training a BDT classifier to distinguish this process from SM ZH production and first cutting on this discriminant before performing the two alternative SM vs EFT significance analyses. The discriminant was able to effectively reduce this background contribution down by two orders of magnitude.

Overall, very large significances can be expected for the benchmarks saturating the current limits, while the benchmarks for the smaller Wilson coefficients are not likely to be identified beyond 3σ until the High-Luminosity LHC run. We observe that the final performance of the BDT analysis does not differ significantly from the differential information in Z-boson p_T offered by the STXS, with the exception of the $c_{HW} = -0.01$ case, which predicts the smallest deviation from the SM case. Here, the discriminating power of the BDT output over the differential p_T distributions becomes apparent, suggesting that once the sensitivity of the STXS measurements is saturated, moving towards optimised multivariate methods remains well-motivated. The exercise was performed in a simplified situation, largely ignoring detector effects besides a parametrised b-jet smearing implementation and b-tagging efficiency corrections as well as all other potential sources of systematic uncertainty. We leave a more thorough investigation, including these effects as well as the possibility of including other significant backgrounds to a follow-up study.

By comparing the optimised BDT discriminants for the different EFT benchmarks, we conclude that there is significant information overlap between them but that some parameter dependence remains. This means that one would benefit from a parametrised learning approach, in which the new physics parameter is also fed in as an input to the discriminant training. This can be understood from the presence of both an interference and squared contribution of the EFT ZH amplitude in the new physics signal. The shape of EFT squared contribution has the benefit of being independent of the value of the Wilson coefficient, while the relative impact of the interference term depends very much on this value. In the 'large' c_{HW} benchmarks, the contribution from the quadratic term in the Wilson coefficient is clearly dominant at high energies, as evidenced by the positive relative contribution over the SM prediction for both

± 0.03 in the STXS overflow bin, see Figure 3. On the other hand the -0.01 case consistently predicts a deficit with respect to the SM. The fact that the BDT outperforms for this benchmarks may imply that one can obtain better sensitivity using these methods for EFT signals in which the interference with the SM amplitude is significant, which may also be considered more 'well-behaved' concerning the EFT expansion. However, this effect may also be caused by the greater loss in acceptance post $Zb\bar{b}$ BDT cut suffered by the negative c_{HW} benchmarks and should be further investigated.

One should bear in mind that in this first study, a rather kinematically simple process has been chosen. Indeed, in ZH production the p_T Z-boson is strongly correlated to the energy flow through the production vertex, in which the EFT effects occur. It is therefore not surprising that we do not observe a huge difference in significance in this case. Further investigations concerning a comparison between BDT and STXS for more complicated kinematic environments would be interesting, *e.g.*, for other $2 \to 3$ production modes such as vector boson fusion or $t\bar{t}H$ associated production. Furthermore, it should be noted that although our BDT analysis is touted as an 'optimised' discriminating method, the fully potential of the BDT information was not exploited in this analysis. In short, by cutting on the SM vs $Zb\bar{b}$ variable and fitting on the resulting one-dimensional discriminant, some amount of exclusion power was sacrificed for the sake of simplicity. In the ideal case, a two-dimensional fit on the initial BDT classifier would be performed, an exercise which we leave for the follow-up study.

Acknowledgments

We thank the organizers and conveners of the Les Houches workshop, "Physics at TeV Colliders", for a stimulating meeting. K.L. is supported by the European Union's Horizon 2020 research and innovation programme under ERC grant agreement No. 715871. K. M. is supported in part by the Belgian Federal Science Policy Office through the Interuniversity Attraction Pole P7/37 and by the European Union's Horizon 2020 research and innovation programme under the Marie Skłodowska-Curie grant agreement No. 707983. P. M. was supported in part by the Swiss National Science Foundation under the project 200020_162665.

Contribution 11

Improved BSM Sensitivity in Diboson Processes at Linear Colliders

D. M. Lombardo, F. Riva, P. Roloff

Abstract
We study diboson processes at CLIC and asses the reach of linear colliders to new physics effects in the form of effective field theory (EFT) operators. Given that inclusive measurements in diboson process suffer from certain SM-BSM non-interference rules, we perform non-inclusive analyses that include azimuthal differential information.

1 Motivation

Standard Model (SM) precision tests are an increasingly important tool in new physics searches. New dynamics at a mass scale M can leave an imprint in observables at energies $E \ll M$, whose size is proportional to some power of E/M. These effects can be captured generically and systematically through an Effective Field Theory (EFT), organised as operators of increasing dimension, in addition to the SM. In most scenarios, the leading effects arise at the dimension-6 level (see however Refs. [279, 280] for exceptions).

Given the upcoming European Strategy for particle physics, it is important to find benchmarks and scenarios that can be readily accessed by different types of experiments; these scenarios allow for a comparison of the reach of radically different machines. In this note we study W^+W^- production at future linear e^+e^- colliders (see also [281–285]). Diboson processes have a rich variety of physical information, incapsulated at high-energy in the lognitudinal and transverse polarizations: from a BSM perspective these can be considered genuinely different processes testing genuinely different physics. Beside their interest for future planning, linear colliders also offer an interesting playground for complex studies: they allow to isolate and understand in detail analyses that can then be brought over to the framework of hadron machines. W^+W^- processes are a perfect example of this. Indeed, for what concerns new physics in the transverse polarizations, SM and BSM exhibit different helicity structures (see Ref. [286] for a recent discussion), so that the two amplitudes do not interfere in inclusive measurements: an important drawback of traditional analyses in the context of a precision program. Non-inclusive differential distributions in the azimuthal angles of the W boson decay planes do bear the interference information (see [287]), in the form of a modulating signal that vanishes once integrated over (to reproduce the non-interference results)[1]. At linear colliders this modulating signal is very visible, as we will show in this note. This will allow us to discuss it in isolation and quantify the impact of interference.

Even when new physics is in the longitudinal polarizations, BSM searches as precision tests are challenging. In the SM, the unpolarized cross section is dominated by the transverse-

[1] Interference information is also present in the off-shell region [288].

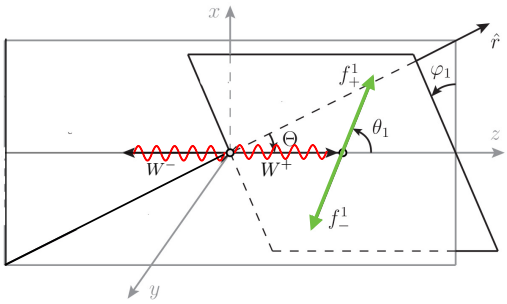

Figure 1: Definitions of the polar angle Θ and azimuthal angle φ.

transverse components, and the longitudinals are small. Therefore, while the SM and BSM do interfere here, the dominant SM contribution acts as an irreducible background that reduces the sensitivity of the experiment. In this note we point out that beam polarization can play a crucial rôle in this context, as it can substantially reduce the transverse component, which receives the largest contribution from a t-channel involving left-handed electrons.

2 BSM in Transverse Polarizations

Diboson processes are often presented as measurements of anomalous trilinear gauge couplings (TGCs), associated with the parameters λ_γ, g_1^Z and κ_γ of Ref. [289]. These are in correspondence with dimension-6 operators.

For our scope, these effects can be divided into two classes: couplings that contribute to the transverse and longitudinal amplitude. In the former class, which we discuss in this section, we have the CP-even operator

$$\mathcal{O}_{3W} = \epsilon^{ijk} W_\mu^{i\nu} W_\nu^{j\rho} W_\rho^{k\mu} \,. \tag{1}$$

BSM effects in the transverse amplitudes are difficult to test, as we now explain. The problem of the BSM $\mathcal{O}_{3W}$ operator is that it produces, at tree-level and at high-energy, dominantly $++$ or $--$ helicities in the final states, with amplitudes $\mathcal{A}^{++}_{BSM} = \mathcal{A}^{--}_{BSM}$. This does not interfere, in inclusive $2 \to 2$ scattering, with the SM amplitude $\mathcal{A}_{SM}$ [286]. SM processes have, in the high-energy and classical limits, dominantly $+-$, $-+$ or 00 helicity. The latter is however smaller and has little impact on this part of the analysis.

Nevertheless, the amplitude for $e^+e^- \to 4f$ decays into fermions can in principle interfere. This interference is proportional to a function of the azimuthal angles of the decay planes of the fermion/anti-fermion originating from the W^+ and W^- respectively.

In this note we focus on a single-differential distribution and study the azimuthal distribution of the decay products of one of the two Ws only, as illustrated in Fig. 1. We remain inclusive about the other W, which can then be thought as a state of well defined helicity. The interference term, between the transverse-transverse amplitudes, reads [290]

$$I^{WW} \propto \mathcal{A}^{\text{BSM}}_{++} \left[\mathcal{A}^{\text{SM}}_{-+} + \mathcal{A}^{\text{SM}}_{+-}\right] \cos 2\varphi \,, \tag{2}$$

see also [287] for more details.

Interference vanishes when integrated over, reproducing the above non-interference result. The question we want to address here is how this measurement performs in lepton colliders: how much an azimuthal differential distribution improves upon an inclusive measurement, in terms of BSM reach?

2.1 Ambiguity and Channel Selection

The angle φ is defined in Fig. 1 making reference to the outgoing fermion of positive helicity (f_+ in the figure). When the W is decaying hadronically, this information is unaccessible[2], implying an ambiguity

$$\{\Theta, \varphi\} \leftrightarrow \{\pi - \Theta, \varphi + \pi\}\,. \tag{3}$$

Such ambiguity doesn't prevent us, however, from observing distributions of the form Eq. (2).

For leptonically decaying W-bosons the situation is different: here the charged lepton has always well-defined helicity (depending of whether it's a W^+ or W^-), but the plane is defined only if the neutrino momentum is also known. This can be in principle reconstructed from the kinematics if only one neutrino is present in the event.

Here we focus on the semileptonic channel $\nu l^+ \bar{q} q$. This channel has a large branching ratio, because of the hadronic contribution, and at the same time allows to (almost) fully reconstruct the neutrino, for which the transverse components of momentum can be identified as missing energy. By requiring that the invariant mass of charged lepton and neutrino exactly reconstruct the W-mass, one finds an equation with two solutions for the longitudinal momentum of the neutrino. At hadron machines it is impossible to single out which of these two solutions corresponds to the real one, and this introduces a further ambiguity in the angle reconstruction that forbids, for instance, observation of CP-odd effects. At linear lepton colliders, however, the total center-of-mass energy is known, up to initial state radiation (ISR) and beam-strahlung. Now, the two solutions have different neutrino longitudinal momentum and therefore different amounts of ISR, hence different energy. So, it is possible, by appropriately cutting on the energy of the hadronically decaying W, to avoid the ambiguity completely. We assume here that this is the case, and leave a more thorough study of this possibility for future work. In this work we therefore assume that the decay plane of the leptonic W is fully reconstructible and study its distribution, while ignore the hadronic W distribution.

2.2 Amplitudes and Choice of Cuts

Knowledge of the SM amplitude can guide us through the most appropriate choice of cuts and binning. In the high-energy limit, the SM amplitudes for inclusive dibosons read

$$\mathcal{A}_{\text{SM}}^{-+} = -g^2 \sin\Theta \qquad \mathcal{A}_{\text{SM}}^{+-} = 2g^2 \sin^4\frac{\Theta}{2} \csc\Theta \qquad \mathcal{A}_{\text{SM}}^{00} = \frac{1}{2}(g^2 + g'^2)\sin\Theta \tag{4}$$

where Θ is the polar angle, corresponding to the angle between the incoming electron and the outgoing W^+. The SM amplitudes are illustrated in Fig. 2 for $\sqrt{s} = 380$ GeV. The BSM amplitude is instead

$$\mathcal{A}_{++}^{\text{BSM}} = \mathcal{A}_{--}^{\text{BSM}} \approx C_{3W} 6e\sqrt{2} M_{W\gamma}^2 \sin\Theta \tag{5}$$

where C_{3W} is the (dimensionfull) coefficient of the $\mathcal{O}_{3W}$ operator as it appears in the Lagrangian.

The important lessons here are:

– In the forward region $\cos\Theta \approx 1$ both SM and BSM vanish, so that this region is not favorable

[2] In this context it would be interesting to study decays including charm quarks; we leave this for the future.

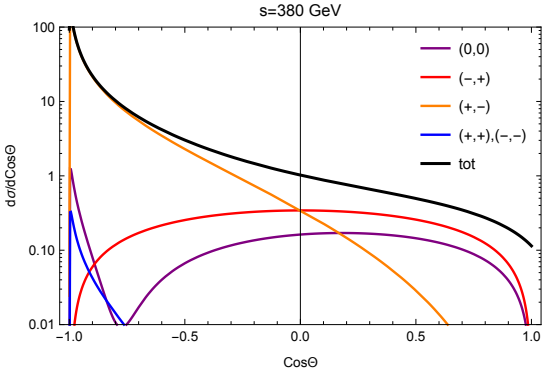

Figure 2: Polar angle distribution of the different helicity amplitudes in the SM.

– In the backward region $\cos\Theta \approx -1$ the BSM vanishes and the SM explodes because of the t-channel neutrino pole; the interference term is in fact finite. The signal over sqrt-background vanishes in the backward point, but increases rapidly ($\sim \Theta^{3/2}$) as we approach the central region, so that even this backward region can have interesting information.

– In the central region $\cos\Theta \approx 1$ the BSM amplitude has its maximum, and the SM switches from being dominated by the $+-$ to being dominated by $-+$. Most importantly, since the latter SM amplitudes have opposite sign (see Eq. (4)): the overall SM amplitude changes sign!

In light of these, we understand that the most important region for our analysis will be $\cos\Theta \sim 0$. Moreover, it is important to separate the analysis (or implement an asymmetry) for

$$\cos\Theta < 0 \quad \text{and} \quad \cos\Theta > 0; \tag{6}$$

because of the opposite SM amplitude sign, the sum of the interference terms from these distinct regions tends to cancel (see Fig. 3). So, in what follows, we consider 4 bins in polar angle

$$\cos\Theta \in [-1, -0.5, 0, 0.5, 1] \tag{7}$$

with particular hopes on the central bins.

3 Analysis

As benchmarks for future colliders we consider CLIC at 380 GeV, with 500 fb^{-1} of integrated luminosity, and CLIC at 3 TeV with 3 ab^{-1} of luminosity [281]. We leave the study of a richer variety of scenarios for the future.

For this preliminary study we use MADGRAPH [95] and simulate the process $e^+e^- \to W^+W^-$ where we take the W^- to decay hadronically and the W^+ to decay into $e^+ + \nu$; we then multiply the crossection by a factor of 4 to account for decays into muons, and for the charge inverse process; we include an acceptance of 50% to be conservatives.

An example of the azimuthal distribution that we are interested in, is shown in Fig. 3. There it is also visible the fact that in the regions $\cos\Theta > 0$ and $\cos\Theta < 0$ the SM-BSM interference changes sign. The SM distribution is flat.

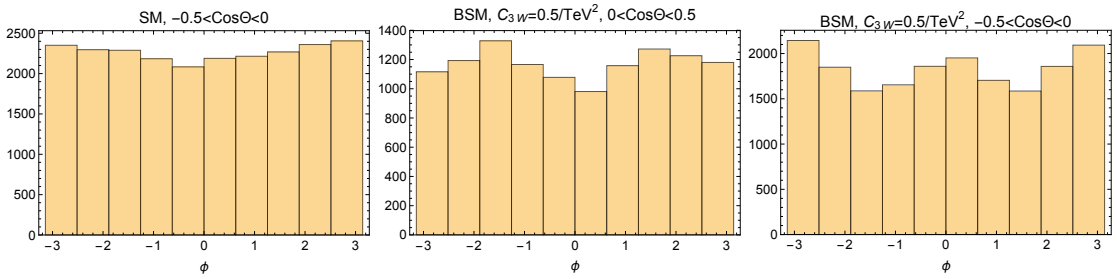

Figure 3: Un-normalized histograms for the azimuthal differential distribution for different values of the BSM parameters.

To access the azimuthal distribution, we bin φ in 10 parts (in addition to the 4 bins in polar angle Eq. (7)) and perform a binned χ^2-analysis in two different ways: differential in every φ bin and inclusive. We study the reach in two different CLIC configurations: a low-energy one at 380 GeV, and a high-energy one at 3 TeV. We include a 50% acceptance, but extend the analysis to both elctrons and muons and to leptonic decays of either W^+ or W^-.

Low Energy Run (380 GeV). We assume a luminosity 500 fb^{-1} and compare two scenarios with 1% and 10% systematic uncertainty δ_{syst} in all bins. Without azimuthal binning we find that the CLIC reach on the (dimensionful) Wilson coefficient of the operator Eq. (1), is

$$\text{Without } \varphi \text{ distribution: } c_{3W} \in [-1.4, 1.1]\,\text{TeV}^{-2}\ (\delta_{syst} = 1\%) \tag{8}$$
$$c_{3W} \in [-15, 6]\,\text{TeV}^{-2}\ (\delta_{syst} = 10\%) \tag{9}$$

while including azimuthal data we obtain

$$\text{With } \varphi \text{ distribution: } c_{3W} \in [-0.6, 0.6]\,\text{TeV}^{-2}\ (\delta_{syst} = 1\%) \tag{10}$$
$$c_{3W} \in [-2.5, 2]\,\text{TeV}^{-2}\ (\delta_{syst} = 10\%) \tag{11}$$

We also find that the bounds are dominated by the central bins, as expected.

High Energy Run (3000 GeV). In this case we take 3 ab^{-1} of luminosity and find

$$\text{Without } \varphi \text{ distribution: } c_{3W} \in [-0.12, 0.12]\,\text{TeV}^{-2}\ (\delta_{syst} = 1\%) \tag{12}$$
$$c_{3W} \in [-0.13, 0.13]\,\text{TeV}^{-2}\ (\delta_{syst} = 10\%) \tag{13}$$

$$\text{With } \varphi \text{ distribution: } c_{3W} \in [-0.10, 0.10]\,\text{TeV}^{-2}\ (\delta_{syst} = 1\%) \tag{14}$$
$$c_{3W} \in [-0.11, 0.11]\,\text{TeV}^{-2}\ (\delta_{syst} = 10\%) \tag{15}$$

4 Outlook

In this short note we have initiated an improved study of the BSM search prospects in diboson processes at future linear colliders. In particular, to overcome the fact that SM and BSM amplitudes do not interfere in inclusive measurements, we have studied the possibility of accessing interference via differential azimuthal measurements. Focussing on the angle spanned by a leptonically decaying W in semileptonic processes, we have compared the reach with and without

the azimuthal measurement, and found that the former is indeed better. In the near future we plan to extend the analysis in a number of ways that we mention in what follows.

First, complete double differential distribution (in both azimuthal angles) can be advantageous. This should be studied together with the possibility of looking at the fully hadronic amplitude (and investigate whether the ambiguity of not knowing which one is the positively charged W has an impact on the BSM reach). This also opens the door to accessing independently the CP even and CP odd distributions. Finally, a more refined simulation setup, including WHIZARD [291], fast and full simulations, should be performed.

On a different front, it is interesting to study BSM physics in the longitudinal polarizations (e.g. the operator $\mathcal{O}_W$). This certainly interferes with the SM, but suffers here from another problem: the longitudinal amplitude is small in the SM compared to the transverse one, and acts in measurements of the inclusive (longitudinal+transverse) crossection as a background. In [292], in the context of LHC, a possible way out of this is described: selecting the central region, where the longitudinals are suppressed. At linear lepton colliders it is possible to polarize the beam. Taking the electron to be right-handed, implies that (in the high-E limit and assuming massless electrons) diboson processes can occur only through an s-channel diagram that allows only for longitudinal final states. Thus, beam polarization kills the transverse channel that dominates the crossection (which is what makes the analysis of this channel poor). Interestingly, because of the equivalence theorem, new physics that modifies WW processes, also affects Zh processes (see e.g. [293–295]): it would be nice to compare the reach of these different probes (along the lines of [296]).

We leave all these open question for a future detailed study.

Contribution 12

Comparing effective field theory operator bases numerically

R. Gröber, O. Mattelaer, K. Mimasu

Abstract

We compare numerically different processes computed with different operator bases in Standard Model effective field theory. We show that while as expected at the dimension six level, they lead to the same numerical results for zero width of the propagating particles in the Feynman diagrams, once a non-zero width is introduced, different bases can lead to different results at the dimension six level. As in the SM this is related to the breaking of gauge invariance once particle widths are introduced. We show how the width can be consistently included in Standard Model effective field theory and provide first steps towards a consistent inclusion into the package `MadGraph5_aMC@NLO`.

1 INTRODUCTION

So far no signs of new physics has been detected at the LHC. It is hence sensible to assume that there is a gap between the electroweak scale and the new physics scale. In this paradigm, effective field theories (EFT) are a reasonable, model independent tools to interpret searches for Beyond the Standard Model (BSM) interactions. They supplement the Standad Model (SM) Lagrangian with higher dimensional operators that parametrise deviations in interactions between SM fields. The way in which these are organised/classified depends on the set of assumptions one makes with respect to the possible global and gauge symmetries imposed at the Lagrangian level. Since all current Higgs boson measurements point to a SM like, CP-even Higgs boson that is part of an $SU(2)$ doublet, one can for instance assume that the $SU(2) \times U(1)$ symmetry is linearly realised. Then the SM effective Lagrangian can be organised such that operators with higher dimensionality are suppressed by $(v/\Lambda)^{d-4}$, where d denotes the dimensionality of the operator, v the electroweak scale and Λ the new physics scale.

Given the SM field content and assuming flavour universality as well as lepton and baryon number conservation, the leading BSM effects can be parametrised in terms of 59 dimension six operators [297]. In an earlier construction of an EFT basis [298] 80 operators were found, however the differences were shown to be redundant operators that could be removed by equations of motions. So by using equations of motions or, alternatively, by redefinition of the SM fields different sets of operators can be obtained. Along this line, different operator bases have been proposed in the literature, such as the Warsaw basis [297], the BSM primaries basis [268, 285, 299, 300] and the SILH basis [266, 267]. The different bases are equivalent up to suppressed higher dimensional effects of $d > 6$. A tool to translate between the different bases is `Rosetta` [276].

Our goal in this study is to verify that different operators connected by a field redefinition really lead to numerically equivalent results. It is expected that, up to dimension-6, one should obtain identical results for on-shell scattering amplitudes for two equivalent, dimension-6 operator

sets. In order to test this, we pick a single operator that we add to the Standard Model and then compare the results for several processes to the ones obtained from the operator set in which the original operator has been removed by performing a field redefinition.
Computations with unstable particles require the inclusion of the width of the particle. We will test how the inclusion of the width affects our comparison and will comment on how to consistently include the width in SMEFT.
This contribution is structured as follows: in section 2 we give more details on the operators we chose and how we redefine the fields to obtain a new basis and in section 3 we show our numerical results and comment on the inclusion of the width for unstable particles.

2 OPERATORS

We exemplify the effect of the change in the basis by using the SM and a single new operator

$$\text{Model 1:} \quad \mathcal{L} = \mathcal{L}_{SM} + \frac{c}{\Lambda^2} i(H^\dagger \sigma^i \overleftrightarrow{D}_\mu H)(\bar{q}_3 \gamma_\mu \sigma^i q_3) \tag{1}$$

with σ^i ($i = 1, 2, 3$) the SU(2) generators and $\{\sigma_i, \sigma_j\} = \delta_{ij}/2$, and q_3 are the third generation fermion SU(2) doublets. The scale Λ is assumed to be much larger than the electroweak scale. The Wilson coefficient c is generic. We define

$$(H^\dagger \sigma^i \overleftrightarrow{D}_\mu H) = H^\dagger \sigma^i (D_\mu H) - (D_\mu H)^\dagger \sigma^i H \tag{2}$$

and $H = 1/\sqrt{2}\,(0, v + h)^T$ in the unitary gauge. This operator leads to a modification of the Wtb, Ztt and Zbb vertices, as well as associated contact interactions with one and two Higgs bosons. We now eliminate the dimension-6 operator in eq. (1) by a field redefinition.

$$W_a^\mu \to W_a^\mu + \frac{\tilde{c}}{\Lambda^2} \bar{q}_3 \gamma^\mu \sigma_a q_3 \,. \tag{3}$$

The field redefinition adds a contribution to the original Lagrangian at order $1/\Lambda^2$ that is proportional to the W equation of motion. The operator is removed by setting $\tilde{c} = -c$. Note that an alternative field redefinition could also be used to remove the operator in eq. (1), namely $W_a^\mu \to W_a^\mu + i\frac{\tilde{c}}{\Lambda^2}(H^\dagger \sigma^i \overleftrightarrow{D}_\mu H)$. Such a redefinition leads to an operator contribution to muon decay, which would change the definition of the electroweak vacuum expectation value as a function of the Fermi constant. This leads to a proliferation of 'hidden' EFT effects which, in numerical computations such as those we will be performing in this study, unavoidably lead to higher order terms in the EFT expansion parameter via. *e.g.*, the squaring of EW parameters in matrix element evaluations. Such effects are both known and distinct from the comparison study we would like to perform and would complicate the task by having to disentangle two effects. We therefore refrain from discussing it here any further.
We can now define the second model,

$$\text{Model 2:} \quad \mathcal{L} = \mathcal{L}_{SM} - \frac{c}{\Lambda^2}\left[\sum_q (\bar{q}\gamma_\mu \sigma^i q)(\bar{q}_3 \gamma^\mu \sigma^i q_3) + \sum_l (\bar{l}\gamma_\mu \sigma^i l)(\bar{q}_3 \gamma^\mu \sigma^i q_3) + \frac{1}{g}(\bar{q}_3 \gamma^\mu \sigma^i q_3) D_\nu W^i_{\nu\mu}\right], \tag{4}$$

with l and q denoting the lepton and quark doublets and g the SU(2) coupling. The sums run over the three generations of fermion doublets. We have also defined

$$D_\rho W^i_{\mu\nu} = \partial_\rho W^i_{\mu\nu} + g\epsilon^{ijk} W^j_\rho W^k_{\mu\nu}, \tag{5}$$

process (interference)	Model 1	Model 2	relative difference
$b\bar{b} \to w^+w^-z$	$-2.560957 \cdot 10^{-06}$	$-2.560957 \cdot 10^{-06}$	$1.95 \cdot 10^{-13}$
$\bar{d}u \to \bar{b}tz$	$8.006993 \cdot 10^{-09}$	$8.006993 \cdot 10^{-09}$	$1.24 \cdot 10^{-15}$
$bw^+ \to bw^+$	$2.708079 \cdot 10^{-01}$	$2.708079 \cdot 10^{-01}$	$3.69 \cdot 10^{-15}$
$hw^+ \to t\bar{t}w^+$	$-1.767258 \cdot 10^{-05}$	$-1.767258 \cdot 10^{-05}$	$1.96 \cdot 10^{-14}$
$b\bar{b} \to t\bar{t}$	$3.380570 \cdot 10^{-03}$	$3.380570 \cdot 10^{-03}$	$8.79 \cdot 10^{-15}$

Table 1: Comparison between Model 1 and 2 setting the width in the propagators to zero.

process (interference)	Model 1	Model 2	relative difference
$b\bar{b} \to w^+w^-z$	$-2.562000 \cdot 10^{-06}$	$-2.571304 \cdot 10^{-06}$	$1.81 \cdot 10^{-03}$
$\bar{d}u \to \bar{b}tz$	$8.005881 \cdot 10^{-09}$	$8.003428 \cdot 10^{-09}$	$1.53 \cdot 10^{-04}$
$bw^+ \to bw^+$	$2.708134 \cdot 10^{-01}$	$2.706435 \cdot 10^{-01}$	$3.14 \cdot 10^{-04}$
$hw^+ \to t\bar{t}w^+$	$-1.760324 \cdot 10^{-05}$	$-1.754204 \cdot 10^{-05}$	$1.74 \cdot 10^{-03}$
$b\bar{b} \to t\bar{t}$	$3.380570 \cdot 10^{-03}$	$3.380510 \cdot 10^{-03}$	$8.79 \cdot 10^{-06}$

Table 2: Comparison between Model 1 and 2 setting the width in the propagators to their SM values.

with $W_{\mu\nu}$ the usual SU(2) field strength. We see that this operator can be traded for some 4-fermion operators involving lepton and quark doublets, as well as a higher-derivative gauge boson interaction with the fermion current.

3 NUMERICAL ANALYSIS

The model described in the previous section have been implemented into `FeynRules` [91, 301] to produce Universal FeynRules Output (UFO) [93] models.[1] For an implementation of the Higgs effective Lagrangian see [271]. Our numerical results are obtained using the `MadGraph5_aMC@NLO` package [95] (dubbed `MG5aMC`). To show the level of agreement between the two models, we start by evaluating the interference term between the SM and the EFT contributions at a single phase-space point for a series of key processes. Those phase-space points are generated with RAMBO [302] at a centre-of-mass energy of 1 TeV.

In table 1, we have set $\frac{c}{\Lambda^2} = 1\ \text{TeV}^{-2}$ and all of the particle widths to zero. While in this proceeding we restrict ourselves to only five different processes for brevity, we emphasise that more than one hundred different processes were checked in the complete study. As can be inferred from table 1 we observe a perfect agreement of both models at the pure dimension-6 level (the dimension-8 contribution originating from the dimension-6 contribution squared will obviously also be identical in this case). In order to study the impact of the width in the propagators, we present table 2 were we have kept all particle widths to their SM value. We now see that the two models do not agree anymore. This disagreement is related to the fact that the width is formally a higher order effect and its inclusion amounts to a mixing of perturbative orders. This also breaks gauge invariance once a decay width is introduced into

[1] We have cross-checked our model files by two independent implementations.

the gauge boson propagators. This is a well known problem that can be for instance solved by employing the complex mass scheme [303]. The level of disagreement worsens with the number of possible propagators with modified widths appearing in the Feynman diagrams for each process. We stress that the observed difference is not an artefact of introducing the wrong width in the propagator (i.e. not including the effects of dimension-6 operators consistently). In order to show this explicitly we perform the same computation but also including the dimension-6 contribution to the width, see table 3.

For the sake of the example let's focus of the width of the top (the same can be done for the Z propagator). We dubbed Γ^t_{SM} the standard model contribution and Γ^t_6 the dimension-6 contribution to the width (the interference term):

$$\Gamma^t_{SM} = \frac{(M_t^2 - M_w^2)e^2}{64\pi M_t^3 s_w^2}(M_t^2 - 2M_w^2 + \frac{M_t^4}{M_w^2}), \tag{6}$$

$$\Gamma^t_6 = \frac{c}{\Lambda^2}\frac{v^2}{2}\Gamma^t_{SM}. \tag{7}$$

Computing Feynman rules with $\Gamma^t_{SM} + \Gamma^t_6$ is actually not consistent for an EFT point of view since due to the presence of the width in the propagator, this is equivalent to add higher order term of the EFT inside the computation. To avoid such higher order term we use a Taylor expansion of the propagator:

$$\frac{1}{q^2 - m^2 + im(\Gamma^t_{SM} + \Gamma^t_6)} \approx \frac{1}{q^2 - m^2 + im\Gamma^t_{SM}} - \frac{im\Gamma^t_6}{(q^2 - m^2 + im\Gamma^t_{SM})^2} \tag{8}$$

Such expansion is converging for all phase-space points as long as $\Gamma^t_6 < \Gamma^t_{SM}$, i.e. as long as $\frac{c}{\Lambda^2}\frac{v^2}{2} < 1$. We can then see the second term of the Taylor expansion as generating some additional effective vertex and compute their interference with the SM amplitude. Interestingly, this then extends the impact of the EFT operators to processes where they do not contribute otherwise, as e.g. to $e^+e^- \to \mu^+\mu^-$ using only the operators of eq. (1) or (4).

The computation of Eq. 8 cannot be performed using the `MG5aMC` package 'out of the box'. To allow the numerical computation using this method, we then created an extension of the usermod of `MG5aMC` in order to generate a new dedicated UFO package. The idea is to add two new particles ($\tilde{t}$, $\tilde{Z}$) associated to a custom propagator [304, 305] that provides the contribution from the second term in eq. (8). Then for each interaction with either a top or Z boson, we add to the model one copy of that interaction with (at most one) top/Z replaced by it's equivalent $\tilde{t}$, $\tilde{Z}$. The coupling of such interactions is also tagged in a way to allow to compute interference terms in `MG5aMC`. Additionally the parameter Γ_6 is added to the model as an internal parameter associated to the analytical formula automatically extracted from the *decays.py* file [306] from the original model. A tool fully automating such feature is in preparation.[2]

With this consistent inclusion of the width at dimension-6 level we obtain the results presented in table 3, in which it can be seen that the level of agreement is not improved. This confirms our previous statement, that the problem is deeper that just consistently including the dimension-6 contributions to the width and points to an issue regarding the presence of the decay width itself. Comparing table 2 and 3 one can also see the impact of including the dimension-6 terms to the width. The differences displayed here are quite small but one should keep in mind

[2]The semi-automatic version can be downloaded with the following command: `bzr branch lp: maddevelopers/mg5amcnlo/eft_width_expansion`.

process (interference)	Model 1	Model 2	relative difference
$b\bar{b} \to w^+w^-z$	$-2.561587 \cdot 10^{-06}$	$-2.570890 \cdot 10^{-06}$	$1.81 \cdot 10^{-03}$
$\bar{d}u \to \bar{b}tz$	$8.005881 \cdot 10^{-09}$	$8.003428 \cdot 10^{-09}$	$1.53 \cdot 10^{-04}$
$bw^+ \to bw^+$	$2.708370 \cdot 10^{-01}$	$2.706671 \cdot 10^{-01}$	$3.14 \cdot 10^{-04}$
$hw^+ \to t\bar{t}w^+$	$-1.760429 \cdot 10^{-05}$	$-1.754309 \cdot 10^{-05}$	$1.74 \cdot 10^{-03}$
$b\bar{b} \to t\bar{t}$	$3.380538 \cdot 10^{-03}$	$3.380479 \cdot 10^{-03}$	$8.79 \cdot 10^{-06}$

Table 3: Comparison between Model 1 and 2 using the implementation of the width as given in eq. (8).

process (interference)	Model 1	Model 2	relative difference
$e^+e^- \to b\bar{b}b\bar{b}$	$1.434685 \cdot 10^{-12}$	$1.434685 \cdot 10^{-12}$	$2.96 \cdot 10^{-15}$
$b\bar{b} \to e^+\nu_e e^-\bar{\nu}_e$	$7.661298 \cdot 10^{-14}$	$7.661298 \cdot 10^{-14}$	$1.07 \cdot 10^{-14}$
$gg \to b\bar{b}e^+\nu_e\mu^-\bar{\nu}_\mu$	$5.186028 \cdot 10^{-20}$	$5.186028 \cdot 10^{-20}$	$2.44 \cdot 10^{-15}$
$u\bar{u} \to b\bar{b}\mu^+\mu^-$	$-4.947679 \cdot 10^{-15}$	$-4.947679 \cdot 10^{-15}$	$3.12 \cdot 10^{-14}$
$b\bar{b} \to e^+\nu_e\mu^-\bar{\nu}_\mu$	$2.045529 \cdot 10^{-14}$	$2.045529 \cdot 10^{-14}$	$7.71 \cdot 10^{-15}$

Table 4: Comparison between Model 1 and 2 using the standard model width using the complex mass scheme. The width is set to his SM value.

that such statement is highly phase-space dependent and should be maximal for onshell decay where it is of the order of Γ_6/Γ_{SM} and therefore proportional to the EFT expansion parameter $\frac{c}{\Lambda^2}$

As stated above, in order to include the width effect in a fully consistent way inside the SM to insure gauge invariance, one needs to use a dedicated method like for instance the complex mass scheme [303] or the overall-factor scheme [307, 308] (for an application to BSM see [309]). It therefore makes sense to do the same in our two models. However, in order to have consistent result in the complex mass scheme one has to decay all particles. Therefore we can not present results for the same set of processes as shown before.[3]. As a first step we neglect the effect of Γ_6 and use only the SM width (see table 4). This result shows that using the complex mass scheme is actually crucial in the context of EFT in order to have results independent of the basis.

The latest result is however not fully satisfactory since it does not include correctly the modification by the EFT operator to the width. On the one hand we have to include the dimension-6 contribution in the propagators as we have outlined before. On the other hand, for a fully consistent result at the dimension-6 level, contributions stemming from the replacement of the mass by

$$m^2 \to m^2 + im\left(\Gamma_{SM} + \Gamma_6\right) \tag{9}$$

[3]We also test close to one hundred different processes in this case.

process (interference)	Model 1	Model 2	relative difference
$e^+e^- \to b\bar{b}b\bar{b}$	$1.442082 \cdot 10^{-12}$	$1.442082 \cdot 10^{-12}$	$1.61 \cdot 10^{-15}$
$b\bar{b} \to e^+\nu_e e^-\bar{\nu}_e$	$7.664749 \cdot 10^{-14}$	$7.664749 \cdot 10^{-14}$	$1.07 \cdot 10^{-14}$
$gg \to b\bar{b}e^+\nu_e\mu^-\bar{\nu}_\mu$	$5.185849 \cdot 10^{-20}$	$5.185849 \cdot 10^{-20}$	$3.54 \cdot 10^{-15}$
$u\bar{u} \to b\bar{b}\mu^+\mu^-$	$-4.927938 \cdot 10^{-15}$	$-4.927938 \cdot 10^{-15}$	$3.47 \cdot 10^{-14}$
$b\bar{b} \to e^+\nu_e\mu^-\bar{\nu}_\mu$	$2.045606 \cdot 10^{-14}$	$2.045606 \cdot 10^{-14}$	$1.28 \cdot 10^{-14}$

Table 5: Comparison between Model 1 and 2 using the standard model width using the complex mass scheme for the SM width and including the effect due to the modification of the width only via the propagator as given in eq. (8).

or the replacement of the weak mixing angle by

$$\begin{aligned}\cos^2\theta_W = \frac{m_W^2}{m_Z^2} \to & \frac{m_W^2 + im_W(\Gamma_{SM}^W + \Gamma_6^W)}{m_Z^2 + im_Z(\Gamma_{SM}^Z + \Gamma_6^Z)} \\ \approx & \frac{m_W^2 + im_W\Gamma_{SM}^W}{m_Z^2 + im_Z\Gamma_{SM}^Z} + \frac{im_W\Gamma_6^W}{m_Z^2 + im_Z(\Gamma_{SM}^Z)} - \frac{im_Z\Gamma_6^Z(m_W^2 + im_W\Gamma_{SM}^W)}{(m_Z^2 + im_Z\Gamma_{SM}^Z)^2}\end{aligned} \tag{10}$$

with $\Gamma_{SM,6}^{Z/W}$ denoting the SM (dimension-6) contributions to the width of the Z/W boson, in the complex mass scheme in the SM matrix elements is necessary. Note that for our operators $\Gamma_6^W = 0$. The correct solution would be to do a Taylor expansion not only on the propagator like in Eq. 8 but on all parts of the matrix elements which now depends on the width, which again includes dimension-6 contributions, due to the complex mass scheme approach. This is in principle similar to the shifts in the SM dependent parameters in the presence of dimension-6 operators [310], as we discussed briefly in the previous section. These effects will be the focus of future work. As a first approximation we present in table 5 results using Eq. 8 on top of using the complex mass scheme for the SM width. The two models are in perfect agreement but we emphasize again, that this does not mean that all the dimension-6 effects are correctly included.

CONCLUSIONS

We have shown by example that, while different EFT operator bases are equivalent under field redefinitions if the width of the propagating particles in the numerical evaluation is set to zero, this is not the case if a non-zero width is used. As in the SM, this is related to the fact that the width is already a higher order effect in the perturbative expansion and formally breaks gauge invariance. In analogy to the SM the problem can be addressed by a complex mass scheme, where all the masses in propagators and couplings are replaced by a complex parameter including the physical width of the particle in the imaginary component. We showed that indeed this resolves the issue. The inclusion of the width however gives additional contributions at the dimension-6 level: 1.) the width in the particle propagators gets a dimension-6 piece. This part has to be Taylor expanded up to first order to keep it strictly at the dimension-6 level. We have provided a model for that in `MG5aMC`. 2.) Employing a complex mass scheme redefines also the masses of the unstable particles in the couplings, that compared to the SM complex mass scheme, now also obtain a contribution at the dimension-6 level from the particle's width. For

consistency this contribution also needs to be included. We leave the numerical impact of this contribution to future work.

ACKNOWLEDGEMENTS

We thank the organisers of the Les Houches Workshop Series "Physics at TeV Colliders" 2017 for the nice and fruitful atmosphere during the workshop. We thank Céline Degrande for useful discussions. RG is supported by a European Union COFUND/Durham Junior Research Fellowship under the EU grant number 609412. KM is supported in part by the Belgian Federal Science Policy Office through the Interuniversity Attraction Pole P7/37 and by the European Union's Horizon 2020 research and innovation programme under the Marie Skłodowska-Curie grant agreement No. 707983.

Contribution 13

On the use of Higgs fiducial cross sections for constraining new physics

S. Kraml, U. Laa, K. Lohwasser

Abstract
We discuss the potential of the measured Higgs fiducial cross sections for deriving constraints on anomalous Higgs production from BSM processes. Using the examples of three SUSY processes, we show that these constraints can be complementary to those from dedicated searches for new physics.

1 INTRODUCTION

The increasingly precise data on the 125 GeV Higgs boson from Run 1 and Run 2 of the LHC provide severe constraints on new physics beyond the Standard Model (BSM). A well-established approach to assess the compatibility of a BSM Higgs boson with the experimental results is the use of signal strengths, which compare—preferably in a detailed breakdown of production×decay modes—the observed state to Standard Model (SM) expectations; see [311–313] for detailed discussions. There has indeed been a boom of phenomenological studies making use of the signal strength measurements to work out the implications of the 125 GeV Higgs boson for non-standard Higgs sectors by simple scaling of production cross sections and decay branching ratios relative to the SM. In-depth studies concerned two-Higgs-doublet models, supersymmetric (SUSY) models, Randall-Sundrum (with Higgs-radion mixing) models, technicolor, little Higgs, composite Higgs models, and so on. The underlying assumption is that the signal selection efficiencies are to good approximation the same in the new model and the SM.

In situations in which the kinematic distribution of the signal depends on model parameters, simple scaling of production cross sections and decay branching ratios relative to the SM is, however, not appropriate — one must account for the change in the signal selection efficiencies. Such situations can arise from the presence of new tensor structures (anomalous couplings, higher-dimensional operators), as well as from the presence of new Higgs production modes through decays of heavier new states. To address these cases, [313] advocated the measurement of fiducial cross sections, i.e. cross sections, whether total or differential, for specific final states within the phase space defined by the experimental selection and acceptance cuts. Fiducial cross sections can be interpreted in the context of whatever theoretical model, provided it is possible to compute its predictions for the given fiducial volume (typically by means of a Monte Carlo event simulation) and that no significant extrapolation has been applied to define the fiducial cross section (e.g., to correct for an event-level selection based on machine learning that has a different acceptance for SM and BSM events). Fiducial cross sections also have the advantage of largely separating experimental and theoretical uncertainties, such that a re-evaluation of constraints is possible when more precise theoretical prediction become available

without re-analysing the data.

Higgs fiducial cross sections were the subject of a dedicated task force for the Yellow Report 4 [263] of the LHC Higgs cross section working group. Differential measurements are particularly interesting in this context, as the shapes of distributions may provide more sensitive tests than integrated event rates, for instance in the presence of interference effects.[1]

Both ATLAS and CMS provide total and differential fiducial cross section measurements for specific Higgs decay modes, concretely $H \to \gamma\gamma$ [314–317], $H \to ZZ^* \to 4$ leptons [318–320] and $H \to WW^* \to 2l2\nu$ [321]. These measurements are agnostic of the Higgs production mode and thus potentially sensitive for constraining additional Higgs production from BSM (cascade) decays.[2] The facts that the definition of the fiducial volume is based on simple cuts and the results are unfolded to the particle level are big advantages for interpretation studies. The downside is that precise SM predictions to compare to require highly sophisticated computations.

In this contribution, we investigate the use of fiducial cross section measurements to constrain new Higgs boson production modes in BSM models. We concentrate on the $H \to \gamma\gamma$ [314] and $H \to ZZ^* \to 4\ell$ [318] measurements from ATLAS at $\sqrt{s} = 8$ TeV, for which detailed HEPData entries [323, 324] and validated Rivet [325] routines [326, 327] are available. (A Rivet routine is also available for the combination of the $H \to \gamma\gamma$ and $H \to ZZ^* \to 4\ell$ analyses of ATLAS [328], but this effectively assumes stable Higgs bosons; CMS provides the results for $H \to \gamma\gamma$ at 8 TeV on HEPData, but no Rivet routine.)

2 BACK-OF-THE-ENVELOP CONSIDERATIONS

In [314], ATLAS reported the $pp \to H \to \gamma\gamma$ fiducial cross section at 8 TeV as 43.2 ± 9.4(stat.) $^{+3.2}_{-2.9}$(syst.) ± 1.2(lumi) fb for a Higgs boson of mass 125.4 GeV decaying to two isolated photons with pseudorapidity $|\eta| < 2.37$ and $p_T/m_{\gamma\gamma} > 0.35$ (0.25) for the leading (subleading) photon. The SM prediction is 30.5 ± 3.3 [312] following the recommendatons of the HXSWG, but ranges from $27^{+3.6}_{-3.2}$ [329] to $34.1^{+3.6}_{-3.5}$ [330] using other calculations. An overview of the experimental and theoretical values for the seven fiducial regions considered in [314] is given in Table 1. We see that that data agree quite well with SM expectations, but uncertainties are sizable, and there is still room for contributions from new physics.

With these numbers, we can make some back-of-the envelop estimates. The total SM Higgs production cross section at 8 TeV is 19.15 pb for $m_h = 125.4$ GeV [312]. With BR$(H \to \gamma\gamma) = 0.228\%$, this gives a total cross section in the diphoton channel of 43.66 fb, which means the diphoton baseline fiducial volume contains about 70% of the total production. Approximating the SM prediction for the baseline fiducial region as 30.85 ± 6.85 and summing experimental and theoretical uncertainties in quadrature, an additional BSM contribution of up to about 36 fb would be allowed at 2σ (not accounting for additional BSM uncertainties). Assuming Higgs branching ratios and a fiducial acceptance like in the SM, this means up to about 23 pb of Higgs production from BSM processes is allowed. If, however, the BSM Higgs production always includes 2, 3, or more hard jets, e.g., because of cascade decays, this room shrinks considerably, see Table 1. For Higgs + 3 jets, a total BSM cross section of the

[1] See also the contribution by A. Carvalho, R. Gröber, S. Liebler and J. Quevillon in these proceedings.

[2] In contrast, the so-called "simplified template cross sections" (STXS) [263, 322] are cross sections per production mode, split into mutually exclusive kinematic bins for each of the main production modes. They are determined from the experimental categories by a global fit that combines all decay channels, with the SM serving as kinematic template.

Fiducial region	Measured cross section (fb)	SM predictions (fb)
Baseline	43.2 ± 10.0	[24.0, 37.7]
$N_{\text{jets}} \geq 1$	21.5 ± 5.8	[8.1, 15.5]
$N_{\text{jets}} \geq 2$	9.2 ± 3.1	[3.4, 6.52]
$N_{\text{jets}} \geq 3$	4.0 ± 1.5	0.94 ± 0.15
VBF-enhanced	1.68 ± 0.63	0.87 ± 0.08
$N_{\text{leptons}} \geq 1$	< 0.80	0.27 ± 0.02
$E_T^{\text{miss}} > 80$ GeV	< 0.74	0.14 ± 0.01

Table 1: Measured $pp \to H \to \gamma\gamma$ fiducial cross section at $\sqrt{s} = 8$ TeV from ATLAS [314] in the baseline, $N_{\text{jets}} \geq 1$, $N_{\text{jets}} \geq 2$, $N_{\text{jets}} \geq 3$ and VBF-enhanced fiducial regions, and cross-section limits at 95% confidence level in the single-lepton and high-E_T^{miss} fiducial regions. The ranges given for the SM prediction correspond to the envelope of the theory predictions, incl. 1σ uncertainties, quoted in Table 4 of [314].

order of 4 pb can be excluded, still assuming BR$(H \to \gamma\gamma) = 0.228\%$ and an acceptance of around 0.7. With the same reasoning, one could expect to exclude BSM Higgs + W associated production above about 2 pb due to the $N_{\text{leptons}} \geq 1$ fiducial limit.[3] Likewise, if BSM Higgs production always leads to large $E_T^{\text{miss}} > 80$ GeV, its total cross section should be below about 0.4 pb. Of course, these are very rough estimates which may easily be off by a factor of a few, especially because the acceptance does not stay constant. (Besides also the Higgs branching ratios can vary in BSM models.) Nonetheless they may serve as guidelines for the order of magnitude of possible constraints on new physics. We also note that stronger constraints can come from the differential distributions presented in [314], limiting for instance highly boosted Higgs production.

Turning to the $H \to ZZ^* \to 4\ell$ channel, Ref. [318] reports a total fiducial cross section of $\sigma_{\text{fid}}^{\text{tot}} = 2.11^{+0.53}_{-0.47}\,(\text{stat.}) \pm 0.08\,(\text{syst.})$ fb, to be compared to the theoretical prediction in the SM of 1.30 ± 0.13 fb [312] for a Higgs boson mass of 125.4 GeV. The paper moreover shows the differential fiducial cross sections as a function of $p_{T,H}$, y_H, m_{34}, $|\cos\theta_*|$, $N(\text{jets})$, and $p_{T,\text{jet}}$. All these results are available on HEPData. Moreover, upon request, also the SM predictions used in [318] were made available on HEPData, which is extremely useful for the purpose of constraining additional BSM contributions.[4] From the numbers above, a BSM contribution to $\sigma_{\text{fid}}^{\text{tot}}$ of 1.9 fb or larger can be excluded. Performing the same exercise as above, that is taking BR$(H \to ZZ^* \to 4\ell) = 1.286 \times 10^{-4}$ and assuming an acceptance similar to the one in the SM, this would correspond to a total inclusive BSM production cross section of 28 pb, i.e. comparable but a bit larger than for $H \to \gamma\gamma$. More sensitive constraints come again from the differential distributions, in particular when the BSM production leads to high $p_{T,H}$ or high jet multiplicity.

[3] In reality this is somewhat too optimistic, partly because of the $p_T > 15$ GeV and $|\eta| < 2.47$ requirements for letopns.

[4] Unfortunately, the same was not done for the $pp \to H \to \gamma\gamma$ differential distributions.

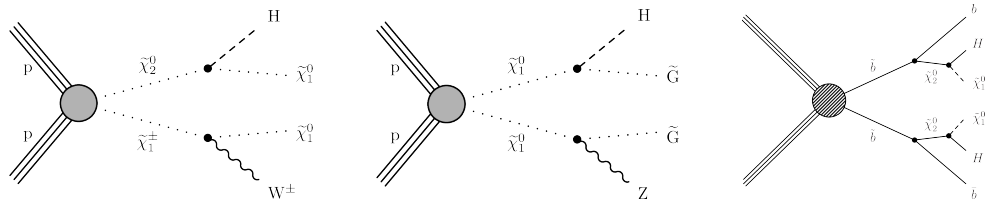

Figure 1: Examples for Higgs production in SUSY cascade decays considered in ATLAS and/or CMS SUSY searches.

3 HIGGS PRODUCTION FROM SUSY CASCADES

Anomalous Higgs production was considered by ATLAS and CMS in the context of SUSY searches. This provides a welcome possibility to compare constraints from Higgs fiducial cross sections to constraints from dedicated BSM searches.

As first example, we consider chargino-neutralino production in the MSSM, $pp \to \tilde{\chi}_1^\pm \tilde{\chi}_2^0$ followed by $\tilde{\chi}_1^\pm \to W^\pm \tilde{\chi}_1^0$ and $\tilde{\chi}_2^0 \to H\tilde{\chi}_1^0$, see the left diagram in Fig. 1.[5] The 8 TeV ATLAS analysis [331] puts a limit of $m_{\tilde{\chi}_1^\pm,\tilde{\chi}_2^0} \gtrsim 170$ GeV for $m_{\tilde{\chi}_1^0} \lesssim 40$ GeV in the $\ell\gamma\gamma + E_T^{\text{miss}}$ channel ($W \to \ell\nu$, $H \to \gamma\gamma$). The median expected limit is $m_{\tilde{\chi}_1^\pm,\tilde{\chi}_2^0} \gtrsim 154$–$160$ GeV for $m_{\tilde{\chi}_1^0} \lesssim 30$ GeV with a very large uncertainty. The 8 TeV CMS analysis [332] includes a search in the $H \to \gamma\gamma$ channel with $W \to \ell\nu$ or $W \to 2\,\text{jets}$. Combining the result with that of [333] the CMS limit reaches $m_{\tilde{\chi}_1^\pm,\tilde{\chi}_2^0} \gtrsim 210$ GeV for (very) small $\tilde{\chi}_1^0$ mass; at $m_{\tilde{\chi}_1^\pm,\tilde{\chi}_2^0} = 150$ GeV, the reach in $m_{\tilde{\chi}_1^0}$ is about 20 GeV. We therefore take $m_{\tilde{\chi}_1^\pm,\tilde{\chi}_2^0} = 150$ GeV and $m_{\tilde{\chi}_1^0} = 20$ GeV as our test point. The production cross section at NLO+NLL accuracy is 2.41 pb [334] for wino-like $\tilde{\chi}_1^\pm$ and $\tilde{\chi}_2^0$. We assume $\text{BR}(\tilde{\chi}_1^\pm \to W^\pm\tilde{\chi}_1^0) = \text{BR}(\tilde{\chi}_2^0 \to H\tilde{\chi}_1^0) = 1$, and a perfectly SM-like Higgs boson H with mass of 125 GeV. The SUSY signal is simulated with Pythia 8.2 [97] and then passed to the Rivet analysis routines [326, 327]. The result for the $H \to \gamma\gamma$ fiducial regions from Table 1 is shown in Fig. 2, examples for two differential distributions for the $H \to ZZ^* \to 4\ell$ selection in Fig. 3. While the $H \to ZZ^* \to 4\ell$ distributions are not very sensitive to this signal, the limit in the $E_T^{\text{miss}} > 80$ GeV fiducial region of the $H \to \gamma\gamma$ measurements excludes the benchmark point. The signal in the $N_{\text{leptons}} \geq 1$ fiducial region is also close to the 95% CL limit, consistent with the naive expectations from the previous section.

Our second example is a related topology giving $HZ + E_T^{\text{miss}}$ or $HH + E_T^{\text{miss}}$ final states. This was considered by CMS in [332, 335] in the context of higgsino-like neutralino production with $\tilde{\chi}_1^0$ decaying into Higgs or Z and a gravitino $\tilde{G}$, shown as the middle diagram in Fig. 1. Although in the MSSM the $\tilde{\chi}_1^0 \to Z\tilde{G}$ always dominates over $\tilde{\chi}_1^0 \to H\tilde{G}$, the topology is interesting per se. Adopting one of the simplified models of the CMS study, we assume $\text{BR}(\tilde{\chi}_1^0 \to Z\tilde{G}) = \text{BR}(\tilde{\chi}_1^0 \to H\tilde{G}) = 0.5$. Moreover, to have a concrete benchmark point, we fix $m_{\tilde{\chi}_1^0} = 150$ GeV and $m_{\tilde{G}} = 1$ GeV. The expected limit of the 8 TeV CMS search [332] in the $\ell\gamma\gamma + E_T^{\text{miss}}$ channel is about 15 pb for this point, an order of magnitude larger than the total higgsino production cross section, see Fig. 19 of [332]. (It has to be added that a much stronger limit is obtained in the $3\ell + E_T^{\text{miss}}$ final state and the analysis actually excludes higgsino masses below about 300 GeV by combining all channels.) The result from using the $H \to \gamma\gamma$ fiducial cross section is shown in Fig. 4. Following CMS, the cross section obtained from Pythia has been rescaled to the total higgsino production cross section of 2.14 pb [334], assuming the decays of $\tilde{\chi}_1^\pm, \tilde{\chi}_2^0$ to the $\tilde{\chi}_1^0$ plus soft pions are effectively invisible. As in the example for SUSY

[5] For simplicity, we keep using upper case H for the SM-like Higgs boson also in the SUSY case.

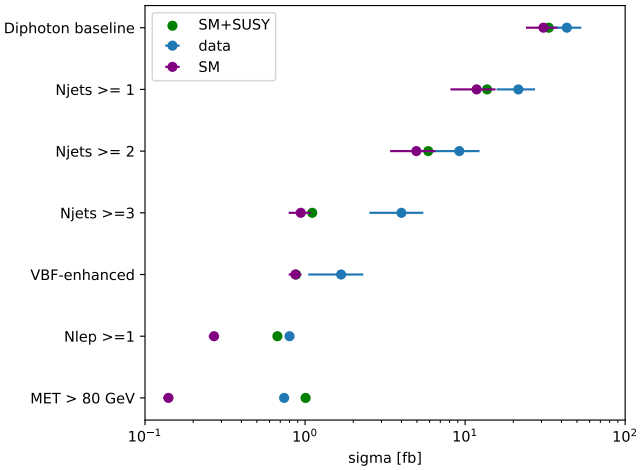

Figure 2: Results for the $H \to \gamma\gamma$ fiducial regions from ATLAS [314]. The SUSY signal considered is $pp \to \tilde{\chi}_1^{\pm}\tilde{\chi}_2^0$ followed by $\tilde{\chi}_1^{\pm} \to W^{\pm}\tilde{\chi}_1^0$ and $\tilde{\chi}_2^0 \to H\tilde{\chi}_1^0$ for $m_{\tilde{\chi}_1^{\pm},\tilde{\chi}_2^0} = 150$ GeV and $m_{\tilde{\chi}_1^0} = 20$ GeV and $\sigma_{\text{tot}}(\tilde{\chi}_1^{\pm}\tilde{\chi}_2^0) = 2.41$ pb.

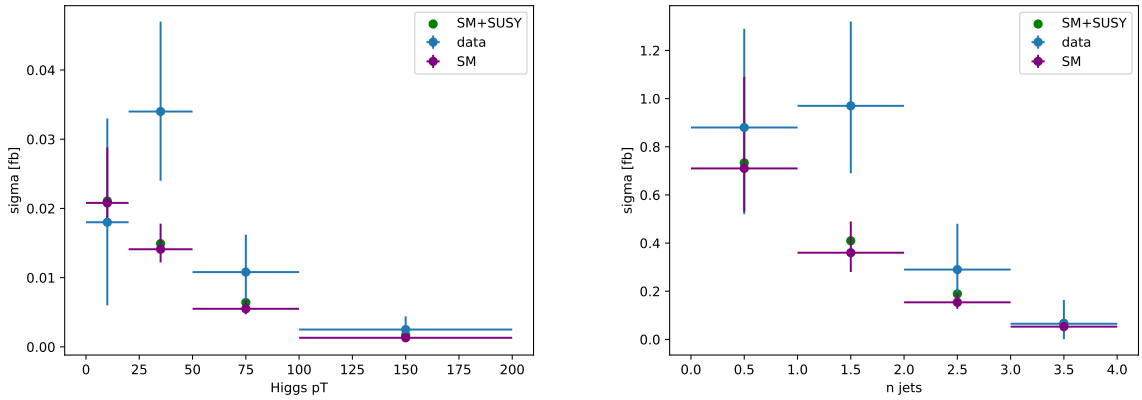

Figure 3: Differential distributions of $p_{T,H}$ (left) and N(jets) for $H \to ZZ^* \to 4\ell$ of ATLAS [318]. The SUSY signal considered is $pp \to \tilde{\chi}_1^{\pm}\tilde{\chi}_2^0$ followed by $\tilde{\chi}_1^{\pm} \to W^{\pm}\tilde{\chi}_1^0$ and $\tilde{\chi}_2^0 \to H\tilde{\chi}_1^0$ for $m_{\tilde{\chi}_1^{\pm},\tilde{\chi}_2^0} = 150$ GeV and $m_{\tilde{\chi}_1^0} = 20$ GeV and $\sigma_{\text{tot}}(\tilde{\chi}_1^{\pm}\tilde{\chi}_2^0) = 2.41$ pb.

WH production above, the scenario is excluded by the limit in the $E_T^{\text{miss}} > 80$ GeV fiducial region, although by a smaller margin.

Finally, we consider sbottom-pair production with both sbottoms decaying into $\tilde{b}_1 \to b\tilde{\chi}_2^0$ followed by $\tilde{\chi}_2^0 \to H\tilde{\chi}_1^0$ (right diagram in Fig. 1). This was proposed in [336] to explain a local 2.9σ excess in the 8 TeV search for electroweak SUSY partners in $H \to \gamma\gamma$ + 1 jet events [337], and followed up by a dedicated interpretation in the 13 TeV CMS analysis [335]. In this contribution, we choose a benchmark point with $m_{\tilde{b}_1} = 300$, $m_{\tilde{\chi}_2^0} = 280$ and $m_{\tilde{\chi}_1^0} = 150$ GeV, which lies just outside the CMS SUSY exclusion at 13 TeV (because the spectrum is rather compressed). The sbottom-pair production cross section for 300 GeV at 8 TeV is 1.996 pb [334]. The simulation is again done with Pythia 8.2 and the events fed to Rivet. The result for the diphoton fiducial regions from ATLAS is shown in Fig. 5 (left). Note the important

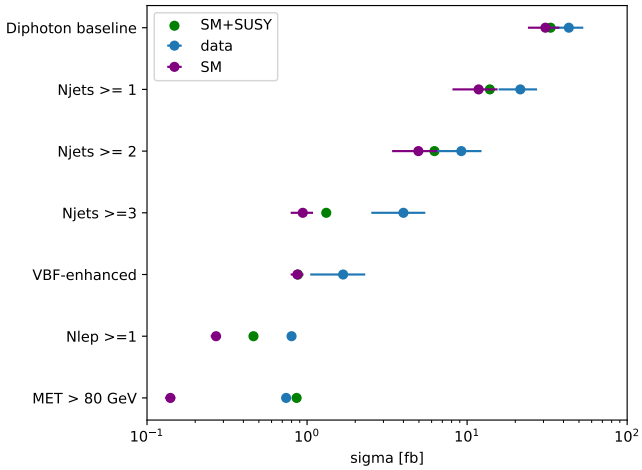

Figure 4: Results for the $H \to \gamma\gamma$ fiducial regions from ATLAS [314]. The SUSY signal considered is higgsino production with $\mathrm{BR}(\tilde{\chi}_1^0 \to Z\tilde{G}) = \mathrm{BR}(\tilde{\chi}_1^0 \to H\tilde{G}) = 0.5$ for $m_{\tilde{\chi}_1^0} = 150$ GeV and $m_{\tilde{G}} = 1$ GeV and $\sigma_{\mathrm{tot}}(higgsino) = 2.14$ pb.

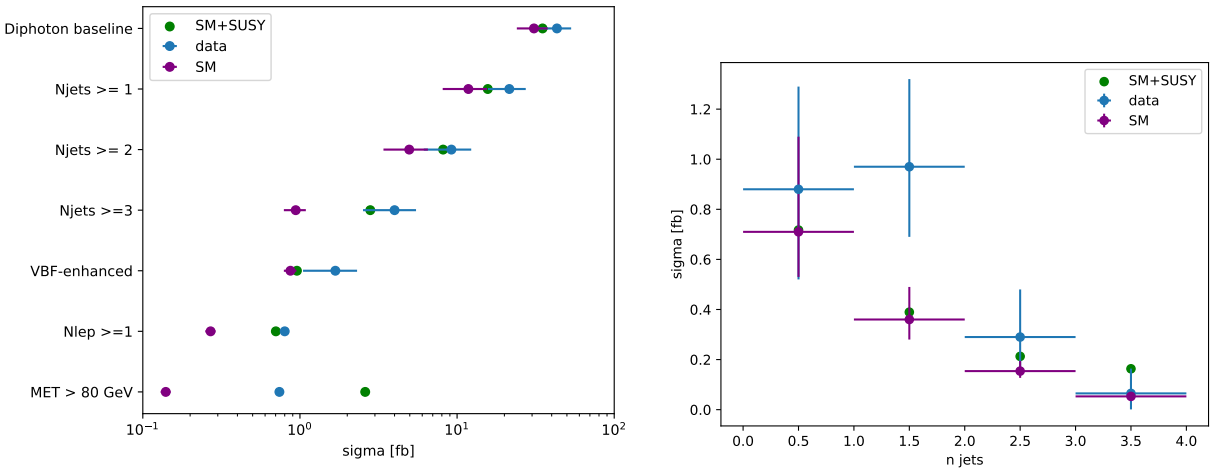

Figure 5: On the left, results for the $H \to \gamma\gamma$ fiducial regions from ATLAS [314]. On the right, the N(jets) distribution for $H \to ZZ^* \to 4\ell$ of ATLAS [318]. The SUSY signal considered is $pp \to \tilde{b}_1\tilde{b}_1$ followed by $\tilde{b}_1 \to b\tilde{\chi}_2^0$ and $\tilde{\chi}_2^0 \to H\tilde{\chi}_1^0$ for $m_{\tilde{b}_1} = 300$, $m_{\tilde{\chi}_2^0} = 280$ and $m_{\tilde{\chi}_1^0} = 150$ GeV with a total inclusive cross section of about 2 pb.

SUSY contribution to the $N_{\mathrm{jets}} \geq 2$ and $N_{\mathrm{jets}} \geq 3$ fiducial regions. Moreover, because the signal contains two Higgs bosons, $H \to \gamma\gamma$ and $H \to WW^*, ZZ^*$ combinations can give $H \to \gamma\gamma$ events with additional leptons, getting us close to the 95% CL exclusion in the $N_{\mathrm{leptons}} \geq 1$ fiducial region. Finally, the $E_T^{\mathrm{miss}} > 80$ GeV fiducial region excludes the benchmark point. The presence of the additional jets in the SUSY cascade process also leads to a small effect in the N(jets) distribution for $H \to ZZ^* \to 4\ell$, see Fig. 5 (right).

CONCLUSIONS

We showed that fiducial Higgs cross section measurements can provide interesting constraints on anomalous Higgs production from BSM processes. These are complementary to and sometimes extend the constraints from dedicated BSM searches in final states with Higgs bosons. This is particularly useful for interpretation studies when the scenario of interest has not been considered by the ATLAS and CMS collaborations in any of their searches and/or when the relevant BSM searches cannot easily be reproduced outside the experimental collaboration, e.g., because they use a signal selection based on machine learning. In turn, it can be instructive to consider the existing constraints from fiducial measurements when constructing a search/interpretation for a new BSM signal.

Here we focussed on SUSY scenarios, for which dedicated searches exist. Analogous studies will be interesting for non-SUSY models featuring new heavy scalars, new vector bosons, etc., which can decay into the SM-like Higgs boson. We leave this for future work, noting that fiducial measurements for 36 fb^{-1} of data at 13 TeV are already available for $H \to \gamma\gamma$ [317] and $H \to ZZ^* \to 4\,\ell$ [320] from ATLAS.

To make the fiducial Higgs cross section measurements maximally useful, we kindly ask the ATLAS and CMS collaborations to provide the SM predictions used in the plots of differential distributions available in HEPData, together with the measured data. Moreover, it is highly appreciated when Rivet routines are provided, as they greatly facilitate the re-use of these important data. The ATLAS $H \to ZZ^* \to 4\ell$ fiducial measurements from Run 1 are an example of good practise and we hope that other analyses will follow this example.

ACKNOWLEDGEMENTS

We thank the ATLAS Higgs group for providing the SM predictions used in [328] on HEPData, and Christian Gutschow and Jonathan Stahlman for providing a Rivet routine for this analysis in time for being used in these proceedings.

K.L. is supported by the European Union's Horizon 2020 research and innovation programme under ERC grant agreement No. 715871.

Contribution 14

Death and the Model: A Contur Case Study

J. M. Butterworth, D. Grellscheid, K. Lane, K. Lohwasser and L. Pritchett

Abstract

This report summarizes the use of Contur to constrain a two-Higgs-doublet model explanation of an apparent $30\,\mathrm{GeV}$ dimuon resonance observed in a reanalysis of $Z \to \bar{b}b$ events in ALEPH data taken in 1992–95 and reported in arXiv:1610.06536. The model was proposed by two of us in arXiv:1701.07376. Contur is used to limit the mass of the model's charged Higgs boson, $h^{\pm}$, which is produced in pairs or in association with the extra neutral CP-even and odd scalars h and η_A. The limit obtained excludes $h^{\pm}$ and the 2HDM model for the ALEPH dimuon excess.

1 Introduction

In addition to the extensive programme of searches, the growing 'library' of measurements from the LHC experiments is placing ever-more-stringent requirements on proposed extensions of the Standard Model (SM). Measurements defined in terms of final-state particles, in fiducial regions reflecting the acceptance of the detectors, are rather model-independent and are thus particularly suited for confrontation with the predictions of new models. Many of these measurements are made differentially in key kinematic variables. In this contribution, we take an extension of the SM which has been proposed [338] to address a feature in ALEPH data [339], and confront it with such data from ATLAS and CMS. The model and its motivation are outlined in Sec. 2. The analysis tools we use are described in Sec. 3, and the analysis and results are presented in Sec. 4, before we present our conclusions.

2 Two-Higgs-doublet model of the 30 GeV dimuon

In 2016 Heister presented an analysis of archived data of the ALEPH experiment at LEP and found evidence for a narrow dimuon ($\mu^+\mu^-$) resonance at $30\,\mathrm{GeV}$ [339]. The data, taken in 1992-95, involve 1.9 million hadronic decays of Z-bosons produced at rest in e^+e^- annihilation. This excess appears in $Z \to \bar{b}b\mu^+\mu^-$ events. The opposite-sign dimuon spectrum data is shown in Fig. 1 (left) along with the expected background. The same-sign dimuon spectrum in Fig. 1 (right) has no significant excesses. The data have the following characteristics:

1.) Two benchmark methods were used to estimate the significance of the excess. One gave a local significance of about $2.6\,\sigma$, the other $5.4\,\sigma$. The second method requires using the look-elsewhere effect; it reduces its significance by 1.4–$1.6\,\sigma$. See Ref. [339] for details.

2.) There is an excess of 32 ± 11 events in the resonant peak of Fig. 2 corresponding to a mass of $30.40\,\mathrm{GeV}$ with a Breit-Wigner width of $1.78\,\mathrm{GeV}$ (Gaussian width of $0.74\,\mathrm{GeV}$), consistent with the expected ALEPH dimuon mass reconstruction performance at $30\,\mathrm{GeV}$.

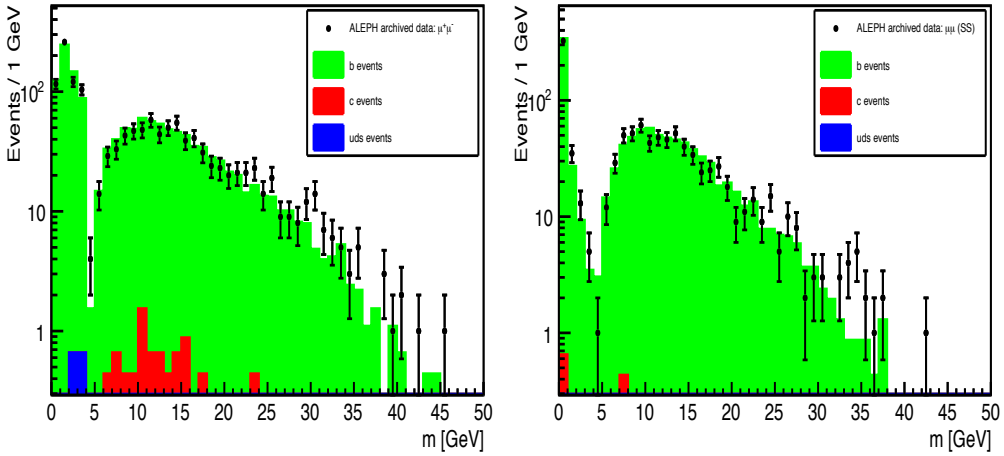

Figure 1: The opposite-sign (left) and same-sign (right) dimuon mass spectra in $Z \to \bar{b}b\mu\mu$ data taken by the ALEPH Collaboration; from Ref. [339].

Using the ALEPH b-tag and single-muon-ID efficiencies of 38% and 86% [339] and $B(Z \to \bar{b}b)/B(Z \to \text{hadrons}) = 0.216$ yields the branching ratio

$$B(Z \to \bar{b}b\, X(\to \mu^+\mu^-)) = (2.77 \pm 0.95) \times 10^{-4}. \tag{1}$$

If the dimuon excess is due to the decay of a new particle X, it is not known whether it is emitted from the Z, as in $Z \to Z^*X$ with $Z^* \to \bar{b}b$ and $X \to \mu^+\mu^-$, or from one of the b-quarks, as in $Z \to \bar{b}b \to \bar{b}b + X$, or from two new particles, $Z \to XY$, with $X \to \mu^+\mu^-$ and $Y \to \bar{b}b$.

3.) There is a small excess of 8.0 ± 4.5 events near $M_{e^+e^-} = 30\,\text{GeV}$ in the $Z \to \bar{b}be^+e^-$ data. This is not considered in the model described below.

4.) There is no evidence for the 30 GeV dimuon excess in events for which the b-tag has been inverted; see Fig. 3, from Ref. [339].

The obvious and simplest explanation of these features of the ALEPH data is that the 30 GeV excess is just a statistical fluctuation in semileptonic $Z \to \bar{b}b$ decays. If that possibility is set aside, however, no Monte Carlo of semileptonic b-decays in $Z \to \bar{b}b$ at LEP or elsewhere has produced such an excess. It is tempting, therefore, to construct a model which can account for the ALEPH data and suggest searches by LHC experiments that might confirm – or refute – the existence of the $30\,\text{GeV}$ dimuon in Z decays.

Two of us proposed such a model [338]. It is a two-Higgs doublet model (2HDM) in which the heavier CP-even Higgs boson H is the $125\,\text{GeV}$ Higgs boson discovered in 2012 at the LHC [260, 340]. The two other neutral Higgs bosons are a CP-even one h and a CP-odd one η_A. It is these that will account for the ALEPH signal. In this model, one Higgs doublet, $\varphi_1 = (\varphi_1^+, v_1 + \rho_1 + i\pi_1)/\sqrt{2}$, couples in the usual way to all the quark doublets as well as to the τ-lepton doublet. The other doublet, φ_2, couples only to the muon and electron doublets. This set-up is not one of the commonly studied classes of 2HDM's [341]. Nevertheless, it can be enforced by a softly broken $U(1)$ symmetry and it does not give rise to observable charged lepton flavor violation.

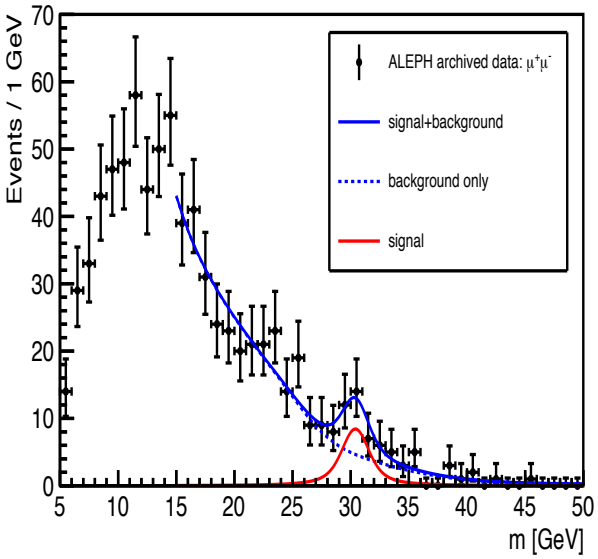

Figure 2: ALEPH $Z \to \bar{b}b\mu^+\mu^-$ data with signal+background model used to extract the 30 GeV signal parameters in Ref. [339].

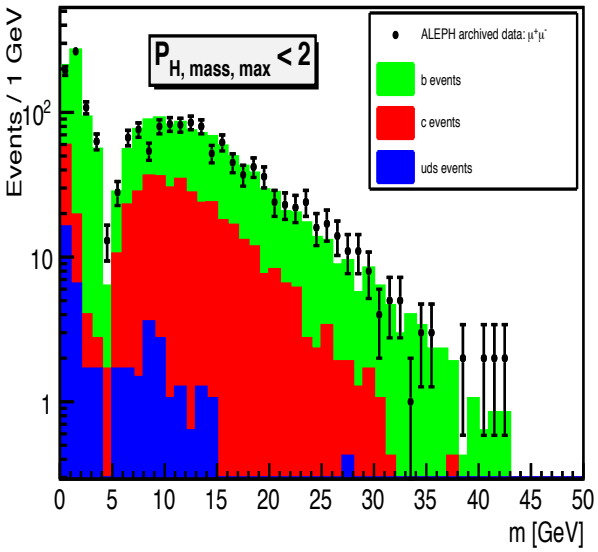

Figure 3: The opposite-sign dimuon mass spectrum in $Z \to \text{hadrons} + \mu^+\mu^-$ events in which the b-tag has been inverted, indicating no evidence for an excess near 30 GeV; from Ref. [339].

By choosing the vacuum expectation values (vevs) so that $v \equiv \sqrt{v_1^2 + v_2^2} = 246\,\text{GeV} \cong v_1$, the 125 GeV Higgs boson $H \cong \rho_1$ and its couplings to the electroweak (EW) gauge bosons and all the fermions — except for muons, electrons and their neutrinos — are very nearly as in the standard model (SM) with a single Higgs doublet. This is effectively the situation referred to as "alignment"; see e.g. Ref. [342]. The model's additional Higgs bosons, $h \cong \rho_2$, $\eta_A \cong \pi_2$

and $h^\pm \cong \varphi_2^\pm$ couple directly to the μ and e doublets and singlets.

The most natural choice of Higgs self-coupling parameters — the only one with $H \cong \rho_1$ and which can account for the ALEPH dimuon signal — has $M_{\eta_A} \cong M_h = 30\,\mathrm{GeV}$.[1] Their main decay modes are $h, \eta \to \mu^+\mu^-$ and, through φ_1–φ_2 mixing, $h, \eta_A \to \bar{b}b$ at the percent level. The decay $Z \to h\eta_A$ can then easily account for the $\mathcal{O}(10^{-4})$ branching ratio in Eq. (1) by choosing $\tan\beta = v_2/v_1 \simeq 1/20$.[2] This is the origin of the ALEPH signal in this model.

To prevent a very large contribution to the H width from $H \to h^+h^-$, it is simplest to take $M_{h^\pm} > M_H/2$. This can be arranged by taking a particular scalar quartic coupling negative, a choice that is consistent with vacuum stability. Up to $M_{h^\pm} \simeq 125\,\mathrm{GeV}$, its main decay mode is $h^\pm \to \mu^\pm\nu_\mu$. No searches for charged Higgses at LEP, the Tevatron and the LHC look in this mode, assuming instead that charged Higgses decay to the heaviest quark pairs allowed kinematically. The strongest limit for a simple $\mu^+\mu^- + E_T^{\mathrm{miss}}$ signal appears to come from searches at LEP for pair-production of supersymmetric partners of the muon, $\tilde{\mu}^\pm$. They limit $M_{h^\pm} > 95\,\mathrm{GeV}$; see, Ref. [343], e.g. While the $h^+\bar{t}b$ coupling in this model is suppressed by $\tan\beta$ relative to the large coupling m_t/v generally assumed in collider searches, it is still large enough to make $h^+ \to t\bar{b}$ an important decay mode if allowed. It is excluded by a CMS search for $t(b)h^\pm$ production followed by $h^+ \to t\bar{b}$ with large branching ratio [344]. With the $\tan\beta$ suppression, we estimate the upper limit implied by this search to be $M_{h^\pm} \lesssim 200\,\mathrm{GeV}$.

Important constraints on the model come from the Higgs couplings to EW bosons. The relevant couplings in the unitary gauge are:

$$\begin{aligned}
\mathcal{L}_{EW} &= ie\left[A^\mu + Z^\mu \cot 2\theta_W\right] h^+ \overleftrightarrow{\partial_\mu} h^- \\
&+ \frac{e}{\sin 2\theta_W}\left[\left(h\cos(\beta-\alpha) - H\sin(\beta-\alpha)\right)\overleftrightarrow{\partial_\mu}\,\eta_A\right] Z^\mu \\
&+ \frac{e}{2\sin\theta_W}\left[\left(\eta_A \pm ih\cos(\beta-\alpha) \mp iH\sin(\beta-\alpha)\right)\overleftrightarrow{\partial_\mu}\,h^\pm\right] W^{\mp\mu} \\
&+ \left[\left(eA_\mu + e\cot 2\theta_W Z_\mu\right)^2 + \frac{e^2}{2\sin^2\theta_W} W^{+\mu}W^-_\mu\right] h^+h^- \\
&+ \left[\frac{e^2}{\sin^2 2\theta_W} Z^\mu Z_\mu + \frac{e^2}{2\sin^2\theta_W} W^{+\mu}W^-_\mu\right] \\
&\quad \times \left[v(H\cos(\beta-\alpha) + h\sin(\beta-\alpha)) + \tfrac{1}{2}(H^2+h^2+\eta_A^2)\right]. \qquad (2)
\end{aligned}$$

Here, α is the angle diagonalizing the H-h mass matrix.

For small α and β, the gauge couplings of H are close to the SM in all cases that are measurable in the near future. Note the strong $Zh\eta_A$, $W^\pm h^\mp h$ and $W^\pm h^\mp \eta_A$ couplings, determined by gauge invariance. This presents an immediate problem for this 2HDM. For $B(h, \eta_A \to \mu^+\mu^-) \cong 1$,

$$\Gamma(Z \to h\eta_A \to \mu^+\mu^-\mu^+\mu^-) \cong \Gamma(Z \to h\eta_A) = \frac{2\alpha_{EM}\,p^3}{3M_Z^2\sin^2 2\theta_W}\cos^2(\beta-\alpha), \qquad (3)$$

where p is the momentum of h in the Z rest frame. For $M_h = M_{\eta_A} = 30\,\mathrm{GeV}$, this gives $B(Z \to 4\mu) \cong 0.0141$, about 3300 times larger that the measured branching ratio of $4.2 \times$

[1] This h–η degeneracy in 2HDM's with alignment was noticed earlier, in e.g. Ref. [342].

[2] Rates for the "Higgstrahlung" processes such as $Z \to Z^*h$ with $Z^* \to \bar{b}b$ and $h \to \mu^+\mu^-$ are 5–6 orders of magnitude smaller than $Z \to h\eta_A \to \bar{b}b\mu^+\mu^-$.

10^{-6} [158]. While it appears impossible to evade this problem in a 2HDM [338], it may be possible with the added flexibility of Higgs-fermion couplings in a 3HDM.[3]

The new Higgs bosons of the model are all in the mass range where they can easily be produced at the LHC. While no dedicated searches exist, measurements of final states containing muons have been made and may be expected to have sensitivity to this model, quite apart from the Z width issue. The main focus of this report is to use these measurements to limit the charged Higgs in the apparently allowed range $95\,\mathrm{GeV} < M_{h^\pm} < 200\,\mathrm{GeV}$. The signal processes to be tested are the Drell-Yan productions

$$\bar{q}q \;\rightarrow\; \gamma^*, Z^* \rightarrow h^+h^- \rightarrow \mu^+\mu^- + E_T^{\mathrm{miss}}, \tag{4}$$

$$\bar{q}q' \;\rightarrow\; W^* \rightarrow h^\pm h,\; h^\pm\eta_A \rightarrow \mu^\pm\mu^+\mu^- + E_T^{miss}. \tag{5}$$

In order to investigate the limits from the existing LHC measurements, we use the the Contour analysis tools described in the next section. The analysis itself is in Sec. 4.

3 Analysis Tools

The key tools for our analysis are the Herwig event generator [345, 346], the Rivet library of analysis routines [325], and the Contur comparison package [347].

Herwig simulates complete LHC events, starting from the matrix element for a hard scatter and including leading-logarithmic QCD partons showers, the conversion of partons into hadrons, hadronic decays and a simulation of the underlying event. An important feature for this analysis is the fact that it provides an interface to read in the Universal FeynRules Output (UFO [93]) files produced by the Feynrules [301] package used to encode the model, and incorporates the new matrix elements implied by the model into its event generator machinery. It then allows inclusive generation of any or all of the new particles and processes, along with SM contributions if desired. In this analysis we use Herwig 7.1.2 [348].

Rivet contains a library of analysis routines corresponding to published measurements made at colliders. Many of the analyses are provided by the experiments themselves. The majority of them are particle-level, differential cross sections made in a fiducial kinematic region. This means that the experiments have defined a measurement based on 'true' final state particles and have corrected for detector effects such as resolution and efficiency, but have not extrapolated beyond their acceptance. These measurements thus have a high degree of model independence. Rivet applies the same analysis as the experiment to generated final state particles, in our case from Herwig, and reproduces the measurements as histograms. Rivet also contains the published data and uncertainties, derived from HEPDATA [349], which can then be compared to the results from Herwig. In this analysis we use Rivet 2.5.4.

Contur takes the output of Rivet for a range of generated model parameters, and makes a statistical comparison between the prediction and the data. At present, the comparison made is between the data alone, and the data plus the generated BSM contribution. This approach will evaluate the room for new physics contributions which is left by the uncertainties on the measurement, under the assumption that the measurement is identical to the SM. Since all the measurements used have been shown to agree with the SM, this assumption is not unreasonable, although it neglects the theory uncertainties and will thus potentially give an over-aggressive exclusion limit when these are large, or if the data diverge from the SM. [4] The current aim of

[3] Lane and Pritchett are investigating the possibility of this.

[4] Planned future versions of Contur will allow direct comparison to the SM predictions, with their uncertainties.

Contur is to provide a rapid 'health check' for new physics models, to identify those regions already disfavoured by existing measurements.

4 Contur analysis: Limits on the charged Higgs mass

A key advantage of Herwig is that it is simple to select the inclusive production of any given particle, including the new particles introduced by the ALEPH dimuon model of Sec. 2. This capability is particularly well suited to the Contur approach, where all available measurements can be used simultaneously. This already led to the unexpected observation [347] that the precise measurements of vector bosons produced in association with jets have sensitivity to benchmark Dark Matter models. As we shall see shortly, it also leads to unexpected results in the current analysis.

As discussed above, events in which a Z boson decays into $h\eta_A$ produce copious 4-muon final states, inconsistent with the measured branching ratio [158]. For this reason we exclude those processes (assuming that a modified model may be constructed to suppress them). We focus on the charged sector of the model, requiring all events to have at least one charged Higgs — i.e., using Herwig to generate inclusive $h^\pm$ production. The dominant processes are h^+h^-, $h^\pm h$ and $h^\pm\eta_A$ production. As an additional constraint, for events which contain a W or a Z boson, only those W and Z decays involving an electron or a muon are generated. As we shall see, this gives conservative exclusion limits, as the events containing other decay channels of W bosons also have sensitivity.

We assume the primary data set of interest to be the leptonic "diboson" measurements, since the decays $h^\pm \to \mu^\pm\nu$ and $h, \eta_A \to \mu^+\mu^-$ will lead to contributions to $N\mu + E_T^{\text{miss}}$ final states, which will show up in the selections used in measurements aimed at the fully-leptonic W^+W^- and WZ diboson processes. The most relevant analysis available in Rivet is the ATLAS 8 TeV measurement [350]. The equivalent CMS analysis is not available, although its $H \to WW$ measurement [351] is, and was also included. The 7 TeV ATLAS measurements of the low-mass Drell-Yan process [352], $ZZ \to \mu^+\mu^- + E_T^{\text{miss}}$ [353] and fully-leptonic WW [354] are also available, and have some sensitivity. Since Herwig, Rivet and Contur are designed to generate and study all processes together with little additional overhead, several other measurements were also studied for potential sensitivity, most importantly the ATLAS measurement of the four-lepton line shape [355]. Other potentially useful measurements either have no significant sensitivity, or were not yet available in Rivet at the time of writing.

The W^+W^- measurement in the muon channel does indeed have sensitivity, excluding the model at the 97% c.l. for $M_{h^\pm} = 100$ GeV, though this sensitivity dies away at higher masses (13% by $M_{h^\pm} = 200$ GeV). But, the model is excluded at a confidence level greater than 99.9% over the otherwise allowed mass range 95 to 200 GeV discussed in Sec. 2 by the ATLAS four-lepton line shape. This may seem surprising, since the ATLAS measurement requires at least one lepton pair close to the Z mass ($50 < M_{ll} < 120$ GeV). However, the inclusive Herwig calculation reveals that, over the considered mass range, the by far dominant decay modes of the charged Higgs are $h^\pm \to hW^\pm$ and $h^\pm \to \eta_A W^\pm$, both at branching fractions close to 50%; also see Fig. 4. The near 100% decays of h or η_A to $\mu^+\mu^-$ give four muons per event. The $BR(W^\pm \to \mu^\pm\nu) = 10.6\%$ for decay to a muon or electron and a neutrino, mean that h^+h^- events can in fact contain up to six muons, (or four muons and an e^+e^- pair, or five muons and an electron); similarly, $h^\pm h$ and $h^\pm\eta_A$ events will mostly contain four muons and can contain up to five. In the absence of vetos on missing energy or

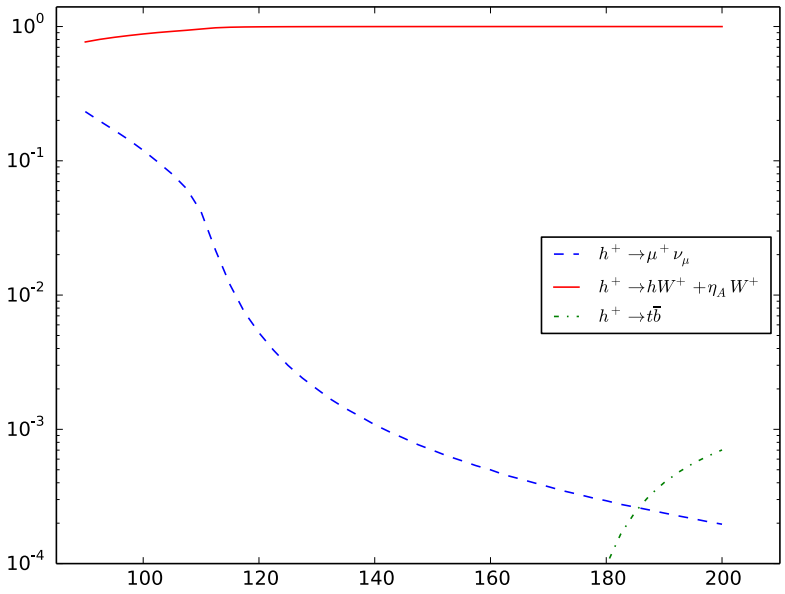

Figure 4: Decay branching ratios of the charged Higgs $h^\pm$ in Ref. [338] to $\mu^\pm\nu$, $W^\pm h$+$W^\pm\eta_A$ and to $t\bar{b}$. In the model of Ref. [338], the $h^+ \to t\bar{b}$ decay rate is suppressed from its SM value by $\tan^2\beta \simeq 1/400$.

if additional leptons within the rapidity acceptance do not exceed the veto thresholds (7 GeV for muons, 6 GeV for electrons), all these final states can potentially contribute to either a 4μ or $2\mu 2e$ final state. In fact, parton luminosities and phase space considerations ($M_h = M_{\eta_A} = 30\,\text{GeV} \ll M_{h^\pm} = 100$–$200\,\text{GeV}$) imply that the dominant processes being excluded are $u\bar{d}$, $c\bar{s} \to W^{+*} \to h^+h$, $h^+\eta_A \to W^+hh$, $W^+h\eta_A$, $W^+\eta_A\eta_A \to W^+ + 4\mu$. This is borne out by Fig. 5.

We note that the measurement includes the four-electron channels, for which there will be no contribution from our model. This illustrates a feature likely to be common in such studies: while from a SM point of view the combination is of most interest, since the events predominantly involve Z/γ propagators; the muon-only measurement, produced without a combination with electrons, would often be even more sensitive to BSM physics.

While individual pairs of the muons produced in the model primarily come from either low mass h or η_A decays, and other pairings have no mass peak, the high multiplicity and high cross section mean that many events pass the fiducial selection given in Table 2 of Ref. [355] and implemented in Rivet.

As noted above, the muons for events passing the analysis cuts come mainly from the decays of pairs of h and/or η_A; leptons from W decay make only a small contribution. Therefore, the other decays of W bosons, to jets and $\tau\nu$ — which were not generated in this analysis — are expected to add even further exclusion, since there is no jet veto in the ATLAS analysis.

The mass distributions in Fig. 5 are made after the application of the mass and lepton p_T selections, but before any selection on the p_T of the Z bosonss or the ΔR between leptons. They show the effect of the ATLAS muon selection that defines the fiducial cross section. In a multi-muon event, the muons are paired according to how close the mass of the pair is to the Z mass - the "leading" pair is the closest. The "alternative" pairings are those not selected by the ATLAS algorithm, and exhibit the 30 GeV mass peak expected from h and η_A decays. Whenever either

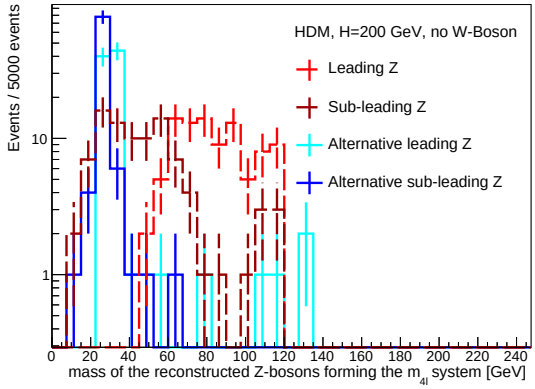

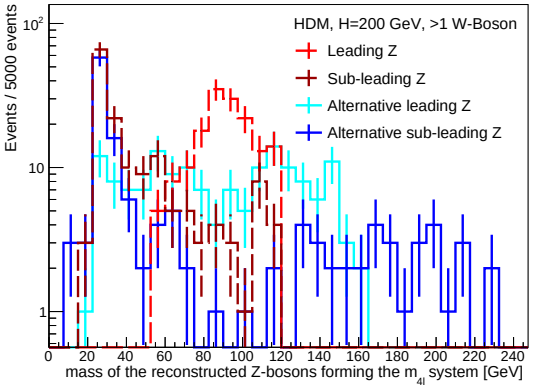

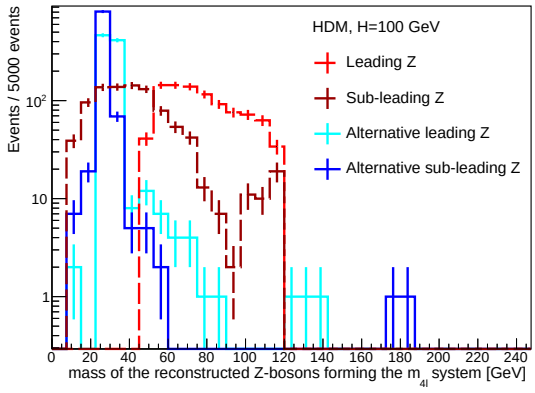

Figure 5: Di-lepton mass distributions for a sample of 5000 generated events passing the four-lepton selection cuts. Upper left: for $M_{h^\pm} = 100\,\text{GeV}$, practically all events have all four muons coming from the h or η_A decay; upper right: for $M_{h^\pm} = 200\,\text{GeV}$, those events which have all four muons coming from the h or η_A decay are shown; lower left: for $M_{h^\pm} = 200\,\text{GeV}$, those events which have one muon coming from a W decay are shown. The peaks at 30 GeV are due to the model's $h, \eta_A \to \mu^+\mu^-$.

of the alternative pairings has a mass differing from 30 GeV, this implies that at least one of the leptons used to form the pair does not come directly from a h or η_A decay. As demonstrated in Fig. 5, only half the events at $M_{h^\pm} = 200\,\text{GeV}$ have one lepton not coming from either the h or η_A decay and being off-peak. There are no off-peak events for $M_{h^\pm} = 100\,\text{GeV}$.

The comparisons to data, which give the exclusions, are shown in Figs. 6 and 7 for $M_{h^\pm} = 100\,\text{GeV}$ and $200\,\text{GeV}$.

5 Conclusions

The two Higgs-doublet model considered here leads to large contributions to already-measured differential cross sections. Even bearing in mind that the current incarnation of Contur does not fully take into account theoretical uncertainties on the SM predictions, the effects of this model would be so large that it can be considered ruled out. Other explanations for the ALEPH dimuon excess must be sought. More generally, this study demonstrates the power of precision cross-section measurements at LHC in terms of constraining BSM physics, when such measurements are made with as few theoretical assumptions as possible. It hopefully helps motivate a redoubling of efforts to produce such measurements, made in fiducial regions and based on final-state particles, as the LHC continues to survey physics above the electroweak symmetry-breaking scale.

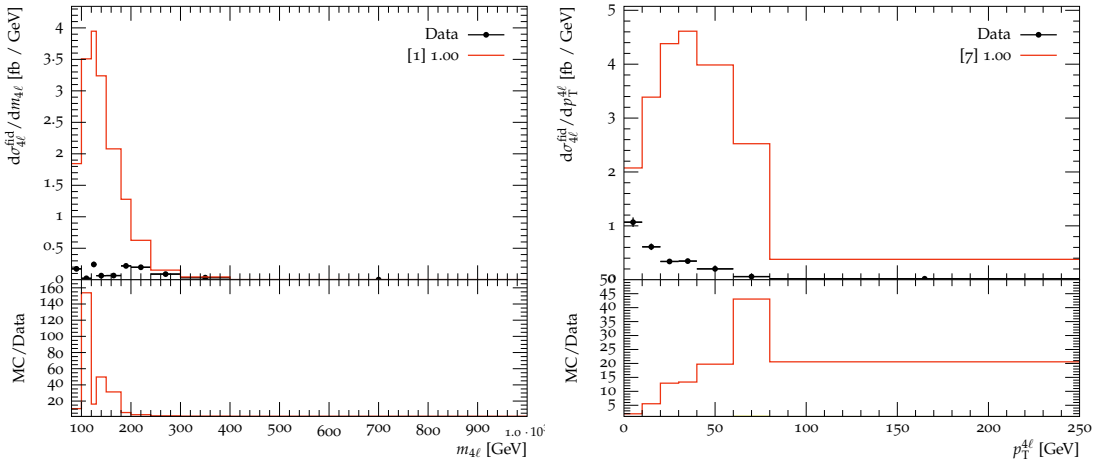

Figure 6: Projection of the contribution of our model, for $M_{h^\pm} = 100$ GeV, on to the ATLAS four-lepton differential cross-section mass measurement (left) and transverse momentum of the four-lepton system (right). Black points indicate the data, the red upper histogram is the data+BSM. The lower sections of the plots show the ratio of (data+BSM)/data. The uncertainty in the measurement is suppressed by the axis scale. The numbers in the legend show the bin number of the most powerful bin, and the exclusion from that bin expressed as a probability.

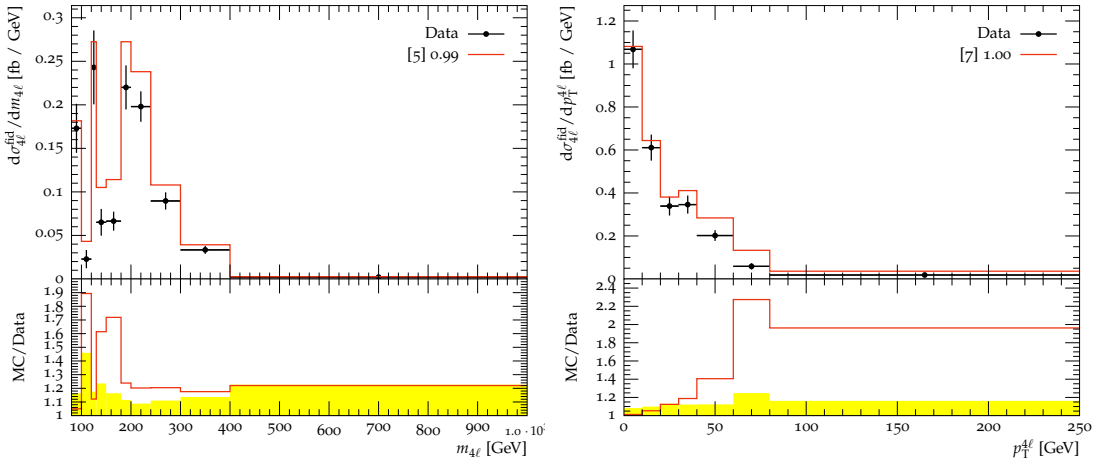

Figure 7: As in Fig.6, but for $M_{h^\pm} = 200$ GeV. The yellow error band indicates the uncertainty on the measurement.

Acknowledgments

We thank the organizers and conveners of the Les Houches workshop, "Physics at TeV Colliders", for a stimulating meeting. We also thank T. Hryn'ova for a valuable suggestion that helped initiate this study. K. Lane thanks A. Heister for many informative discussions on the ALEPH dimuon data. He also thanks the Laboratoire d'Annecy-le-Vieux de Physique Théorique (LAPTh) and the CERN Theory Group for their support and hospitality during the initial stage of this research. This work has received funding from the European Union's Horizon 2020 research and innovation programme as part of the Marie Sklodowska-Curie Innovative Training Network MCnetITN3 (grant agreement no. 722104) and ERC Grant Agreement no.

715871.

Contribution 15

Collider constraints on light pseudoscalars

U. Haisch, J. F. Kamenik, A. Malinauskas, M. Spira

Abstract

We investigate the bounds on light pseudoscalars that arise from a variety of collider searches. Special attention is thereby devoted to the mass regions $[3, 5]\,\mathrm{GeV}$ and $[9, 11]\,\mathrm{GeV}$, in which a meaningful theoretical description has to include estimates of non-perturbative effects such as the mixing of the pseudoscalar with QCD bound states. A compendium of formulas that allows to deal with the relevant corrections is provided. It should prove useful for the interpretation of future LHC searches for light CP-odd spin-0 states.

1 INTRODUCTION

The most significant achievement of the LHC Run-I physics programme has been the discovery of a new spin-0 resonance (h) with a mass of $125\,\mathrm{GeV}$ and with properties consistent with that of the standard model (SM) Higgs boson [260–262]. Besides precision measurements of processes involving a h, the LHC Higgs physics programme however also includes a wide spectrum of searches for additional Higgses (a summary of LHC Run-I results can be found in [356] for instance). Such states are predicted in many SM extensions such as supersymmetry or models where the Higgs is realised as a pseudo Nambu-Goldstone boson (PNGB) of a new approximate global symmetry.

In fact, if the extended electroweak (EW) symmetry breaking sector contains a PNGB, this state can be significantly lighter than the other spin-0 particles. A well-known example of a model that includes a light pseudoscalar (a) is provided by the next-to-minimal supersymmetric SM (NMSSM) where this state can arise as a result of an approximate global $U(1)_R$ symmetry [357]. Since in this case the amount of symmetry breaking turns out to be proportional to soft breaking trilinear terms, the mass of the a can naturally be less than half of the SM Higgs mass, if the trilinear terms are dialled to take values in the GeV range. Non-supersymmetric theories that can feature a light pseudoscalar are, to just name a few, simplified models where a complex singlet scalar is coupled to the Higgs potential of the SM or the two-Higgs doublet model (2HDM), Little Higgs models and hidden valley scenarios (see [358] and references therein for details).

Irrespectively of the precise ultraviolet (UV) realisation, a light pseudoscalar can lead to distinctive collider signatures. The most obvious consequence are exotic decays of the SM Higgs, namely $h \to aa$ for $m_a < m_h/2$ [359, 360] and $h \to aZ$ for $m_a < m_h - m_Z$ [358, 361]. Another feature that can have important phenomenological implications is that in the presence of the heavy-quark transition $a \to b\bar{b}$ ($a \to c\bar{c}$) the pseudoscalar a can mix with bottomonium (charmonium) bound states with matching quantum numbers [362–368].

LHC searches for $h \to aa$ have been performed in the 4μ [369, 370], 4τ [371, 372],

$2\mu 2\tau$ [372] and $2\mu 2b$ [372] final states. The obtained results have been used to set upper bounds on the $h \to aa$ branching ratio in 2HDMs with an extra complex singlet (2HDM+S) for pseudoscalar masses in the range of $[1, 62.5]\,\text{GeV}$. The analyses [369,371,372] however all exclude m_a values in the regions $[3, 5]\,\text{GeV}$ and $[9, 11]\,\text{GeV}$ for which a–η_c and a–η_b mixing effects as well as open flavour decays to D and $B_{(s)}$ meson pairs can be potentially important.

The main goal of this work is to extend the latter results to the $c\bar{c}$ and $b\bar{b}$ threshold regions by including effects that cannot be properly described in the partonic picture. In order to highlight the complementarity of different search strategies for a light a, we also compare our improved limits to other bounds on the 2HDM+S parameter space that derive from the LHC searches for $h \to Z_d Z \to 4\ell$ [373], $h \to Z_d Z \to 2\mu 2\ell$ [374], $pp \to a \to \mu^+\mu^-$ [375, 376], $pp \to ab\bar{b}$ followed by $a \to \tau^+\tau^-$ [377] or $a \to \mu^+\mu^-$ [378], $pp \to a \to \gamma\gamma$ [379, 380], $pp \to a \to \tau^+\tau^-$ [381], from the BaBar analyses of radiative Υ decays [382–384] and from the LHCb measurements of the production of Υ mesons [367, 385] as well as the inclusive dimuon cross section [386, 387].

This article is organised as follows. In Section 2 we briefly recall the structure of the 2HDM+S scenarios. Our recast of the results [369,371,372] is presented in Section 3, where we also derive the constraints on the 2HDM+S parameter space that follow from the measurements and prosposals [367, 373–387]. We conclude in Section 4. The formulas necessary to calculate the partial decay widths of the pseudoscalar a are collected in Appendix A, while Appendix B contains a concise discussion of the mixing formalism and of open flavour decays that are relevant in the vicinity of the $b\bar{b}$ and $c\bar{c}$ thresholds.

2 THEORETICAL FRAMEWORK

In the following section we will interpret various searches for light pseudoscalars in the context of 2HDM+S scenarios. In this class of models a complex scalar singlet S is added to the 2HDM Higgs potential (see e.g. [341, 388] for 2HDM reviews). The field S couples only to the two Higgs doublets $H_{1,2}$ but has no direct Yukawa couplings, acquiring all of its couplings to SM fermions through its mixing with the Higgs doublets. A light pseudoscalar a can arise in such a setup from the admixture of the 2HDM pseudoscalar A and the imaginary part of the complex singlet S. The corresponding mixing angle will be denoted by θ, and defined such that for $\theta \to 0$ the mass eigenstate a becomes exactly singlet-like.

To eliminate phenomenologically dangerous tree-level flavour-changing neutral currents (FCNCs) the Yukawa interactions that involve the Higgs fields $H_{1,2}$ have to satisfy the natural flavour conservation hypothesis [389, 390]. Depending on which fermions couple to which doublet, one can divide the resulting 2HDMs into four different types. In all four cases the Yukawa couplings between the pseudoscalar a and the SM fermions take the generic form

$$\mathcal{L} \supset -\sum_f \frac{y_f}{\sqrt{2}}\, i\xi_f^{\text{M}}\, \bar{f}\gamma_5 f\, a\,. \tag{1}$$

Here $y_f = \sqrt{2}m_f/v$ denote the SM Yukawa couplings and $v \simeq 246\,\text{GeV}$ is the EW vacuum expectation value. The parameters ξ_f^{M} encode the dependence on the 2HDM Yukawa sector and the factors relevant for the further discussion are given in Table 1. In this table the shorthand notations $s_\theta = \sin\theta$ and $t_\beta = \tan\beta$ have been used. Similar abbreviations will also be used in what follows.

In the presence of (1) the CP-odd scalar a can decay into fermions at tree level and into

type	I	II	III	IV
up-type quarks	s_θ/t_β	s_θ/t_β	s_θ/t_β	s_θ/t_β
down-type quarks	$-s_\theta/t_\beta$	$s_\theta t_\beta$	$-s_\theta/t_\beta$	$s_\theta t_\beta$
charged leptons	$-s_\theta/t_\beta$	$s_\theta t_\beta$	$s_\theta t_\beta$	$-s_\theta/t_\beta$

Table 1: Ratios ξ_f^{M} of the Yukawa couplings of the pseudoscalar a relative to those of the SM Higgs in the four types of 2HDM+S models without tree-level FCNCs.

gluons, photons and EW gauge bosons at loop level. The expressions for the partial decay widths $\Gamma(a \to XX)$ that we employ in our study are given in Appendix A. Since in this work we will assume that the a is lighter than the W, Z, h and the other 2HDM Higgs mass eigenstates H, A, $H^\pm$, decays of the a into the latter states are kinematically forbidden.

If the a is sufficiently light, exotic decays of the SM Higgs into the two final states aZ and aa are however possible. The partial decay width $\Gamma(h \to aZ)$ is in 2HDM+S scenarios entirely fixed by the 2HDM parameters α, β and the mixing angle θ. Explicitly, one has at tree level

$$\Gamma(h \to aZ) = \frac{g_{haZ}^2}{16\pi} \frac{m_h^3}{v^2} \lambda^3\left(m_h^2, m_a^2, m_Z^2\right) , \tag{2}$$

with

$$g_{haZ} = c_{\beta-\alpha}\, s_\theta \,, \tag{3}$$

and

$$\lambda(x,y,z) = \sqrt{1 - \frac{2\,(y+z)}{x} + \frac{(y-z)^2}{x^2}} \,. \tag{4}$$

Notice that in the exact alignment/decoupling limit, i.e. $\alpha = \beta - \pi/2$, in which the lighter CP-even spin-0 state h of the 2HDM becomes fully SM-like, the coupling g_{haZ} and thus $\Gamma(h \to aZ)$ is precisely zero. However, given that the total decay width of the SM Higgs is only about $4\,\mathrm{MeV}$, the process $h \to aZ$ can be important even if deviations from the alignment/decoupling limit are relatively small.

Unlike g_{haZ}, the triple Higgs coupling g_{haa} depends not only on the physical Higgs masses and mixing angles but also on some of the trilinear couplings that appear in the full scalar potential. This feature makes the partial decay width $\Gamma(h \to aa)$ model dependent, and in consequence the two exotic branching ratios $\mathrm{BR}(h \to aZ)$ and $\mathrm{BR}(h \to aa)$ can be adjusted freely by an appropriate choice of parameters. Following this philosophy we will treat $\mathrm{BR}(h \to aZ)$ and $\mathrm{BR}(h \to aa)$ as free parameters in the remainder of this article.

3 NUMERICAL RESULTS

We begin our numerical analysis by interpreting the recent CMS results [369, 371, 372] for the exotic SM Higgs decay $h \to aa$ in the 2HDM+S context. The final states that we consider are 4μ [369], 4τ [371, 372], $2\mu 2\tau$ [372] and $2\mu 2b$ [372]. These searches probe m_a values in the range $[0.25, 3.55]\,\mathrm{GeV}$, $[4, 8]\,\mathrm{GeV}$, $[5, 15]\,\mathrm{GeV}$, $[15, 62.5]\,\mathrm{GeV}$ and $[25, 62.5]\,\mathrm{GeV}$, respectively. To facilitate a comparison between the results obtained by the CMS collaboration and by us, we consider like [372] the following four 2HDM+S benchmark scenarios: the type I model with $t_\beta = 1$, the type II model with $t_\beta = 2$, the type III model with $t_\beta = 5$ and the type IV model with $t_\beta = 0.5$. The fermionic coupling factors ξ_f^{M} corresponding to each 2HDM+S

type are reported in Table 1. It is important to realise that the s_θ-dependence of $\xi_f^{\rm M}$ cancels in $\mathrm{BR}(a \to XX)$ and it is thus possible to translate constraints on signal strengths such as $\sigma(pp \to h)\,\mathrm{BR}(h \to aa)\,\mathrm{BR}^2(a \to \mu^+\mu^-)$ into s_θ-independent bounds on $\mu_h\,\mathrm{BR}(h \to aa)$. Here we have defined $\mu_h = \sigma(pp \to h)/\sigma(pp \to h)_{\rm SM}$.

The results of our recast are shown in the panels of Fig. 1 and should be compared to the exclusion plots displayed in Fig. 8 of [372]. The branching ratios $\mathrm{BR}(a \to XX)$ used to interpret the results in the four particular 2HDM+S scenarios are calculated using the formulas given in Appendix A and include the mixing and threshold effects described in Appendix B. Notice that the inclusion of a–η_c and a–η_b mixing is crucial to obtain meaningful predictions in the m_a regions $[3, 5]\,\mathrm{GeV}$ and $[9, 11]\,\mathrm{GeV}$, which are left unexplored in the CMS analysis [372].

While overall we observe good agreement between the 95% confidence level (CL) exclusions set by CMS and by us, some differences in the derived limits are evident. Firstly, our analysis covers the mass region close to the $c\bar{c}$ ($b\bar{b}$) threshold, where our limits display a resonance-like behaviour as a result of the mixing of the a with the three η_c (six η_b) states included in our study. Second, in the m_a range of $[1, 3]\,\mathrm{GeV}$ our bounds on $\mu_h\,\mathrm{BR}(h \to aa)$ tend to be somewhat weaker than those derived in [372]. The observed difference is again a consequence of the mixing of the a with QCD bound states. In fact, in the very low mass range the total decay width of the unmixed a is below $10^{-3}\,\mathrm{MeV}$ in the considered 2HDM+S scenarios, while that of the lightest η_c state amounts to around $30\,\mathrm{MeV}$ [158]. Hence even a small η_c-admixture in the mass eigenstate a can lead to an enhanced total decay width Γ_a which in turn results in a suppression of $\mathrm{BR}(a \to \mu^+\mu^-)$ and a weakening of the bound on $\mu_h\,\mathrm{BR}(h \to aa)$.

A light pseudoscalar a can also be searched for via the decay $h \to aZ$. The only LHC analyses that presently can be used to set bounds on $\mathrm{BR}(h \to aZ)$ are the ATLAS searches for new dark bosons Z_d produced in $h \to Z_dZ$ [373, 374]. Notice that while the Z_d decays democratically into electrons and muons in the case of the a one has $\Gamma(a \to e^+e^-)/\Gamma(a \to \mu^+\mu^-) = m_e^2/m_\mu^2 \simeq 2 \cdot 10^{-5}$. As a result $4e$ and $2e2\mu$ events originating from $h \to aZ \to 4e$ and $h \to aZ \to 2e2\mu$ give essentially no contribution to the signal strength in $pp \to h \to aZ \to 4\ell$. The $8\,\mathrm{TeV}$ ATLAS study [373] however only provides exclusion bounds on $\mathrm{BR}(h \to Z_dZ \to 4\ell)$ from a combination of final states. To correct for this mismatch we have calculated $r_{\mathcal{A}\varepsilon} = \sum_{X=4\mu,2\mu2e} \mathcal{A}\varepsilon_X / \sum_{X=4\mu,4e,2e2\mu,2\mu2e} \mathcal{A}\varepsilon_X$, where $\mathcal{A}\varepsilon_X$ denotes the product of acceptance and reconstruction efficiency in the final state X — the values for $\mathcal{A}\varepsilon_X$ can be found in the auxiliary material of [373]. We find that $r_{\mathcal{A}\varepsilon}$ has only a mild dependence on m_a and amounts to around 60%. The actual limits are then obtained by equating $r_{\mathcal{A}\varepsilon}\,\mathrm{BR}(h \to aZ)\,\mathrm{BR}(a \to \mu^+\mu^-)\,\mathrm{BR}(Z \to \ell^+\ell^-) = \mathrm{BR}(h \to Z_dZ \to 4\ell)$ and solving for $\mathrm{BR}(h \to aZ)$. To improve upon this naive recast one would need individual bounds for the different combinations of final-state lepton flavours. In fact, the very recent $13\,\mathrm{TeV}$ ATLAS analysis [374] provides $\mathcal{A}\varepsilon_{2\mu2\ell}$ as well as limits on the relevant fiducial cross section. Our recast of the latter results thus only has to rely on the assumption that the product $\mathcal{A}\varepsilon_{2\mu2\ell}$ is roughly the same for the Z_d model and the 2HDM+S scenario, which we indeed believe to be the case.

The exclusion limits on $\mu_h\,\mathrm{BR}(h \to aZ)$ corresponding to the four 2HDM+S benchmark scenarios discussed earlier are presented in Fig. 2. From the panels it is evident that, apart from pseudoscalar masses around $25\,\mathrm{GeV}$ where the data [374] has a local deficit, the constraints that derive from the $13\,\mathrm{TeV}$ analysis [374] are significantly stronger than those that one obtains from the $8\,\mathrm{TeV}$ data [373]. One also observes that the constraints in the first and second benchmark are weak as they just start to probe the region $\mu_h\,\mathrm{BR}(h \to aZ) \lesssim 1$, whereas in the third and fourth 2HDM+S scenario already values of $\mu_h\,\mathrm{BR}(h \to aZ) \lesssim 0.1$ can be probed with the

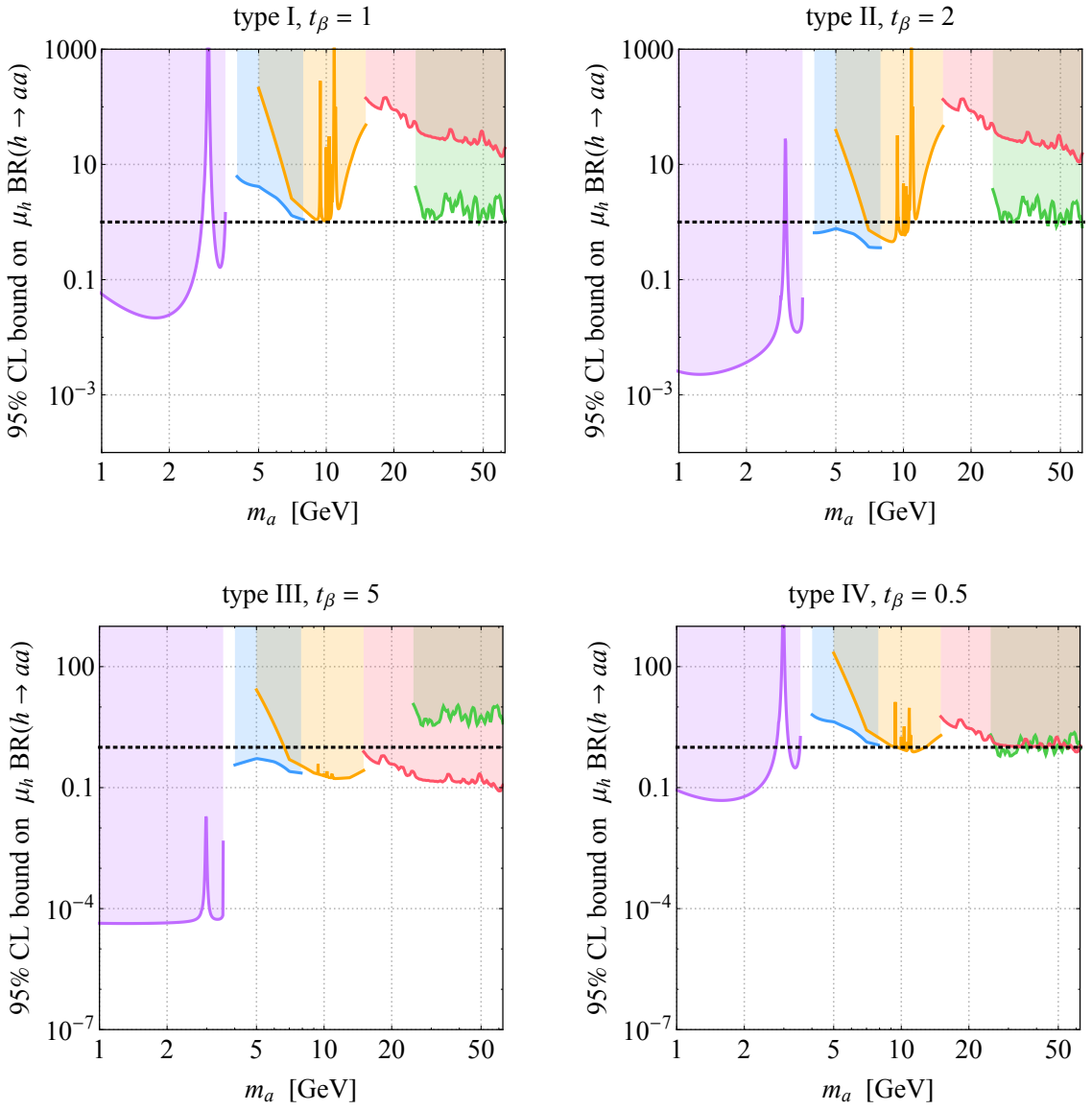

Figure 1: Limits on $\mu_h \,\mathrm{BR}(h \to aa)$ in the 2HDM+S of type I with $t_\beta = 1$ (top left), type II with $t_\beta = 2$ (top right), type III with $t_\beta = 5$ (bottom left) and type IV with $t_\beta = 0.5$ (bottom right). The purple, blue, orange, red and green exclusions correspond to the search for $h \to aa \to 4\mu$ [369], $h \to aa \to 4\tau$ [371], $h \to aa \to 4\tau$ [372], $h \to aa \to 2\mu 2\tau$ [372] and $h \to aa \to 2\mu 2b$ [372], respectively. The dashed black lines indicate $\mu_h \,\mathrm{BR}(h \to aa) = 1$ and all coloured regions are excluded at 95% CL.

available LHC data sets. Since the asymmetry between electron and muon final states from $h \to aZ$ decays is a striking signature of a light pseudoscalar, we strongly encourage our experimental colleagues to provide as in [374] separate bounds for the $2e2\ell$ and $2\mu 2\ell$ final states in future searches for signatures of the type $h \to Z_d Z \to 4\ell$.

Constraints on the parameter space of the four different types of 2HDM+S scenarios can finally be derived from the LHC searches for $pp \to a \to \mu^+\mu^-$ [375, 376], $pp \to ab\bar{b} \to \tau^+\tau^- b\bar{b}$ [377] or $pp \to ab\bar{b} \to \mu^+\mu^- b\bar{b}$ [378], $pp \to a \to \gamma\gamma$ [379], $pp \to a \to \tau^+\tau^-$ [381], from the studies of $\Upsilon \to a\gamma$ decays performed at BaBar [382–384] and from the LHCb mea-

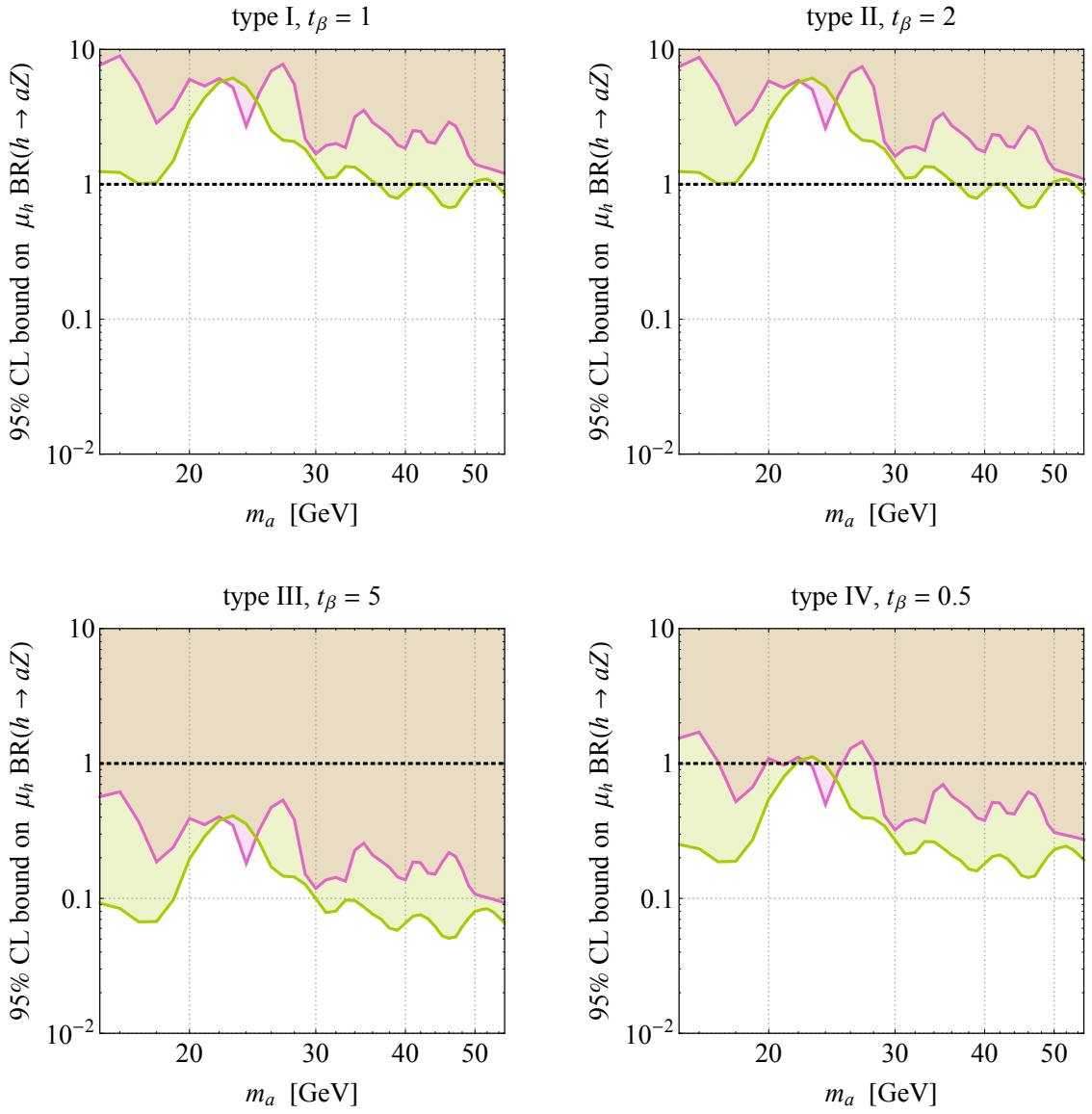

Figure 2: Limits on $\mu_h \,\mathrm{BR}(h \to aZ)$ in the 2HDM+S of type I with $t_\beta = 1$ (top left), type II with $t_\beta = 2$ (top right), type III with $t_\beta = 5$ (bottom left) and type IV with $t_\beta = 0.5$ (bottom right). The red and green bounds correspond to the ATLAS search for $pp \to h \to Z_d Z \to 4\ell$ [373] and $pp \to h \to Z_d Z \to 2\mu 2\ell$ [374], respectively. The dashed black lines indicate $\mu_h \,\mathrm{BR}(h \to aZ) = 1$ and all coloured regions are excluded at 95% CL.

surements of Υ production [367,385] as well as of the inclusive dimuon cross section [386,387]. Since these search strategies all rely on the production of a pseudoscalar a the resulting constraints all scale as s_θ^2. For a given type of 2HDM+S model and a fixed value of t_β, the measurements [375–379, 381–384, 387] can therefore be used to set limits on $|s_\theta|$ as a function of the pseudoscalar mass m_a.

For concreteness we study the same four 2HDM+S scenarios that we have already considered before. The most stringent limits on $|s_\theta|$ that can be derived at present are displayed in Fig. 3. In order to recast the results of the CMS searches for $a \to \mu^+\mu^-$ [376], $pp \to ab\bar{b} \to \tau^+\tau^- b\bar{b}$ [377], $pp \to a \to \gamma\gamma$ [379], $pp \to a \to \tau^+\tau^-$ [381], the LHCb measurements of

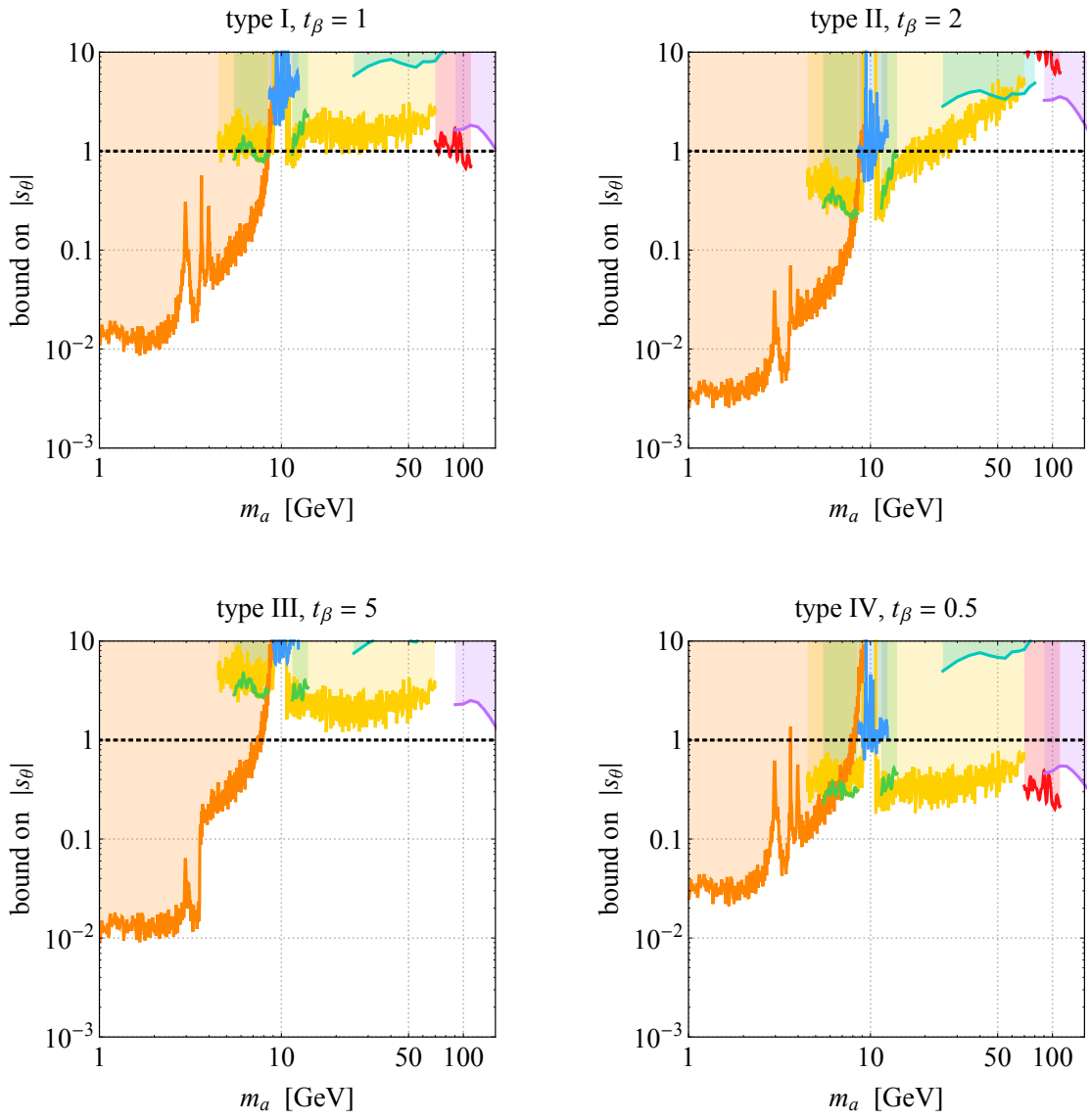

Figure 3: Limits on $|s_\theta|$ in the 2HDM+S of type I with $t_\beta = 1$ (top left), type II with $t_\beta = 2$ (top right), type III with $t_\beta = 5$ (bottom left) and type IV with $t_\beta = 0.5$ (bottom right). The green, turquoise, red, purple, orange, blue and yellow exclusions correspond to the searches for $a \to \mu^+\mu^-$ [376], $pp \to ab\bar{b} \to \tau^+\tau^- b\bar{b}$ [377], $pp \to a \to \gamma\gamma$ [379], $pp \to a \to \tau^+\tau^-$ [381] and $\Upsilon(1S) \to a\gamma \to \mu^+\mu^-\gamma$ [383], the measurements of Υ production [367, 385] and the inclusive dimuon cross section [387], respectively. The dashed black lines indicate $|s_\theta| = 1$ and all coloured regions are excluded at 95% CL apart from the orange and yellow contours which only hold at 90% CL.

Υ production [367, 385] and the inclusive dimuon cross section [387], one needs to know the production cross sections of a light a in gluon-fusion and in association with $b\bar{b}$ pairs. Our predictions for $gg \to a$ production are obtained at next-to-next-to-leading order in QCD using `HIGLU` [391], while the $pp \to ab\bar{b}$ cross sections are calculated at next-to-leading order (NLO) in QCD in the four-flavour scheme with `MadGraph5_aMCNLO` [95] employing an `UFO` implementation [93] of the 2HDM model discussed in the publication [151].

Our recast of the results of the LHCb search for dark photons A' [387] proceeds as fol-

lows. We calculate the inclusive $pp \to A'$ production cross section at NLO in QCD using `MadGraph5_aMCNLO` [95], while we extract $\mathrm{BR}(A' \to \mu^+\mu^-)$ from the well-measured cross section ratio $R = \sigma(e^+e^- \to \text{hadrons})/\sigma(e^+e^- \to \mu^+\mu^-)$ [158]. Following [386, 387], model-dependent A'–Z mixing effects are included in our calculation employing the formulas given in [392]. We have also taken into account detector acceptance differences between $pp \to A' \to \mu^+\mu^-$ and $pp \to a \to \mu^+\mu^-$ by computing the ratio $r_{\mathcal{A}} = \mathcal{A}_a/\mathcal{A}_{A'}$ of signal acceptances. We find that $r_{\mathcal{A}}$ amounts to around 2.0, 1.3, 1.0 at $m_a = 5\,\mathrm{GeV}, 15\,\mathrm{GeV}, 70\,\mathrm{GeV}$ and scales approximately linear between the quoted m_a values. Concerning the detection efficiencies $\varepsilon_{A'}$ and ε_a we assume that they are identical for $A' \to \mu^+\mu^-$ and $a \to \mu^+\mu^-$, which should be a good approximation when the dimuon signal is prompt [387]. We finally add that in our recast of the LHCb dark photon results, we only consider the mass region $m_a > 4.5\,\mathrm{GeV}$ to avoid a–η_c mixing contributions to the $pp \to a$ cross section associated to $pp \to \eta_c$ production. The mass region $m_a \in [9.1, 10.6]\,\mathrm{GeV}$ is also not covered by our recast, because in [387] the LHCb collaboration does not present bounds on the kinetic mixing of the A' close to the $b\bar{b}$ threshold.

The main conclusion that can be drawn from the results presented in Fig. 3 is that only in the 2HDM+S scenario of type IV with $t_\beta = 0.5$ it is possible to set physical meaningful bounds on the sine of the mixing angle θ, i.e. $|s_\theta| < 1$, over the entire range of studied pseudoscalar masses. One furthermore observes that solely the BaBar search for the radiative decay $\Upsilon(1S) \to a\gamma \to \mu^+\mu^-\gamma$ [383] allows to probe parameter regions with $|s_\theta| < 0.1$. This search is however kinematically limited to $m_a < m_{\Upsilon(1S)} \simeq 9.5\,\mathrm{GeV}$. Improvements in the existing LHC search strategies (and/or new approaches) are needed to reach the same sensitivity on $|s_\theta|$ for pseudoscalar masses above around $10\,\mathrm{GeV}$ in the examined 2HDM+S benchmark models. Measurements of the inclusive dimuon cross section [386, 387] seem to be quite promising in this context.

4 CONCLUSIONS

Beyond the SM theories with an extended Higgs sector can naturally lead to pseudoscalar resonances with masses significantly below the EW scale if these states serve as PNGBs of an approximate global $U(1)$ symmetry. The R-symmetry limit in the NMSSM and the case of spontaneously broken $U(1)$ subgroups in Little Higgs models are just two working examples of this general idea. Searches for light CP-odd spin-0 states are thus theoretically well-motivated and in the case of a detection could help to illuminate the structure and dynamics of the underlying UV model.

The existing collider searches for pseudoscalars with masses of approximately $[1, 100]\,\mathrm{GeV}$ fall into two different classes. Firstly, searches that look for the presence of a light a in the decay of a SM particle. Searches for $h \to aa$ and $h \to aZ$, but also the radiative decays $\Upsilon \to a\gamma$ belong to this category. In the case of the exotic Higgs decays the resulting signature that the ATLAS and CMS experiments have explored are four-fermion final states containing at least two opposite-sign leptons [369–374], while what concerns the radiative Υ decays, BaBar has considered the hadronic, dimuon and ditau decays of pseudoscalars [382–384]. The second type of searches instead relies on the direct production of the a in pp collisions and its subsequent decays to either charged lepton or photon pairs. Both the gluon-fusion channel [367, 375, 376, 379–381, 385] and $ab\bar{b}$ production [377, 378] have so far been exploited to look for light pseudoscalars at the LHC in this way.

In this work, we have performed a global analysis of the present collider constraints on light pseudoscalar states. To facilitate a comparison with the recent CMS study [372], we have considered the class of 2HDM+S models, treating the parameters t_β and s_θ as well as the branching ratios $\mathrm{BR}(h \to aa)$ and $\mathrm{BR}(h \to aZ)$ as free parameters — see Section 2 for a concise introduction to the 2HDM+S setup. A complication that arises in our analysis is that in the mass regions $[3, 5]\,\mathrm{GeV}$ and $[9, 11]\,\mathrm{GeV}$, non-perturbative effects such as the mixing of the pseudoscalar with QCD bound states have to be taken into account to allow for a meaningful interpretation of the experimental data. We have worked out the theoretical formalism necessary to calculate the most relevant short-distance and long-distance effects and provide a collection of the corresponding formulas in the two Appendices A and B.

Our numerical analysis consists of three parts. In the first part, we have derive 95% CL exclusion limits on the signal strength $\mu_h\,\mathrm{BR}(h \to aa)$ that follow from the latest CMS searches for the exotic $h \to aa$ decay [369–372], while in the second part we present the limits on $\mu_h\,\mathrm{BR}(h \to aZ)$ that stem from the ATLAS searches for $h \to Z_d Z \to 4\ell$ [373] and $h \to Z_d Z \to 2\mu 2\ell$ [374]. The exclusion bounds on $|s_\theta|$ that arise from the searches [367, 376, 377, 379, 381, 383, 385, 387] are finally derived in the third part of our numerical study. In all three cases, we have considered four specific 2HDM+S benchmark scenarios that differ in the choice of Yukawa sector and t_β. We have found that the inclusion of a–η_c $\left(a\text{–}\eta_b\right)$ mixing effects as well as open flavour decays to D $\left(B_{(s)}\right)$ meson pairs has a visible impact on the obtained limits only in the mass region of approximately $[1, 4]\,\mathrm{GeV}$ $\left([10, 15]\,\mathrm{GeV}\right)$, while perturbative calculations are perfectly adequate for m_a values away from the $c\bar{c}$ and $b\bar{b}$ thresholds.

The main conclusion that can be drawn from the results presented in Figs. 1, 2 and 3 is that existing collider constraints on the parameter space of 2HDM+S models are in general not very strong. Exceptions are the $[1, 3]\,\mathrm{GeV}$ region in which $\mu_h\mathrm{BR}(h \to aa)$ is well-constrained by the CMS search for $h \to aa \to 4\mu$ [369] and the $[1, 9.5]\,\mathrm{GeV}$ range where the $\Upsilon(1S) \to a\gamma \to \mu^+\mu^-\gamma$ search of BaBar [383] provides stringent limits on $|s_\theta|$. Much to the opposite, the 2HDM+S parameter space turns out to be least constrained for m_a values in the range of approximately $[15, 70]\,\mathrm{GeV}$. The development of improved or new search techniques (such as for instance dedicated searches for $h \to aZ$ [374] and inclusive diphoton [380] or dimuon [386, 387] cross section measurements) that specifically focus on the latter mass region therefore seems to be a worthwhile scientific goal.

ACKNOWLEDGEMENTS

We are grateful to Kai Schmidt-Hoberg for providing details on the estimate of $\Gamma(a \to KK\pi)$ as given in [393]. We furthermore thank Ulrich Ellwanger, Filippo Sala, Dominik Stöckinger and Mike Williams for their interest in our work, constructive feedback and their useful suggestions. UH appreciates the continued hospitality and support of the CERN Theoretical Physics Department. JFK acknowledges the financial support from the Slovenian Research Agency (research core funding No. P1-0035 and J1-8137). MS would like to thank the organisers of Les Houches for the great and fruitful atmosphere of the workshop.

Appendix

A Decay width formulas

In the calculation of the total decay width Γ_a of the unmixed pseudoscalar a, we employ the following expressions for the partial decay widths (see the reviews [394–397] for instance)

$$\Gamma(a \to \ell^+\ell^-) = \frac{\left(\xi_\ell^{\rm M}\right)^2 m_\ell^2 m_a}{8\pi v^2}\,\beta_{\ell/a}\,, \tag{A.1}$$

$$\Gamma(a \to q\bar{q}) = \frac{3\left(\xi_q^{\rm M}\right)^2 \overline{m}_q^2 m_a}{8\pi v^2}\left(1 + \Delta_q + \frac{\xi_t^{\rm M}}{\xi_q^{\rm M}}\Delta_t\right)\,, \tag{A.2}$$

$$\Gamma(a \to Q\bar{Q}) = \frac{3\left(\xi_Q^{\rm M}\right)^2 m_Q^2 m_a}{8\pi v^2}\,\beta_{Q/a}\,(1 + \Delta_Q)\,, \tag{A.3}$$

$$\Gamma(a \to gg) = \frac{\alpha_s^2 m_a^3}{32\pi^3 v^2}\left|\sum_{q=t,b,c,s} \xi_q^{\rm M}\,\mathcal{P}(\tau_{q/a})\right|^2 K_g\,, \tag{A.4}$$

$$\Gamma(a \to \gamma\gamma) = \frac{\alpha^2 m_a^3}{64\pi^3 v^2}\left|\sum_{q=t,b,c,s} 3\xi_q^{\rm M} Q_q^2\left(\mathcal{P}(\tau_{q/a}) + \Delta_\gamma\right) + \xi_\tau^{\rm M}\mathcal{P}(\tau_{\tau/a})\right|^2\,, \tag{A.5}$$

where $\overline{\rm MS}$ masses are indicated by a bar while masses without a bar are evaluated in the pole scheme. We have furthermore defined $\tau_{f/a} = 4m_f^2/m_a^2$ and $\beta_{f/a} = \sqrt{1-\tau_{f/a}}$ and used the symbol Q_q to denote the electric charge of the quark in question. All $\overline{\rm MS}$ masses as well as the coupling constants α_s and α are renormalised at the scale $\mu_R = m_a$. Table 1 finally contains the coupling assignments $\xi_f^{\rm M}$ that we consider in our work.

The QCD corrections to the partial decay width into light quarks (A.2) that are included in our numerical analysis read [362, 398–408]

$$\begin{aligned}\Delta_q = {}& \frac{\alpha_s}{\pi}\,5.67 + \left(\frac{\alpha_s}{\pi}\right)^2\left(35.94 - 1.36N_f\right) + \left(\frac{\alpha_s}{\pi}\right)^3\left(164.14 - 25.77N_f + 0.259N_f^2\right)\\ & + \left(\frac{\alpha_s}{\pi}\right)^4\left(39.34 - 220.9N_f + 9.685N_f^2 - 0.0205N_f^3\right),\end{aligned} \tag{A.6}$$

and [409, 410]

$$\Delta_t = \left(\frac{\alpha_s}{\pi}\right)^2\left[3.83 + \ln\left(\frac{m_t^2}{m_a^2}\right) + \frac{1}{6}\ln^2\left(\frac{\overline{m}_q^2}{m_a^2}\right)\right]. \tag{A.7}$$

The symbol N_f introduced above denotes the number of light quark flavours that are active at the scale m_a. For pseudoscalar masses far above the threshold, i.e. $m_a \gg 2m_q$, the results (A.6) and (A.7) represent at the moment the most accurate predictions for the QCD corrections to $\Gamma(a \to q\bar{q})$. In our numerical analysis, we hence use them to calculate the partonic rate of $a \to s\bar{s}$.

In the case of the partial decay width into heavy-quark pairs (A.3) the QCD corrections are given to first order in α_s by [362, 398–402]

$$\Delta_Q = \frac{\alpha_s}{\pi}\left(\frac{4\mathcal{Q}(\beta_{Q/a})}{3\beta_{Q/a}} - \frac{19 + 2\beta_{Q/a}^2 + 3\beta_{Q/a}^4}{12\beta_{Q/a}}\ln x_{\beta_{Q/a}} + \frac{21 - 3\beta_{Q/a}^2}{6}\right). \tag{A.8}$$

Here we have introduced the abbreviation $x_{\beta_{Q/a}} = (1-\beta_{Q/a})/(1+\beta_{Q/a})$ and the one-loop function entering (A.8) takes the form

$$\mathcal{Q}(\beta) = \left(1+\beta^2\right)\left(4\mathrm{Li}_2(x_\beta) + 2\mathrm{Li}_2(-x_\beta) + 4\ln x_\beta \ln\frac{2}{1+\beta} + 2\ln x_\beta \ln\beta\right) - 3\beta\ln\frac{4\beta^{4/3}}{1-\beta^2} \tag{A.9}$$

with $\mathrm{Li}_2(z)$ denoting the usual dilogarithm. In the threshold region, i.e. $m_a \simeq 2m_Q$, mass effects are important and as a result the QCD corrections (A.8) should be used to describe them. Following the prescription implemented in HDECAY [411,412], the transition between the region close to threshold to that far above threshold is achieved by a smooth linear interpolation of the results (A.2) and (A.3). Because this approach yields an optimised description of $\Gamma(a \to c\bar{c})$ $\left(\Gamma(a \to b\bar{b})\right)$ for pseudoscalar masses in the vicinity of $m_a \simeq 3.1\,\mathrm{GeV}$ ($m_a \simeq 11.5\,\mathrm{GeV}$) it is used in our work.

The one-loop function appearing in (A.4) and (A.5) is given by

$$\mathcal{P}(\tau) = \tau\arctan^2\left(\frac{1}{\sqrt{\tau-1}}\right), \tag{A.10}$$

where for analytic continuation it is understood that $\tau \to \tau - i0$.

The multiplicative factor K_g entering (A.4) takes the following form

$$K_g = 1 + 2\mathrm{Re}\left(\frac{\sum_{q=t,b,c,s}\xi_q^{\mathrm{M}}\Delta_g}{\sum_{q=t,b,c,s}\xi_q^{\mathrm{M}}\mathcal{P}(\tau_{q/a})}\right) + \frac{\alpha_s}{\pi}\left(\frac{73}{4} - \frac{7}{6}N_f\right), \tag{A.11}$$

where the second term encodes the virtual two-loop QCD corrections, while the third term corresponds to the finite part of the real QCD corrections in the heavy-quark limit [394,413]. We have verified that quark mass effects of the real corrections not included in (A.11) amount to no more than 5%. The virtual corrections can be written as

$$\Delta_g = \frac{\alpha_s}{\pi}\left(\mathcal{G}(y_{q/a}) + 2\tau_{q/a}\mathcal{P}'(\tau_{q/a})\,\ln\frac{\mu_q^2}{m_q^2}\right), \tag{A.12}$$

where $y_{q/a} = -x_{q/a}$ with $\tau_{q/a} \to \tau_{q/a} + i0$ for analytic continuation and the prime denotes a derivative with respect to $\tau_{q/a}$. To reproduce the position of the $a \to q\bar{q}$ threshold correctly, we set $\mu_q = m_a/2$ in our study. The two-loop function appearing in (A.12) reads [413,414]

$$\begin{aligned}
\mathcal{G}(y) = \frac{y}{(1-y)^2}\Bigg[&48\mathrm{H}(1,0,-1,0;y) + 4\ln(1-y)\ln^3 y - 24\zeta_2\mathrm{Li}_2(y) - 24\zeta_2\ln(1-y)\ln y \\
&- 72\zeta_3\ln(1-y) - \frac{220}{3}\mathrm{Li}_3(y) - \frac{128}{3}\mathrm{Li}_3(-y) + 68\mathrm{Li}_2(y)\ln y \\
&+ \frac{64}{3}\mathrm{Li}_2(-y)\ln y + \frac{94}{3}\ln(1-y)\ln^2 y - \frac{16}{3}\zeta_2\ln y + \frac{124}{3}\zeta_3 + 3\ln^2 y\Bigg] \\
&- \frac{24y\,(5+7y^2)}{(1-y)^3\,(1+y)}\mathrm{Li}_4(y) - \frac{24y\,(5+11y^2)}{(1-y)^3\,(1+y)}\mathrm{Li}_4(-y) \\
&+ \frac{8y\,(23+41y^2)}{3(1-y)^3\,(1+y)}\Big[\mathrm{Li}_3(y) + \mathrm{Li}_3(-y)\Big]\ln y - \frac{4y\,(5+23y^2)}{3(1-y)^3\,(1+y)}\mathrm{Li}_2(y)\ln^2 y
\end{aligned} \tag{A.13}$$

$$
\begin{aligned}
&- \frac{32y\,(1+y^2)}{3(1-y)^3\,(1+y)}\,\mathrm{Li}_2(-y)\ln^2 y + \frac{y\,(5-13y^2)}{36(1-y)^3\,(1+y)}\ln^4 y + \frac{2y\,(1-17y^2)}{3(1-y)^3\,(1+y)}\,\zeta_2 \ln^2 y \\
&+ \frac{4y\,(11-43y^2)}{3(1-y)^3\,(1+y)}\,\zeta_3 \ln y + \frac{24y\,(1-3y^2)}{(1-y)^3\,(1+y)}\,\zeta_4 + \frac{2y\,(2+11y)}{3(1-y)^3}\ln^3 y\,.
\end{aligned}
$$

Here $\mathrm{H}(1,0,-1,0;z)$ is a harmonic polylogarithm of weight four with two indices different from zero, which we evaluate numerically with the help of the program `HPL` [415]. The polylogarithm of order three (four) is denoted by $\mathrm{Li}_3(z)$ $\big(\mathrm{Li}_4(z)\big)$, while $\zeta_2 = \pi^2/6$, $\zeta_3 \simeq 1.20206$ and $\zeta_4 = \pi^4/90$ are the relevant Riemann's zeta values.

In the case of (A.5) we decompose the relevant QCD corrections as

$$
\Delta_\gamma = \frac{\alpha_s}{\pi}\left(\mathcal{A}(y_{q/a}) + 2\tau_{q/a}\mathcal{P}'(\tau_{q/a})\,\ln\frac{\mu_q^2}{m_q^2}\right)\,, \tag{A.14}
$$

with [413, 414, 416]

$$
\begin{aligned}
\mathcal{A}(y) = &-\frac{y\,(1+y^2)}{(1-y)^3(1+y)}\bigg[72\mathrm{Li}_4(y) + 96\mathrm{Li}_4(-y) - \frac{128}{3}\big[\mathrm{Li}_3(y) + \mathrm{Li}_3(-y)\big]\ln y \\
&+ \frac{28}{3}\mathrm{Li}_2(y)\ln^2 y + \frac{16}{3}\mathrm{Li}_2(-y)\ln^2 y + \frac{1}{18}\ln^4 y \\
&+ \frac{8}{3}\zeta_2\ln^2 y + \frac{32}{3}\zeta_3\ln y + 12\zeta_4\bigg] \\
&+ \frac{y}{(1-y)^2}\bigg[-\frac{56}{3}\mathrm{Li}_3(y) - \frac{64}{3}\mathrm{Li}_3(-y) + 16\mathrm{Li}_2(y)\ln y + \frac{32}{3}\mathrm{Li}_2(-y)\ln y \\
&+ \frac{20}{3}\ln(1-y)\ln^2 y - \frac{8}{3}\zeta_2\ln y + \frac{8}{3}\zeta_3\bigg] + \frac{2y\,(1+y)}{3(1-y)^3}\ln^3 y\,.
\end{aligned} \tag{A.15}
$$

B Mixing and threshold effects

Even though the decay $a \to b\bar{b}$ ($a \to c\bar{c}$) is kinematically forbidden below the open-flavour threshold, the presence of heavy quarks can become relevant through mixing between the pseudoscalar a and bottomonium (charmonium) bound states with the same quantum numbers [362–368]. Such mixings can effectively be described through off-diagonal contributions $\delta m^2_{a\eta_b(n)}$ to the pseudoscalar mass matrices squared. In the case of a–η_b mixing, we employ

$$
M^2_{a\eta_b} = \begin{pmatrix}
m_a^2 - i m_a \Gamma_a & \delta m^2_{a\eta_b(1)} & \dots & \delta m^2_{a\eta_b(6)} \\
\delta m^2_{a\eta_b(1)} & m^2_{\eta_b(1)} - i m_{\eta_b(1)}\Gamma_{\eta_b(1)} & \dots & 0 \\
\vdots & 0 & \ddots & 0 \\
\delta m^2_{a\eta_b(6)} & 0 & 0 & m^2_{\eta_b(6)} - i m_{\eta_b(6)}\Gamma_{\eta_b(6)}
\end{pmatrix}\,, \tag{B.16}
$$

with

$$
\delta m^2_{a\eta_b(n)} = \xi_b^{\mathrm{M}}\sqrt{\frac{3}{4\pi v^2}\,m^3_{\eta_b(n)}\big|R_{\eta_b(n)}(0)\big|}\,. \tag{B.17}
$$

	$m_{\eta_b(n)}$	$\left\|R_{\eta_b(n)}(0)\right\|$	$m_{\eta_c(n)}$	$\left\|R_{\eta_c(n)}(0)\right\|$
$n=1$	9.4	2.71	2.98	0.90
$n=2$	10.0	1.92	3.64	0.73
$n=3$	10.3	1.66	3.99	0.67
$n=4$	10.6	1.43	—	—
$n=5$	10.85	1.41	—	—
$n=6$	11.0	0.91	—	—

Table B.1: Masses of the $\eta_b(n)$ and $\eta_c(n)$ bound states in units of GeV and the corresponding values of the radial wave functions in units of $\mathrm{GeV}^{3/2}$.

The masses and radial wave functions of the $\eta_b(n)$ states are denoted by $m_{\eta_b(n)}$ and $R_{\eta_b(n)}$, respectively. The latter quantities can be extracted from the $\Upsilon(n)$ leptonic decay widths (see [417] for instance) which are measured rather precisely [158]. In the case of a–η_c mixing, we only include the first three states in the pseudoscalar mass matrix squared (B.16) and rely on the potential model calculations of [418] to determine the radial wave functions $R_{\eta_c(n)}$. The values of the $\eta_b(n)$ and $\eta_c(n)$ masses and radial wave functions that are used in our numerical analysis are collected in Table B.1 for convenience.

To be able to determine the eigenvalues and eigenvectors of (B.16) one also needs to know the total decay widths of the $\eta_b(n)$ and $\eta_c(n)$ states. The digluon decay widths of the $\eta_b(n)$ states are given to leading order in α_s by (see [362] for example)

$$\Gamma(\eta_b(n) \to gg) = \frac{\alpha_s^2}{3m_{\eta_b(n)}^2} \left|R_{\eta_b(n)}(0)\right|^2 , \tag{B.18}$$

and an analogous formula holds in the case of the charmonium resonances.

The partial decay widths (B.18) essentially saturate $\Gamma_{\eta_b(n)}$ with $n \neq 5, 6$. For $\eta_b(5)$ and $\eta_b(6)$, however, also decays to final states involving π and $B_{(s)}$ mesons are relevant. In the case of the decays to pion final states, we employ [158]

$$\Gamma(\eta_b(5) \to \pi \text{ mesons}) = 1.5\,\mathrm{MeV} , \tag{B.19}$$

$$\Gamma(\eta_b(6) \to \pi \text{ mesons}) = 3\,\mathrm{MeV} , \tag{B.20}$$

while the $B_{(s)}$ decays are incorporated via the approximate relations [366]

$$\Gamma(\eta_b(5) \to B + B_s \text{ mesons}) \simeq 0.9\,\Gamma(\Upsilon(5) \to B \text{ mesons}) + 0.65\,\Gamma(\Upsilon(5) \to B_s \text{ mesons}) , \tag{B.21}$$

$$\Gamma(\eta_b(6) \to B + B_s \text{ mesons}) \simeq \Gamma(\Upsilon(5) \to B \text{ mesons}) + \Gamma(\Upsilon(5) \to B_s \text{ mesons}) , \tag{B.22}$$

in our numerical analysis. Here [158]

$$\Gamma(\Upsilon(5) \to B \text{ mesons}) = 42\,\mathrm{MeV} , \tag{B.23}$$

$$\Gamma(\Upsilon(5) \to B_s \text{ mesons}) = 11\,\mathrm{MeV} . \tag{B.24}$$

In the case of the charmonium bound states, we use directly $\Gamma_{\eta_{c(1)}} = 31.8\,\mathrm{MeV}$ and $\Gamma_{\eta_{c(2)}} = 11.3\,\mathrm{MeV}$ [158], while for $\eta_c(3)$ we include besides (B.18) an open-charm contribution. Applying the approach of [366] to relate the $\eta_c(3)$ decays to those of $\psi(3770)$ results in

$\Gamma(\eta_c(3) \to D \text{ mesons}) \simeq 30\,\Gamma(\psi(3770) \to D \text{ mesons})$. However, the $\psi(3770)$ lies very close to the open-charm threshold and is thus highly susceptible to strong rescattering effects. Using instead the $\psi(4040)$ properties as input, we obtain the approximate result

$$\Gamma(\eta_c(3) \to D \text{ mesons}) \simeq 0.5\,\Gamma(\psi(4040) \to D \text{ mesons})\,, \tag{B.25}$$

where $\Gamma(\psi(4040) \to D \text{ mesons}) \simeq \Gamma_{\psi(4040)} = 80\,\text{MeV}$ [158].

We furthermore emphasise that the branching ratios $\eta_b(n) \to \mu^+\mu^-$ are all below the 10^{-10} level [367] and therefore can be safely ignored in the mixing formalism. The effects of the ditau decays of the bottomonium bound states are negligible as well and so are the dilepton decays of the $\eta_c(n)$ mesons. Effects of a–η_b mixing in $h \to aa$ such as for instance $h \to 2\eta_b(n) \to aa$ are part of $\text{BR}(h \to aa)$ and thus effectively included in our numerical analysis. The same is true for contributions of intermediate $\eta_c(n)$ states to the exotic decay $h \to aa$ of the SM Higgs.

Above the $b\bar{b}$ ($c\bar{c}$) threshold a perturbative description of the production and the decay of the pseudoscalar a breaks down. In this region one can however approximate the $b\bar{b}$ ($c\bar{c}$) contributions to the total decay width Γ_a through a heuristic model that is inspired by QCD sum rules [362, 366, 367] and interpolates to the continuum sufficiently above threshold. The interpolations take the form

$$\mathcal{N}_a^b = 1 - \exp\left[-8.0\left(1 - \frac{(m_B + m_{B^*})^2}{m_a^2}\right)^{2.5}\right], \tag{B.26}$$

$$\mathcal{N}_a^c = 1 - \exp\left[-6.5\left(1 - \frac{(m_D + m_{D^*})^2}{m_a^2}\right)^{2.5}\right], \tag{B.27}$$

with $m_B = 5.28\,\text{GeV}$, $m_{B^*} = 5.33\,\text{GeV}$, $m_D = 1.86\,\text{GeV}$ and $m_{D^*} = 2.01\,\text{GeV}$ [158]. In our analysis, the interpolation is achieved by simply multiplying the partonic decay width $\Gamma(a \to b\bar{b})$ and $\Gamma(a \to c\bar{c})$ by the factor $\mathcal{N}_a^b$ and $\mathcal{N}_a^c$, respectively.

For $m_a > 2m_K$ decays into kaons become kinematically allowed. The decay $a \to KK$ however violates CP, and as a result a can in practice only decay into three-body final states such as $KK\pi$. Following [393], we estimate the hadronic width $\Gamma(a \to s\bar{s} \to KK\pi)$ by multiplying $\Gamma(a \to s\bar{s})$ by the suppression factor

$$\mathcal{N}_a^s = \frac{16\pi}{m_a^2}\left(\frac{m_s^*}{m_s}\right)^2 \frac{\rho(m_K, m_K, m_\pi, m_a)}{\beta_{s/a}}\,, \tag{B.28}$$

with $m_s^* = 450\,\text{MeV}$ [419], $m_K = 439\,\text{MeV}$ and $m_\pi = 140\,\text{MeV}$ [158]. Here $\rho(m_1, m_2, m_3, m_4)$ denotes the phase space for isotropic three-body decays. It can be written as

$$\begin{aligned}\rho(m_1, m_2, m_3, m_4) = \frac{1}{(4\pi)^3}\int_{m_1}^{\frac{m_1^2+m_4^2-(m_2+m_3)^2}{2m_4}} dE_1\, 2\sqrt{E_1^2 - m_1^2} \\ \times \lambda\left(m_1^2 + m_4^2 - 2E_1 m_1, m_2^2, m_3^2\right)\,,\end{aligned} \tag{B.29}$$

with $\lambda(x, y, z)$ defined in (4).

Contribution 16

Light scalar boson searches at the LHC through associated production with a Z boson

A. Angelescu, S. Fichet, L. Finco, S. Gascon-Shotkin, G. Moreau, S. Zhang

Abstract

Light scalar bosons with mass typically below $\sim$ 65 GeV, predicted in several scenarios beyond the Standard Model (SM), might have been missed by the present experimental searches based on the Large Hadron Collider (LHC) data. Here we show that such generic neutral CP-odd or CP-even scalar fields, thanks to their production in association with a detectable Z gauge boson, exhibit specific kinematical distributions which could allow to distinguish between their signatures at LHC and the SM background. The theoretical framework consists of an effective field theory including various types of interactions, that turns out to be potentially testable separately at colliders. From the experimental side, Monte Carlo simulations for the signal and background are confronted with each other. The production of heavier scalar bosons (masses considered here up to $\sim$ 110 GeV) in association with a Z boson might be useful as well, for measuring their coupling to a Z boson pair. Hence we also derive the exclusion limits on generic heavy scalar production rates for such a process combined with the vector boson fusion mechanism, by using Large Electron-Positron (LEP) and LHC Run 1 data recorded by the CMS experiment. We demonstrate that the attractive and specific scalar field example of the radion, arising in the usual SM extensions to a warped extra dimension, is not yet excluded by those data.

1 INTRODUCTION

Several extensions of the Standard Model (SM) of elementary particle physics include an electrically neutral scalar boson in their field content with a mass below a hundred GeV: light Higgs bosons, the radion, the dilaton, the axion... Although in 2012 the Large Hadron Collider (LHC) discovered a particle compatible with the SM Higgs boson as a 125 GeV resonance, one should thus consider the possibility that some lighter scalar particles might have been missed so far in the LHC data analyses. With scalar boson masses below typically $\sim$ 65 GeV, the golden scalar decay into a pair of on-shell Z bosons is kinematically closed while its decay into a diphoton is extremely difficult to detect experimentally as the LHC diphoton triggers are bandwidth-limited for such soft photon production.[1] Therefore, in the present study, instead of considering the dominant gluon-gluon fusion mechanism, we consider the promising light scalar boson production in association with a Z gauge boson allowing to trigger on the charged

[1] At low diphoton invariant masses, boosted diphoton events with high p_T transverse momentum can still be triggered, but at the price of a weaker selection efficiency.

leptons of the Z decay. We adopt a generic theoretical approach based on an effective field theory for CP-odd and CP-even (under the combined Charge Parity symmetry) scalar fields coupled to ElectroWeak (EW) gauge bosons via the main structures of interactions. The Monte Carlo simulations of the events for the signal are performed with the `Feynrules` code [93] interfaced with `MadGraph5_aMC@NLO` [95] while the final-state SM background is generated with `MadGraph5_aMC@NLO`.

In addition, the production of a scalar boson in association with a Z boson might be interesting also for scalar masses above a hundred GeV, particularly as regards the determination of the scalar coupling to the two SM neutral gauge bosons. Motivated by this feature, we also work out generic exclusion limits on heavier scalar production rates for this process together with the Vector Boson Fusion (VBF) mechanism (involving also the scalar coupling to EW gauge bosons), as deduced from the Large Electron-Positron (LEP) [420] and LHC Run 1 (8 TeV center-of-mass energy) CMS [421] data. Finally, we study the precise case of the scalar boson represented by the so-called radion, which arises in any model with at least one extra spatial dimension, and we focus on the attractive scenario with bulk matter [422] in a slice of AdS_5 space [423] addressing both the flavour and gauge hierarchy problems.

2 THE EFFECTIVE MODEL

Diagrammatically, the studied scalar boson production in association with a Z gauge boson occurs through the radiation of the scalar field from a Z boson produced in the s-channel. This process involves only the scalar coupling to two Z bosons. We use an effective theory approach to describe the scalar interaction with SM EW gauge bosons. The scalar mass can be smaller than the EW symmetry-breaking scale. When it is the case, we make the extra assumption that the scalar has large tree-level $SU(2)_L \times U(1)_Y$ couplings, so that the loop-induced EW-breaking contributions are subleading. Under this condition, the interactions of a neutral CP-even or CP-odd scalar φ with the EW gauge bosons are respectively described by the following dimension-5 effective gauge invariant Lagrangians

$$\mathcal{L}_{\text{eff}} \supset \varphi \left(\frac{1}{f_G} G^{\mu\nu\, a} G^a_{\mu\nu} + \frac{1}{f_W} W^{\mu\nu\, b} W^b_{\mu\nu} + \frac{1}{f_B} B^{\mu\nu} B_{\mu\nu} + \frac{1}{f_H} |D^\mu H|^2 \right) \tag{1}$$

$$\mathcal{L}_{\text{eff}} \supset \varphi \left(\frac{1}{\tilde{f}_G} G^{\mu\nu\, a} \tilde{G}^a_{\mu\nu} + \frac{1}{\tilde{f}_W} W^{\mu\nu\, b} \tilde{W}^b_{\mu\nu} + \frac{1}{\tilde{f}_B} B^{\mu\nu} \tilde{B}_{\mu\nu} \right) \tag{2}$$

where $\tilde{V}^{\mu\nu} = \frac{1}{2}\epsilon^{\mu\nu\rho\sigma} V_{\rho\sigma}$, H represents the SM Higgs doublet, D^μ the covariant derivative, the f's denote high-energy scales of new physics, a, b are summed group generator indices whereas μ, ν stand for summed Lorentz indices and the rank-2 tensors are the field strengths for all the SM gauge bosons before EW symmetry breaking (using standard notations). After this breaking, the effective Lagrangian, for example in the CP-even case, contains the φZZ interactions

$$\mathcal{L}_{\text{eff}} \supset \frac{1}{f_Z} \varphi (Z_{\mu\nu})^2 + \frac{m_Z^2}{2 f_H} \varphi (Z_\mu)^2 \,, \tag{3}$$

where $f_Z^{-1} = s_w^2 f_B^{-1} + c_w^2 f_W^{-1}$ and $s_w^2 \equiv \sin^2(\theta_w) \approx 0.23$. The effective theory is valid as long as the f's (related to Kaluza-Klein mass scales for instance) are larger than the typical energies going through the vertices. The φ scalar mixing with the SM Higgs boson is assumed to be small to ensure that the SM Higgs field has SM-like couplings compatible with the LHC

signal strength measurements. The scalar fields entering Eq. (1)-(2) are taken to be the mass eigenstates.

The CP-even couplings might be those of a radion in a model with a warped extra dimension along which matter is propagating. Notice that if EW brane kinetic terms are negligible in such models, one has $f_W = f_B$ [424, 425] which implies that the $\varphi F^{\mu\nu} Z_{\mu\nu}$ coupling vanishes, a property which can be used for model discrimination [426].

The CP-odd scalar field can be a pseudo Nambu-Goldstone boson from an approximate global symmetry, just like those appearing in composite Higgs models. The couplings to gauge fields are then induced by the many fermion resonances populating the TeV scale (see e.g Ref. [427] or Ref. [428]).

3 NUMERICAL ANALYSES

3.1 MONTE CARLO SIMULATIONS FOR LIGHT SCALAR FIELDS

As stated in the introduction, bandwidth considerations at the LHC currently limit the invariant diphoton mass range that can be probed for a new light scalar using pure diphoton triggers to no lower than ~ 65 GeV [379, 421, 429]. For this reason, it is interesting to envisage a dedicated analysis targeting the associated production of a light scalar with a Z boson, where the Z boson decays to a pair of oppositely-charged electrons or muons. In such a scenario the events could be triggered by dilepton rather than diphoton triggers, thus potentially allowing the lower limit of the light scalar-to-diphoton search range to decrease to ~ 20 GeV.

In order to investigate the capability of such an analysis to be able to distinguish the production of a CP-even from a CP-odd scalar particle as defined in the above effective model, and from SM background processes, we constructed both CP-even and CP-odd instances of the model with the `Feynrules` code in the form of Universal FeynRules Output (UFO) files. These were then propagated to the `MadGraph5_aMC@NLO_v2_5_5` program for generation of parton-level events at $\sqrt{s} = 8$ TeV of the process $pp \to \varphi + Z$, $\varphi \to \gamma\gamma$, $Z \to \mu^+\mu^-$, for each of $m_\varphi = 20$ and 70 GeV, as well as for generation of events of the process $pp \to \gamma\gamma + Z$, $Z \to \mu^+\mu^-$ within the SM. The event generations were performed for the following three choices of parameters:

- Two different cases of a CP-even scalar boson:
  - $f_B = 1$ TeV and $f_{H,W} \to \infty$, corresponding to the case of a CP-even scalar boson coupling to two Z bosons via the $(Z_{\mu\nu})^2$ Lorentz structure, called CP-even$_{1/f_Z}$
  - $f_H = 1$ TeV and $f_{B,W} \to \infty$, corresponding to the case of a CP-even scalar boson coupling to two Z bosons via the $(Z_\mu)^2$ Lorentz structure, called CP-even$_{1/f_H}$
- The case of a CP-odd scalar field with $\tilde{f}_B = 1$ TeV and $\tilde{f}_W \to \infty$, in which the coupling to two Z bosons always occurs via the $Z_{\mu\nu}\tilde{Z}^{\mu\nu}$ Lorentz structure.

No selection or acceptance criteria were applied.

Figures 1 and 2 show kinematical distributions for $m_\varphi = 20$ and 70 GeV respectively, for each of the above three cases of light scalar: CP-even$_{1/f_Z}$, CP-even$_{1/f_H}$, and CP-odd, as well as for the SM background. The areas of all distributions have been normalized to unity. For both φ mass values, the shape of the distribution of ΔR (where $\Delta R^2 = \sqrt{\Delta\eta^2 + \Delta\varphi^2}$ and η can be approximated by $-ln\tan(\theta/2)$, θ and φ here denoting the polar and azimuthal angles,

respectively) between the two muons, $\Delta R_{\mu^+\mu^-}$, is clearly different for each of the CP-even$_{1/f_Z}$, CP-odd, and SM cases, whilst the CP-even$_{1/f_H}$ and SM cases can only be distinguished from each other for $m_\varphi = 70$ GeV. The shapes of the transverse momentum of the dimuon system, $p_{T_{\mu^+\mu^-}}$, of all four cases can be distinguished from each other for both masses (case of $m_\varphi = 20$ GeV not shown), with the CP-odd light scalar posessing the hardest spectrum. Finally, the invariant mass of the dimuon system, $M_{\mu^+\mu^-}$, offers some distinction betweeen the CP-even$_{1/f_H}$ case and the other cases, but only for $m_\varphi = 20$ GeV ($m_\varphi = 70$ GeV not shown). However, for both φ masses, the dimuon invariant mass distributions illustrate the possibility of incorporating a window around the nominal Z boson mass into the trigger. Where they exist, the nature of the shape differences would seem to favor use in multivariate techniques rather than in the application of sequential selection criteria. Since the distributions shown are at parton level, further studies must be undertaken to determine whether the differences in shape are as marked after parton showering/hadronization, reflecting in particular the influence of the underlying event, and after detector simulation.

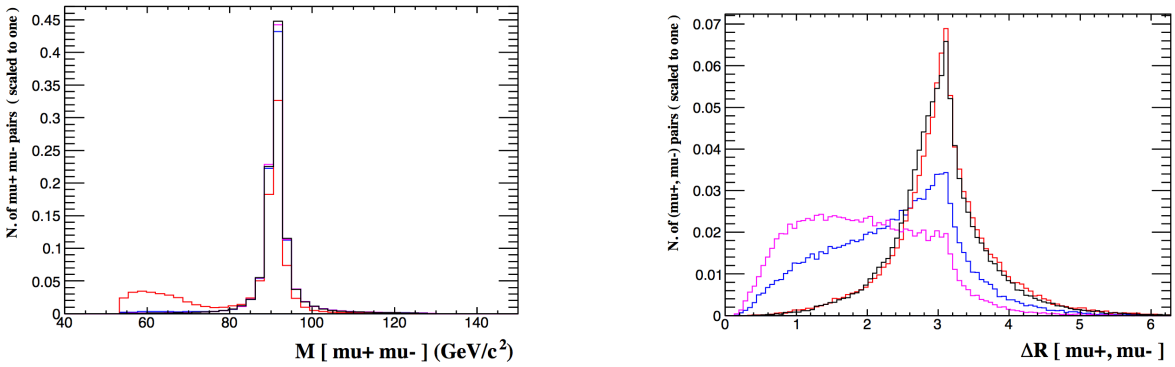

Figure 1: Distributions of the dimuon invariant mass, $M_{\mu^+\mu^-}$ [GeV/c^2] (left) and ΔR between the two muons, $\Delta R_{\mu^+\mu^-}$ (right), for a light scalar φ with $m_\varphi = 20$ GeV for the following cases: CP-even$_{1/f_Z}$ (blue), CP-even$_{1/f_H}$ (red), and CP-odd (purple), superimposed on the same distributions for the SM background (black).

3.2 EXCLUSION LIMITS FOR HEAVY SCALAR BOSONS

Using the LEP [420] and LHC Run 1 (CMS Collaboration) [421] data combined with the SM background estimates, we have derived conservative upper constraints on the scalar production rates for scalar masses above $\sim$ 80 GeV (as performed in Ref. [430] with these LHC data for a lighter Higgs boson in the two Higgs doublet model). Both the $pp \to Z\varphi$ production and the VBF mechanism, $pp \to \varphi qq$ [$q \equiv$ quark], were taken into account. In this work we have not turned on the $\varphi(W^b_{\mu\nu})^2$ interaction so that φ does not couple to $W^\pm$ (in other words $f_W, \tilde{f}_W \to \infty$). The now experimentally detectable diphoton decay channel $\varphi \to \gamma\gamma$ was exclusively used to select the signal, but some cuts based on the associated Z boson or quark pair should be added to select the two studied production processes and to optimise the signal selection over backgrounds. From the obtained rate constraints, we have derived the bounds at 95% C.L. on the combinations of effective parameters and the free diphoton branching ratio $B_{\varphi\to\gamma\gamma}$ entering the scalar rates, as displayed in Fig. 3 for the considered $1/\tilde{f}_Z$ ($1/f_Z$) coupling of the CP-odd (CP-even) scalar field and in Fig. 4 (left) for the $1/f_H$ coupling of the CP-even scalar boson (for simplification reasons only one coupling is non-vanishing at a time).

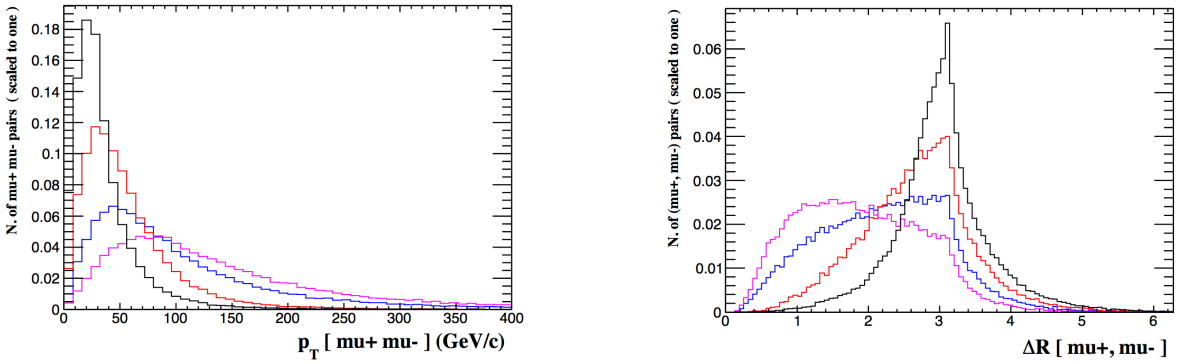

Figure 2: Distributions of the dimuon system transverse momentum, $p_{T_{\mu^+\mu^-}}$ [GeV/c] , (left) and ΔR between the two muons, $\Delta R_{\mu^+\mu^-}$ (right), for a light scalar φ with $m_\varphi = 70$ GeV for the following cases: CP-even$_{1/f_Z}$ (blue), CP-even$_{1/f_H}$ (red), and CP-odd (purple), superimposed on the same distributions for the SM background (black).

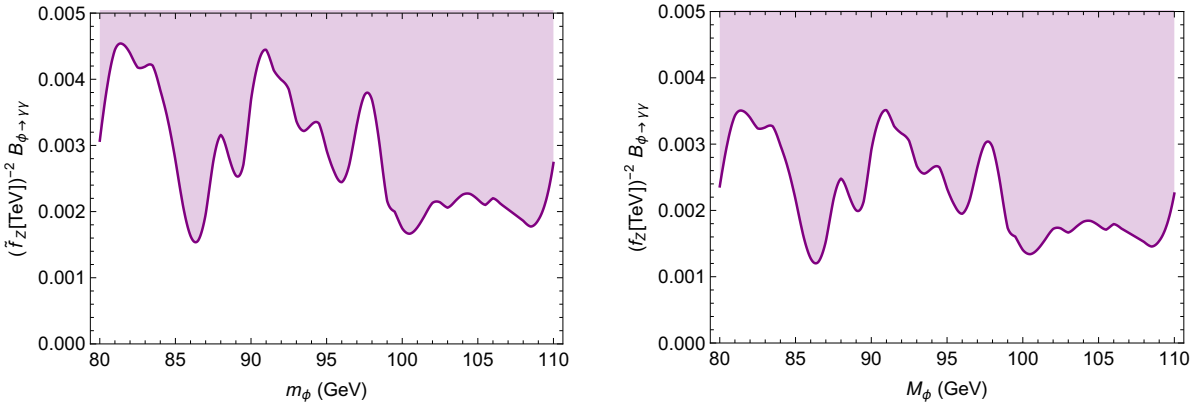

Figure 3: Colored regions excluded by the LHC Run 1 (CMS Collaboration) data in the plane $B_{\varphi\to\gamma\gamma}/\tilde{f}_Z^2$ [in TeV^{-2}] versus the scalar mass m_φ [in GeV] (left) and $B_{\varphi\to\gamma\gamma}/f_Z^2$ [in TeV^{-2}] versus m_φ [in GeV] (right).

We have also studied the precise case of the radion scalar boson arising in the scenario with bulk matter in a slice of AdS_5 space [431]. The radion is in fact associated to the fluctuations of the metric along the extra spatial dimensions (here a unique warped extra dimension). As justified in Section 2, we take the example of a relatively small Higgs-radion mixing generated by a parameter, $\xi = 0.3$, a first Kaluza-Klein photon mass quite heavy compared to m_φ, $M_{KK} = 3$ TeV, and also $\Lambda = 10$ TeV (see Ref. [431]). We consider the limiting case $f_Z \to \infty$ which is realistic as a first approximation since the radion derivative couplings (kinetic-like) to gauge bosons are not the dominant ones generally speaking [2]. The prediction for the quantity $1/f_H^2$ for the radion case is then drawn on Fig. 4 (right) as a function of the radion mass. For $B_{\varphi\to\gamma\gamma} < 1$, the prediction lies below the red line, further from the exclusion regions. The conclusion from the comparison between this prediction and the superimposed LEP and LHC limits is that, with the considered choice of parameters, the radion particle is clearly not excluded by

[2]Indeed, the radion derivative couplings to (massive) gauge bosons receive a suppression factor of about ~ 70, equal to twice the so-called extra-dimensional volume factor, which is not present in the f_H^{-1} couplings between the radion and gauge bosons. However, for certain values of ξ and m_φ, the f_H^{-1} couplings can achieve values close to 0 and thus become subdominant compared to the derivative f_Z^{-1} couplings.

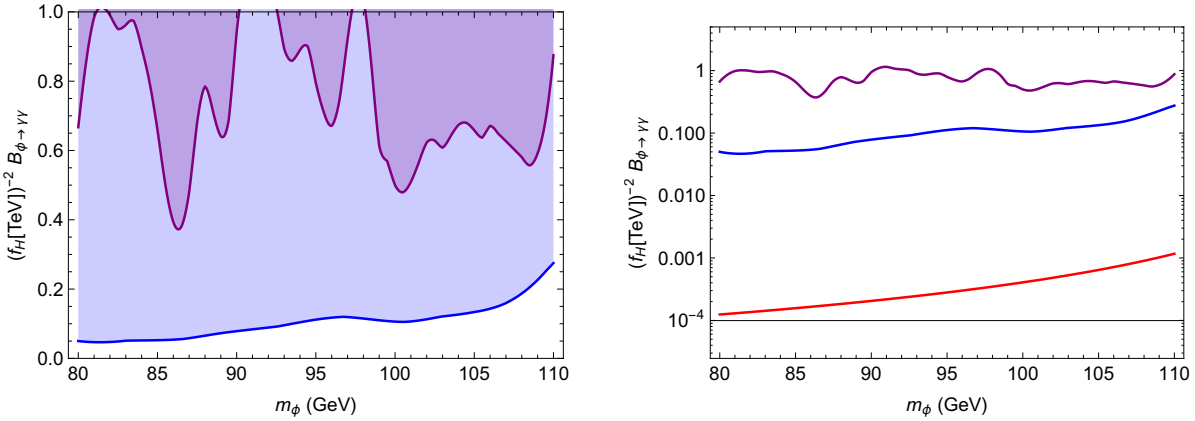

Figure 4: Colored domains excluded by the LEP [in blue] and LHC Run 1 (CMS) [in purple] data in the plane $B_{\varphi\to\gamma\gamma}/f_H^2$ [in TeV^{-2}] versus m_φ [in GeV] (left). The right-hand plot is identical but with a prediction for the radion scalar field superimposed [the plain red line].

the present combined high-energy collider results.

CONCLUSIONS

For two examples of low scalar masses at 20 GeV and 70 GeV, we have shown that some selected relevant kinematical distributions for the charged muon pair resulting from the Z leptonic decay, subsequent to $Z\varphi$ production, have specific shapes which may allow to distinguish them from the displaced SM background (for large enough production rates / φ couplings). The characteristic shapes might even allow to discriminate between the $1/f_Z$ and $1/f_H$ couplings of the CP-even scalar boson and the $1/\tilde{f}_Z$ coupling of the CP-odd field. These results motivate experimental direct and exploratory searches for light neutral scalar particles, using the LHC Run 1 and Run 2 data collected at the 8 TeV and upgraded 13 TeV center- of-mass energies.

Furthermore, we have provided generic exclusion limits from LEP and LHC Run 1 CMS searches on the (Z associated and VBF) production rates (including $B_{\varphi\to\gamma\gamma}$) for heavier scalar masses (up to 110 GeV) and translated these limits into constraints on the scalar parameter space, more precisely on combinations of the f-scales with the free diphoton branching fraction. In particular, the specific radion field, arising from a standard warped model with bulk matter, has been studied quantitatively to show that the present collider bounds do not exclude its presence. Those results encourage the experimental LHC collaborations to extend present analyses to the (present and future) LHC Run 2 data to determine in particular whether the LHC sensitivity can reach that of LEP for light scalar bosons in the mass range of $80 - 110$ GeV.

ACKNOWLEDGEMENTS

The work of A.A. and G.M. is supported by the ERC advanced grant "Higgs@LHC". G.M. would like to thank as well the support from the CNRS LIA (Laboratoire International Associé), THEP (Theoretical High Energy Physics) and the INFRE-HEPNET (IndoFrench Network on High Energy Physics) of CEFIPRA/IFCPAR (Indo-French Centre for the Promotion of Advanced Research). S.G.-S. and S.Z. would like to acknowledge the support of HiggsTools, an Initial Training Network (ITN) supported by the 7th Framework Programme of the European Commission. All the authors acknowledge the organisers of the "Les Houches" Workshop for

the whole organisation and the friendly atmosphere during the workshop.

Contribution 17

MSSM Higgs Boson Production via Gluon Fusion

M. Mühlleitner, H. Rzehak and M. Spira

Abstract
Higgs boson production via gluon fusion is discussed within the minimal supersymmetric extension of the Standard Model with particular emphasis on the genuine SUSY–QCD corrections at NLO. When comparing these corrections with the usual Δ_b corrections that are absorbed in effective bottom Yukawa couplings we are left with significant remainders beyond this approximation.

1 Introduction

The Standard-Model (SM) Higgs boson production cross section via gluon-fusion $gg \to H$ is known up to N^{3}LO in QCD [413, 414, 432–450] in the limit of heavy top quarks and up to NLO QCD [413, 414, 434, 435] and NLO electroweak [451–459] including finite quark mass effects supplemented by soft and collinear gluon resummation up to the N^{3}LL level [460–473]. These results, however, can only partly be applied to the minimal supersymmetric extension (MSSM), since for large values of tgβ the bottom Yukawa couplings are enhanced leading to the dominance of the bottom-loop contributions where bottom mass effects are large. In addition scalar squark loops contribute to the gluon-fusion cross sections of the light and heavy scalar MSSM Higgs bosons. The QCD corrections to the squark contributions are known up to NLO in QCD including the full squark mass dependence [416, 474–476]. The pure QCD corrections are large in general. The full supersymmetric (SUSY–) QCD corrections have been calculated first in the limit of heavy SUSY particles [477–481] analytically and later involving the full mass dependences numerically [482–484]. However, a rigorous analysis of the results within the MSSM is still missing. This addresses in particular the well-known Δ_b approximation of the genuine SUSY–QCD and -electroweak corrections in comparison to the full results in case of bottom-loop dominance as e.g. for large values of tgβ.

2 Effective Bottom Yukawa couplings

The dominant correction to the bottom Yukawa couplings originates from the coupling of the 'wrong' doublet φ_2 to the bottom quarks at one-loop level and can be discussed in terms of the effective Lagrangian

$$\begin{aligned}
\mathcal{L}_{eff} &= -\lambda_b \overline{b_R} \left[\varphi_1^0 + \frac{\Delta_b}{\mathrm{tg}\beta} \varphi_2^{0*} \right] b_L + h.c. \\
&= -m_b \bar{b} \left[1 + i\gamma_5 \frac{G^0}{v} \right] b - \frac{m_b/v}{1+\Delta_b} \bar{b} \left[g_b^h \left(1 - \frac{\Delta_b}{\mathrm{tg}\alpha\, \mathrm{tg}\beta} \right) h \right. \\
&\qquad \left. + g_b^H \left(1 + \Delta_b \frac{\mathrm{tg}\alpha}{\mathrm{tg}\beta} \right) H - g_b^A \left(1 - \frac{\Delta_b}{\mathrm{tg}^2\beta} \right) i\gamma_5 A \right] b \qquad (1)
\end{aligned}$$

in the low-energy limit where the relations between current $(\varphi_1^0, \varphi_2^0)$ and mass (h, H, A, G^0) eigenstates of the neutral Higgs components

$$\begin{aligned} \varphi_1^0 &= \frac{1}{\sqrt{2}}\left[v_1 + H\cos\alpha - h\sin\alpha + iA\sin\beta - iG^0\cos\beta\right] \\ \varphi_2^0 &= \frac{1}{\sqrt{2}}\left[v_2 + H\sin\alpha + h\cos\alpha + iA\cos\beta + iG^0\sin\beta\right] \end{aligned} \tag{2}$$

have been used with G^0 being the neutral would-be Goldstone component. Here, α and β denote the mixing angles in the CP–even and CP-odd scalar sectors, respectively. The MSSM modifications of the SM bottom-quark Yukawa coupling can be expressed in terms of the mixing angles α, β as

$$g_b^h = -\frac{\sin\alpha}{\cos\beta}, \quad g_b^H = \frac{\cos\alpha}{\cos\beta}, \quad g_b^A = \text{tg}\beta \tag{3}$$

The indices L, R denote the chiralities of the bottom states, λ_b the bottom Yukawa coupling of the MSSM Lagrangian and $v \approx 246$ GeV the SM vacuum expectation value. The leading NLO contributions to the correction Δ_b are given by [485–495]

$$\begin{aligned} \Delta_b &= \Delta_b^{QCD} + \Delta_b^{elw,t} \\ \Delta_b^{QCD} &= \frac{C_F}{2}\frac{\alpha_s}{\pi}\, m_{\tilde{g}}\, \mu\, \text{tg}\beta\, I(m^2_{\tilde{b}_1}, m^2_{\tilde{b}_2}, m^2_{\tilde{g}}) \\ \Delta_b^{elw,t} &= \frac{\lambda_t^2}{(4\pi)^2}\, A_t\, \mu\, \text{tg}\beta\, I(m^2_{\tilde{t}_1}, m^2_{\tilde{t}_2}, \mu^2) \end{aligned} \tag{4}$$

where $C_F = 4/3$, α_s denotes the strong coupling constant and λ_t the top Yukawa coupling. The masses $m_{\tilde{b}_{1,2}}$ and $m_{\tilde{t}_{1,2}}$ are the sbottom and stop masses and μ the higgsino mass parameter. The function I is generically defined as

$$I(a,b,c) = \frac{ab\log\frac{a}{b} + bc\log\frac{b}{c} + ca\log\frac{c}{a}}{(a-b)(b-c)(a-c)} \tag{5}$$

Two-loop QCD corrections to the leading Δ_b^{QCD} and $\Delta_b^{elw,t}$ contributions have been calculated. They modify the size by a moderate amount of about 10% and reduce the scale dependence considerably to the level of a few per-cent [496–501] and thus yield a reliable prediction of the effective bottom Yukawa couplings.

3 Gluon Fusion

At leading order the gluon fusion processes $gg \to h/H$ are mediated by heavy quark and squark triangle loops, *cf.* Fig.1, the latter contributing significantly for squark masses $\lesssim 400$ GeV. The LO cross section in the narrow-width approximation can be obtained from the h/H gluonic decay widths, [394–396, 502]

$$\begin{aligned} \sigma_{LO}(pp \to h/H) &= \sigma_0^{h/H}\tau_{h/H}\frac{d\mathcal{L}^{gg}}{d\tau_{h/H}} \\ \sigma_0^{h/H} &= \frac{\pi^2}{8M^3_{h/H}}\Gamma_{LO}(h/H \to gg) \end{aligned} \tag{6}$$

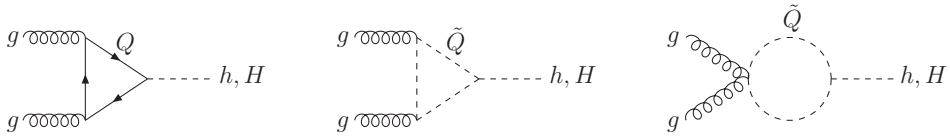

Figure 1: Diagrams contributing to $gg \to h, H$ at leading order.

$$\sigma_0^{h/H} = \frac{G_F \alpha_s^2(\mu_R)}{288\sqrt{2}\pi} \left| \sum_{Q=t,b} g_Q^{h/H} A_Q^{h/H}(\tau_Q) + \sum_{\widetilde{Q}=\widetilde{t}_{1,2},\widetilde{b}_{1,2}} g_{\widetilde{Q}}^{h/H} A_{\widetilde{Q}}^{h/H}(\tau_{\widetilde{Q}}) \right|^2 \quad (7)$$

where $\tau_{h/H} = M_{h/H}^2/s$ with s being the squared hadronic c.m. energy and $\tau_{Q/\tilde{Q}} = 4m_{Q/\tilde{Q}}^2/M_{h/H}^2$. The MSSM top couplings relative to the SM top-quark Yukawa coupling can be expressed as

$$g_t^h = \frac{\cos\alpha}{\sin\beta}, \quad g_t^H = \frac{\sin\alpha}{\sin\beta}, \quad g_b^A = \frac{1}{\mathrm{tg}\beta} \quad (8)$$

The Higgs couplings to stops and sbottoms are given by

$$\begin{aligned}
m_{\widetilde{Q}_1}^2 g_{\widetilde{Q}_1}^{h/H} &= g_{\widetilde{Q},LL}^{h/H} c_Q^2 + g_{\widetilde{Q},RR}^{h/H} s_Q^2 + 2 g_{\widetilde{Q},LR}^{h/H} s_Q c_Q \\
m_{\widetilde{Q}_2}^2 g_{\widetilde{Q}_2}^{h/H} &= g_{\widetilde{Q},LL}^{h/H} s_Q^2 + g_{\widetilde{Q},RR}^{h/H} c_Q^2 - 2 g_{\widetilde{Q},LR}^{h/H} s_Q c_Q \\
g_{\widetilde{Q},LL/RR}^{h} &= m_Q^2 g_Q^h \mp M_Z^2 \left(I_{3Q} - e_Q \sin^2\theta_W\right) \sin(\alpha+\beta) \\
g_{\widetilde{Q},LL/RR}^{H} &= m_Q^2 g_Q^H \pm M_Z^2 \left(I_{3Q} - e_Q \sin^2\theta_W\right) \cos(\alpha+\beta) \\
g_{\widetilde{t},LR}^{h/H} &= -\frac{m_t}{2}(\mu g_b^{h/H} - A_t g_t^{h/H}) \\
g_{\widetilde{b},LR}^{h/H} &= -\frac{m_b}{2}(\mu g_t^{h/H} - A_b g_b^{h/H})
\end{aligned} \quad (9)$$

The variables $s/c_{t,b} = \sin / \cos\theta_{t,b}$ are related to the stop/sbottom mixing angles $\theta_{t,b}$, θ_W is the Weinberg angle, I_{3Q} denotes the third component of the left-handed isospin and e_Q the electric charge of the corresponding quark state, while A_Q are the soft-SUSY-breaking trilinear coupling parameters. The LO form factors are given by

$$\begin{aligned}
A_Q^{h/H}(\tau) &= \frac{3}{2}\tau[1 + (1-\tau) f(\tau)] \\
A_{\tilde{Q}}^{h/H}(\tau) &= -\frac{3}{4}\tau[1 - \tau f(\tau)] \\
f(\tau) &= \begin{cases} \arcsin^2 \dfrac{1}{\sqrt{\tau}} & \tau \geq 1 \\ -\dfrac{1}{4}\left[\log \dfrac{1+\sqrt{1-\tau}}{1-\sqrt{1-\tau}} - i\pi\right]^2 & \tau < 1 \end{cases}
\end{aligned} \quad (10)$$

And the gluon luminosity at the factorization scale μ_F is defined as

$$\frac{d\mathcal{L}^{gg}}{d\tau} = \int_\tau^1 \frac{dx}{x}\, g(x,\mu_F^2) g(\tau/x, \mu_F^2)$$

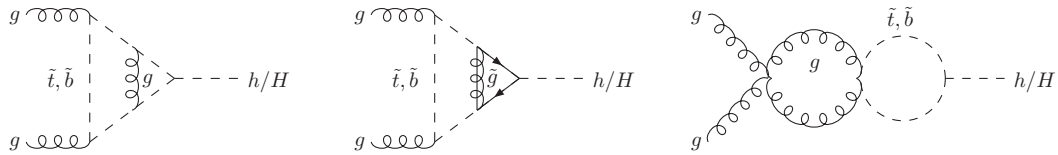

Figure 2: Some generic diagrams for the virtual NLO SUSY-QCD corrections to Higgs boson production via gluon fusion.

where $g(x, \mu_F^2)$ denotes the gluon parton density of the proton. The NLO SUSY-QCD corrections consist of the virtual two-loop corrections, *cf.* Fig.2, and the real corrections due to the radiation processes $gg \to gh/H, gq \to qh/H$ and $q\bar{q} \to gh/H$, *cf.* Fig.3. The final result for the total hadronic cross sections can be split accordingly into five parts,

$$\sigma(pp \to h/H + X) = \sigma_0^{h/H} \left[1 + C^{h/H} \frac{\alpha_s}{\pi}\right] \tau_{h/H} \frac{d\mathcal{L}^{gg}}{d\tau_{h/H}} + \Delta\sigma_{gg}^{h/H} + \Delta\sigma_{gq}^{h/H} + \Delta\sigma_{q\bar{q}}^{h/H} \quad (11)$$

where the second term corresponds to the virtual and the last three terms to the real corrections. The strong coupling constant is defined in the $\overline{\rm MS}$ scheme, with the top quark, gluino and squark contributions decoupled from the scale dependence. The quark and squark masses are renormalized on-shell. The parton densities are factorized in the $\overline{\rm MS}$ scheme with five active flavors, i.e. the top quark, the gluino and the squarks are not included in the factorization scale dependence. After renormalization we are left with collinear divergences in the sum of the virtual and real corrections which are absorbed in the renormalization of the parton density functions, so that the result Eq. (11) is finite and depends on the renormalization and factorization scales μ_R and μ_F, respectively. The natural scale choices turn out to be $\mu_R = \mu_F \sim M_{h/H}$.

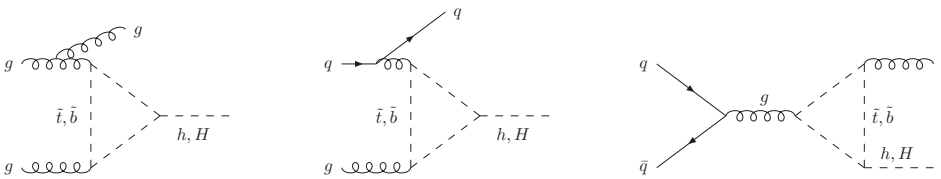

Figure 3: Typical diagrams for the real NLO QCD corrections to the squark contributions to the gluon fusion processes.

The pure QCD corrections described by the first (generic) diagram of Fig. 2 for the virtual corrections and the diagrams of Fig. 3 for the real corrections are known to be large, i.e. of similar size as those to the top quark loops [416, 474–476]. The genuine SUSY–QCD corrections are described by the generic second and third diagrams of Fig. 2 and contribute only to the virtual corrections at NLO. The renormalization of the squark sector has been performed along the lines of Ref. [503] in order to absorb potentially large contributions of the sbottom sector in the renormalized parameters. In addition we have absorbed the NLO Δ_b terms originating from the effective Lagrangian of Eq. (1) in the corresponding bottom Yukawa couplings. This removes the dominant genuine SUSY–QCD corrections to the bottom loop contributions and thus also provides a test of the Δ_b-approximation in terms of the residual corrections as the remainder.

For the numerical results we have adopted the τ-phobic scenario [504], defined by the following choices of MSSM parameters [$m_t = 173.2$ GeV],

$$\begin{aligned} &\text{tg}\beta = 30, \quad M_{\tilde{Q}} = 1.5 \text{ TeV}, \quad M_{\tilde{\ell}_3} = 500 \text{ GeV}, \quad M_{\tilde{g}} = 1.5 \text{ TeV}, \\ &M_2 = 200 \text{ GeV}, \quad A_b = A_t = 4.417 \text{ TeV}, \quad A_\tau = 0, \quad \mu = 2 \text{ TeV} \end{aligned} \tag{12}$$

In this scenario the squark masses amount to

$$\begin{aligned} m_{\tilde{t}_1} &= 1.347 \text{ TeV}, & m_{\tilde{t}_2} &= 1.739 \text{ TeV}, \\ m_{\tilde{b}_1} &= 1.521 \text{ TeV}, & m_{\tilde{b}_2} &= 1.583 \text{ TeV} \end{aligned} \tag{13}$$

Fig. 4 displays the genuine SUSY-QCD corrections for the heavy scalar Higgs boson normalized to the LO quark form factors, *i.e.* $A_Q^{h/H}(\tau_Q) \to A_Q^{h/H}(\tau_Q)\left[1 + C_{SUSY}^{Q,h/H}\frac{\alpha_s}{\pi}\right]$ $(Q = t, b)$. The corrections can be sizeable. For the top contributions they amount to about $-15\frac{\alpha_s}{\pi} \sim -50\%$. However, the top contribution is strongly suppressed for these large values of tgβ. The residual corrections to the bottom contributions range at the level of about $-5\frac{\alpha_s}{\pi} \sim -15\%$[1]. In addition Fig. 4 shows the corrections to the bottom contribution without the absorption of the Δ_b terms into the bottom Yukawa coupling (red dashed line). In this case the corrections are much larger thus signalizing that the dominant part of the genuine SUSY–QCD corrections is indeed originating from these Δ_b terms. However, the remainder of the corrections after absorbing these Δ_b terms is sizeable and should be taken into account in reliable analyses.

4 Conclusions

We have presented results for the NLO SUSY-QCD corrections to gluon fusion into CP-even MSSM Higgs bosons, including the full mass dependence of the loop particles. The genuine SUSY-QCD corrections can be sizeable and deviate from the results in terms of the effective bottom Yukawa couplings containing the Δ_b terms by a significant amount, i.e. the remainder should be take into account.

[1] It should be noted that these corrections correspond to the *amplitudes* that have to be squared in order to arrive at the corrections to the cross sections.

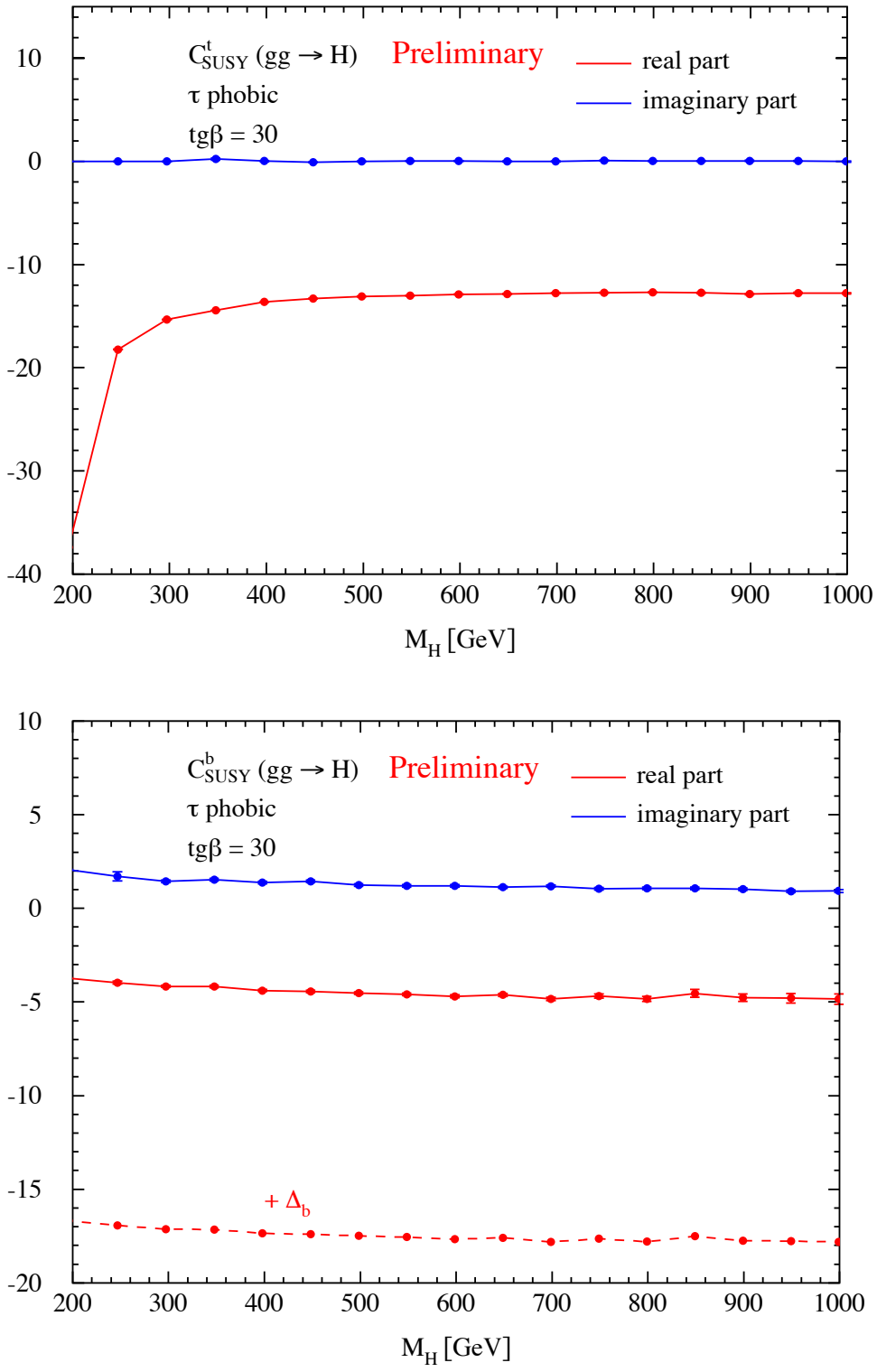

Figure 4: The genuine SUSY-QCD corrections to the top (upper) and bottom (lower) quark form factors normalized to the individual LO expressions. Real parts: red, imaginary parts: blue, compared to the corrections to the bottom quark form factor including the fixed-order Δ_b contribution, i.e. without absorbing it in the bottom Yukawa coupling (red dashed line).

Contribution 18

Extending LHC resonant di-Higgs searches to discover new scalars: $H_1 \to H_2 H_2 \to b\bar{b}b\bar{b}$

D. Barducci, K. Mimasu, J. M. No, C. Vernieri, J. Zurita

Abstract

We extend the coverage of 13 TeV LHC resonant di-Higgs searches in the $b\bar{b}b\bar{b}$ final state to the process $H_1 \to H_2 H_2 \to b\bar{b}b\bar{b}$, with both H_1 and H_2 states beyond the Standard Model. The decay $H_1 \to H_2 H_2$ could constitute a joint discovery mode for H_1 and H_2 within non-minimal Higgs sectors such as two-Higgs-doublet models or the NMSSM. We present here the first sensitivity study of this channel, using public CMS resonant di-Higgs production data to validate our analysis.

1 Introduction

Searches for heavy scalars in non-standard decay channels are needed to fully cover the parameter space of theories beyond the Standard Model (BSM). A prime example are resonant di-Higgs searches $pp \to H \to hh$, where the scalar H is resonantly produced and decays into a pair of 125 GeV Higgs bosons (h). ATLAS and CMS look for these processes in various final states, including $b\bar{b}b\bar{b}$ [505–509], $b\bar{b}W^+W^-$ [28, 510, 511], $b\bar{b}\tau^+\tau^-$ [512, 513] and $b\bar{b}\gamma\gamma$ [514–516]. Searching for such additional Higgs bosons decaying to the SM Higgs at the LHC is a key avenue to probe non-minimal scalar sectors. For Higgs sectors with several new states beyond the SM (BSM), such as two-Higgs-doublet models (2HDM) or the next-to-minimal supersymmetric Standard Model (NMSSM), "*Higgs to Higgs*" decays can occur between several BSM scalars in the presence of sizable mass splittings. In this case, such *Higgs to Higgs* decays are potential discovery channels for both the decaying particle and its decay products[1]. Generalising searches for additional Higgs bosons to probe new scalar decay modes beyond the SM Higgs is therefore of great importance for the LHC Higgs physics programme.

We present here a sensitivity study of the channel $H_1 \to H_2 H_2 \to b\bar{b}b\bar{b}$ as a probe for BSM states H_1 and H_2, where H_1 is produced via gluon fusion at the LHC. For $m_{H_1} \gg m_{H_2}$, $H_1 \to H_2 H_2$ can be the dominant decay mode of H_1, and moreover $H_2 \to b\bar{b}$ generally yields the largest branching fraction (for $m_{H_2} < 2\, m_t$) of H_2, making it challenging to discover H_2 through direct production. A concrete example of such a scenario would be a 2HDM, where $H_1 \equiv H_0$, $H_2 \equiv A$ and $m_{H_0} \gg m_A$. The large *Higgs to Higgs* branching fractions induced by significant mass splittings combined with the typically dominant $b\bar{b}$ branching fractions of light scalars make the channel considered here a potentially important, unexplored probe of non-minimal Higgs sectors.

[1] This is e.g. the case for $A \to ZH$ / $H \to ZA$ decays in 2HDM scenarios [517, 518] (see also [519]), which have been searched for by CMS at 8 TeV [520] and 13 TeV [521].

While no ATLAS/CMS analysis of the $pp \to H_1 \to H_2 H_2 \to b\bar{b}b\bar{b}$ signature (with both H_1 and H_2 BSM states) exists at present[2], we can use its similarity to resonant di-Higgs searches in the $b\bar{b}b\bar{b}$ final state to validate our analysis for $m_{H_2} = 125$ GeV, before extending it to the two-dimensional mass plane (m_{H_1}, m_{H_2}). We follow the recent LHC $\sqrt{s} = 13$ TeV CMS search for a narrow di-Higgs resonance in the $b\bar{b}b\bar{b}$ final state with 35.9 fb^{-1} of integrated luminosity [508], reproducing the reported selection efficiencies with our simulations. We then perform an analysis of the expected signal efficiencies for the $pp \to H_1 \to H_2 H_2 \to b\bar{b}b\bar{b}$ process in the mass plane (m_{H_1}, m_{H_2}), and finally provide an estimate of the 95% C.L. exclusion sensitivity on the H_1 production cross section multiplied by the branching fractions to H_2 and $4b$ at 13 TeV LHC with 35.9 fb^{-1} from this search.

2 CMS resonant di-Higgs searches for $\sqrt{s} = 13$ TeV in the $b\bar{b}b\bar{b}$ final state

To validate our analysis, we use the 13 TeV CMS $pp \to X \to hh \to b\bar{b}b\bar{b}$ search [508] (see also [509]). This considers X to be both a spin-0 ("radion") and spin-2 ("KK graviton") state, and it provides the signal efficiencies at various stages (ranging from the initial event selection to the definition of the final signal region) for the spin-2 scenario[3]. The search defines two kinematic regions which feature different event selection criteria: a low-mass-region (LMR) for masses $m_X \in [250, 620]$ GeV, and a medium-mass-region (MMR) for masses $m_X \in [550, 1200]$ GeV. The transition region $m_X \sim 580$ GeV is determined by the respective sensitivities of the LMR and MMR selection strategies [508].

In this work we concentrate on the MMR selection, for reasons that we explain below. As an online trigger selection, Reference [508] requires either of two conditions:

i) 4 reconstructed jets of $p_T > 30$ GeV, of which two satisfy $p_T > 90$ GeV, and three are b-tagged.

ii) 4 reconstructed jets of $p_T > 45$ GeV, of which three are b-tagged.

The analysis subsequently requires all four selected jets to be b-tagged and have $|\eta| < 2.4$. This initial selection stage, labelled *4b*, is common to both LMR and MMR selections. For the MMR selection, the analysis then identifies two 125 GeV Higgs boson candidates (*HH candidate*) by requiring two b-jet pairs with $\Delta R_{bb} < 1.5$ for each pair[4]. We note that ΔR_{bb} depends only on the mass ratio m_X/m_h [522], and as such the ratio of signal efficiencies at *4b* and *HH candidate* stage can in principle be directly extrapolated to a two-dimensional mass plane (this partially justifies our choice of MMR selection). Finally, the signal region (*SR*) is defined in the two dimensional space of the reconstructed masses of the Higgs boson candidates, m_{h_1} and m_{h_2}, as the circular region with $\chi < 1$, where χ is defined as

$$\chi = \sqrt{\left(\frac{m_{h_1} - C}{R}\right)^2 + \left(\frac{m_{h_2} - C}{R}\right)^2}. \tag{1}$$

[2]We however note there are existing LHC analyses for $h \to AA$, with h the 125 GeV Higgs boson (see e.g. [372]).

[3]The signal efficiencies for spin-0 and spin-2 are nevertheless found to be very similar [508]. We will provide a detailed analysis validation for both spin-0 and spin-2 efficiencies elsewhere.

[4]In case of multiple *HH candidates* in an event, the combination that minimizes χ as defined in (1) is chosen.

The values of these parameters are set to $(C,\ R) = (115,\ 23)$ GeV in [509] while [508] chooses $(C,\ R) = (125,\ 20)$ GeV for the MMR category. However, Reference [508] applies a multivariate regression technique to improve the $b\bar{b}$ invariant mass resolution[5], which we cannot mimic in the present analysis). We therefore keep the values used in the older analysis which are found to better capture the centre of the Higgs peak post- parton shower and detector simulation.

In order to reproduce the CMS signal efficiencies in [508], we use the Randall-Sundrum model available in MADGRAPH5_AMC@NLO [95] to generate $pp \to X \to hh \to b\bar{b}b\bar{b}$ (with X a spin-2 state) event samples merged with up to two additional jets using the MLM procedure [523], with XQCUT=30 GeV. We simulated m_X in the range 400 GeV – 1200 GeV with a fixed width of 10 GeV to match the MMR selection efficiencies provided by [508]. We then shower/hadronise our events with PYTHIA 8.2 [97], matched using the shower-k_T scheme and use DELPHES [186] for a simulation of the CMS detector performance which also makes use of FASTJET [99] to cluster anti-k_T jets with radius 0.4. A crucial ingredient in this last step concerns the 13 TeV CMS b-tagging efficiencies (as well as the c-jet and light-jet mistag rates) as a function of the jet p_T and η. We model these using the information from [274], assuming the performance of the *DeepCSV* b-tagging algorithm for the same operating point as used in [508].

Our simulated signal efficiencies at the HH *candidate* and *SR* stages are shown in Figure 1, together with the corresponding CMS efficiencies from [508] for comparison. We find good agreement, with a moderate mismatch at the HH selection level within the expected accuracy of a fast detector simulation. The agreement is particularly good for the *SR* selection with $m_X > 600$ GeV, precisely where the MMR category is expected to yield the strongest sensitivity. This allows for a fairly robust extension of the CMS signal efficiencies to the mass plane (m_{H_1}, m_{H_2}), which we do in the next section.

3 Extending CMS resonant di-Higgs searches to search for new scalars: $H_1 \to H_2 H_2 \to b\bar{b}b\bar{b}$

Once we have validated the CMS analysis, we can proceed to extend the search to the two dimensional mass plane: we implement the (Type I) 2HDM model in FEYNRULES [91] and generate $pp \to H_1 \to H_2 H_2 \to b\bar{b}b\bar{b}$ event samples with MADGRAPH5_AMC@NLO (we follow the procedure discussed in the previous section with the only difference being the generation of samples merged with up to one additional jet to reduce computing time) in a (m_{H_1}, m_{H_2}) mass grid, in order to obtain the signal efficiencies at the SR selection stage in the (m_{H_1}, m_{H_2}) plane. The widths of the two scalar states are kept at 1 GeV to ensure consistency with the narrow width hypothesis of the search.

Our mass grid scan is defined as follows: we vary m_{H_2} in the range $m_{H_2} \in [65,\ 290]$ GeV in steps of 15 GeV; For each m_{H_2}, the minimum value of m_{H_1} we consider is given by $m_{H_1}^{\min} = m_{H_2} \times 400/125 = 3.2 \times m_{H_2}$, since the minimum mass ratio in the CMS MMR region is $m_X/m_h = 400/125$, and we choose not to extrapolate the CMS efficiencies from [508] outside of regions that we did not explicitly validate for the 125 GeV case. Similarly, the maximum value of m_{H_1} we consider is given by $m_{H_2} \times 1200/125$. Since we only perform our search up to $m_{H_1} = 1200$ GeV, we define $m_{H_1}^{\max} = \text{Min}\,(1200\,\text{GeV},\ m_{H_2} \times 1200/125)$, and consider values of m_{H_1} in the range $m_{H_1} \in [m_{H_1}^{\min}, m_{H_1}^{\max}]$. In principle, given that we have validated the

[5]Incidentally, this is also a reason why we focus on the MMR, since for LMR this technique is also applied at the HH *candidate* level.

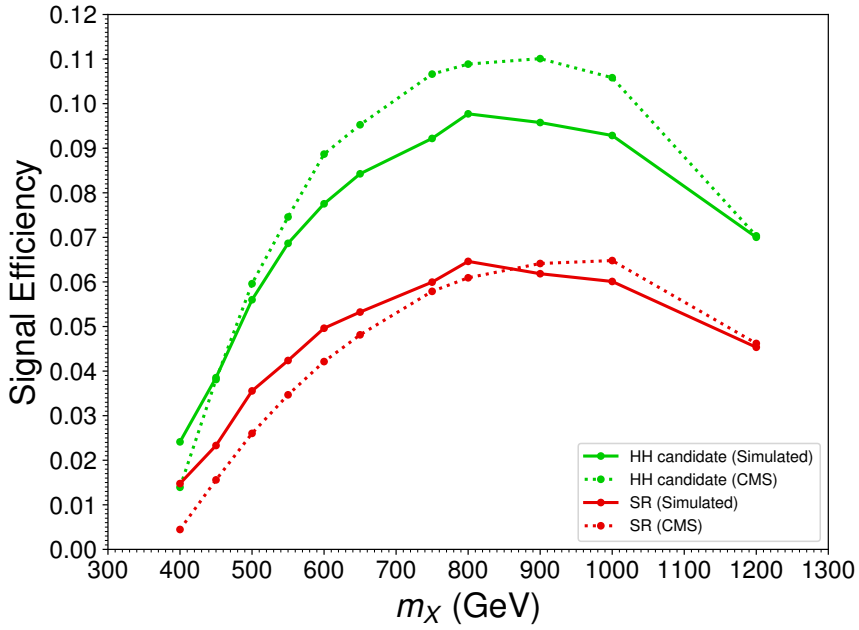

Figure 1: Signal efficiencies as a function of m_X at HH (green) and SR (red) selection stages (as defined in the text) for spin-2 X resonant di-Higgs production in the $b\bar{b}b\bar{b}$ final state. Solid lines correspond to our simulation, while dotted lines correspond to the efficiencies from the 13 TeV CMS analysis [508].

analysis over a fairly broad mass range, the possibility of extrapolating our analysis outside of the validation region is not unreasonable, however we opt to remain somewhat conservative and postpone this to a future investigation.

Next, we implement the same MMR category event selection described in the previous section for the case of $pp \to X \to hh \to b\bar{b}b\bar{b}$, up to the HH selection stage. In order to perform the SR selection, we use Equation (1) with a varying $C = m_{H_2} - 10$ GeV to account for the shift in the signal di-jet invariant mass peak as m_{H_2} changes (since now the invariant mass distributions m_{h_1} and m_{h_2} from Equation (1) are observed to peak around $\sim m_{H_2} - 10$ GeV). The resulting signal efficiency map for the SR selection stage in the (m_{H_1}, m_{H_2}) plane is shown in Figure 2. We note that, similarly to the case of the previous section, we expect an analysis based on the LMR selection from [508] to yield higher signal efficiencies than those shown in Figure 2 for the lower mass ratios $m_{H_1} < m_{H_2} \times 580/125 \simeq 4.6 \times m_{H_2}$. At the same time, for $m_{H_1} > m_{H_2} \times 900/125 = 7.2 \times m_{H_2}$ an analysis clustering each H_2-candidate into a fat-jet would also be more sensitive [508] than the present one. Still, the present analysis provides a conservative estimate of the prospective sensitivity a search for $pp \to H_1 \to H_2 H_2 \to b\bar{b}b\bar{b}$ could yield.

The 13 TeV CMS $pp \to X \to hh \to b\bar{b}b\bar{b}$ analysis [508] also provides a data-driven estimate of event yields for the dominant SM multi-jet background after HH selection as a function of the invariant mass of the reconstructed b-jet pairs, m_{h_1} and m_{h_2}. This allows us to directly apply our modified SR selection to the multi-jet background. Using the similar mass grid to the one discussed above for the signal (varying m_{H_2} in the range $m_{H_2} \in [65,\ 290]$ GeV), we compute the expected number of SM background events after SR selection as a function of m_{H_2}. With this information, we can estimate the number of signal events after SR selection that would be excluded at 95% C.L. as a function of m_{H_2}, based on the number of

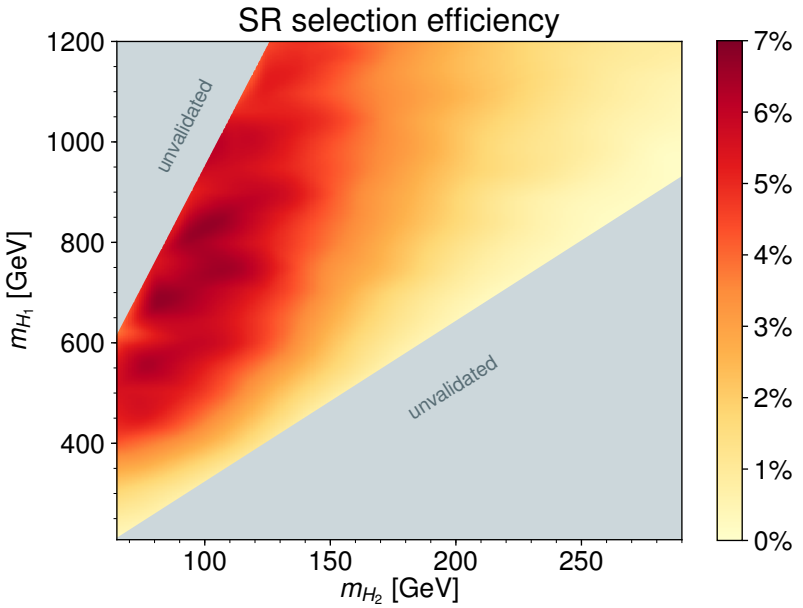

Figure 2: Signal ($pp \to H_1 \to H_2H_2 \to b\bar{b}b\bar{b}$) efficiency at the SR selection stage for the MMR selection category (see text for details), in the (m_{H_1}, m_{H_2}) mass plane.

signal and background events after SR selection and assuming that only the multi-jet yield is observed. We use here an approximate $S/\sqrt{S+B} = 2$ criterion, and leave a more precise assessment, including also background systematic uncertainties, for the future. We stress that our estimate does not make use of any information regarding m_{H_1} for the signal, and as such could be significantly improved by a dedicated search. Combining the corresponding number of excluded signal events with the signal efficiency map from Figure 2, we finally extract the 95% C.L. cross section times branching ratio exclusion sensitivity (in fb) for $pp \to H_1 \to H_2H_2 \to b\bar{b}b\bar{b}$ in the (m_{H_1}, m_{H_2}) plane, for LHC 13 TeV with an integrated luminosity of 35.9 fb^{-1}, shown in Figure 3.

While we leave model-dependent interpretations of the projection to a future study, it is interesting to see that production cross sections times branching fractions in the region of several tens of fb can be accessed in the optimal high m_{H_1} region above 600 GeV in this albeit simplified approximation of the analysis at hand. The very large multijet background at the lower end of the invariant mass spectra has as significant degrading effect on the overall sensitivity which combines with the reduced selection efficiency in this region, as seen in Figure 2. One can compare the ∼pb sensitivity to the typical SM Higgs production cross section by gluon fusion of around 40 pb, suggesting that one may still retain sensitivity to realistic models of new scalars around this mass. In this regard, it will be important to re-examine the validity of the narrow width approximation employed throughout this analysis in future work given the fact that bosonic partial widths tend to grow relatively fast with the resonance mass.

4 Conclusions

Searches for additional Higgs bosons at the LHC via new scalar decay modes are a key avenue to explore extensions of the SM Higgs sector. We have presented here the first study of the $pp \to H_1 \to H_2H_2 \to b\bar{b}b\bar{b}$ channel, with both H_1 and H_2 being BSM states. A relatively

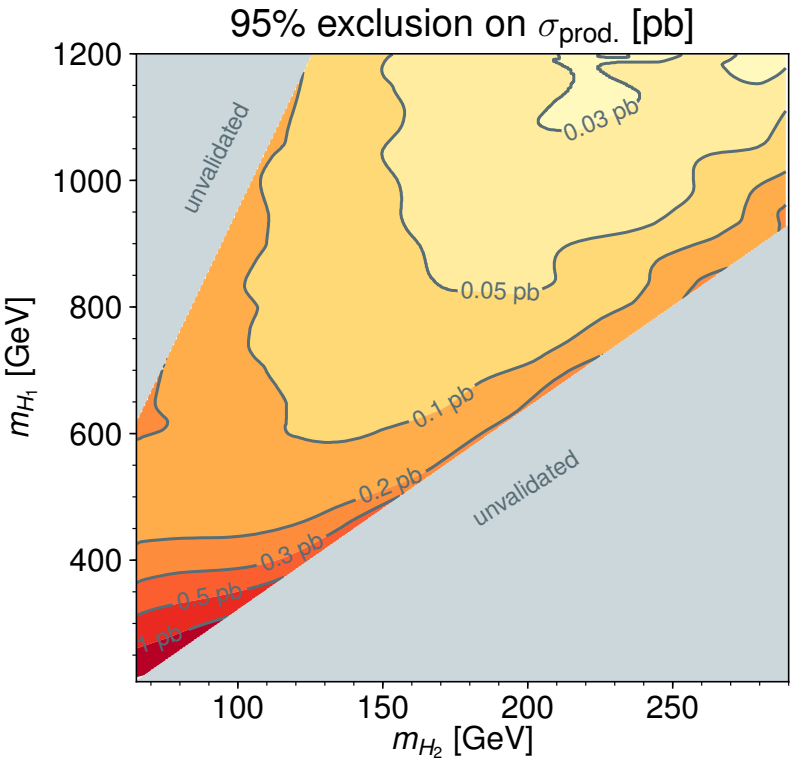

Figure 3: Estimated 95% C.L. $\sigma\times$ BR exclusion sensitivity for $pp \to H_1 \to H_2H_2 \to b\bar{b}b\bar{b}$ in the (m_{H_1}, m_{H_2}) plane for LHC 13 TeV with an integrated luminosity of 35.9 fb^{-1}.

precise estimate of the LHC sensitivity of such a search is possible given its similarity with CMS and ATLAS resonant di-Higgs searches, which we have benefited from to validate our analysis, specifically using for this purpose the latest $\sqrt{s} = 13$ TeV CMS resonant di-Higgs search in the $b\bar{b}b\bar{b}$ final state [508].

Production cross sections time branching fractions for the heavy scalar state ranging from the picobarn to tens of femtobarns appear accessible at the price of a simple generalisation of an existing LHC search. Further optimisation taking into account the heavy resonance mass is likely to yield appreciable improvements in this sensitivity. Our study shows promising prospects for this yet unexplored probe of heavy Higgs bosons, and shows explicitly how extending the coverage of current LHC searches for new scalars can yield new avenues to search for non-minimal Higgs sectors.

Acknowledgements

K.M. is supported in part by the Belgian Federal Science Policy Office through the Interuniversity Attraction Pole P7/37 and by the European Union's Horizon 2020 research and innovation programme under the Marie Skłodowska-Curie grant agreement No. 707983. J.M.N. is supported by the European Research Council under the European Union's Horizon 2020 program (ERC Grant Agreement no.648680 DARKHORIZONS). The work of C.V. is supported by Fermi Research Alliance, LLC under Contract No. DE-AC02-07CH11359 with the U.S. Department of Energy, Office of Science, Office of High Energy Physics.

Contribution 19

Interferences in searches for heavy Higgs bosons

A. Carvalho, R. Gröber, S. Liebler, J. Quevillon

Abstract

We study the relevance of interferences in the search for heavy Higgs bosons in hh and Zh final states, where h labels the SM-like Higgs boson at 125 GeV and Z is the Z boson. We study generic scenarios in terms of a few parameters, which we choose in accordance with simple extended Higgs sectors. Interferences do not only enhance or weaken signal contributions, but through a peak-dip-like structure can also shift the invariant mass distributions in terms of the final state in both directions. For their classification we introduce three parameters. We find the signal-over-background ratio very helpful in discriminating the relevance of interference effects.

1 INTRODUCTION

After the discovery of the Standard Model (SM)-like Higgs boson at 125 GeV the quest for additional Higgs bosons, part of extended Higgs sectors, is ongoing. Extensions of the SM Higgs sector can contain several new CP-even H and/or CP-odd Higgs bosons A, or in case of CP violation also mixtures of them. In the following we denote such additional Higgs bosons generically by φ. Searches for them are performed in a variety of final states involving SM particles, among them also the newly discovered SM-like Higgs boson h. In such studies most experimental analysis use a narrow width approximation, which allows to split production $gg \to \varphi$ and decay $\varphi \to F$, where F denotes a generic final state. In that case the cross section for $gg \to \varphi \to F$ is obtained according to $\sigma = \sigma(gg \to \varphi)\text{BR}(\varphi \to F)$, which allows to take into account higher order corrections independently for the initial state production of the particle φ and it subsequent decay into F. The narrow-width approximation on the other hand misses the inclusion of interference effects of Feynman diagrams involving the s-channel Higgs boson φ and SM background diagrams $gg \to F$, which can also involve an s-channel SM Higgs boson h. Such interferences do not only enhance or lower the signal contribution $gg \to \varphi \to F$, but also distort the peak structure in the invariant mass distribution m_F of the final state substantially. Interference effects on the φ line-shape might be able to provide crucial information on both the real and imaginary parts of the $gg \to \varphi \to F$ amplitude, providing supplementary constraints on the properties of the new state φ.

There is an extensive literature on interference effects on the corresponding signals of the SM-like 125 GeV Higgs boson h, in the $\gamma\gamma$ and $ZZ^\star$ final states, which might generate an observable difference between the apparent masses measured in these final states [524, 525] and/or provide loose indirect constraints on the total width of the SM Higgs [312].

There have also been pioneering studies of possible interference effects in the decays of a heavy Higgs boson into $t\bar{t}$ final states, in both the SM [526–528] and Two-Higgs-Doublet

models [529–535]. Within the last years various theoretical works pointed out the relevance of interference effects in the search for heavy Higgs bosons. Such effects are dependent on the initial and final state, and model dependent. Rather generic studies beyond concrete model realizations were performed for the $t\bar{t}$ and the $\gamma\gamma$ final states in Refs. [536, 537]. Interference effects in $gg \to \varphi \to t\bar{t}$ in a Two-Higgs-Doublet Model were studied including NLO QCD effects in Refs. [538, 539]. An exhaustive discussion with polarization and spin effects can also be found in Refs. [540, 541]. A search for heavy pseudoscalar and scalar Higgs bosons decaying into a top quark pair including interference effects has been performed by ATLAS with $20.3\,\text{fb}^{-1}$ of collected data at a center-of-mass energy of $\sqrt{s} = 8\,\text{TeV}$ [542].

For rather model independent and generic studies for $pp \to \varphi \to gg$ and to different fermionic final states we refer to Ref. [543] and Ref. [534], respectively. The final state VV, where V denotes a vector boson, is more involved, since generic models miss to properly account for the right unitarization of the cross section at high invariant masses. It is thus recommendable to work in a concrete model setup, which are usually the extension of the SM Higgs sector with one singlet or one doublet. Note also that in this case φ is supposed to be CP-even. For $gg \to \varphi \to VV$ in the SM+singlet we refer to Refs. [544, 545], for vector boson fusion in the same model setup to Ref. [546], for a study with decays into two leptons and two quarks, i.e. $gg \to \varphi \to VV \to 2l2q$, to Ref. [547]. In the context of the Two-Higgs-Doublet Model studies were carried out in Refs. [548, 549]. The final state hh in $gg \to \varphi \to hh$ was covered in the context of a Two-Higgs-Doublet in Ref. [550] and in the SM+singlet in Ref. [551] and in Ref. [552] taking into account NLO corrections. Lastly the final state involving a Z boson and the SM-like Higgs boson, i.e. the process $gg \to A \to Zh$ shows similar effects. Here φ is CP-odd in concrete model interpretations. In the context of the Two-Higgs-Doublet Model we refer to Refs. [553, 554]. Finally another interesting aspect is the interference of Higgs bosons among themselves, which was for example discussed in Refs. [555–557].

In this work we focus on the two final states $gg \to hh$ and $gg \to Zh$, which are of relevance for SM Higgs precision measurements and the search for new physics in various aspects: The process $gg \to hh$ allows for a measurement of the triple Higgs coupling [558–560], which can be strongly modified in scalar extensions of the SM [561], or for an anomalous $t\bar{t}hh$ coupling [562–565]. The $gg \to Zh$ process, which is formally part of the next-to-next-to leading order corrections to associated production of Zh, where the leading order process is the Drell-Yan process, allows for the measurement of couplings of the Higgs boson to vector boson and the bottom-quark or anomalous interactions of the Higgs bosons and of top quarks to SM states [553, 566, 567]. In order to reduce background experimental analysis often consider high transverse momenta of the vector boson, where the relevance of the gluon-induced component $gg \to Zh$ compared to the Drell-Yan like component is substantially enhanced [553].

For the two mentioned processes we want to classify interferences and provide a recipe that allows to estimate when such interference effects are of relevance. The relevance of interferences is not only classified by the ratio of the width Γ_φ and the mass m_φ, Γ_φ/m_φ, but in particular the strength of the signal contribution over the background is a strong indication, how large interference effects are expected to be. On the other hand the narrow-width approximation usually only assumes the ratio Γ_φ/m_φ to be small. Moreover a distortion of the peak structure is usually visible already before a significant effect on the total peak-integrated signal cross section including interferences is observed. For this purpose we define two asymmetric parameters.

Our contribution is structured as follows: We first describe our calculational setup in-

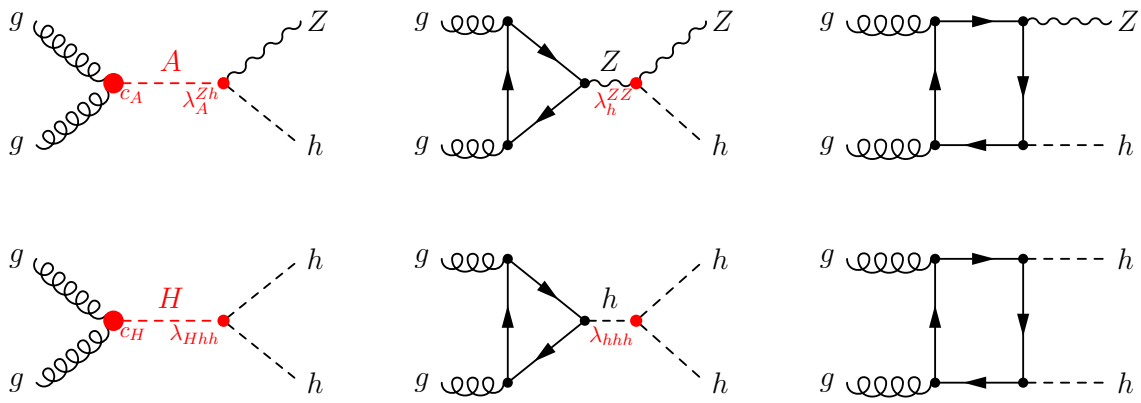

Figure 1: Feynman diagrams of the two processes $gg \to Zh$ (upper row) and $gg \to hh$ (lower row). The two left Feynman diagrams form the signal amplitudes A_S, see Sct. 2.3, the other diagrams enter the background amplitudes A_B.

cluding the simplified parametrization of the process that we employ. We continue with its implementation into our codes used for the numerical analysis. Subsequently we provide the classification of interferences in terms of three parameters and then present our results, before we comment on their relevance for the experimental searches.

2 CALCULATIONAL SETUP

2.1 Simplified parametrization of the processes

We discuss the two processes $gg \to H \to hh$ and $gg \to A \to Zh$ in this manuscript. Relevant sample Feynman diagrams are depicted in Fig. 1. We assume effective couplings of the Higgs bosons H and A to two gluons according to

$$L \supset \frac{\alpha_s}{12\pi v} c_H \, H G^a_{\mu\nu} G^{a,\mu\nu} + \frac{\alpha_s}{8\pi v} c_A \, A G^a_{\mu\nu} \tilde{G}^{a,\mu\nu} \,. \tag{1}$$

These formulas include the strong-coupling constant α_s, the vacuum expectation value $v = 1/\sqrt{\sqrt{2} G_F} \approx 246\,\text{GeV}$ and Wilson coefficients c_H and c_A, which are normalized such, that for $c_A = c_H = 1$ the coupling of H and A to two gluons resembles the one obtained through a top-quark loop with an infinitely heavy top-quark mass. $G^a_{\mu\nu}$ denotes the gluonic field strength tensor with color index a and Lorentz indices μ and ν, and $\tilde{G}^a_{\mu\nu} \equiv \varepsilon_{\mu\nu\rho\sigma} G^{a,\rho\sigma}$ is its dual with $\varepsilon^{0123} = +1$.

We allow the two coefficients $c_\varphi = |c_\varphi| e^{i\theta_\varphi}$ to be complex, since particles Q, which run in a potential loop and couple φ to two gluons, induce a complex contribution to the amplitude for $2m_Q \leq m_\varphi$. Formally the description through an effective operator for such loop contributions is not valid, but since we are not restricted to a specific model and treat c_φ as a generic parameter it makes sense to condense the amplitude in a (complex-valued) Wilson coefficient of the given form. We assume the masses and total widths of H and A to be free parameters. In summary we have the following parameters, that are identical for both processes:

$$|c_\varphi|, e^{i\theta_\varphi}, m_\varphi, \Gamma_\varphi \tag{2}$$

In addition we have the following process-specific parameters: The process $gg \to hh$ involves the trilinear Higgs self-couplings λ_{hhh} and λ_{Hhh}, which are both normalized with respect to the SM Higgs self-coupling. We allow both to be free, but any variation of λ_{Hhh} can also be condensed into the Wilson coefficient c_H. The process $gg \to Zh$ includes the coupling of the light Higgs boson to gauge bosons, λ_h^{VV}, which we normalize with respect to the SM coupling. In addition the pseudoscalar coupling to the light Higgs and the Z boson is of relevance, which we name λ_Z^{Ah} and which corresponds to g_Z^{Ah} in the Appendix of Ref. [553]. Inspired by the Higgs sector of a Two-Higgs-Doublet Model we set the relative strength of the coupling λ_Z^{Ah} equal to $\lambda_H^{VV} = \sqrt{1-(\lambda_h^{VV})^2}$. The coupling λ_h^{VV} is experimentally restricted to be close to 1. Practically again any variation of λ_Z^{Ah} can also be shifted into the Wilson coefficient c_A, but due to the assumed correlation of Higgs and gauge boson couplings we change its value. For both processes the light Higgs h is assumed to couple with SM strength to all quarks in our simplified parametrization.

2.2 Employed codes

For the evaluation of the differential cross sections we use a modified version of `HPAIR` [568] for di-Higgs production and `vh@nnlo` [569] for Zh production. Both `vh@nnlo` and `HPAIR` include the s-channel propagator $gg \to \varphi \to F$, i.e. $gg \to A \to Zh$ and $gg \to H \to hh$ respectively, in the form of a Breit-Wigner propagator

$$\frac{1}{m_F^2 - m_\varphi^2 + i\Gamma_\varphi m_\varphi} \tag{3}$$

with the final state invariant mass m_F. Even though higher order corrections to gluon fusion processes are generically quite high, we restrict ourselves to the leading-order result. In the infinite top mass limit the K-factors in beyond-the Standard Model extensions are not expected to vary much with respect to the SM, even in the presence of a new resonance, [552,570–572], so when showing ratios we can assume them to drop out. Our results are based on hadronic cross sections for the LHC integrated over the gluon luminosities. Still, for simplicity our studies could be performed at the partonic level also, since only the relative importance of interferences in the vicinity of the internal masses are investigated. This on the other hand implies that our results are mostly independent of the center-of-mass energy of a hadron collider and even more of the employed parton distribution functions.

2.3 Classification of interferences

In order to classify the interferences we split the cross section as a function of the invariant mass of the final state $d\sigma/dm_F$ in three contributions

$$\frac{d\sigma}{dm_F} = \frac{d\sigma_S}{dm_F} + \frac{d\sigma_I}{dm_F} + \frac{d\sigma_B}{dm_F}\,. \tag{4}$$

Therein, the signal contribution S only includes the s-channel Feynman diagram $gg \to \varphi \to F$ involving the heavy scalar φ, whereas the background B sums up the square of all other Feynman diagrams, including the s-channel Feynman diagrams involving SM particles, i.e. h and Z. With background we mean the non-resonant di-Higgs contribution or the non-resonant $gg \to Zh$ production.

The interference contribution I is proportional to $2\mathrm{Re}(A_S A_B^*)$, where A_S and A_B denote the amplitudes of signal and background diagrams, respectively. This split of amplitudes is

gauge-invariant. We define

$$\begin{aligned}
\eta &= \int_{m_\varphi-10\Gamma_\varphi}^{m_\varphi+10\Gamma_\varphi} dm_F \left(\frac{d\sigma_S}{dm_F}+\frac{d\sigma_I}{dm_F}\right) \Bigg/ \int_{m_\varphi-10\Gamma_\varphi}^{m_\varphi+10\Gamma_\varphi} dm_F \left(\frac{d\sigma_S}{dm_F}\right) \\
\eta_- &= \int_{m_\varphi-10\Gamma_\varphi}^{m_F^I} dm_F \left(\frac{d\sigma_S}{dm_F}+\frac{d\sigma_I}{dm_F}\right) \Bigg/ \int_{m_\varphi-10\Gamma_\varphi}^{m_F^I} dm_F \left(\frac{d\sigma_S}{dm_F}\right) \\
\eta_+ &= \int_{m_F^I}^{m_\varphi+10\Gamma_\varphi} dm_F \left(\frac{d\sigma_S}{dm_F}+\frac{d\sigma_I}{dm_F}\right) \Bigg/ \int_{m_F^I}^{m_\varphi+10\Gamma_\varphi} dm_F \left(\frac{d\sigma_S}{dm_F}\right) .
\end{aligned} \tag{5}$$

The definition includes the overall factor η, which is a relative factor that, if multiplied with the signal cross section σ_S, yields the overall change of the signal cross section due to interference effects. Still, as already indicated, interference effects also distort the peak structure substantially. If the two curves $d(\sigma_S+\sigma_I)/dm_F$ and $d\sigma_S/dm_F$ intersect once, at $m_F = m_F^I$, we in addition split the integrals into two components and define the corresponding factors η_- and η_+. Example for both cases are given in Fig. 2. If the two curves do not intersect, we set $\eta_\pm = 0$. If non-zero, $\eta_\pm$ can be quite large, whereas the overall effect of the interference remains small. An example is given in Fig. 2 (right), where $\eta = 1.34$, $\eta_- = 35.02$ and $\eta_+ = -30.28$. If the peak structure of the the heavy scalars φ can be experimentally resolved, the factors $\eta_\pm$ thus yield a useful classification of interference effects, since they allow to deduce in which direction the peak shift occurs and in which way a peak-dip structure appears. The boundaries of the integrals being $m_\varphi \pm 10\Gamma_\varphi$ capture the majority of the peak structure, which is suppressed by the form of the Breit-Wigner propagator, see Eq. 3.

In our subsequent scans over the parameter space we will thus deal with the three factors η, η_- and η_+ to classify interference effects. For very large width the boundaries $\pm 10\Gamma_\varphi$ span a large invariant mass range. In case it includes thresholds in the background Feynman diagrams, like at $m_F \approx 2m_t$ in the triangle loop producing a Z boson or the SM-like Higgs, we leave out the corresponding width choice, since such cases need a more thorough study of the interference effects.

We will present the parameters η, $\eta_\pm$ as a function of the ratio Γ_φ/m_φ and as a function of the signal-over-background cross sections. For this purpose we define

$$\sigma_{sig} = \int_{m_\varphi-10\Gamma_\varphi}^{m_\varphi+10\Gamma_\varphi} dm_F \frac{d\sigma_S}{dm_F} \qquad \text{and} \qquad \sigma_{back} = \int_{m_\varphi-10\Gamma_\varphi}^{m_\varphi+10\Gamma_\varphi} dm_F \frac{d\sigma_B}{dm_F} , \tag{6}$$

which are integrated signal and background cross sections within an invariant mass window of $\pm 10\Gamma_\varphi$.[1] The choice $\pm 10\Gamma_\varphi$ captures the majority of the signal contribution. Normalizing each, σ_{sig} and σ_{back}, to $20\Gamma_\varphi$ is not needed, since we only consider their ratio $\sigma_{sig}/\sigma_{back}$ subsequently. Lastly keep in mind that the background in the Zh case includes only the gluon-induced component, but omits the Drell-Yan like component starting with light quarks in the initial state.

[1] For a comparison with the experiment, it might instead be useful to define σ_{sig} and σ_{back} in terms of the bin width in the invariant mass of different experimental searches. We leave this for future work.

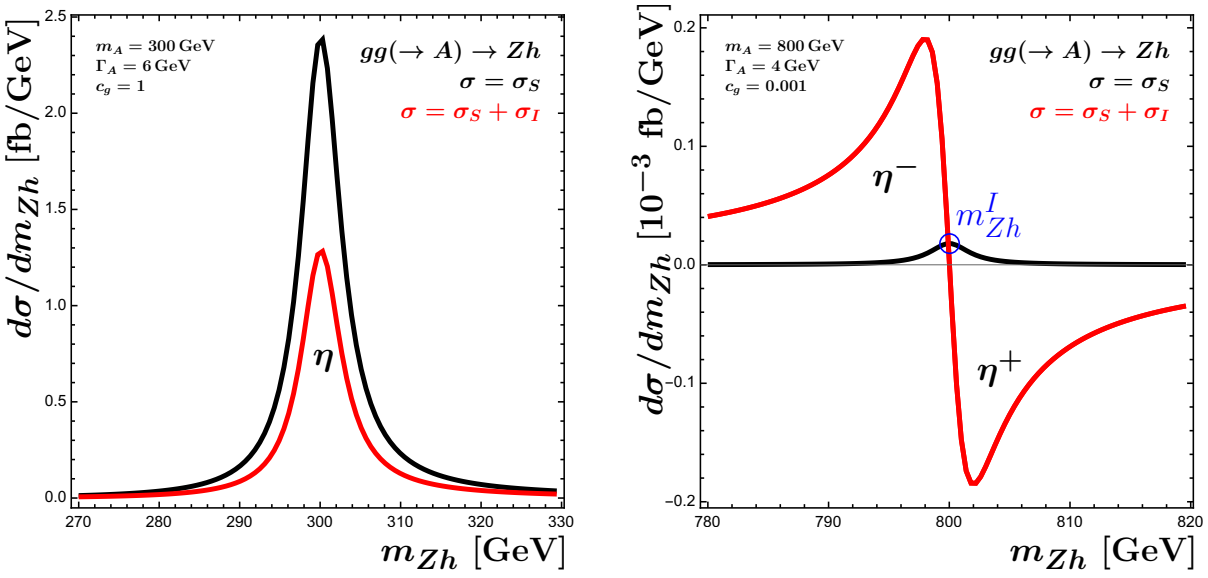

Figure 2: Classification of interference effects through η, η_+ and η_- for two parameter sets of $gg(\to A) \to Zh$. Only a window of $\pm 5\Gamma_A$ in m_{Zh} is shown.

3 NUMERICAL RESULTS

In order to show numerical results we vary the parameters involved in both processes within the following ranges

$$|c_\varphi| \in [0.001, 5]\,, \quad \theta_\varphi \in \{0, \frac{\pi}{4}, \frac{\pi}{2}\}, \quad m_\varphi \in [0.3, 1.4]\ \text{TeV}, \quad \Gamma_\varphi/m_\varphi \in [10^{-4}, 0.2]\,. \tag{7}$$

As already mentioned, we abandon very large width choices of $\Gamma_\varphi/m_\varphi = \{0.1, 0.2\}$, if they capture thresholds in background diagrams. For λ_{hhh} we choose the values $\lambda_{hhh} = \{0, 1, 2\}$, and we leave $\lambda_{Hhh} = 1$. Keep in mind that both are normalized to the SM, i.e. $\lambda_{hhh} = 1$ yields the SM Higgs self coupling. Any variation in λ_{Hhh} can be shifted to the Wilson coefficient c_H. For the Zh process we pick two choices of λ_h^{VV}, namely 0.97 and 0.995, which yield a SM-like Higgs coupling to gauge bosons λ_h^{VV} compatible with the experimental results, namely differing by 6% and 1% from the SM expectation, respectively. It is well possible that some of the choices are non-physical in the sense that large values of the Wilson coefficient or the involved couplings would also trigger a large decay width, since the heavy intermediate resonance can decay at least into gg and hh or Zh. However, our choices of small widths generally induce a large signal cross section, for which in turn interference effects are small. We thus leave such points in our scan and emphasize that a concrete model realization would properly correlate the total width Γ_φ with the other parameters.

3.1 The process $gg \to hh$

We show the impact of the interference for the hh final state in Fig. 3, where in different colors the values of the overall interference factor η as a function of both ratios Γ_H/m_H and $\sigma_{sig}/\sigma_{back}$ is presented. We split the range of η into four regions, namely in one region in which η differs from 1 by less than 3%, one with more than 3%, one with more than 10% and the fourth one with more than 50%. It is apparent that for all values of Γ_H/m_H large interferences can occur.

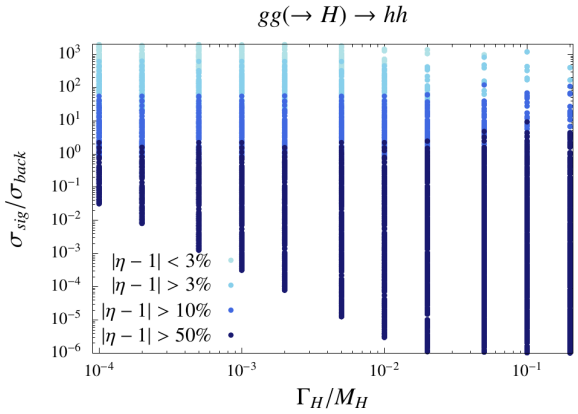

Figure 3: Relative difference of the interference factor η for $gg \to H \to hh$ from 1 in percent in the Γ_H/m_H-$\sigma_{sig}/\sigma_{back}$ plane. The scan was performed in a simplified model for $gg \to H \to hh$, see text.

This implies that Γ_H/m_H is not ideal for discriminating interference effects. On the other hand η clearly correlates with the value of the ratio $\sigma_{sig}/\sigma_{back}$. Even for relatively large ratios of $\sigma_{sig}/\sigma_{back} > 1$ interferences of 50% are observed.

In Fig. 4 we show $|\eta|$ (left side) and $|\eta_+|$ (right side) as a function of Γ_H/m_H. For any value of Γ_H/m_H the interference factors $|\eta_{(\pm)}|$ can vanish. On the other hand their largest values are only reached for large width Γ_H. Taking Fig. 3 and Fig. 4 together we can see that the interference effects mostly depend on the ratio of signal-over-background rather than Γ_H/m_H, however, for lower Γ_H/m_H we usually find larger signal-over-background ratios. Lastly we show $|\eta|$ (black points), $|\eta_+|$ (red points) and $|\eta_-|$ (blue points) as a function of $\sigma_{sig}/\sigma_{back}$ in Fig. 5, where the right figure is a zoom of the left figure. It can be inferred, that the interference increases with decreasing $\sigma_{sig}/\sigma_{back}$. The figure can hence give indication when the interference needs to be taken into account in experimental searches. We see that already for $\sigma_{sig} = 10\,\sigma_{back}$ we can have interference effects leading to a cross section increased by a factor of 1.5. The interference factors η_+ and η_- take generally larger values than η, i.e. the peak structure is already distorted before an overall effect on the signal cross section gets significant.

3.2 The process $gg \to Zh$

We continue with a presentation of our results for $gg \to Zh$. Again we present the relative difference of η from 1 in the Γ_A/m_A and $\sigma_{sig}/\sigma_{back}$ plane in Fig. 6 on the left side. The right side shows $|\eta_{(\pm)}|$ as a function of Γ_A/m_A. Even for small width $\Gamma_A/m_A \sim 10^{-4}$ the factors $\eta_\pm$ are non-zero and clearly differ from 1. Finally in Fig. 7 we depict $|\eta|$ and $|\eta_\pm|$ as a function of $\sigma_{sig}/\sigma_{back}$. Significant interferences are observed already at large values of $\sigma_{sig}/\sigma_{back}$. The peak distortion sets in before a significant effect on the overall signal cross section is observed, i.e. at even larger $\sigma_{sig}/\sigma_{back}$. In the context of this figure we emphasize that the peak distortion is strongly dependent on the phase of the Wilson coefficient, for both discussed processes. In almost all cases either η_+ or η_- turns negative, which is mainly dependent on the phase and partially the width Γ_A. A detailed analysis of such effects in concrete model realizations is left for future work.

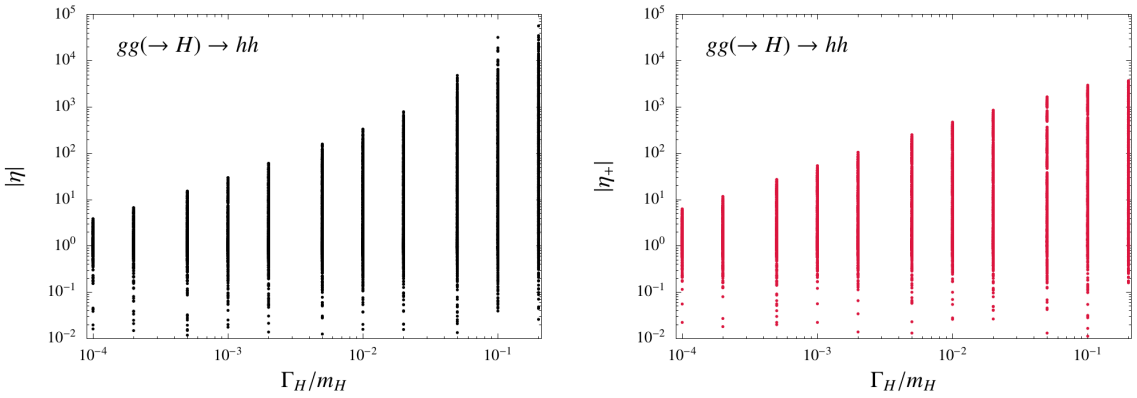

Figure 4: Interference factors η (left side) and η_+ (right side) as a function of Γ_H/m_H for $gg \to H \to hh$.

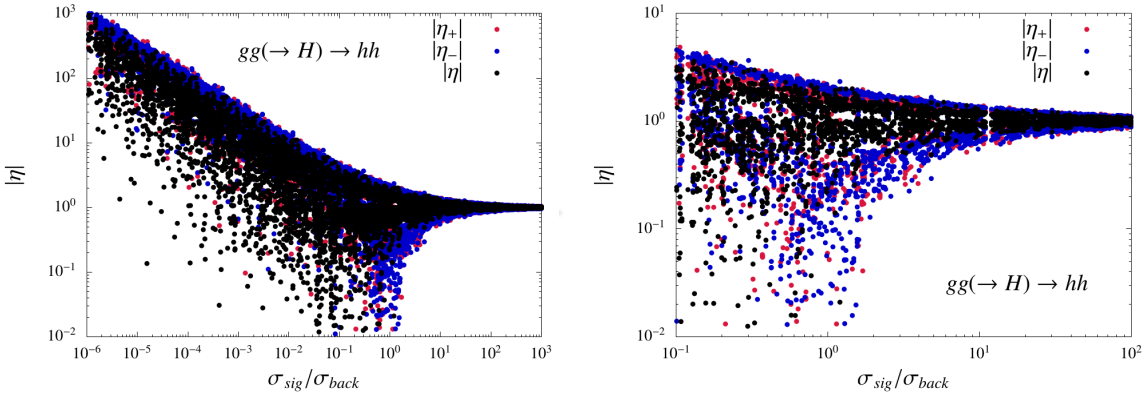

Figure 5: Interference factors η, η_+ and η_- as a function of $\sigma_{sig}/\sigma_{back}$ for $gg \to H \to hh$. The right figure is a zoomed version of the left figure.

4 APPLICATION AT THE LHC

In this study we proposed a parametrization that allows to infer the size of the interference between a heavy intermediate resonance and the SM background in the two processes $gg \to hh$ and $gg \to Zh$. Our results are based on a generic setup and are thus mostly model independent. For a bump search the experimental sensitivity depends mainly on the total width of the resonance and the peak position of the resonance with respect to the true resonance mass. Up to width values of roughly 10% of the mass of the intermediate resonance, the experimental sensitivity is independent of the width, since the peak structure is experimentally not resolvable. When interpreting the experimental results the factor η, being a function of all parameters of the model under consideration, can then be multiplied to the theoretical signal cross section to yield exclusion bounds including interference effects.

On the other hand, our setup is not sufficient to quantify peak shifts, since $\eta_\pm$ only give an estimate of the peak distortion. Again assuming an experimental resolution of 10% in the

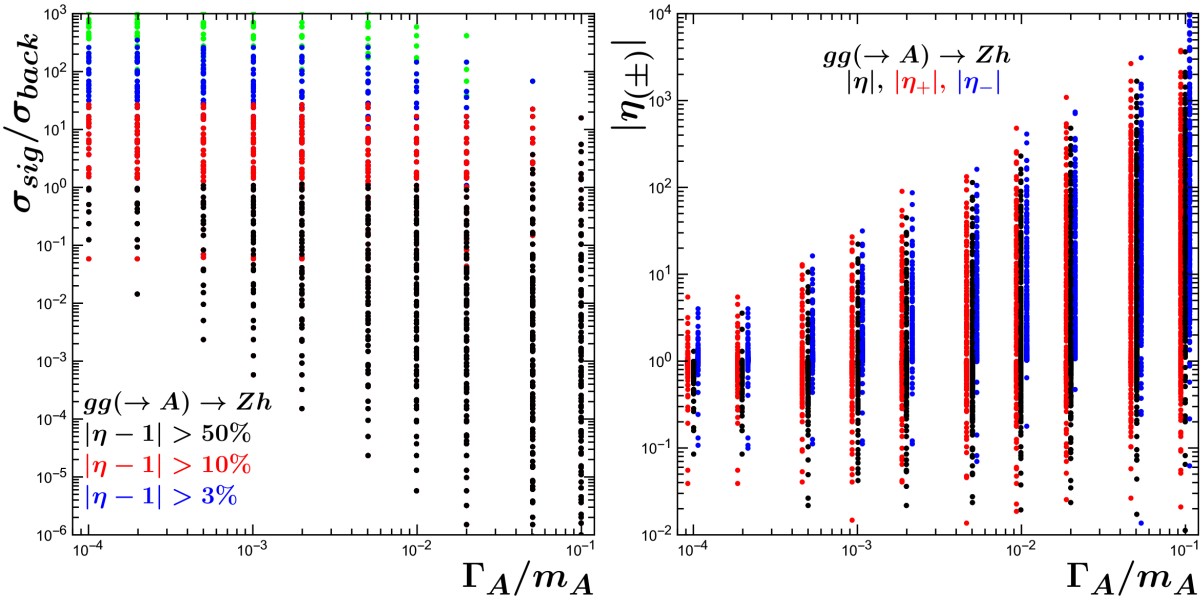

Figure 6: Relative difference of the interference factor η for $gg \to A \to Zh$ from 1 in percent in the Γ_A/m_A-$\sigma_{sig}/\sigma_{back}$ plane (left side). Interference factors η, η_+ and η_- for $gg \to A \to Zh$ as a function of Γ_A/m_A. The scan was performed in a simplified model for $gg \to A \to Zh$, see text.

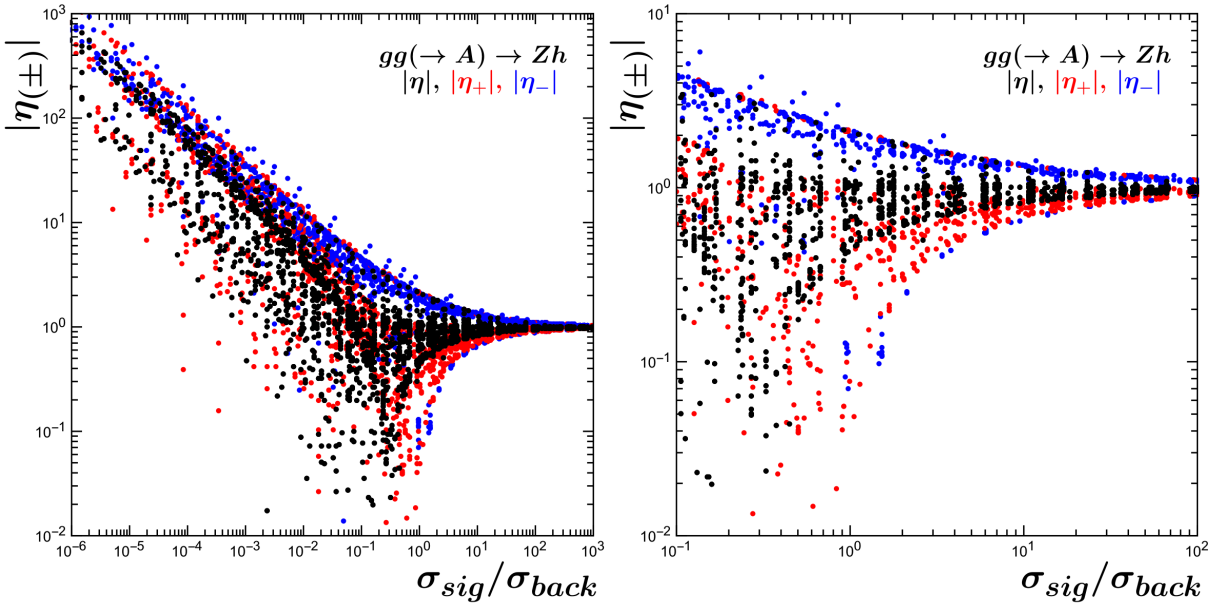

Figure 7: Interference factors η, η_+ and η_- as a function of $\sigma_{sig}/\sigma_{back}$ for $gg \to A \to Zh$. The right figure is a zoomed version of the left figure.

invariant mass spectrum a shift in the mass peak can only be observed if the peak is shifted by more than 10% from the true resonance mass. In such a case only a proper (Monte-Carlo) modeling of the peak-dip like structure allows to infer the true resonance mass. Such a setup was for example used in a heavy resonance search decaying to a top-quark pair, see the ATLAS analysis in Ref. [542], where the signal from a scalar resonance interfere with a huge $t\bar{t}$ background continuum. Therein the changes to the line-shape are drastic and a fit of the mass line-shape to determine the peak mass needs to account for the parameter dependence of the interferences, which is non-trivial. A simplified parametrization of the underlying relevant parameters in terms of a few free parameters, as done here for hh and Zh, is very helpful in this context. Still keep in mind, that the values $\eta_\pm$ alone do not allow to reconstruct the true resonance mass.

For what concerns the hh and Zh final state it is also crucial, which subsequent decays of the final state particles h and Z are considered in the experimental analysis. The invariant mass of the resonance is not always directly used in the signal extraction method of the experimental analysis, or even in intermediate selections. In most of the channels for $\varphi \to hh$ and $\varphi \to Zh$ the mass of φ is not fully reconstructed and alternatively transverse variables or multivariate approaches are used. There are also cases where the invariant mass of the final state is fully reconstructed, but the resolution might not be good enough for the signal extraction when compared to a multivariate approach. One example of the former for both hh and Zh channels is the final state $\tau^+\tau^- b\bar{b}$, where the most sensitive sub-channel is the one where one of the τ's decays leptonically [511, 513]. One example for multivariate approaches are $Zh \to l^+l^- b\bar{b}$ from CMS [573], where a Boosted Decision Tree is used, or $hh \to b\bar{b}b\bar{b}$ from ATLAS where the invariant mass of the reconstructed $H \to b\bar{b}$ decays is used in a 2-dimensional selection [506]. There are indeed examples where the mass of the new resonance is fully reconstructable with a fair resolution to allow it to be used for signal extraction. Examples for the hh final state are $hh \to \gamma\gamma b\bar{b}$ [574, 575].

5 CONCLUSIONS

We classified interference effects between heavy resonances and SM background contributions for the two processes $gg \to hh$ and $gg \to Zh$ through three parameters. We find that the ratio Γ_φ/m_φ involving the width and mass of the intermediate resonance φ is not the best observable to judge if interference effects are large, but at the same time the ratio of the signal-over-background ratio should be considered. In a concrete model realization $\sigma_{sig}/\sigma_{back}$ can be predicted. It can also be experimentally accessed when providing experimental exclusions on the signal cross section. Even for large signal contributions, where $\sigma_{sig}/\sigma_{back}$ is larger than 1, interference effects are sizable and should be taken into account in current experimental analysis. An overall interference factor η to be multiplied with the signal cross section can then be employed while interpreting the bounds in a concrete model realization. More difficult are peak distortions, which we classified in terms of the two parameters $\eta_\pm$. Since η_- and η_+ usually mostly cancel, they individually can be much larger than the overall interference factor η and thus point at large interference effects for even higher ratios $\sigma_{sig}/\sigma_{back}$. We expect very similar observations for the process $gg \to VV$, which we leave to future work. Another aspect for future studies are intermediate spin-2 resonances, which are often considered in the di-Higgs final state. Moreover our generic parameter set might not cover any concrete model realization. A more thorough discussion of concrete models and their mapping to our generic parameter set is thus desirable.

ACKNOWLEDGEMENTS

The authors thank the organizers of the Les Houches Workshop Series “Physics at TeV Colliders” 2017 for the fruitful and pleasant atmosphere. RG is supported by a European Union COFUND/Durham Junior Research Fellowship under the EU grant number 609412. SL acknowledges support from ”BMBF Verbundforschung Teilchenphysik“ under grant number 05H15VKCCA.

Tools and Methods

Contribution 20

Sensitivity of current (and future?) LHC measurements to a new light scalar particle

J. M. Butterworth, S. Fichet, L. Finco, S. Gascon-Shotkin, D. Grellscheid, G. Moreau, P. Richardson, D. Yallup, S. Zhang

Abstract

Additional scalar particles are a generic feature of many well-motivated extensions of Standard Model. Here we use a simplified model in which a light scalar particle couples to electroweak gauge bosons via dimension-5 operators. For the masses considered, decays to pairs of weak bosons are suppressed, and the $\gamma\gamma$ mode dominates. We find that existing measurements from Run I of the LHC already exclude the model over a significant parameter range.

1 INTRODUCTION

Additional light scalar particles are a common feature in extensions of the SM, for example appearing in composite Higgs scenarios, or as the radion in models with extra dimensions [431]. Consideration of precision electroweak measurements, collider searches and flavour physics does not completely exclude the existence of light neutral CP-odd or CP-even scalar particles below the mass of the observed Higgs boson [430]. In this contribution we use a simplified model to examine whether measurements from Run I at the LHC can give information about such possible particles.

2 THE MODEL

We use an effective theory (EFT) approach to describe a scalar with mass M_φ interacting with gauge bosons. The effective theory has $SU(2) \times U(1)_Y$ symmetry. This EFT gives a generic parametrization if $M_\varphi \gg v$ [576], where v is the electroweak scale. Whenever the scalar is light so that $M_\varphi \gg v$ is not true, we make the extra assumption that the scalar has large tree-level $SU(2) \times U(1)_Y$ couplings, so that the loop-induced electroweak-breaking contributions are subleading. Under these conditions the interactions of a CP-even and CP-odd scalars with gauge bosons are respectively described by the following dimension-5 effective Lagrangians

$$\mathcal{L}_{\text{eff}} \supset \varphi \left(\frac{1}{f_G} G^{\mu\nu\, a} G^a_{\mu\nu} + \frac{1}{f_W} W^{\mu\nu\, I} W^I_{\mu\nu} + \frac{1}{f_B} B^{\mu\nu} B_{\mu\nu} + \frac{1}{f_H} |D^\mu H|^2 \right) \tag{1}$$

$$\mathcal{L}_{\text{eff}} \supset \varphi \left(\frac{1}{f_G} G^{\mu\nu\, a} \tilde{G}^a_{\mu\nu} + \frac{1}{f_W} W^{\mu\nu\, I} \tilde{W}^I_{\mu\nu} + \frac{1}{f_B} B^{\mu\nu} \tilde{B}_{\mu\nu} \right) \tag{2}$$

where $\tilde{V}^{\mu\nu} = \frac{1}{2}\epsilon^{\mu\nu\rho\sigma} V_{\rho\sigma}$. The effective theory is valid as long as the f's are larger than the energy going through the vertices. Mixing with the SM Higgs is assumed to be small to ensure that the SM Higgs has SM-like couplings compatible with observations.

The CP-even scalar can for instance be identified as the radion mode present in warped extra-dimension models with bulk gauge fields. Interestingly, if EW brane kinetic terms are negligible in such models, one has $f_W = f_B$ [424, 425], which implies that the $\varphi F^{\mu\nu} Z_{\mu\nu}$ coupling vanishes, a property which can be used for model discrimination [426]. The CP-odd scalar is typically a pseudo Nambu Goldstone boson from an approximate global symmetry, just like those appearing in composite Higgs models. The couplings to gauge fields are induced by the many fermion resonances populating the TeV scale (see e.g [427] or also [428]).

In the following, as a first exercise, we assume a common scale Λ for all couplings,

$$f_G \sim f_B \sim f_W \sim f_H \sim \Lambda\,, \tag{3}$$

and similarly for the CP-odd case.

3 SENSITIVITY OF EXISTING MEASUREMENTS

3.1 Herwig Implementation

The new processes defined by the model described above are exported as UFO file [93] which is read by Herwig 7.2.1 [345, 346]. This requires the four-boson vertices, which were added to the Herwig UFO interface as part of this work and are now available in this subsequently released version. The five-boson vertices implied by the model are not yet implemented but are assumed not to have a major impact. This assumption is supported by a cross-check using MadGraph5_aMC@NLO_v2_5_5 [95] for a selection of the parameter points considered. MadGraph5_aMC@NLO includes the full set of vertices, as well as some higher-order QCD contributions; the cross sections predicted by MadGraph5_aMC@NLO are generally higher than the Herwig values, but are consistent with a factor of two. Thus any limits derived using Herwig are likely to be somewhat conservative.

The scale which suppresses couplings to the Higgs and weak bosons is varied across the range $1 < \Lambda < 10$ TeV; all other BSM coupling are heavily suppressed ($\Lambda = 1000$ TeV). All allowed φ-production processes are generated inclusively.

3.2 Rivet and Contur

Generated Herwig events are passed to the Rivet library of analysis routines [325]. This contains a signficant number of published ATLAS and CMS analyses. Measurements which have been corrected for detector effects to a particle-level fiducial phase space are rather model-independent. Rivet allows the particle-level analysis as performed by the experiments to be applied to the BSM events generated by Herwig. Since the measurements considered have all been compared to precision SM calculations and shown to agree, there is limited room for additional BSM contributions. The Contur comparison package [347] quantifies the level of contribution which could still be consistent with the data. Currently this is done on the assumption that the data are identical to the SM; a more complete approach would be to use the SM predictions and their uncertainties directly; such a capability is a planned future development of Contur, but the present implementation is enough to give a reasonable indication of the sensitivity of the data to BSM models.

3.3 Measurements

All available ATLAS and CMS Rivet analyses are used to study the data. However, since the branching ratio $\varphi \to \gamma\gamma$ is ≈ 1, the measurements of interest are those involving isolated

photons, or pairs of photons, in the final state. These have been measured inclusively [577–579], and in association with jets [580–582], W or Z bosons [583, 584] (i.e. leptons and/or missing energy).

The Higgs fiducial diphoton measurements [314] are also of interest. These were studied and in principle have some sensitivity – events generated by the models considered do contribute to the fiducial region. However, since the value of M_φ considered here lie below the SM Higgs mass, the events which will enter the fiducial phase space of the Higgs measurement will arise from combinatorial backgrounds of pairs of photons, and thus will not exhibit a peak at the Higgs mass. Because of this, they are likely to removed as part of the background fitting and subtraction process in that analysis. We therefore do not include the Higgs cross sections when calculating the exclusion limits.

3.4 Results

For the CP-even scalar, the cross section in 8 TeV pp collisions calculated by Herwig ranges from 110 pb for $\Lambda = 1$ TeV to 1.3 pb for $\Lambda = 10$ TeV for $M_\varphi = 10$ GeV, and from 8.2 pb for $\Lambda = 1$ TeV to 0.12 pb for $\Lambda = 10$ TeV for $M_\varphi = 90$ GeV. For the CP-odd scalar, the cross section in 8 TeV pp collisions calculated by Herwig ranges from 15 pb for $\Lambda = 1$ TeV to 0.26 pb for $\Lambda = 10$ TeV for $M_\varphi = 10$ GeV, and from 4.3 pb for $\Lambda = 1$ TeV to 0.077 pb for $\Lambda = 10$ TeV for $M_\varphi = 90$ GeV. In all cases, the associated production of φ with a Z or W boson makes the biggest contribution to the cross section, although the $\varphi+\gamma$ process is significant (10-20%), and the $\varphi + g$ process contributes up to 20% (40%) for the highest scale and mass values considered for the CP even (odd) scalar.

At low M_φ and low-ish Λ, one of the most sensitive measurements is the $\gamma + E_T^{\text{miss}}$ measurement from [583]. The differential cross section as a function of the transverse momentum of the photon is shown in Fig. 1, and alone is enough to excludes the model at the 97% cl. The inclusive photon measurements are also sensitive, with the 7 TeV diphoton measurement extending to the lowest mass and p_T values, and the 8 TeV measurement (shown) playing a role once $M_\varphi \geq 20$ GeV.

As mentioned in the previous section, events from the model can contribute to the Higgs fiducial two-photon cross section, and this is seen in the Rivet routine. The major contribution occurs for relatively low M_φ, presumably due to $pp \to \gamma\varphi + X \to \gamma\gamma\gamma + X$ processes in which one pair of photons has a mass close to 125 GeV. An example, for $M_\varphi = 20$ GeV, $\Lambda = 3.5$ TeV, is shown in Fig. 2. The event contribute mainly at low values of p_T for the photon pair. As discussed, this analysis is not used in deriving the final sensitivity, and is shown only for illustration. **TODO check this. Looks like it is used.**

The CP-even model contributes to the same final states, but with a larger cross section for a given coupling. The distributions for the this model with the same parameter settings as Fig. 1 are shown in Fig.3

The sensitivity of the combined 7 and 8 TeV data to the CP-odd scalar model is illustrated in Fig. 4. Dependent on M_φ, the Λ values up to 4.5 to 8.5 TeV are excluded, under the assumptions of our procedure. Similar sensitivity plots for the CP-even model are shown in Fig. 5. comment on the range. Precision 13 TeV data can be expected to extend the reach still further; possible dedicated analyses which might extend the sensitivity still further are discussed in the following section.

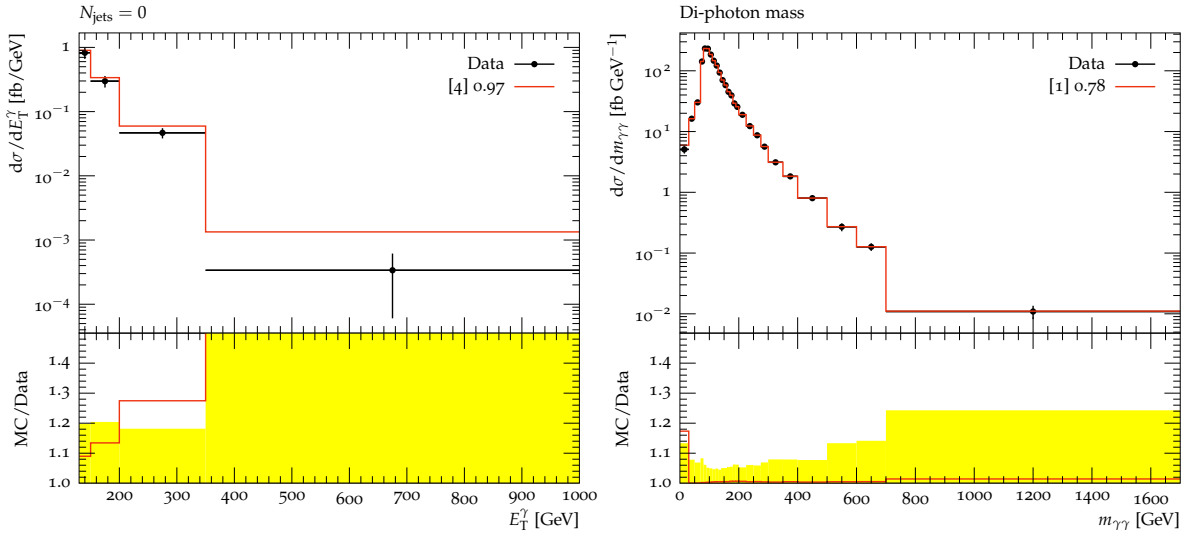

Figure 1: Projection of the contribution of the CP-odd model, (left) for $M_\varphi = 10$ GeV and $\Lambda = 3500$ TeV, on to the 8 TeV ATLAS $\gamma + E_T^{\text{miss}}$ differential E_T^γ cross-section measurement and (right) on the diphoton mass measurement, now with $M_\varphi = 20$ GeV – which brings the mass peak from the φ within the range of the measurement. Black points indicate the data, the red upper histogram is the data+BSM. The lower sections of the plots show the ratio of (data+BSM)/data, with the yellow band indicating the uncertainty in the measurement. The numbers in the legend show the bin number of the most powerful bin, and the exclusion from that bin expressed as a probability.

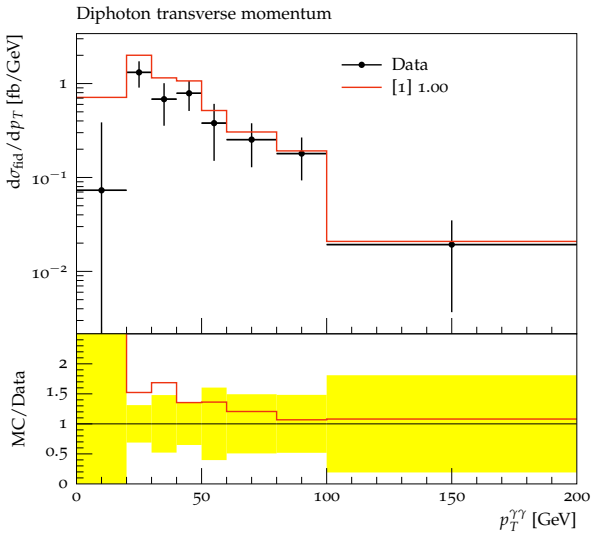

Figure 2: Projection of the contribution of the CP-odd model, for $M_\varphi = 20$ GeV and $\Lambda = 3500$ TeV, on to the 8 TeV ATLAS $H \to \gamma\gamma$ differential $p_T^{\gamma\gamma}$ cross-section measurement. Legend as Fig.1

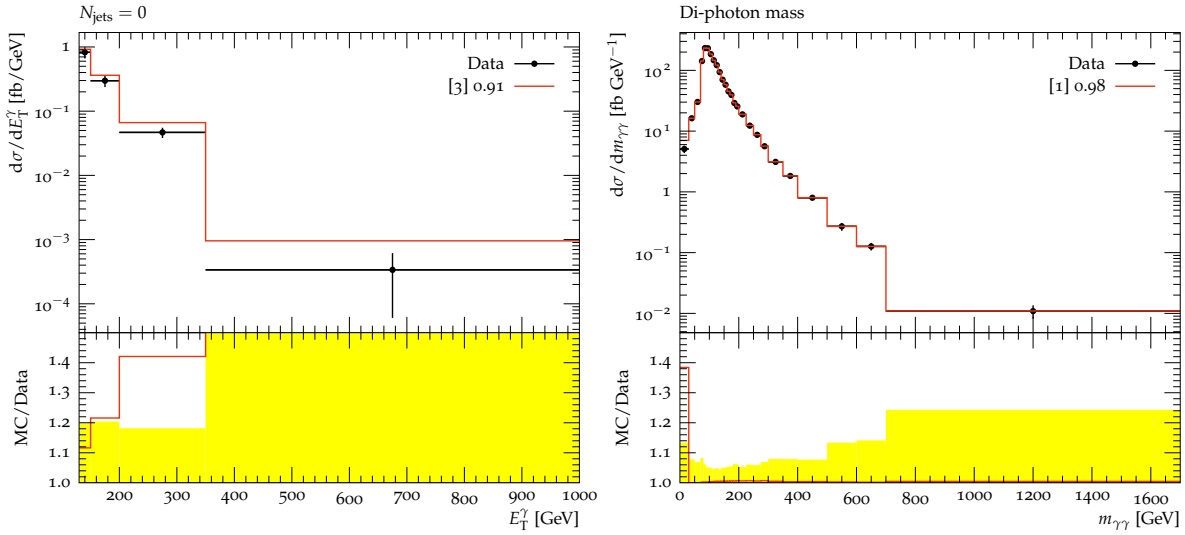

Figure 3: Projection of the contribution of the CP-even model, for $M_\varphi = 10$ GeV and $\Lambda = 3500$ TeV, on to the 8 TeV ATLAS $\gamma + E_T^{\text{miss}}$ differential E_T^γ cross-section measurement (left) and (right) the diphoton mass measurement playing a role now with $M_\varphi = 20$ GeV, which brings the mass peak from the φ within the range of the measurement. Legend as Fig. 1

CONCLUSIONS

The generic light scalar models considered here imply significant contributions to differential cross sections involving weak bosons and/or isolated photons which have already been measured at the LHC and shown to be consistent with the Standard Model. While a rigorous exclusion would require a treatment of the theory uncertainties on the SM photon cross sections, these models can be considered highly disfavoured for scales below about 4 TeV for $M_\varphi = 10$ GeV and up to about 8.5 TeV for $M_\varphi = 90$ GeV.

ACKNOWLEDGEMENTS

We thank the organizers and conveners of the Les Houches workshop, "Physics at TeV Colliders", for a stimulating meeting. This work has received funding from STFC (UK), and the European Union's Horizon 2020 research and innovation programme as part of the Marie Sklodowska-Curie Innovative Training Network MCnetITN3 (grant agreement no. 722104).

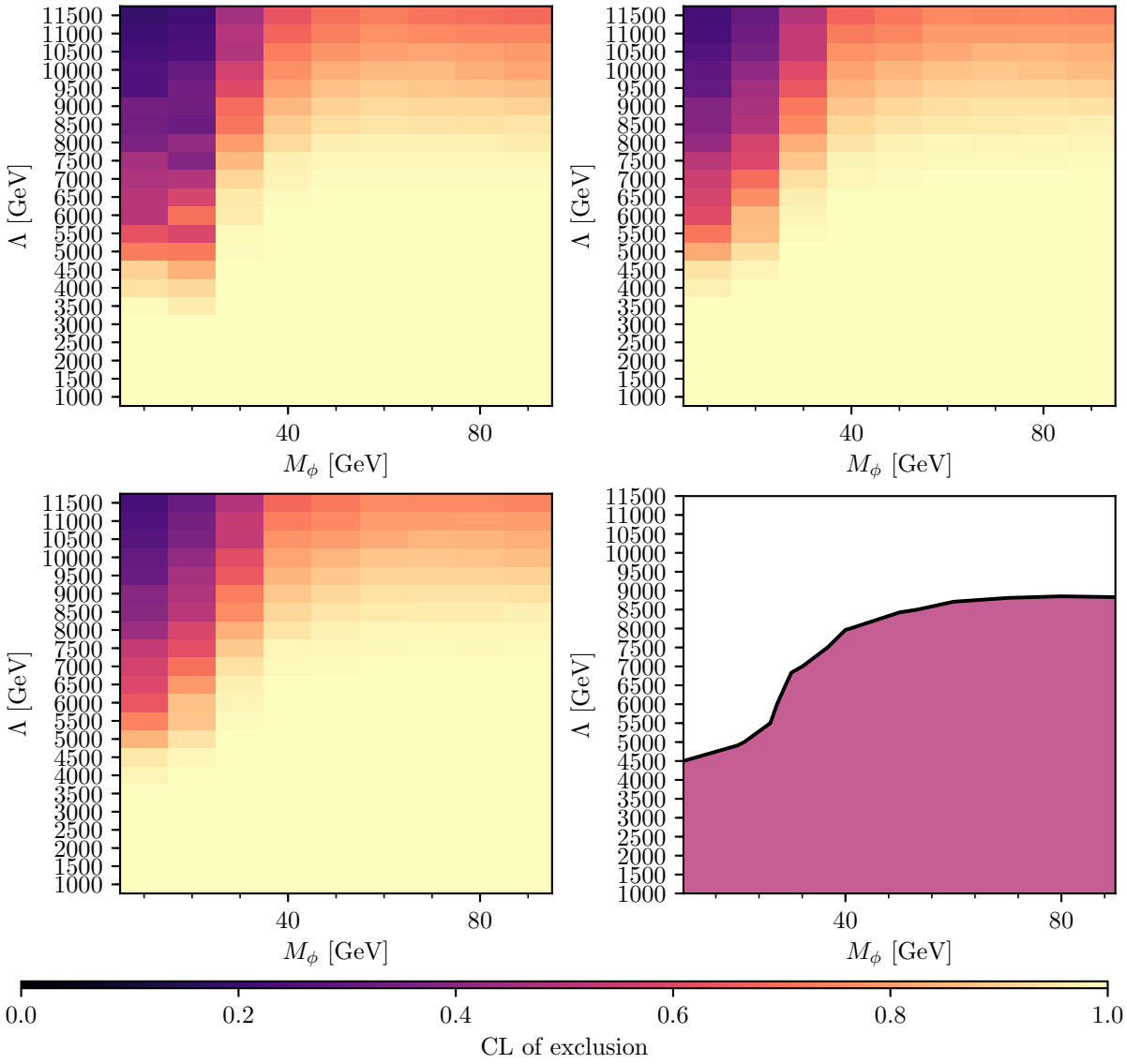

Figure 4: CP-odd scalar model: Top left, exclusion heatmap (with the key below the figure) for 7 & 8 TeV diboson measurements (i.e. final states consistent with $WW, ZZ, W + \gamma(\gamma), Z + \gamma(\gamma)$) from ATLAS and CMS. Top right, exclusion heatmap for 7 & 8 TeV photon and diphoton measurements, lower left combined exclusion heatmap, bottom right, combined exclusion contour at 95% c.l.

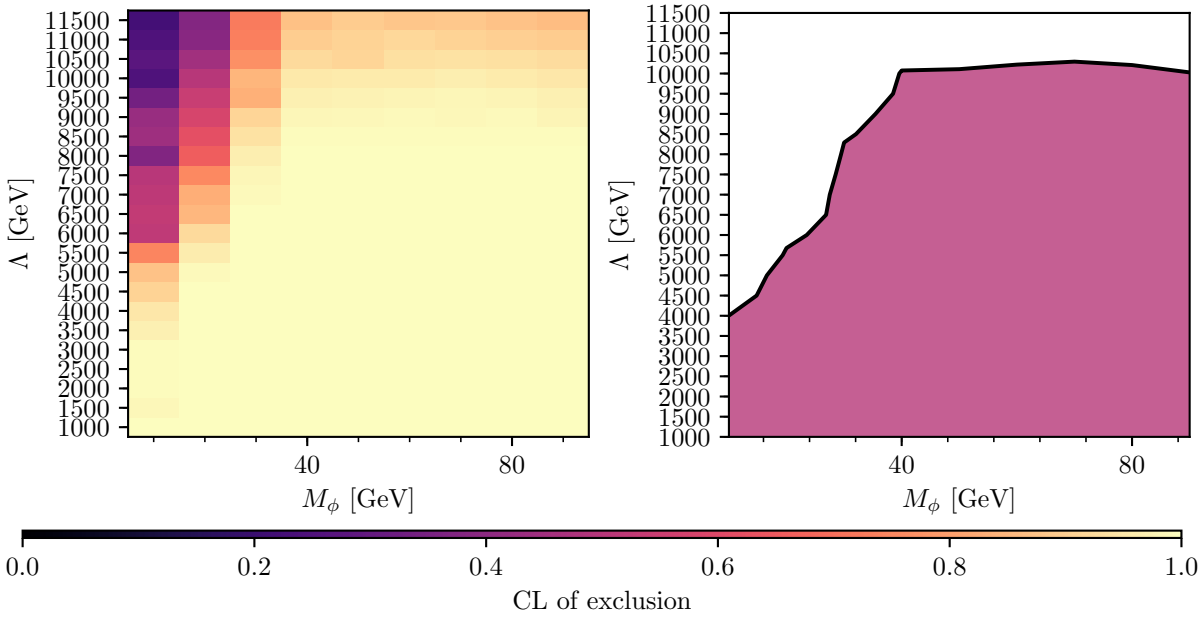

Figure 5: As the lower row of Fig.4, but for the CP-even scalar model.

Contribution 21

Recasting activities at LH2017

A. Buckley, N. Desai, B. Fuks, P. Gras, D. Grellscheid, F. Maltoni, O. Mattelaer, L. Perrozzi, P. Richardson, S. Sekmen

Abstract
We discuss a first benchmark comparison assessing the performance of different public recasting tools in reproducing ATLAS and CMS analysis results.

1 Introduction

Searches for new physics constitute a primary objective of the LHC physics program. Their large number and variety pose severe challenges to both the experimental and theory communities. In fact, a plethora of searches in different final states are performed by different physics groups in ATLAS and CMS, while new ideas to probe new models and non-trivial signatures and to improve the sensitivity of existing searches constantly emerge. The ultimate goal of this effort is to discover new physics if such exists within the reach of the LHC, and to test the widest possible range of hypothetical new physics models.

A typical analysis defines quantities to classify events as signal or background. They include properties of analysis objects such as jets, electrons, muons, or global event variables such as object multiplicities, transverse momenta or transverse masses. An analysis can be very complex and feature many intricate definitions of object and event variables, some of which cannot be expressed in closed algebraic form and must be defined algorithmically. This complexity renders the tasks of visualizing, understanding, developing and interpreting analyses increasingly challenging.

In the paper publications describing the analyses and their results, the experimental collaborations provide interpretations of the results in terms of one or more theoretical scenarios the analysis has been designed for. Often this is done in the context of so-called simplified models, which consider just a subset of physics states and production/decay modes out of a full theory. There are, however, a multitude of theories beyond the Standard Model and they come in ever increasing variants. To fully assess the implications of the LHC searches for new physics requires the interpretation of the experimental results in the context of all these models. This is a very active field with close theory-experiment interaction, see e.g. [585], and with several public tools being developed for the (re)interpretation of the experimental results.[1] In particular, CheckMate [588, 589], MadAnalysis [272, 590, 591] and Rivet [325, 592] aim at reproducing experimental analyses in Monte Carlo simulation, including an approximate emulation of detector effects, as new physics searches, which have given only null results so far, are typically not unfolded. The scope of this contribution is to provide a first benchmark to compare different

[1] This includes also dedicated efforts at Les Houches to provide "Recommendations for Presentation of LHC Results" [72, 586, 587].

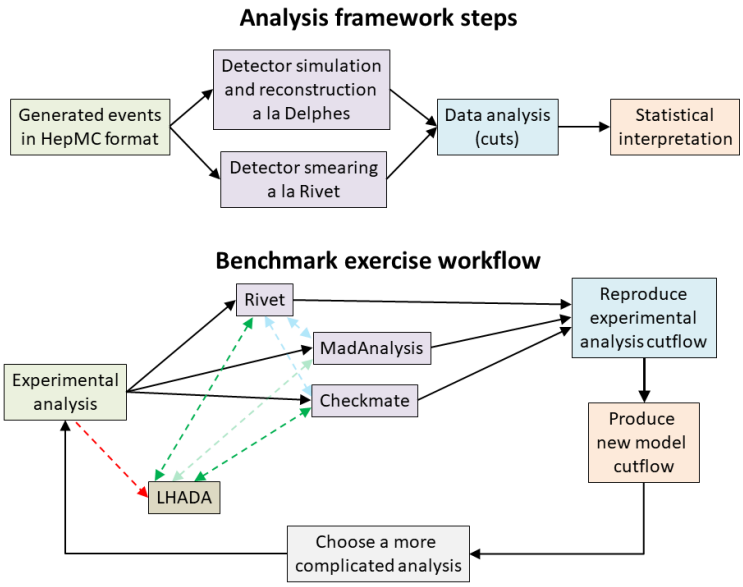

Figure 1: Sketch of the recasting exercise workflow.

public tools in reproducing ATLAS and CMS analysis results.[2]

2 Benchmarking tools and comparison strategy

The idea behind the exercise described in this section is the implementation of LHC analyses of increasing complexity, in different frameworks followed by a comparison of the results. The exercise is performed with three frameworks, CheckMate [588,589], MadAnalysis [272,590,591] and Rivet [325,592], followed by a comparison of the results. We choose two analyses for which a detailed cutflow and detector effects were available. In the future it might be beneficial to use dedicated parsers to convert the analysis described in a common format (denoted LHADA in Fig. 1) into different recasting codes using for instance the technique described in Contribution 23. Once the analysis are available in the needed format, we attempt to reproduce the new physics interpretations presented in the original experimental research papers, validating in this way our reimplementations. A further step consists in the recasting of the analyses within different new physics contexts and compare the results among the different frameworks. A sketch of the recasting exercise workflow is presented in Fig. 1.

Aside the current scope of the exercise, it is interesting to check how the performance of the Delphes simulation behave across different phase spaces, since they are generally referred to as analysis-spedfic.

2.1 Analysis frameworks and tools

In this section we describe the analysis frameworks and tools used for the comparison and benchmarking

[2]It is highly appreciated that many of these results are provided numerically through HEPDATA [349] or on the collaboration twiki pages.

2.1.1 *CheckMate*

CheckMATE [588,589] takes simulated event files in .hep or .hepmc for any model as input and simply returns if the underlying model is 'excluded' or 'allowed' after performing a detector simulation and testing various implemented analyses. The embedded AnalysisManager allows for the embedding of additional current and prospective future LHC results from ATLAS and CMS which have not yet been implemented. Detector effects are modeled by Delphes with a tune containing efficiency functions for lepton reconstruction and flavour tagging. The soon-to-be published version 2.0 of the code adds the possibility of using Pythia 8 [593] to generate supersymmetric events on-the-fly or to shower provided Les Houches event files for any model. Currently, the collaboration is working on an extension to enable the on-the-fly simulation of events for any model.

2.1.2 *MadAnalysis*

MadAnalysis 5 [272, 590] is a generic user-friendly framework for phenomenological investigations at particle colliders, *i.e.* to perform physics analyses of Monte Carlo event files. While prospective analyses of hard scattering events, parton showered events, hadronized events or reconstructed events can be designed easily thanks to its Python-based meta-language, MadAnalysis also allows for the recasting of LHC analyses on new physics signals provided under the form of .hep and .hepmc event files. The output here consists in the confidence level at which the model signals are excluded. Its Public Analysis Database [591] comprises a growing collection of LHC analyses which have been implemented in the MadAnalysis 5 framework for the purpose of recasting. Delphes is used for the detector simulation. For each implemented analysis, a detailed validation note is provided and the public analysis database follows an open-source policy. Only contributed codes provided with a detailed validation note are published, and they are moreover citable via Inspire. The framework being integrated within MadGraph5_aMC@NLO [95], it provides a full recast chain linking a model and its associated signatures to limit setting.

2.1.3 *Rivet*

Originally developed as a toolkit for the validation of Monte Carlo event generators, Rivet [325, 592] (Robust Independent Validation of Experiment and Theory) has become a standard for documenting (unfolded) Standard Model (SM) measurements. The top and Higgs physics working groups of all LHC experiments are increasingly providing Rivet routines for their analyses. Rivet analyses are written in a user-friendly subset of C++11, and are picked up at runtime as 'plugin libraries'; they can be executed on an event stream either through a Python script interface, or by direct code interfacing to a C++ API. The original SM-focused requirement of unfolded observables made Rivet inappropriate for beyond the Standard Model (BSM) searches (other than those using just jets and missing energy) until the addition of detector-smearing/efficiency machinery in Rivet 2.5.0. This detector machinery provides equivalent efficiency effects to a Delphes-type simulation, and imitates the less important kinematic smearing of physics objects to within a few percent. A novel feature is that the Rivet detector implementation allows for using different jet algorithms, lepton and b-tagging operating points, full-detailed object isolation algorithms, and resolutions/efficiencies specific to each analysis procedure and event selection. This hence allows for a more accurate detector modelling and more robust analysis preservation than 'global' detector simulations in addressing some experiment requests for 'official fast-sim' tools. The aim is to encourage Rivet code provision directly from BSM data

analysers, as is already the case for SM results: additional tools to assist BSM analysis implementation are being added on request.

3 Analyses benchmarking, comparisons and results

3.1 An ATLAS search for supersymmetry in a final state with jets and missing energy (13 TeV, 3.2 fb^{-1})

In the analysis of Ref. [594], the ATLAS collaboration targets the production of the strongly-interacting superpartners of the Standard Model QCD partons, followed by their decay into jets and missing energy carried by neutralinos. 3.2 fb^{-1} of proton-proton LHC collisions at a center-of-mass energy of 13 TeV are analyzed.

The analysis focuses on jets reconstructed by means of the anti-k_T algorithm [98] with a radius parameter set to $R = 0.4$, with a transverse momentum larger than 20 GeV and a pseudorapidity $|\eta| < 2.8$. Events featuring loosely reconstructed electrons and muons are vetoed. Event preselection requires a significant amount of missing energy, $\not{E}_T > 200$ GeV and the transverse-momentum of the leading jet is imposed to be larger than 200 GeV and 300 GeV if two or more than two jets are reconstructed, respectively.

The analysis is then divided into seven signal regions focusing on different jet multiplicities (from 2 to 6) with different transverse-momentum thresholds. The missing transverse momentum is then enforced to be well separated from the leading reconstructed jets, and its significance is constrained for events featuring only two jets. For cases where at least four jets are reconstructed, additional selections on the aplanarity variable and the effective mass, *i.e* the scalar sum of the transverse momenta of the reconstructed and the missing transverse energy.

Implementations of this analysis are available in Checkmate, MadAnalysis 5 (recast code [595]) and Rivet (ATLAS_2016_I1458270 [596]).

We generated signal events for a gluino pair production in the simplified model considered in Ref [594] with a direct decay of the gluino into SM particles and the lighest supersymmetric particle (LSP). The gluino mass is set to 1.6 TeV mass and the LSP is assumed to be massless. The pseudo-data samples have been generated by using MadGraph5_aMC@NLO [95] and Pythia8 [97].

The comparison of predictions for the cutflows as obtained with MadAnalysis 5 and Rivet are reported in Table 1 and Table 2 for all seven signal regions. The tables include the total number of events surviving each selection, the associated cut efficiency and the total efficiency evaluated with respect to the initial number of events. Partially available Checkmate results are also indicated for what concern the total efficiencies and for a few signal regions. An excellent agreement between the three codes has been obtained.

3.2 An ATLAS search for dark matter in the monophoton final state (13 TeV, 36.1 fb^{-1})

In the analysis of Ref. [39], the ATLAS collaboration has searched for dark matter when it is produced in association with a very energetic photon. The search results have been reinterpreted in dark matter simplified scenarios in which a pair of dark matter particles is produced in association with a photon arising from initial state radiation. 36.1 fb^{-1} of proton-proton LHC collisions at a center-of-mass energy have been analyzed.

The analysis requires the presence of at least one tightly-isolated photon with a transverse energy $E_T > 150$ GeV and with a pseudorapidity satisfying $|\eta| < 2.37$, the pseudorapidity region

$1.37 < |\eta| < 2.37$ being excluded. Events featuring loose eletrons and muons and more than one jets with a transverse momentum larger than 30 GeV and a pseudorapidity $|\eta| < 4.5$ are vetoed. As in the previous analysis, jets are reconstructed by means of the anti-k_T algorithm [98] and a radius parameter set to $R = 0.4$. In addition, event selection requires a missing transverse energy significance larger than 8.5 GeV$^{1/2}$, and the missing transverse momentum has top be well separated from the photon and the jet (for events featuring one reconstructed jet).

Five signal regions are defined according to different requirements on the amount of missing transverse energy, namely three inclusive regions and two non-overlapping exclusive regions.

We generated events using the simplified model of dark matter (DM) production involving an axial-vector operator, Dirac DM and couplings $g_q = 0.25$ and $g_\chi = 1$ with $m_\chi = 10$ GeV and $m_{med} = 800$ GeV described in Ref. [39].

In Table 3, we compare the total number of events surviving each selection, the associated cut efficiency and the total efficiency evaluated with respect to the initial number of events as obtained with MadAnalysis5 (recast code [597]) and Rivet. Whilst a fair agreement is obtained between two codes, differences of 5%–10% are observed for a few cuts. This can be traced

	Rivet			**MadAnalysis 5**			**CheckMATE**
Description	#evt	tot.eff	rel.eff	#evt	tot.eff	rel.eff	tot.eff
2jl cut-flow	31250	1	-	31250	1	-	
Pre-sel+MET+pT1	28592	0.91	0.91	28626	0.92	0.92	
Njet	28592	0.91	1	28625	0.92	1	
Dphi_min(j,MET)	17297	0.55	0.6	17301	0.55	0.6	
pT2	17067	0.55	0.99	17042	0.55	0.99	
MET/sqrtHT	8900	0.28	0.52	8898	0.28	0.52	
m_eff(incl)	8896	0.28	1	8897	0.28	1	
2jm cut-flow	31250	1	-	32150	1	-	1
Pre-sel+MET+pT1	28472	0.91	0.91	28478	0.91	0.91	0.91
Njet	28472	0.91	1	28477	0.91	1	0.91
Dphi_min(j,MET)	22950	0.73	0.81	22889	0.73	0.8	0.73
pT2	22950	0.73	1	22889	0.73	1	0.73
MET/sqrtHT	10730	0.34	0.47	10710	0.34	0.47	0.33
m_eff(incl)	10630	0.34	0.99	10609	0.34	0.99	0.32
2jt cut-flow	31250	1	-	31250	1	-	
Pre-sel+MET+pT1	28592	0.91	0.91	28626	0.92	0.92	
Njet	28592	0.91	1	28625	0.92	1	
Dphi_min(j,MET)	17297	0.55	0.6	17301	0.55	0.6	
pT2	17067	0.55	0.99	17042	0.55	0.99	
MET/sqrtHT	5083	0.16	0.3	5098	0.16	0.3	
Pass m_eff(incl)	4861	0.16	0.96	4889	0.16	0.96	

Table 1: Number of events surviving each selection, total and relative selection efficiencies as obtained with Rivet and MadAnalysis 5 for the dijet signal regions of the multijet+missing energy ATLAS analysis of Ref. [594]. Partly available Checkmate results for the total efficiencies are also indicated.

	Rivet			MadAnalysis 5			CheckMATE
Description	#evt	tot.eff	rel.eff	#evt	tot.eff	rel.eff	tot.eff
4jt cut-flow	31250	1	-	31250	1	-	1
Pre-sel+MET+pT1	28592	0.91	0.91	28626	0.92	0.92	0.91
Njet	27322	0.87	0.96	27128	0.87	0.95	0.87
Dphi_min(j,MET)	18929	0.61	0.69	18829	0.6	0.69	0.6
pT2	18715	0.6	0.99	18825	0.6	1	–
pT4	16610	0.53	0.89	16430	0.53	0.87	0.52
Aplanarity	11849	0.38	0.71	11395	0.36	0.69	0.36
MET/m_eff(Nj)	8334	0.27	0.7	7971	0.26	0.7	0.25
m_eff(incl)	7201	0.23	0.86	6972	0.22	0.87	0.21
5j cut-flow	31250	1	-	31250	1	-	1
Pre-sel+MET+pT1	28592	0.91	0.91	28626	0.92	0.92	0.91
Njet	21234	0.68	0.74	21185	0.68	0.74	0.68
Dphi_min(j,MET)	14294	0.46	0.67	14292	0.46	0.67	0.45
pT2	14146	0.45	0.99	14289	0.46	1	–
pT4	13229	0.42	0.94	13228	0.42	0.93	0.42
Aplanarity	9836	0.31	0.74	9576	0.31	0.72	0.3
MET/m_eff(Nj)	4643	0.15	0.47	4506	0.14	0.47	0.13
m_eff(incl)	4620	0.15	1	4476	0.14	0.99	0.13
6jm cut-flow	31250	1	-	31250	1	-	1
Pre-sel+MET+pT1	28592	0.91	0.91	28626	0.92	0.92	0.91
Njet	13235	0.42	0.46	13236	0.42	0.46	0.41
Dphi_min(j,MET)	8520	0.27	0.64	8553	0.27	0.65	0.26
pT2	8436	0.27	0.99	8551	0.27	1	–
pT4	8135	0.26	0.96	8217	0.26	0.96	0.25
Aplanarity	6365	0.2	0.78	6307	0.2	0.77	0.19
MET/m_eff(Nj)	2675	0.09	0.42	2665	0.09	0.42	0.08
m_eff(incl)	2670	0.09	1	2656	0.08	1	0.08
6jt cut-flow	31250	1	-	31250	1	-	
Pre-sel+MET+pT1	28592	0.91	0.91	28626	0.92	0.92	
Njet	13235	0.42	0.46	13236	0.42	0.46	
Dphi_min(j,MET)	8520	0.27	0.64	8553	0.27	0.65	
pT2	8436	0.27	0.99	8551	0.27	1	
pT4	8135	0.26	0.96	8217	0.26	0.96	
Aplanarity	6365	0.2	0.78	6307	0.2	0.77	
MET/m_eff(Nj)	3900	0.12	0.61	3839	0.12	0.61	
m_eff(incl)	3715	0.12	0.95	3672	0.12	0.96	

Table 2: Same as in Table 1 but for the signal regions targeting final states containing four, five and six

	Rivet			MadAnalysis 5		
Description	#evt	tot.eff	rel.eff	#evt	tot.eff	rel.eff
Initial	1198	1	-	1198	1	-
ETmiss $>$ 150 GeV	798.3	0.67	0.67	736	0.61	0.61
Photon w/ ET $>$ 150 GeV	703.5	0.59	0.88	700	0.58	0.95
Pass Tight photon	598.1	0.50	0.85	658	0.55	0.94
Pass Isolated photon	598.1	0.50	1.00	620	0.52	0.94
Pass $\delta\varphi$(gamma,MET) $>$ 0.4	597.5	0.50	1.00	596	0.50	0.96
Pass MET/sqrt(SET) $>$ 8.5	538.2	0.45	0.90	-	-	
Pass Jet veto	476.8	0.40	0.89	461	0.38	0.77
Pass Lepton veto	475.5	0.40	1.00	460	0.38	1.00

Table 3: Number of events surviving each selection, total and relative selection efficiencies as obtained with Rivet and MadAnalysis 5 for the SRI1 signal region of the monophoton ATLAS analysis of Ref. [39].

back to the missing energy modelling that is complicated to reproduce. The final acceptances of about 40% (Rivet) and 38% (MadAnalysis) are however in good agreement.

CONCLUSIONS

We presented a first benchmark comparison of the performance of different recasting tools which reproduce LHC analyses in Monte Carlo simulation. For the two cases treated here, good agreement is found between the different frameworks and detector simulation techniques. The comparison is ongoing with several more analyses which are currently being validated. It will also be interesting to compare performances for different signal scenarios, to assess the reliability of the recasting methods in, e.g. extreme regions of phase space and/or for very different signal hypotheses the the one the analyses have been designed for.

ACKNOWLEDGEMENTS

The authors thank the organizers of the Les Houches Workshop Series "Physics at TeV Colliders 2017" for the fruitful and pleasant atmosphere, and Sabine Kraml for the numerous discussions and the help in finalising the contribution.

Contribution 22

Recasting Long-Lived Particles Searches

G. Cottin, N. Desai, J. Heisig, A. Lessa

Abstract

Long-lived particles (LLPs) arise in several beyond the Standard Model (BSM) theories, and they provide striking (non-standard) signatures at colliders. Several LHC searches look for LLP models in a broad range of final states, and limits have been presented for specific BSM models. However, extrapolating such limits to other scenarios often proves to be a difficult task outside the experimental collaborations. This note discusses the recasting of three types of LLP signatures: displaced vertices, displaced leptons and heavy stable charged particles. Several conclusions are obtained from these recasting attempts and recommendations to the experimental collaborations are made.

1 INTRODUCTION

The key scientific goal for the second run of the LHC is to explore physics beyond the Standard Model (BSM). Motivated by a variety of BSM theories, there has been a growing interest in non-standard signatures, such as long-lived particles (LLP). A large variety of LLP signatures have been explored by the experimental searches and the re-interpretation of these results within the context of new BSM theories is extremely relevant to exploit the full potential of the LHC experiment. However, in most cases it is not possible to reinterpret LLP searches using fast detector simulation and a cut-and-count based analysis, as it is usually done for prompt searches. In particular, efficiencies for object reconstruction (such as displaced vertices) and event selection are much more analysis dependent in LLP searches and difficult to reproduce using fast simulation. Furthermore, trigger and pile-up vetoes included in prompt searches are difficult to reproduce and can invalidate the extrapolation of prompt search results and limits to long-lived (displaced) scenarios.

In this note we discuss the difficulties of recasting LLP searches. In order to make the discussion concrete, we present results for the recasting of three distinct LLP signatures: displaced vertices, displaced leptons and heavy stable charged particles. As a way to discuss the typical issues encountered when recasting LLP searches, we try to reproduce the official exclusion curves presented in the 13 TeV ATLAS displaced vertex plus missing energy [598], the 8 TeV CMS displaced lepton [599] and the 13 TeV CMS heavy stable charged particle [120] searches. Although the issue of recasting prompt searches within the context of LLP models is a very relevant one, we do not discuss it here.

The first difficulty related to recasting LLP searches concerns the detector simulation of such signatures. While the relevant signatures for stable particles (in detector scales) are charged tracks and missing energy, for a particle decaying within the detector several signatures are possible, depending on the LLP nature and its decay. The lifetime of the particle and its boost

are also essential features, since only certain parts of the detector are capable of observing specific decay products. Furthermore, the Standard Model background typically decreases as the LLP decay moves further away from the primary vertex. In general the LLP signatures can be classified as follows:

- *charged track* (stable charged particle)
- *disappearing track* (charged LLP decaying to a neutral/soft final state)
- *displaced vertex* (charged or neutral LLP decaying to charged final states)
- *track kink* (charged LLP decaying to neutral and charged final states)
- *trackless jets, displaced leptons* (neutral LLP decaying to charged final states)
- *missing energy*[1] (stable neutral particle)

Typical fast detector simulators do not yet include the information required for dealing with the above signatures. As a result, dedicated recasting tools must be developed to deal with LLP searches. In this note we mainly make use of MADGRAPH5 [95] and PYTHIA [97, 145] to simulate hadron level events and no fast detector simulation is employed. Several approaches are then discussed in order to emulate the experimental selection and reconstruction efficiencies and reproduce the official exclusion curves presented in the corresponding analyses.

The recasting of the ATLAS displaced vertex search is presented in Section 2, where two methods are employed in order to reproduce the exclusion curves for a simplified long-lived gluino scenario. While the first method makes use of the limited information provided by the corresponding conference note, the second uses the full efficiencies provided by the ATLAS auxiliary material. The goal of comparing these two approaches is to illustrate how lack of experimental information drastically decreases the recasting performance. Sections 3 and 4 discuss searches based on isolated tracks, which, in principle, are much simpler to recast. Although CMS has provided detailed efficiencies for the 8 TeV searches, we will show that these can not be easily extrapolated to the 13 TeV results. We illustrate this by recasting two CMS searches — displaced lepton search (Section 3) and the long-lived charged particle search (Section 4). Finally, in Section 5 we present the overall conclusions and recommendations drawn from the recasting of these particular searches.

2 DISPLACED VERTEX SEARCH

The ATLAS displaced vertex + missing energy analysis presented in Ref. [598] investigate an important BSM scenario: long-lived gluinos decaying to jets and missing energy. The analysis searches for displaced vertices (DV) in association with large missing transverse energy, a signature present in several BSM models (long-lived stops, hidden valley scenarios and others). Hence it is relevant to investigate how well it is possible to recast this analysis and extend its constraints to other LLP models. One important feature of the ATLAS search is that it does not rely on the gluino (or R-hadron) charge, so it can be directly applied to both charged and neutral LLPs.

[1] The missing energy signature is usually not classified as a LLP search, since it is covered by several prompt searches. Nonetheless, we include it here for completeness.

In Ref. [598] the results are interpreted in the long-lived gluino scenario with R-Parity conservation, the lightest neutralino being the LSP and the gluino the NLSP. Hence, after being pair produced, the gluinos hadronize and then decay to jets and the LSP with a 100% branching ratio:

$$pp \to \tilde{g}\tilde{g} \to (jj\tilde{\chi}_1^0) + (jj\tilde{\chi}_1^0) \tag{1}$$

Limits are presented for gluino lifetimes between 0.02 ns and 20 ns, gluino masses of 1.4 and 2 TeV and several values of $m_{\tilde{\chi}_1^0}$.
The search imposes the following criteria for selecting displaced vertices:

1. Missing energy selection in the event: $E_{\mathrm{T}}^{\mathrm{miss}} > 250$ GeV.
2. *Base vertex selection* (at least one DV in the event):
   - The DV coordinates must satisfy: $R_{\mathrm{DV}} = \sqrt{x^2 + y^2} < 300$ mm and $|z_{\mathrm{DV}}| < 300$ mm.
   - The DV must not fall into a material rich area. This criterion corresponds to discarding approximately 42% of the fiducial volume.
   - The vertex must be separated by more than 4 mm from all primary vertices.
3. Signal region selection:
   - the invariant mass of the DV must be $m_{\mathrm{DV}} > 10$ GeV, assuming all its tracks have the pion mass.
   - $n_{\mathrm{tracks}} \geq 5$, where n_{tracks} corresponds to the number of tracks originating from the vertex and satisfying: $p_{\mathrm{T}} > 1$ GeV and $|d_0| > 2$ mm.

After applying the above selections, no displaced vertices were observed in 32.1 fb^{-1} of data at $\sqrt{s} = 13$ TeV. The number of expected background displaced vertices is:

$$N_{\mathrm{DV}}^{\mathrm{BG}} = 0.02 \pm 0.02 \tag{2}$$

This analysis is particularly interesting because it provides a large set of information useful for recasting.[2] Specially useful are the efficiency grids provided for DV reconstruction and event selection as a function of the relevant (truth level) variables: number of tracks, DV mass, DV position and missing energy. We point out that these detailed efficiencies are usually not provided for most LLP searches. The corresponding 8 TeV search in Ref. [147], for instance, only provided reconstruction and event-level efficiencies as a function of a single parameter. Therefore, we will discuss below how recasting performs when distinct levels of information are available. In particular, we will discuss two approaches:

- *Method 1*: recasting using correction functions for the vertex reconstruction efficiency and the track efficiency.
- *Method 2*: recasting using the efficiency grids provided by ATLAS in Ref. [598].

[2]We point out that the conference note ATLAS-CONF-2017-026, which has been superseded by Ref. [598], included only a subset of the information present in the publication.

2.1 Method 1: Recasting using correction functions

The first approach only makes use of the displaced vertex reconstruction efficiency provided by ATLAS and shown as red points in Fig.1. We point out that this data is provided only for $m_{\tilde{g}} = 1.2$ TeV and $\tau = 1$ ns. The method discussed below tries to construct functions which aim to approximate the experimental track and vertex reconstruction efficiencies. These will then be applied to the event selection and used to compute upper limits for the same gluino scenarios considered by ATLAS.

In order to recast the ATLAS displaced vertex + missing energy search, we use PYTHIA 8 [97] for the simulation of gluino production, hadronization and decays. No smearing is applied and the truth-level $E_{\rm T}^{\rm miss}$ is considered. All charged particles generated by the R-hadron decay are considered as potential charged tracks and only these are included when computing $m_{\rm DV}$. Furthermore, d_0 is calculated with the assumption of a zero magnetic field. The veto of decays in material rich area is implemented simply as an overall fiducial volume cut. Since a dedicated algorithm was used by the collaboration to identify and select DV candidates, it can not be easily reproduced. However the vertex reconstruction efficiency as a function of $R_{\rm DV}$ has been provided in Ref. [598] for $\left(m_{\tilde{g}}, m_{\tilde{\chi}_1^0}, \tau\right) = (1200\ \text{GeV}, 100\ \text{GeV}, 1\ \text{ns})$ and $\left(m_{\tilde{g}}, m_{\tilde{\chi}_1^0}, \tau\right) = (1200\ \text{GeV}, 1170\ \text{GeV}, 1\ \text{ns})$.

As a first step in the recasting procedure, we test how well the vertex reconstruction efficiency ($\epsilon_{\rm DV}$) can be reproduced under the assumption that all displaced vertices satisfying the *base vertex selection* cuts are reconstructed. The efficiencies provided by ATLAS and the result obtained from recasting are shown in Fig.1. As we can see, $\epsilon_{\rm DV}$ decreases with $R_{\rm DV}$, except for the first bin ($0\ \text{mm} < R_{\rm DV} < 5\ \text{mm}$). The slope seen in the recasting curve is purely due to the *base vertex selection* cuts applied. The same behavior is seen in the official data, although the efficiency falls much faster, likely due to detector effects and the reconstruction algorithm. For the low bins (except for the first one) the two curves differ by $\simeq 20\%$, while for the largest bins the difference is almost an order of magnitude. The high level of agreement in the first bin ($R_{\rm DV} < 5$ mm) is an artificial effect due to the requirement that the displaced and primary vertices must be separated by at least 4 mm.

As shown in Fig.1, the reconstruction efficiency obtained by recasting can be overestimated by more than an order of magnitude for high values of $R_{\rm DV}$. One is then tempted to directly apply the vertex reconstruction efficiencies provided by ATLAS (red points in Fig.1) to the hadron level events generated in PYTHIA. However these have been derived for the benchmark point $m_{\tilde{g}} = 1.2$ TeV, $m_{\tilde{\chi}_1^0} = 100$ GeV, $\tau = 1$ ns and are not necessarily valid for other values of the gluino and LSP masses or the lifetime. In fact, as shown in Ref. [598], the efficiencies can be affected by the mass difference $m_{\tilde{g}} - m_{\tilde{\chi}_1^0}$. We have also computed the reconstruction efficiency using distinct values of the gluino lifetime. The results are shown in Fig.2. Despite the fluctuations at high $R_{\rm DV}$ (due to limited statistics), we can see that the efficiency also has a strong dependence on the gluino lifetime. Therefore we conclude that the ATLAS efficiencies shown in Fig.1 can not be directly applied to any input model. Also we can not neglect the large impact of detector response and the reconstruction algorithm, as illustrated by the difference between the blue and red points in Fig.1. In order to proceed with the recasting (using only the data from Fig.1) we will adopt the following *strategy*:

i. Apply the *base vertex selection* cuts.

ii. Rescale the DV reconstruction efficiencies obtained from the vertex selection cuts above by a factor $r\,(R_{\rm DV})$. This "correction factor" (r) is defined by the ratio of the red and blue

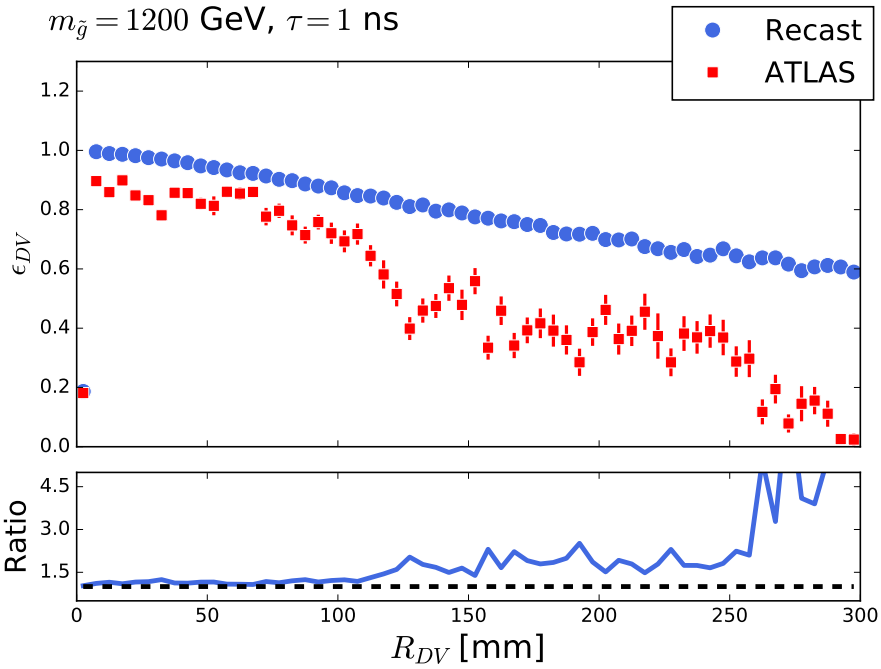

Figure 1: Vertex reconstruction efficiency as a function of the displaced vertex transverse position, $R_{\text{DV}} = \sqrt{x^2 + y^2}$. The red points correspond to the results obtained by ATLAS in Ref. [598], while the blue points correspond to the results obtained through recasting after the *base vertex selection* cuts have been applied. The results refer to the benchmark point $\left(m_{\tilde{g}}, m_{\tilde{\chi}_1^0}, \tau\right) = (1200\text{ GeV}, 100\text{ GeV}, 1\text{ ns})$.

points in Fig.1. This factor aims to encapsulate the experimental features which are not captured by the base vertex selection cuts and is assumed to be model independent.

iii. Apply a constant track efficiency[3], which aims to approximate how many of the truth level charged tracks are actually reconstructed at detector level. This efficiency impacts the event selection efficiency, since events are required to have $n_{\text{tracks}} \geq 5$.

iv. Apply the missing energy and signal region cuts to the surviving events.

With the above procedure we aim to capture the impact of detector effects and the reconstruction algorithm in a model independent way. The validity of this approach clearly relies on strong assumptions about the detector performance and the relation between truth level and detector level observables. However, without further information we believe it is not possible to significantly improve the recasting. Once we apply all the cuts and the correction factor to the events, it is possible to compute signal efficiencies for any input model. These efficiencies can then be used to extract 95% CL upper limits on the total visible cross section using the number of observed events ($N_{\text{obs}} = 0$) and the expected background ($N_{\text{DV}}^{\text{BG}} = 0.02 \pm 0.02$). For reference, a 100% efficiency corresponds to the upper limit $\sigma_{\tilde{g}\tilde{g}} < 0.091$ fb.

[3]The track efficiency clearly depends on the track p_{T} and production position, hence a constant efficiency is an oversimplification. We have tried distinct functional forms for ϵ_{track} following a procedure similar to the one described in Refs. [600, 601]. None of these, however, perform much better (for all values of τ) than the results presented here assuming a constant efficiency.

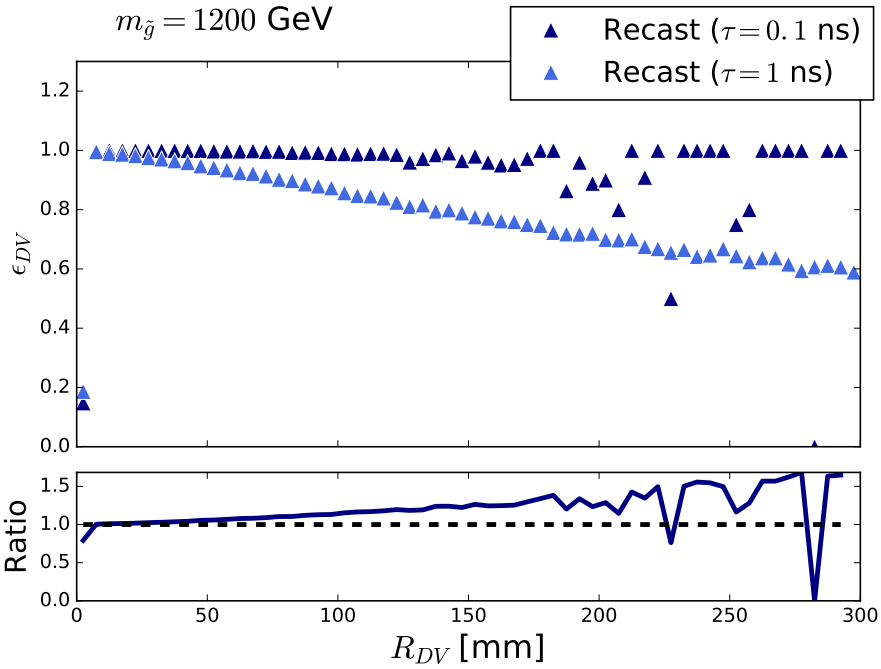

Figure 2: Vertex reconstruction efficiency as a function of the displaced vertex transverse position ($R_{\rm DV}$). The results were obtained through recasting after the *base vertex selection* cuts have been applied. The plot compares the recasting results for a fixed gluino and LSP mass ($m_{\tilde{g}} = 1200$ GeV, $m_{\tilde{\chi}_1^0} = 100$ GeV) and two lifetime values, $\tau = 1$ ns and $\tau = 0.1$ ns.

The results obtained by the above approach for the benchmark points $m_{\tilde{g}} = 1.4$ TeV and $m_{\tilde{g}} = 2$ TeV are shown in Fig. 3. We present recasting curves for three distinct values of the (constant) track efficiency: $\epsilon_{\rm track} = 15\%, 25\%, 100\%$. As we can see, a 25% efficiency can reproduce the official exclusion curve (solid black line) within $\sim 50\%$ for most of the lifetime values. However, in the regions where the efficiency drops significantly ($\tau < 10^{-2}$ ns), the recasting curve is wrong by more than an order of magnitude. Therefore, we conclude that this procedure is not satisfactory for a general purpose recasting of the search presented in Ref. [598]. In the next section we discuss how the recasting improves once we include the detailed efficiencies provided by ATLAS.

2.2 Method 2: Recasting using ATLAS efficiency grids

This approach makes use of the full information provided in the auxiliary material[4] of Ref. [598]: efficiency grids for the event selection (as a function of $R_{\rm DV}$ and $E_{\rm T}^{\rm miss}$) and for the vertex reconstruction efficiency (as a function of $R_{\rm DV}$, $m_{\rm DV}$ and $n_{\rm track}$). These parametrized efficiencies are also given for different regions in the detector, encapsulating the effect of the material veto cut.

According to the note provided by ATLAS, these efficiencies can be applied at truth level once some fiducial cuts have been applied. We use truth level missing energy and identify the truth $R-$hadron decay position and decay products.

[4]This material can be directly access from:
`https://atlas.web.cern.ch/Atlas/GROUPS/PHYSICS/PAPERS/SUSY-2016-08/hepdata_info.pdf`

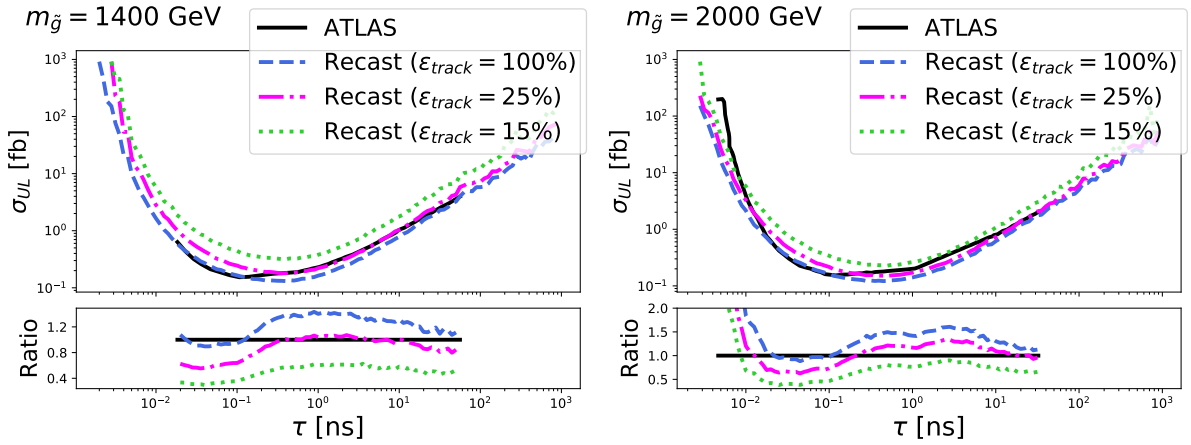

Figure 3: Comparison between the official exclusion curve and the one obtained by recasting the analyses with Method 1 for two values of gluino masses.

The selection of events requires:

- truth level missing energy $E_{\mathrm{T}}^{\mathrm{miss}} > 200$ GeV.
- one trackless jet with $p_T > 70$ GeV, or two trackless jets with $p_T > 25$ GeV. A trackless jet is defined as a jet for which the scalar sum of the p_T of all charged particles inside the jet does not exceed 5 GeV. These jet requirements are applied to 75% of the data. The remaining 25% do not need to satisfy any jet cuts.

In addition, events must have at least one displaced vertex with:

- distance between the interaction point and the decay position > 4 mm.
- the decay position must lie in the fiducial region $R_{\mathrm{DV}} < 300$ mm and $|z_{\mathrm{DV}}| < 300$ mm.
- the number of selected decay products must be at least 5, where selected decay products are charged and stable, with $p_T > 1$ GeV and $|d_0| > 2$ mm.
- the invariant mass of the truth vertex must be larger than 10 GeV, and is constructed assuming all decay products have the mass of the pion.

After imposing the above fiducial cuts, the vertex reconstruction and event selection efficiencies provided by ATLAS can then be applied to compute the final signal efficiencies. The results for the two benchmark points are shown in Fig. 4. Finally, using these efficiencies, we can extract 95% CL upper limits on the total visible cross section using the same procedure described in the previous Section. The results for the exclusion curves are shown in Fig. 5, where we can see that the recasting reproduces the official exclusion curves fairly well for most of the lifetime values. The largest discrepancies are within $\sim 40\%$, which corresponds to a major improvement with respect to the results obtained using only the limited information provided by the ATLAS conference note, as discussed in Section 2.1.

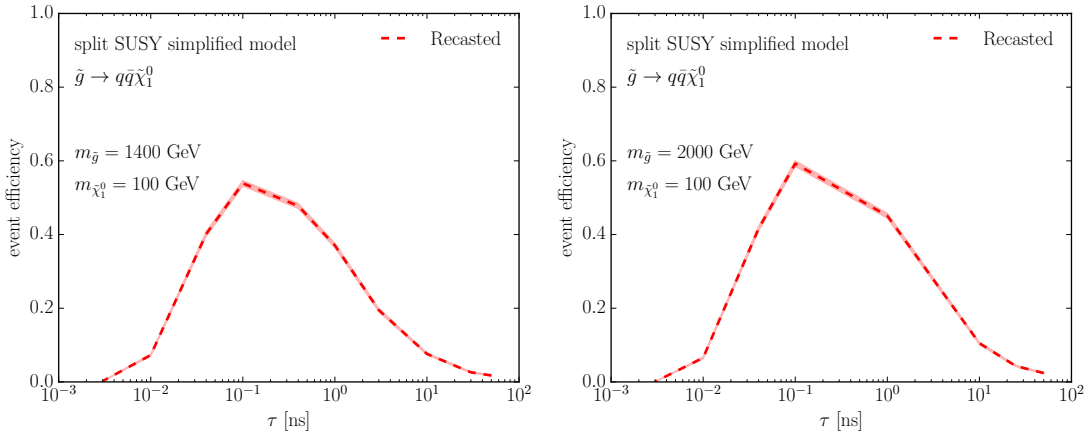

Figure 4: Recasted event-level efficiencies against gluino proper decay lifetime for two values of gluino masses.

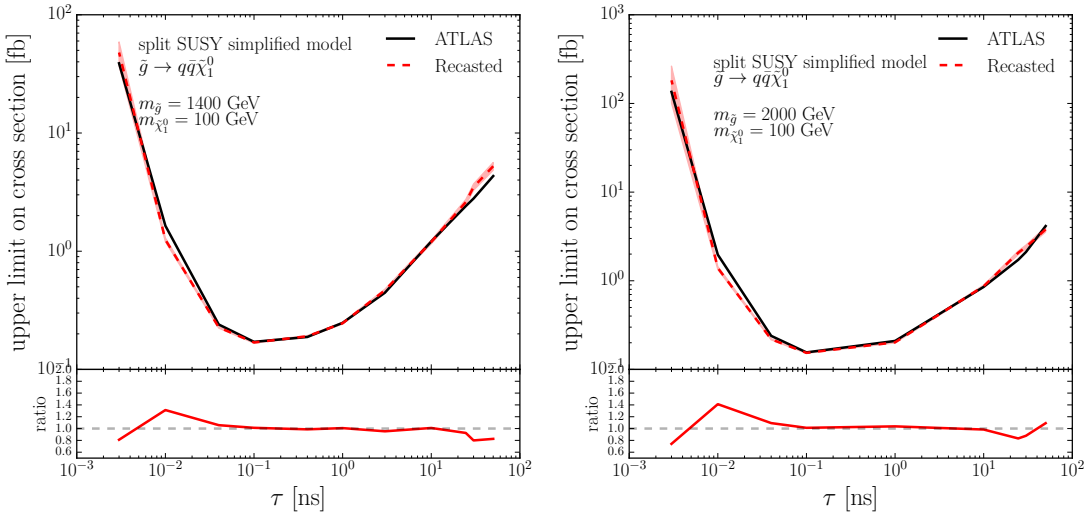

Figure 5: Comparison between the official exclusion curve (solid black line) and the one obtained by recasting the analyses with Method 2 (dotted red line) for two values of gluino masses.

2.3 Comments on the recasting procedure

The results presented in Fig.3 show that it is not possible to recast the ATLAS displaced vertex + missing energy search making use only of the simple vertex reconstruction efficiencies provided in the conference note ATLAS-CONF-2017-026. Although different correction functions can be applied at the vertex and track level to try to capture the impact of detector effects and the vertex reconstruction algorithm, we find that the recasting of the exclusion curves is still off by an order of magnitude at small lifetimes. On the other hand, using the ATLAS efficiency grids highly improves the level of agreement, limiting the discrepancies to be under $\sim 40\%$, as shown by Fig.5. We therefore find that the parametrization of the efficiency grids in terms of truth level variables is extremely useful for recasting, being also straightforward to implement.

Finally, we note that, even though the parametrized selection efficiencies can be in principle

used for any model (and are said to be model independent according to the ATLAS note), we encourage the experimental collaborations to present exclusion curves (or signal efficiencies) for a second model with a distinct event topology. This information is essential to validate the recasting procedure and accurately assess the level of model independence provided by the parametrized efficiencies.

3 DISPLACED LEPTON SEARCHES

One of the cleanest search strategies for long-lived particles decaying into leptons is to look for leptons with a non-zero impact parameter with the primary vertex. Such tracks are normally vetoed to remove contamination from underlying event, cosmics etc., and therefore may not be attributed to the right collision event in standard prompt searches. The CMS displaced lepton search ($\sqrt{s} = 8$ TeV, $\mathcal{L} = 19.7 \pm 0.5\text{fb}^{-1}$) [599] follows a simple strategy of requiring two isolated, oppositely charged, lepton tracks that have a significant impact parameter with respect to the primary vertex. The accompanying material includes efficiency for identification of electrons and muons based on the transverse impact parameter (d_0) and the transverse momentum (p_T) of the lepton. The benchmark scenario for the analysis is stop-pair production $pp \to \tilde{t}\tilde{t}^*$ ($m_{\tilde{t}} = 500$ GeV) followed by an R-parity violating decay via λ'-type coupling $\tilde{t} \to b\ell$, with equal probabilities for $\ell = e, \mu$ and τ.

The recommended recasting procedure is to apply the cuts below on generator-level leptons and reweight the event with the four identification efficiencies and an overall trigger efficiency of 0.95.

1. Select events with one e and one μ, oppositely charged, both coming from a stop
2. Require both leptons to have $|\eta| < 2.5$
3. Require decay vertex of stop to have transverse position $v_0 < 40$ mm, and z-position $v_z < 300$ mm.
4. Require $p_T^{(e,\mu)} > 25$ GeV and $\Delta R_{e\mu} > 0.5$
5. Jet isolation: for each jet (anti-kt, $R = 0.5$, $p_{\text{T}}^{\text{min}} = 10$ GeV), require $\Delta R_{\ell j} > 0.5$
6. Transverse impact parameter 0.1 mm $< d_0 < 20$ mm.
7. Signal regions are further defined as:

   SR3: Both leptons satisfy 1.0 mm $< d_0 < 20$ mm.

   SR2: One or both leptons fail SR3 but satisfy $d_0 > 0.5$ mm

   SR1: One or both leptons fail SR2 but satisfy $d_0 > 0.2$ mm

The updated analysis at 13 TeV ($\sqrt{s} = 13$ TeV, $\mathcal{L} = 2.6\text{fb}^{-1}$, conference note CMS-PAS-EXO-16-022) [120], applies stronger p_{T} cuts by requiring $p_T^{e(\mu)} > 42(45)$ GeV. It also improves isolation cuts on the leptons by requiring that the sum of p_{T} (of all particles) in a cone of 0.3 should be less than 3.5% (6.5%) in the barrel (encdap) for electrons. For muons, cone size is taken to be 0.4 and the sum of p_T is required to be less than 15%. Separation between the two leptons is $\Delta R_{e\mu} > 0.5$, same as before. The mass of the stop in the benchmark point is increased to 700 GeV, however, the decay branching fractions remain unchanged.

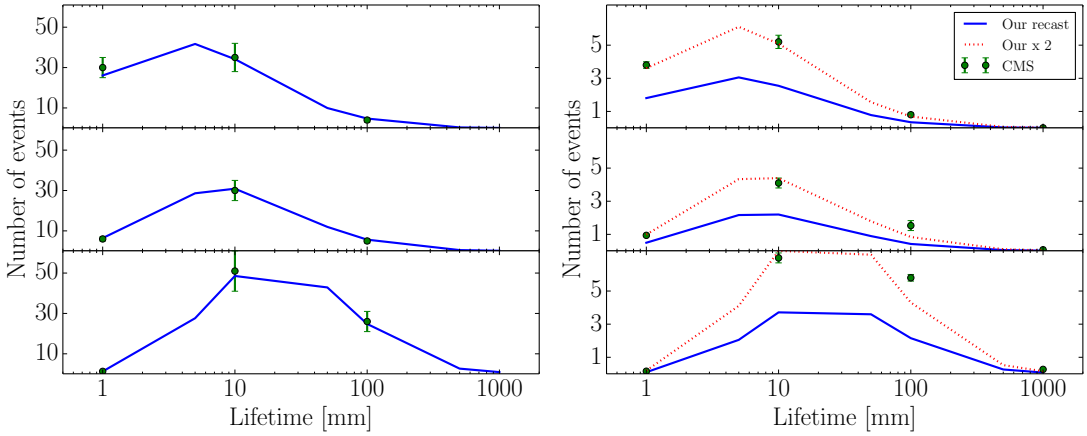

Figure 6: Result from recasting the 8 TeV (left) and 13 TeV (right) displaced lepton analysis comparing number of expected signal events from our simulation (blue) with the published CMS values (green dots). The panels refer to SR1 (top), SR2 (middle) and SR3 (bottom).

A comparison of our validation of the analysis can be seen in Fig. 6. At 8 TeV, the agreement is well within the quoted errors. Using the same efficiency parametrization as 8 TeV for the 13 TeV analysis, we are unable to reproduce the benchmark efficiencies and we find that in general, we have an overall mismatch of a factor of about 2 with respect to the published expected number of signal events. Moreover, we find that the mismatch is higher for longer lifetimes, prompting the inference that the d_0 dependence of the efficiency may have changed between the two runs.

4 CHARGED HEAVY PARTICLE SEARCH

Another important example of LLPs which have been searched for at the LHC are heavy stable charged particles (HSCPs). Here we will consider the searches performed by CMS using 8 TeV [121] and 13 TeV [120] data. These searches are targeted at detector-stable HSCPs and are based on the signature of highly ionizing tracks and anomalous time-of-flight. Below we will discuss the recasting of both of these searches. We point out, however, that while the 8 TeV analysis provided detailed efficiencies for the HSCP reconstruction, the 13 TeV results do not include this information. Therefore, for the 13 TeV search the recasting will make use of an extrapolation of the 8 TeV efficiencies.

4.1 Recasting the 8 TeV search

As mentioned above, the 8 TeV CMS analysis [121] provides efficiency grids for HSCP reconstruction. In particular, probabilities for events to pass the on- and off-line selection criteria are given as a function of the truth-level HSCP kinematics. Due to the inclusive nature of the search, this provides a powerful way to reinterpret the search for arbitrary models containing detector-stable [110, 126, 602–604] or metastable [605] LLPs.

The recasting follows the procedure described in Ref. [121]. We simulate events for HSCP production using MADGRAPH5 [95] for the parton level process and PYTHIA 6 [145] for showering and hadronization. For each event we first identify isolated HSCP candidates imposing the

following isolation criteria:

$$\left(\sum_{i}^{\substack{\text{charged}\\ \Delta R<0.3}} p_{\mathrm{T}}^{i}\right) < 50\,\text{GeV}\,, \qquad \left(\sum_{i}^{\substack{\text{visible}\\ \Delta R<0.3}} \frac{E^{i}}{|\vec{p}|}\right) < 0.3\,, \tag{3}$$

on the truth level events. The sums include all charged and visible particles, respectively, in a cone of $\Delta R = \sqrt{\Delta\eta^2 + \Delta\varphi^2} < 0.3$ around the direction of the HSCP candidate, p_T^i denotes their transverse momenta and E^i their energy. Muons are not considered as visible particles and the HSCP candidate itself is not included in either sum. Once the HSCP candidates are identified, the final signal efficiency (ϵ) is then given by:

$$\epsilon = \frac{1}{N}\sum_{i}^{N} P_{\text{on}}(\vec{k}) \times P_{\text{off}}(\vec{k})\,, \tag{4}$$

where the sum runs over all generated events and P_{on} (P_{off}) is the on-line (off-line) selection efficiency provided by the 8 TeV CMS analysis as a function of the HSCP truth level kinematics ($\vec{k}$). For events containing two HSCP candidates, the above probabilities must be replaced by [121]

$$P^{(2)}_{\text{on/off}}(\vec{k}^1, \vec{k}^2) = P_{\text{on/off}}(\vec{k}^1) + P_{\text{on/off}}(\vec{k}^2) - P_{\text{on/off}}(\vec{k}^1)P_{\text{on/off}}(\vec{k}^2)\,, \tag{5}$$

where $\vec{k}^{1,2}$ are the kinematical vectors of the HSCPs.

In order to validate the above procedure we compute exclusion curves for the same benchmark models considered by the 8 TeV CMS search [126]. The results are shown in Figure 7 for the the gauge-mediated supersymmetry breaking (GMSB) model containing long-lived staus. As we can see both the signal efficiencies (left panel) and the 95% CL upper limits on the inclusive production cross section (right panel) agree with the official CMS results within 5% or less, thus providing an excellent approximation.

4.2 Recasting the 13 TeV search

Given the excellent performance of the recasting method discussed above for the 8 TeV LHC run it would be appealing to be able to use a similar method for the 13 TeV analysis [120]. However, the provision of object efficiencies for the 13 TeV search is so far not pursued. In this section we discuss an attempt to recast the 13 TeV search based on an extrapolation of the object efficiencies from the 8 TeV to the 13 TeV run.

Our aim is to use the 8 TeV efficiencies ($P^{8\,\text{TeV}}_{\text{on/off}}$) for the 13 TeV recasting through the introduction of a correction function that accounts for the differences between both runs. Since the selection criteria for the 8 TeV and 13 TeV searches are very similar, we require the same isolation cuts listed in Eq. 3. We then assume the following ansatz for the 13 TeV efficiencies ($P^{13\,\text{TeV}}_{\text{on/off}}$):

$$P^{13\,\text{TeV}}_{\text{on}}(\vec{k}) = P^{8\,\text{TeV}}_{\text{on}}(\vec{k})\,,\; P^{13\,\text{TeV}}_{\text{off}}(\vec{k}) = F(\beta) \times P^{8\,\text{TeV}}_{\text{off}}(\vec{k})\,, \tag{6}$$

where F is the correction function. The above relations assume that the on-line probability does not change drastically and the main differences between the runs happen in the off-line (trigger) selection. This is a reasonable assumption, since the on-line cuts of both analyses are similar. Furthermore, we expect our treatment to leave enough freedom to account for small corrections in the on-line probability as well. At least for events with only one HSCP candidate there is no

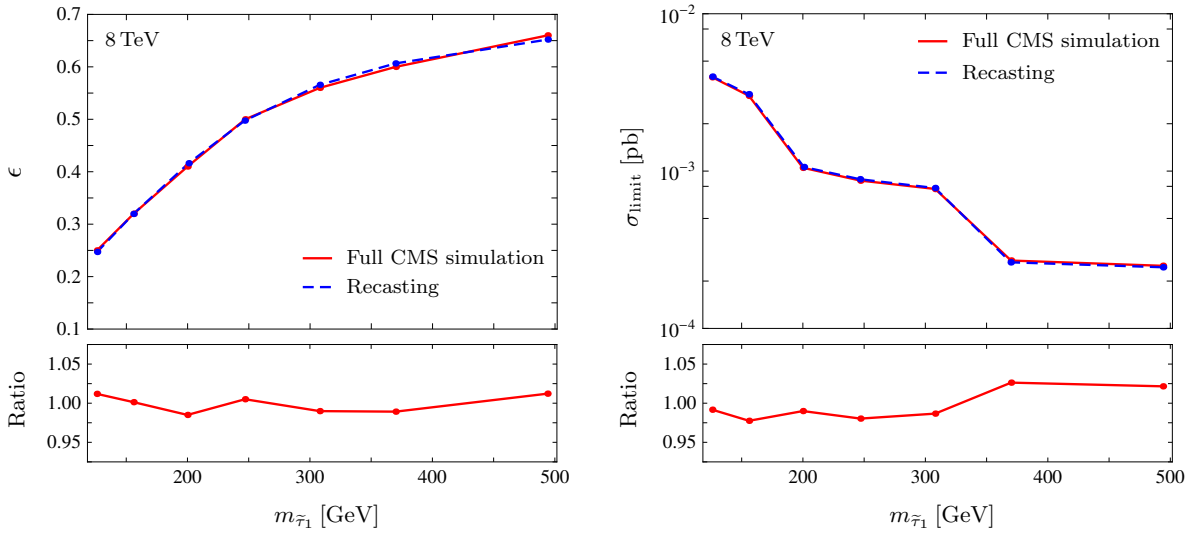

Figure 7: Signal efficiency ϵ (left panel) and 95% CL cross section upper limit (right panel) for the GMSB model as the function of the stau mass. We compare the CMS analysis [121] from the full detector simulation (red solid lines) with the recasting from [121] (blue dashed lines). In the lower frames we show the respective ratios $\epsilon^{\text{Full}}/\epsilon^{\text{Recast}}$, $\sigma^{\text{Full}}_{\text{limit}}/\sigma^{\text{Recast}}_{\text{limit}}$. Taken from [126].

distinction, as the two probabilities are just multiplied. Finally, we assume that F only depends on the HSCP velocity (β) and we parametrize this correction function by eight parameters (C_{β_n}), which corresponds to the value of the function for $\beta = 0, 0.47, 0.6, 0.7, 0.77, 0.83, 0.89, 1.0$. For other values of β we interpolate linearly.

In order to compute the correction function F introduced above we will make use of the official signal efficiencies reported in 13 TeV LHC analysis [120] for specific benchmark points. We determine the parameters C_{β_n} of the correction function in a global fit to these efficiencies using the χ^2 defined as:

$$\chi^2(C_{\beta_n}) = \sum_m \frac{(\epsilon_m(C_{\beta_n}) - \epsilon_m^{\text{CMS}})^2}{\sigma_\epsilon^2}\,, \tag{7}$$

where $\epsilon_m(C_{\beta_n})$ is the efficiency for the benchmark point m using the correction function parameters C_{β_n}, ϵ_m^{CMS} is the respective efficiency reported in [120] and σ_ϵ is the characteristic size of the uncertainty which we (arbitrarily) set to 0.02. We include in the fit the 6 direct stau benchmark points used in the CMS analysis and minimize the χ^2 using MULTINEST [606, 607] for an efficient exploration of the parameter space. The best-fit correction function, $F_{\text{best-fit}}$, and its 1σ uncertainty[5] are shown in figure 8. The deviation of F from 1 implies a decrease or increase of the respective detector and signal efficiencies between the 8 and 13 TeV analysis. We find a slight decrease of efficiencies for large velocities $\beta \gtrsim 0.85$, which is, however, not significant. More surprisingly, the efficiencies at low velocities ($\beta \simeq 0.5$) contain a large and significant increase. From these results it appears that the CMS detector in Run 2 performs significantly better at low velocities. We also point out that the uncertainties for low values of β are quite large, which illustrate the fact that the signal efficiencies provided by the 13 TeV

[5] As stated above the 1σ uncertainty corresponds $\sigma_\epsilon = 0.02$ which is roughly the level of accuracy we aim at in the fit. Note, however, that intrinsic systematic uncertainties in the determination of the efficiencies might be larger, up to around 10%.

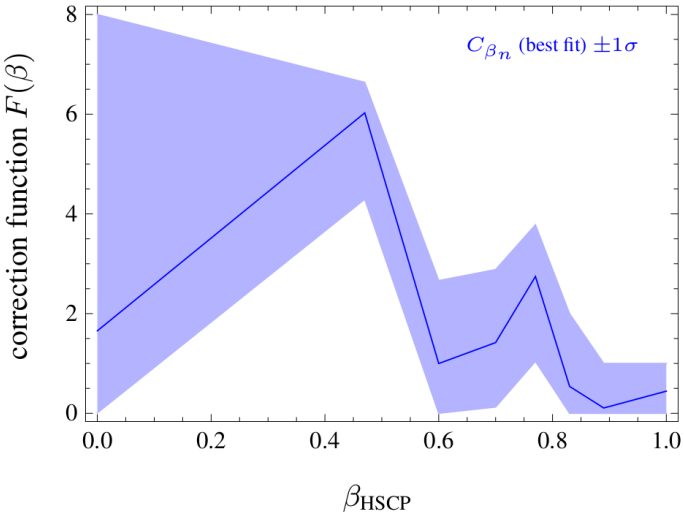

Figure 8: Best-fit correction function $F(\beta)$ and its $\pm 1\sigma$ band.

CMS results are not sufficient to fully constraint the correction function F. However, since no additional information is provided by the 13 TeV CMS analysis, we will use the best fit for F in the following.

Using the off- and on-line probabilities defined in Eq. 6 and the best fit for the correction function ($F_{\text{best-fit}}$) shown in Fig. 8 we can then compute the 13 TeV signal efficiencies for any input model. We first compute efficiencies for the same 6 benchmark points used to obtain F. These benchmarks correspond to direct production of long-lived status with distinct values of the stau mass. The results for the final signal efficiencies for these six benchmark points are shown in Fig. 9 as a function of the HSCP (stau) mass. The solid black line shows the efficiencies reported by CMS in Ref. [120], while the dashed blue curve shows the efficiencies obtained by recasting using the extrapolation of the 8 TeV probabilities and the best fit for F. We also show the recasting efficiencies obtained without the inclusion of the correction function (dashed magenta curve). As expected, $F_{\text{best-fit}}$ reproduces the efficiencies for the six mass points well within the expected fit uncertainties (2%). In particular, it significantly improves the agreement with respect to the naive extrapolation without a correction, *i.e.* for $F = 1$. Formally, in our fit this is reflected in a decrease in the χ^2 from around 130 for $F = 1$ to 0.1 for $F_{\text{best-fit}}$.

The good agreement shown in Fig. 9 between the official CMS results and $F_{\text{best-fit}}$ is expected, since the same benchmark points were used to fit the correction function F. Therefore, a crucial test of the validity of the recasting is its application to an independent set of models. Fortunately, in Ref. [120] CMS has also reported the signal efficiencies for six GMSB points with long-lived staus. These points include both direct production of staus and production through cascade decays of heavier sparticles, resulting in a broader spectrum of event topologies. Using again the extrapolation of the 8 TeV efficiencies and the best fit for the correction function from Fig.8, we compute the final signal efficiencies for these six GMSB points. The results are shown in Fig. 10. As we can see, the efficiencies using $F_{\text{best-fit}}$ now deviate by up to 20% for large HSCP masses, where our recasting undershoots the efficiencies reported by CMS. Although the overall agreement is improved by the correction function, $\chi^2(F_{\text{best-fit}}) \simeq 88$ versus $\chi^2(F = 1) \simeq 240$, the result is much worse than the ones obtained at 8 TeV, where the uncertainties were below

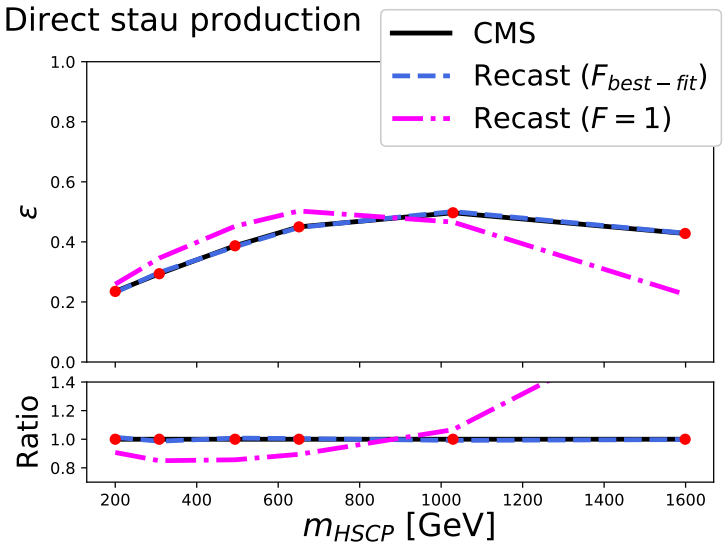

Figure 9: Efficiencies for the six benchmark masses in the direct stau production scenario. The solid black curve shows the efficiencies from [120], while the dashed curves show the efficiencies obtained through recasting. The blue curve corresponds to the best-fit for the correction function, while the magenta shows the efficiencies for $F = 1$.

5%.

The differences between the recasting efficiencies and the ones reported by CMS for the GMSB model might arise from several shortcomings in our recasting procedure. First, we assume F to only dependent on β whereas the full probability maps are parametrized as a function of three kinematic variables: β, p_{T} and $|\eta|$. A parametrization in terms of all three variables, however, is clearly not feasible given the limited amount of information provided in Ref. [120]. As illustrated by Fig. 8, even the parametrization in terms of a single variable can not be fully constrained using only the signal efficiencies reported by CMS. Second, assigning the correction function to the off-line probabilities only might be an over-simplification. For events containing two HSCP candidates, a single correction function F may not be sufficient to parametrize the differences between the two runs. Again, only a better understanding of the underlying changes (*e.g* in the trigger settings) can resolve these ambiguities.

4.3 Comments on the recasting procedure

As illustrated by the results in Section 4.1, the uncertainties in the recasting of HSCP searches can be reduced to the few percent level if efficiencies for the reconstruction and selection of HSCP tracks are provided. This is the case for the 8 TeV CMS analysis, where we were able to successfully recast the HSCP results with a high degree of accuracy [126]. The situation is drastically distinct if these officiencies are not provided by the experimental collaboration, as illustrated by the 13 TeV results in Section 4.2. Even though the CMS analyses for both runs are very similar, the 8 TeV object efficiencies cannot be easily extrapolated to the run 2. Therefore, in order to establish robust reinterpretations of HSCP searches, further information on detector efficiencies are required.

We also point out that the recasting uncertainties for the 13 TeV search could only be properly

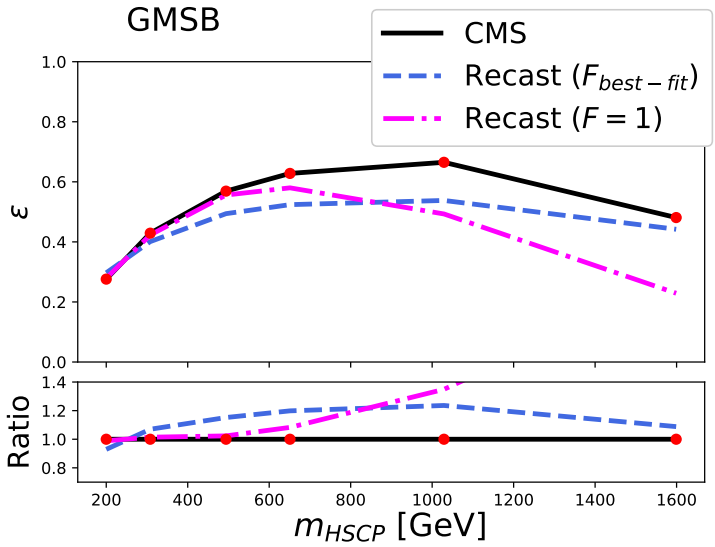

Figure 10: Efficiencies for the six benchmark masses in the GMSB scenario. The solid black curve shows the efficiencies from [120], while the dashed curves show the efficiencies obtained through recasting. The blue curve corresponds to the best-fit for the correction function, while the magenta shows the efficiencies for $F = 1$.

assessed using the official CMS signal efficiencies for two distinct scenarios (the direct stau and GMSB models). This is an important point, since several LLP searches present results for a single model or type of signal topology (see Section 2, for instance). The second model is essential for estimating the validity of the recasting procedure and if it can indeed be extrapolated to other models containing distinct event topologies. As shown by the results in Figs. 9 and 10, the recasting uncertainties would have been highly underestimated if the CMS values for the GMSB scenario were not available.

5 CONCLUSIONS

In this note we have investigate the feasibility of recasting LLP searches within the context of three distinct signatures: displaced vertices, displaced leptons and charged tracks. Although each signature presents its own challenges for recasting, we showed that without detailed object reconstruction and selection efficiencies a satisfactory recasting can not be performed outside the experimental collaborations. The final signal efficiencies or limits in this case can be inaccurate by almost an order of magnitude. On the other hand, for the cases where the object efficiencies were available, such as the ATLAS displaced vertex and the 8 TeV CMS displaced lepton and HSCP searches, we were able to reproduce the official results within 5% to 40%.

In summary, our overall conclusions regarding the relevant information required for a proper recasting of LLP searches are as follows:

1. *Object efficiencies* for reconstruction of the LLP signature must be provided in terms of the relevant truth level observables. As discussed above, without these efficiencies the recasting uncertainties can be over 100%.

2. *Cut-flow tables for expected signal events* would greatly improve the ability to recast these

searches. In the event of a mismatch in the calculation of the final expected signal yield, it is at the moment impossible to pinpoint the source of the problem.

3. *Limits for at least two models (or signal topologies)* should be published so a sanity check can be made before using object efficiencies on a different model. Current standard practice has been to provide object efficiencies with respect to Monte-Carlo truth-level objects for the benchmark model. It is therefore still difficult to understand how well these can be trusted when applied to models or topologies other than the benchmark (e.g. see Figs. 9 and 10).

ACKNOWLEDGEMENTS

This research was supported in part by the São Paulo Research Foundation (FAPESP), projects 2015/20570-1 and 2016/50338-6. GC acknowledges support by the Ministry of Science and Technology of Taiwan under grant No. MOST-106-2811-M-002-035. JH acknowledges support by the German Research Foundation DFG through the research unit “New physics at the LHC”. ND acknowledges the support of the OCEVU Labex (ANR-11-LABX-0060) and the A*MIDEX project (ANR-11-IDEX-0001-02) funded by the "Investissements d’Avenir" French government program managed by the ANR.

Contribution 23

Analysis description for LHC result reinterpretations

P. Gras, H. B. Prosper, S. Sekmen

Abstract

LHADA is a language to describe LHC analysis which has a wide range of applications. In this work, this language is investigated for its usage in the context of LHC result reinterpretation. It would be employed to describe in an unambiguous and concise manner a data analysis including all the details needed for a reinterpretation of the result in the context of a physics theory not considered in the original analysis. A specialisation of the language dedicated to reinterpretation is introduced. The specialisation defines extra syntax rules and constitutes a subset of the language. Three different analyses used as benchmarks are described with this language. Automatic generation of code reproducing the analysis on Monte-Carlo samples for the purpose of result reinterpretation is investigated. We demonstrate that programs that generates code to be used in a result reinterpretation tool can be easily developed and a prototype is presented. In addition, the generated code can be used to validate the accuracy of the analysis description.

1 Introduction

The need for a standard to describe analyses of LHC data in an unambiguous way together with the definition of its requirements has been studied at the 2015 session of Les Houches PhysTeV workshop [72]. The study includes a proposal for this standard (LHADA). In this work, we investigate this proposal in the context of analysis reinterpretation. Three questions are addressed: the coverage of the language, that is its ability to implement a large spectrum of analyses, the completeness of the analysis description, and the capacity to validate this description. The first question is addressed by implementing the description of example analyses with different levels of complexity. The second and third questions were addressed by developing two machine interpreters. The interpreters generate c++ code that reproduces the analysis on an input samples. There is an alternative approach, taken by the `CutLang` [608] interpreter, which does a direct runtime interpretation of its internal text based analysis description language. One of the two interpreters detailed in the following study produces a module, so-called "Rivet analysis", for the RIVET [325] framework, while the second produces a standalone code based on the ROOT [146] framework. The RIVET based code is meant to be used for result reinterpretation. It can also be used to validate an analysis description by reproducing reference numbers provided by the analysis authors. In particular the cut flow, that is the acceptances of the subsequent selections (the "cuts") of the analysis, is well suited for such validation [587]. The completeness of the description is validated at the same time. The second interpreter, called LHADA2TNM is aimed towards running a LHADA analysis on any given type of input ROOT

ntuple, and targets a more generic use, including design and implementation of analyses with the experimental data.

2 Describing analyses in LHADA

In order to test the suitability of the LHADA language to describe LHC analyses, three different new physics searches have been considered. The first analysis is the *Search for new physics in the all-hadronic final state with the MT2 variable* from Ref. [609]. The two other analyses are the *Search for squarks and gluinos in final states with jets and missing transverse momentum at* $\sqrt{s} = 13\,TeV$ *with the ATLAS detector* [594] and *Search for dark matter at* $\sqrt{s} = 13\,TeV$ *in final states containing an energetic photon and large missing transverse momentum with the ATLAS detector* [39], which are used for the comparison of the reinterpretation tools performed in Contribution `\ref{sec:recast}`.

We have described the three analyses with the LHADA language and the descriptions can be found in the analysis descriptions database [610] respectively under `lhada/analyses/CMS-PAS-SUS-16-015` `lhada/analyses /ATLASSUSY1605.03814`, and `lhada/analyses/ATLASEXOT1704. 0384`. No particular difficulty has been encountered. The LHADA17 language subset has been used and a cut flow table has been included [editor's note: to be added] in the description to allow the validation of the descriptions using code generated with the interpreter.

3 Generating a Rivet analysis from LHADA

LHADA is a multipurpose and flexible language. In the case of LHADA2RIVET, the interpreter that generates a Rivet analysis, we have chosen to limit ourselves to the analysis reinterpretation use case and to specify accurately the analysis description language understood by the program. For this purpose, we have derived a subset of the LHADA language, called LHADA17. In this section, we will first draw the specifications of this sublanguage. We will then present the automatic generation of Rivet analyses.

3.1 Describing the description language

The Extended Backus-Naur Form [611, 612] (EBNF) notation has been used to specify the syntax and grammar of LHADA17. The syntax is given in Appendix A. The following rules which have not been included in the EBNF syntax to simplify the notation apply:

- A hash sign (#) can be used to include comments in the LHADA files: all characters of a line starting from a hash sign are comments and ignored for the interpretation based on the EBNF description.
- If the last non-space character of a line is a backslash (\), then the line is merged with the following line before being interpreted according to the EBNF description.
- An entity (`function`, `object` or `cut`) should be declared before being used. For instance if a function is used in a "cut" definition, the corresponding `function` block should appear before the `cut` line. This rule is meant to simplify the parsing and also to avoid circular definitions.

A specificity of LHADA is the usage of programming languages to describe algorithms, via the LHADA `functions` while the main structure of the analysis is described with the dedicated

language. A reference implementation of the algorithm is provided in a "commonly used" programming language. The implementation is given in a code source file, which can group implementations of different LHADA `functions` and can be shipped along with the LHADA description file or provided as an http link. In order to ease machine interpretation LHADA17 includes the following restrictions for the reference `function` implementations.

- the implementation is written in c++11 [613];
- the implementation must depend only on the code provided in the file and libraries from the restricted set defined below; the file should be compilable with c++11 compliant compilers.
- the allowed types for the function parameters are: `int`, `float`, `double`, `std::string`, `LHADAParticle`, `LHADAJet`, `FourMomentum` and `std::std::vector` of the last three types. Parameters are passed by copy (no modifier) or by constant reference (with `const &` modifier, like `const LHADAParticle&`); this rules exclude the use of a templated function; function templates are allowed for auxiliary functions;
- `#include` statements can be used to include header files from the allowed libraries;
- the file, where the functions is defined should be compilable with c++11 compliant compilers;
- self-contained function are encouraged but not mandatory; by self contained we mean that the file is compilable with c++11 compliant compilers after having removed all code except the function and the `#include` that precedes it;
- the function can use the random object to draw pseudo-random numbers, whose scope is global to all functions and which provides the methods described in Table 3;

The `LHADAParticle` and `FourMomentum` types are two classes storing the properties listed in Tables 2 and 1. The `LHADAJet` type is identical to `LHADAParticle`, but without the `pdgid` property; it is introduced to distinguish jets from particles. In the `select` and `reject` statements, the property is referred to with its name, while in the c++ code, a method sharing the same name is used, e.g. `name()` for the property `name`. The complete class definition can be found in the LHADA github repository under `code_lib/include`.

The restricted set of libraries includes the libraries that comes with the c++ standard (`std` libraries) and a common library provided in the LHADA github repository in the directory `code_lib`. The set of libraries can evolve without requiring a revision of the LHADA17 language standard and will be defined by a list stored in the LHADA repository.

The LHADA language does not explicitly specify how the arguments listed in a `function` block are matched to the arguments of the reference implementation of the function. To prevent confusion, LHADA17 requires that the arguments appear in the `function` block in the order of the c++ function argument list of its reference implementation and with the same name. If the names differ, the arguments should be matched according to their order, though in such case the file can simply be considered as invalid.

An `object` block defines an entity, typically a collection of particles, starting from the input defined by the `take` statement that is transformed by a sequence of `apply`, `select`, and `reject`

Table 1: Definition of the FourMomentum type: list of properties.

LHADA	Description
mass	Mass
e	Energy
px	momentum x-component
py	momentum y-component
pz	momentum z-component
pt	absolute transverse momentum
eta	pseudorapidity
rapidity	rapidity

Table 2: Definition of the LHADAParticle type: list of properties coming in addition to the ones of the FourMomentum type.

Property	Description
pdgid	PDG particle id
charge	charge
x	particle production vertex x-coordinate
y	particle production vertex y-coordinate
z	particle production vertex z-coordinate

Table 3: Definition of the random object interface: list of provided methods.

c++ method	Description
uniform(double x)	Returns a pseudorandom number following a uniform distribution over the $[0, \mathrm{x}]$ interval.
gauss(double mean, double sigma)	Returns a pseudorandom number following a Gaussian distribution.
poisson(int mean)	Returns a pseudorandom number following a Poisson distribution.
breitWigner(double mean, double gamma)	Returns a pseudorandom number following a Breit-Wigner distribution.
exp(double tau)	Return a pseudorandom number following the $\exp(-t/\mathrm{tau})$ distribution.
landau(double mean, double sigma)	Returns a pseudorandom number following a Landau distribution.
binomial(int ntot, double prob)	Returns a pseudorandom number in the $[0, \mathrm{ntot}]$ interval following a Binomial distribution.

statements. The `apply` statement specifies a function that transforms the entity. In LHADA17, the function must take as first argument the entity to transform. This argument is specified in the function definition, but not on the `apply` statement, where it is implicit. Collections are filtered with `select` and `reject` statements. A condition to respectively keep or reject a collection element is provided in the form of a boolean expression. In addition to arithmetic and boolean operations, the expression can contain calls to functions. In the examples given in Ref. [72], the functions take the collection element as an implicit argument, but this might not always be the case. In LHADA17 the following rule applies: if the number of passed arguments is less by one with respect to the expected one, then the collection element to filter is assumed to be implicitly passed as first argument. A mismatch between the expected argument type and the collection element type is considered as ill-formed. While the `apply` statement is valid for an entity which is a single object (e.g. missing transverse momentum), the `select` and `reject` statements are restricted to collections. Blocks without a `take` statement are also allowed. In this case there is no implicit argument in the `apply` statement. It is strongly discourage to use this form when the one with a `take` statement can be used.

The event selection is defined with `cut` blocks. In order to simplify the description of the selection flow, the reference in a `cut` block to another `cut` block, introduced in `Lhada` to allow branching, is allowed in the first statement of the block only.

Three extensions to LHADA are introduced in LHADA17. The first is the backslash line continuation marker described above. The second extension concerns the `take external` statement of the `object` block. In LHADA17 is it followed by a label identifying the object. A record of possible objects with their definition and properties (e.g. reconstruction efficiency and resolution in case of reconstructed particles) is kept in the `Lhada` repository. The repository is updated when new objects are needed. Finally, we have introduced two aliases for the keyword `object`: `variable` and `collection`. The `object` block can represent several types of entities. Providing the possibility to use a name reflecting the type of entities, `collection` when dealing with a collection of physics object, `variable` when dealing with a single observable, like an event shape variable, should help in writing more intelligible analysis descriptions. The choice of the name is left to the discretion of the analysis description author.

3.2 Automated generation of Rivet analysis code

The LHADA language will play a role for LHC result reinterpretations only if it is interfaced to commonly used reinterpretation frameworks. The interface can be done in two different ways. The first approach is to interpret the analysis description at run time. The second one, which is adopted here, is to generate code from the description.

An application, called LHADA2RIVET, that produces a Rivet analysis from its description in LHADA17 is being developed. The analysis produces a cut flow table. Special care has been taken to produce code in the RIVET style using facilities provided by the framework, like the projections or the `CutFlow` class.

The detector response effect can be included in two different ways. The interpreter supports a list of reconstructed objects, defined in the LHADA repository, using the RIVET built-in feature. The LHADA description will take reconstructed objects as `external`. Alternatively, the detector effects (efficiency and resolution) can be defined in the LHADA description: it then takes generator-level object (typically HEPMC [614] particles) as `external` and the detector effect is included using `apply` statements and c++ functions. The random object was introduced in LHADA17 for this purpose and the common library includes a help function that can be called

to apply efficiency and resolution effects.

The code produced by the LHADA2RIVET interpreter for the first analysis considered in the previous section can be found in appendix B. The code was produced with an early version of the interpreter that did not include the detector effect simulation. The code is shown for illustration only and is not fully valid. Each LHADA cut block is mapped to a c++ method. RIVET built-in tools, as Projections and Cutflow are used, leading to a clean code that is well integrated in the framework. The calculation of the event count passing each cut using the Cutflow object is not correct and a proper support of cut flow is under development. The RIVET interface to the fastjet [99] library is used to cluster the jets.

With this prototype we have investigated the different aspects that a result reinterpretation code generator based on a LHADA analysis description should cover. We can conclude from this exercise that the development of such a generator that takes as input a description compliant with the LHADA17 specifications is possible with a reasonable effort. The code produced by such a generator can be used to validate the analysis description using analysis cut flow, which needs to be provided by the analysis authors.

4 The LHADA2TNM interpreter

Two key design features of LHADA are human readability and analysis framework independence. As noted above, framework independence can be tested by attempting to implement tools that automatically translate analyses described using LHADA into analyses that can be executed in different analysis frameworks. Human readability is enhanced by limiting the number of rules and syntactical elements in LHADA. But, since we also demand that LHADA be sufficiently expressive to capture the details of LHC analyses, it pays to follow Einstein's advice: "Everything should be made as simple as possible, but not simpler". In the prototype of the LHADA2TNM translator, we have tried to place the burden where it properly belongs, namely, on the translator. For example, it is expected that physicists will write LHADA files so that blocks appear in a natural order. However, the LHADA2TNM translator does not rely on the order of blocks within a LHADA file. The appropriate ordering of blocks is handled by the translator. Given a `cut` block called `signal`, which makes use of another called `preselection`, LHADA2TNM places the code for `preselection` before the code for `signal` in the resulting C++ file.

Another example of placing the burden on the translator rather than on the author of a LHADA file, concerns statements that span multiple lines. Many computer languages have syntactical elements to identify such statements. However, since LHADA is a keyword-value language, continuation marks are not needed because it is possible to identify when the value associated with a statement ends. In order to determine where a statement ends, LHADA2TNM looks ahead one record in the LHADA file during translation.

The LHADA2TNM translator is a `Python` program that translates a LHADA file to a C++ program that can be executed within the TNM n-tuple analysis framework. This framework is the analysis component of a tool developed as a generic mapper from CMS analysis data objects to ntuples comprising integers and floats and arrays thereof. Note, however, that the framework depends on ROOT only and not on any CMS data structures. TNM therefore serves as a generic ntuple-based analysis framework. The LHADA2TNM translator extracts all the blocks from a LHADA file and places them within a data structure that groups the blocks according to type. The `object` and `cut` blocks are ordered according to their dependencies on other object

or cut blocks. It is assumed that a standard, extensible, type is available to model all analysis objects and that an adapter exists to translate input types, e.g., DELPHES, ATLAS, CMS, etc., types to the standard type. This assumption is not an imposition on the LHADA language, but rather is an aid to the writing of translators and, or, interpreters for LHADA. One benefit is that the C++ implementations provide a clear separation between the analysis code, viewed as an algorithm applied to instances of a standard type, and the input types.

In the current version of LHADA2TNM, instances of the standard, extensible, type as well as functions are placed in the global namespace of the C++ program so that the object and cut code blocks that need them can access them without the need to pass objects between code blocks. The name of a function defined in LHADA is assumed to be identical with that of a function, which, ultimately, will be accessed from an online code repository. However, this assumption can be relaxed if warranted in a later iteration of LHADA; for example, the appropriate function can be specified by its DOI. While the technical details of the automatic access of codes from an online repository need to be worked out, we see no insurmountable hurdles.

One of the purposes of the standard, extensible, type is to accomodate the reality that different input types can, and do, have different attributes and sometimes identical attributes with different names. For example, the transverse momentum of a particle may be called `PT`, in DELPHES, while the same attribute may be called `Pt` in other input types. It can be argued that we should try to agree on naming conventions. But, in the real world of particle physics, we cannot even agree on whether the signal strength is to be defined as measured over predicted cross section or the inverse. Trying to enforce naming conventions, at least until such time as LHADA has become mainstream, would be decidedly counter-productive. Therefore, the extensible type used by LHADA2TNM uses the attribute names of the input types. The attributes are modeled as map between a name (as a string) and a floating point value.

5 Conclusion

The sustainability of the LHADA language to be used in the context of analysis reinterpretation has been studied. Three questions have been addressed: the analysis range the language can cover, the completeness of the analysis description, and the capacity to validate the analysis description. The analysis coverage question has been tackled by taking three different LHC searches and implementing their description. The language turns out to be very flexible and no difficulty has been encountered in this exercise giving confidence that the proposed language covers the need. Nevertheless, it will be wise to extend the exercise with a larger number of and more sophisticated analyses. The two other questions have been addressed by developing the prototypes of two applications that interpret analysis descriptions written in LHADA. The development of an application generating reinterpretation code out of a LHADA analysis description can easily be done provided that the syntax used by the description is well-defined and not too flexible. A specialisation, LHADA17, of the LHADA language that fulfils this requirement has been set up. The restrictions introduced by LHADA17 have not been a limitation for the description of the analysis considered in the coverage test.

Acknowledgements

Since the first discussions in Les Houches 2015, many people contributed to developing the LHADA concept. We would especially like to thank Daniel Dercks, Nishita Desai, Sabine Kraml, Suchita Kulkarni, Gokhan Unel, Federico Ambrogi, Wolfgang Waltenberger, Lukas

Heinrich, Roberto Leonardi, Luca Perrozzi, Jim Pivarski, Kati Lassila-Perini, Tibor Simko and the CERN Analysis Preservation Support Group for their valuable input. We also would like to thank the organizers of Les Houches PhysTeV 2017 workshop for a stimulating and fruitful workshop.

Appendices

Appendix

A LHADA17 language syntax

```
(* Definition of the LHADA file structure *)

lhada file = info block, {function block}, {object block}, {cut block}, {table block}


(* Syntax of an info block *)

info block = "info analysis", EOL,
             {space, analysis info}

analysis info = analysis info key, text

analysis info key = "id" | "doc" | "experiment" | "publication" | "sqrtS" | "lumi" |
                    "arXiv" | "hepdata"


(* Syntax of a function block *)

function block = "function", space, function name, EOL,
                 {space}, "#", {char}, EOL,
                 {arg statement}
                 indent, "code", space, extented file path, EOL

function name = identifier
arg statement = indent, "arg", space, arg name, {space, arg name}, EOL
arg name = identifier

(* Syntax of an object block *)

object block = internal objecct | external object

internal object block = object, space, object name, EOL,
                        indent, "take", space, internal input, EOL,
                        {object optional statement}

object = "object" | "collection" | "variable"

object optional statement = apply statement | cut statement

internal input = "Particles" |  defined object

defined object = identifier (* the object must be defined in an object block in
                               the preceding text *)

external object name = identifier
```

```
external object block = object, space, object name, EOL,
                        indent, "take", space, "external", external object name, EOL,

apply statement = indent, "apply", space, function call

cut statement  = indent, "cut", expression

(* Syntax of a cut block *)
cut block = "cut",  space, cut name, EOL
            {"select", space, expression, EOL}

cut name = identifier

(* Syntax of a table block*)

table block = "table", space, table name, EOL,
              indent, "type", space, table type, EOL,
              indent, "columns", {space, column name}, EOL (* header *)
              {indent, "entry", {space, cell content}, EOL} (* lines *)
              (* The number of fields in table lines must match
                 with the number of columns defined in the header*)
              [indent, "hepdata", space, extended file path]

table name = identifier
table type = "events" | "limits" | "cutflow" | "corr" | "bkg"
cell content = (char - space}

(* Syntax for a function call *)

function call =  defined function, "(", arg list, ")"
defined function = function name (* The function must be defined
                                    with a function block before in
                                    the file *)
arg list = "" | arg, { ", ", arg}
arg = arg name, {space}, "=", {space}, expression, { ",", expression }


(* Miscellaneous *)

extended file path = ? http, https, or ftp url as defined in RFC 2386 ? |
                     ? unix-like path name ?


(* Syntax of a mathematical expression *)
(* Note: we have not expressed the operator precedence rules within the grammar below *)
(* The same precedence as the one of c/c++ language applied *)

expression = primary expression, {primary expression}

primary expression = real number | variable | unary operation | binary operation |
                     function call | "(", expression, ")"

variable = identifier

operator = "+" | "-" | "*" | "/" | "**" | "^" | "and" | "or" | "&&" | "||" | "<" | ">" |
```

```
          "<=" | ">=" | "!="
unary operator = "-" | "not" | "!"
unary operation = unary operator, ( real number | variable | unary operation |
                                    function call | "(" expression ")" )
binary operation = expression, binary operator, expression

(* Syntax of identifiers*)
identifier = ( letter | "_" ), {letter | "_" | digit }

(* Definition of character sets *)

letter = "A" | "B" | "C" | "D" | "E" | "F" | "G" | "H" | "I" | "J" | "K" | "L" | "M" |
         "N" | "O" | "P" | "Q" | "R" | "S" | "T" | "U" | "V" | "W" | "X" | "Y" | "Z" |
         "a" | "b" | "c" | "d" | "e" | "f" | "g" | "h" | "i" | "j" | "k" | "l" | "m" |
         "n" | "o" | "p" | "q" | "r" | "s" | "t" | "u" | "v" | "w" | "x" | "y" | "z"

digit = "0" | "1" | "2" | "3" | "4" | "5" | "6" | "7" | "8" | "9"

(* symbols include all 7-bit ASCII characters other than letters, digits and spaces *)
symbol =  "!" | """ | "#" | "$" | "%" | "&" | "'" | "(" | ")" | "*" | "+" | "," | "-" |
          "." | "/" | ":" | ";" | "<" | "=" | ">" | "?" | "@" | "[" | "\" | "]" | "^" |
          "_" | "`" | "{" | "|" | "}" | "~"

space char = " " | (? ISO 6429 character Horizontal tab ?)

char = letter | digit | symbol | space char

sign = "+" | "-"

exp10 sign = "e" | "E"

EOL = ( ?  ISO 6429 character Line Feed ?)

(* Definition of numbers *)

natural number = digit, {digit}

integer = [sign], ( digit - "0" ) , { digit }

real number = decimal, { exp10 sign, integer }

decimal = ( ( integer, [ "." ] ) | ( { integer }, ".", natural number) )

(* Definition of space *)

space = {space char}
indent = space (* Alias used for a space at beginning of a line *)
```

B Example of code produced by the LADHA2RIVET interpreter

```
// -*- C++ -*-
#include <iostream>
#include "Rivet/Analysis.hh"
#include "Rivet/Tools/Cutflow.hh"

#include <math.h>
```

```
#include "Rivet/Projections/FastJets.hh"
#include "Rivet/Projections/FastJets.hh"
#include "Rivet/Projections/MissingMomentum.hh"
namespace Rivet {


  class CMS_PAS_SUS_16_015: public Analysis {
  public:

    ///Cut ids
    enum {kmt2_cut, kdeltaphi_etmiss_jet, kveto, kpreselection,
          kone_jet_selection, kat_least_two_jet_selection,
          k1j_loose_1, k1j_loose_2, k1j_medium_1, k1j_medium_2,
          k1j_medium_3, k1j_medium_4, k1j_medium_5, k1j_medium_6,
          k1j_medium_7, k1j_medium_8} CutIds;
    /// Constructor
    CMS_PAS_SUS_16_015():      Analysis("CMS_PAS_SUS_16_015"),
      cutflow("CutFlow", {"kmt2_cut", "kdeltaphi_etmiss_jet",
            "kveto", "kpreselection", "kone_jet_selection",
            "kat_least_two_jet_selection", "k1j_loose_1",
            "k1j_loose_2", "k1j_medium_1", "k1j_medium_2",
            "k1j_medium_3", "k1j_medium_4", "k1j_medium_5",
            "k1j_medium_6", "k1j_medium_7", "k1j_medium_8"})
    {  }


    /// Book histograms and initialise projections before the run
    void init() {

      FinalState fs;
      VisibleFinalState visfs(fs);

      addProjection(FastJets(fs, FastJets::ANTIKT, 0.4), "jets_eta47");
      addProjection(FastJets(fs, FastJets::ANTIKT, 0.4), "bjets");
      addProjection(MissingMomentum(fs), "met");
    }

    template<typename P>
    double  scalar_pt_sum(const std::vector<P>& momenta){
        double ht  = 0;
        for(const auto& p: momenta){
          ht += p.pt();
        }
        return ht;
    }


    double  btag_eff(const Particles& bjets){
        return 1.;
    }


    template<typename P>
    double  mt2(const P& particle1, const P& particle2, const P& met){
        return P();
    }
```

```
template<typename P1, typename P2>
double  dphi(const P1& p1, const P2& p2){
    double r = acos(p1.px()*p2.px() + p1.px()+p2.py() )
      / sqrt((p1.px()*p1.px() + p1.py()*p1.py())
             * (p1.px()*p1.px() + p1.py()*p1.py()));
    return isnan(r) ? 0 : r;
}


bool cut_mt2_cut(){
    bool r = true;
    return cutflow.fill(kmt2_cut, r);
}

bool cut_deltaphi_etmiss_jet(){
    bool r = true;
    r &= (dphi(met, jets[1 - 1]) > 0.3)  && (dphi(met, jets[2 - 1]) > 0.3)
      && (dphi(met, jets[3 - 1]) > 0.3)  && (dphi(met, jets[4 - 1]) > 0.3);
    return cutflow.fill(kdeltaphi_etmiss_jet, r);
}

bool cut_veto(){
    bool r = true;
    return cutflow.fill(kveto, r);
}

bool cut_preselection(){
    bool r = true;
    r &= cut_mt2_cut();
    r &= cut_deltaphi_etmiss_jet();
    r &= cut_veto();
    return cutflow.fill(kpreselection, r);
}

bool cut_one_jet_selection(){
    bool r = true;
    r &= cut_preselection();
    r &= jets.size() == 1;
    r &= jets[1 - 1].pt() > 200;
    return cutflow.fill(kone_jet_selection, r);
}

bool cut_at_least_two_jet_selection(){
    bool r = true;
    r &= cut_preselection();
    r &= jets.size()> 1;
    r &= cut_mt2_cut()> 200;
    return cutflow.fill(kat_least_two_jet_selection, r);
}

bool cut_1j_loose_1(){
    bool r = true;
    r &= cut_one_jet_selection();
    r &= ht> 575;
```

```
    return cutflow.fill(k1j_loose_1, r);
}

bool cut_1j_loose_2(){
    bool r = true;
    r &= cut_at_least_two_jet_selection();
    r &= bjets.size() < 3;
    r &= ht> 575;
    r &= ht < 1000;
    r &= cut_mt2_cut()> 200;
    return cutflow.fill(k1j_loose_2, r);
}

bool cut_1j_medium_1(){
    bool r = true;
    r &= cut_one_jet_selection();
    r &= bjets.size() < 1;
    r &= ht> 1000;
    return cutflow.fill(k1j_medium_1, r);
}

bool cut_1j_medium_2(){
    bool r = true;
    r &= cut_one_jet_selection();
    r &= bjets.size()> 0;
    r &= ht> 575;
    return cutflow.fill(k1j_medium_2, r);
}

bool cut_1j_medium_3(){
    bool r = true;
    r &= cut_at_least_two_jet_selection();
    r &= jets.size() < 4;
    r &= bjets.size() < 1;
    r &= ht> 575;
    r &= ht < 1000;
    r &= cut_mt2_cut()> 800;
    return cutflow.fill(k1j_medium_3, r);
}

bool cut_1j_medium_4(){
    bool r = true;
    r &= cut_at_least_two_jet_selection();
    r &= jets.size() < 4;
    r &= bjets.size()> 0;
    r &= bjets.size() < 3;
    r &= ht> 575;
    r &= ht < 1000;
    r &= cut_mt2_cut()> 600;
    return cutflow.fill(k1j_medium_4, r);
}

bool cut_1j_medium_5(){
    bool r = true;
    r &= cut_at_least_two_jet_selection();
    r &= jets.size() < 4;
```

```
    r &= bjets.size() < 2;
    r &= ht> 1000;
    r &= ht < 1500;
    r &= cut_mt2_cut()> 800;
    return cutflow.fill(k1j_medium_5, r);
}

bool cut_1j_medium_6(){
    bool r = true;
    r &= cut_at_least_two_jet_selection();
    r &= jets.size() < 4;
    r &= bjets.size() == 2;
    r &= ht> 1000;
    r &= ht < 1500;
    r &= cut_mt2_cut()> 400;
    return cutflow.fill(k1j_medium_6, r);
}

bool cut_1j_medium_7(){
    bool r = true;
    r &= cut_at_least_two_jet_selection();
    r &= jets.size() < 4;
    r &= bjets.size() < 2;
    r &= ht> 1500;
    r &= cut_mt2_cut()> 400;
    return cutflow.fill(k1j_medium_7, r);
}

bool cut_1j_medium_8(){
    bool r = true;
    r &= cut_at_least_two_jet_selection();
    r &= jets.size() < 4;
    r &= bjets.size() == 2;
    r &= ht> 1500;
    r &= cut_mt2_cut()> 200;
    return cutflow.fill(k1j_medium_8, r);
}
/// Perform the per-event analysis
void analyze(const Event& event) {

   const FastJets& jets_eta47Proj = applyProjection<FastJets>(event, "jets_eta47");
   Jets jets_eta47 = jets_eta47Proj.jetsByPt();
   Jets jets;
   for(const auto& p: jets_eta47){
     if((p.eta() < 2.4)){
       jets.push_back(p);
     }
   }

   const FastJets& bjetsProj = applyProjection<FastJets>(event, "bjets");
   Jets bjets = bjetsProj.jetsByPt();
   const MissingMomentum metProj = applyProjection<MissingMomentum>(event, "met");
   met = metProj.missingMomentum();
   ht = scalar_pt_sum(jets);

   cut_1j_loose_1();
```

```
      cut_1j_loose_2();
      cut_1j_medium_1();
      cut_1j_medium_2();
      cut_1j_medium_3();
      cut_1j_medium_4();
      cut_1j_medium_5();
      cut_1j_medium_6();
      cut_1j_medium_7();
    }


    /// Normalise histograms etc., after the run
    void finalize() {
      std::cout << "Analsyis cut flow:\n"
                << "-----------------\n\n"
                << cutflow << "\n";
    }


  protected:

    //@{
    /** Collections and variables
     */
    //@}
     /** Analysis objects
      * @{
      */
     Jets jets_eta47;

     Jets jets;

     Jets bjets;

     FourMomentum met;

     double  ht;
     /** @}
     */    //@{
    /** Histograms
     */
    //@}

    ///Tracks the event counts after each cut
    Cutflow cutflow;

  };
  DECLARE_RIVET_PLUGIN(CMS_PAS_SUS_16_015);
}
```

Bibliography

[1] N. Craig, P. Draper, K. Kong, Y. Ng, and D. Whiteson, 1610.09392. 10

[2] M. Aaboud *et. al.*,, **ATLAS** Collaboration, 1707.02424. 10, 11

[3] M. Aaboud *et. al.*,, **ATLAS** Collaboration, 1710.09748. 10, 11, 12

[4] M. Aaboud *et. al.*,, **ATLAS** Collaboration, 1706.04786. 10, 11

[5] M. Aaboud *et. al.*,, **ATLAS** Collaboration, *JHEP* **08** (2017) 052, [1705.10751]. 10, 12, 17

[6] G. Aad *et. al.*,, **ATLAS** Collaboration, *Phys. Rev.* **D91** (2015), no. 11 112011, [1503.05425]. 10, 12

[7] **ATLAS** Collaboration, Tech. Rep. ATLAS-CONF-2017-001, CERN, Geneva, Jan, 2017. 11

[8] M. Aaboud *et. al.*,, **ATLAS** Collaboration, *Eur. Phys. J.* **C76** (2016), no. 10 541, [1607.08079]. 11

[9] G. Aad *et. al.*,, **ATLAS** Collaboration, *Phys. Rev. Lett.* **112** (2014), no. 9 091804, [1311.2006]. 11

[10] G. Aad *et. al.*,, **ATLAS** Collaboration, *JHEP* **09** (2015) 108, [1506.01291]. 11

[11] M. Aaboud *et. al.*,, **ATLAS** Collaboration, 1709.07242. 11

[12] V. Khachatryan *et. al.*,, **CMS** Collaboration, *Phys. Lett.* **B755** (2016) 196–216, [1508.04308]. 11

[13] **CMS** Collaboration, Tech. Rep. CMS-PAS-EXO-16-006, CERN, Geneva, 2016. 11

[14] A. M. Sirunyan *et. al.*,, **CMS** Collaboration, 1711.08008. 11

[15] M. Aaboud *et. al.*,, **ATLAS** Collaboration, *Phys. Rev.* **D96** (2017), no. 5 052004, [1703.09127]. 11

[16] M. Aaboud *et. al.*,, **ATLAS** Collaboration, *Phys. Lett.* **B759** (2016) 229–246, [1603.08791]. 11

[17] M. Aaboud *et. al.*,, **ATLAS** Collaboration, 1709.10440. 11

[18] A. M. Sirunyan *et. al.*,, **CMS** Collaboration, 1708.05379. 11

[19] A. M. Sirunyan *et. al.*,, **CMS** Collaboration, 1708.08539. 11

[20] Tech. Rep. ATLAS-CONF-2016-014, CERN, Geneva, Mar, 2016. 11

[21] A. M. Sirunyan *et. al.*,, **CMS** Collaboration, *JHEP* **07** (2017) 001, [1704.03366]. 11

[22] A. M. Sirunyan *et. al.*,, **CMS** Collaboration, 1708.01062. 11, 21

[23] M. Aaboud *et. al.*,, **ATLAS** Collaboration, *Phys. Lett.* **B775** (2017) 105–125, [1707.04147]. 11

[24] M. Aaboud *et. al.*,, **ATLAS** Collaboration, *Phys. Lett.* **B764** (2017) 11–30, [1607.06363]. 11

[25] G. Aad *et. al.*,, **ATLAS** Collaboration, *Phys. Lett.* **B738** (2014) 428–447, [1407.8150]. 11

[26] A. M. Sirunyan *et. al.*,, **CMS** Collaboration, *Eur. Phys. J.* **C77** (2017), no. 9 636, [1707.01303]. 11

[27] A. M. Sirunyan *et. al.*,, **CMS** Collaboration, 1710.04960. 11

[28] A. M. Sirunyan *et. al.*,, **CMS** Collaboration, *JHEP* **01** (2018) 054, [1708.04188]. 11, 139

[29] V. Khachatryan *et. al.*,, **CMS** Collaboration, *Phys. Rev.* **D93** (2016), no. 3 032005,

[1509.03750]. [Erratum: Phys. Rev.D95,no.3,039906(2017)]. 12
[30] M. Aaboud *et. al.*,, **ATLAS** Collaboration, *New J. Phys.* **18** (2016), no. 9 093016, [1605.06035]. 12
[31] V. Khachatryan *et. al.*,, **CMS** Collaboration, *Phys. Rev.* **D93** (2016), no. 3 032004, [1509.03744]. 12
[32] V. Khachatryan *et. al.*,, **CMS** Collaboration, *JHEP* **03** (2016) 125, [1511.01407]. 12
[33] A. M. Sirunyan *et. al.*,, **CMS** Collaboration, 1708.07962. 12
[34] A. M. Sirunyan *et. al.*,, **CMS** Collaboration, *JHEP* **07** (2017) 121, [1703.03995]. 12
[35] V. Khachatryan *et. al.*,, **CMS** Collaboration, *Phys. Lett.* **B739** (2014) 229–249, [1408.0806]. 12
[36] V. Khachatryan *et. al.*,, **CMS** Collaboration, *JHEP* **07** (2015) 042, [1503.09049]. [Erratum: JHEP11,056(2016)]. 12
[37] M. Aaboud *et. al.*,, **ATLAS** Collaboration, 1711.03301. 12, 50, 51
[38] A. M. Sirunyan *et. al.*,, **CMS** Collaboration, 1712.02345. 12
[39] M. Aaboud *et. al.*,, **ATLAS** Collaboration, *Eur. Phys. J.* **C77** (2017), no. 6 393, [1704.03848]. 12, 167, 168, 170, 188
[40] M. Aaboud *et. al.*,, **ATLAS** Collaboration, *Phys. Rev. Lett.* **119** (2017), no. 18 181804, [1707.01302]. 12
[41] S. Chatrchyan *et. al.*,, **CMS** Collaboration, *JHEP* **12** (2012) 055, [1210.5627]. 12
[42] G. Aad *et. al.*,, **ATLAS** Collaboration, *Eur. Phys. J.* **C76** (2016), no. 1 5, [1508.04735]. 12
[43] M. Aaboud *et. al.*,, **ATLAS** Collaboration, *Phys. Lett.* **B776** (2018) 318–337, [1708.09624]. 12
[44] A. M. Sirunyan *et. al.*,, **CMS** Collaboration, 1711.00431. 12
[45] A. M. Sirunyan *et. al.*,, **CMS** Collaboration, 1710.00159. 12
[46] G. Aad *et. al.*,, **ATLAS** Collaboration, *JHEP* **11** (2014) 104, [1409.5500]. 12
[47] A. M. Sirunyan *et. al.*,, **CMS** Collaboration, 1710.01539. 12, 17
[48] M. Aaboud *et. al.*,, **ATLAS** Collaboration, *JHEP* **10** (2017) 141, [1707.03347]. 12, 17
[49] G. Aad *et. al.*,, **ATLAS** Collaboration, *Phys. Lett.* **B758** (2016) 249–268, [1602.06034]. 12
[50] G. Aad *et. al.*,, **ATLAS** Collaboration, *JHEP* **08** (2015) 105, [1505.04306]. 12
[51] **ATLAS** Collaboration, Tech. Rep. ATLAS-CONF-2016-032, CERN, Geneva, Jun, 2016. 12
[52] G. Aad *et. al.*,, **ATLAS** Collaboration, *Eur. Phys. J.* **C76** (2016), no. 4 210, [1509.05051]. 12
[53] D. Barducci, A. Belyaev, S. De Curtis, S. Moretti, and G. M. Pruna, *JHEP* **04** (2013) 152, [1210.2927]. 13
[54] D. Greco and D. Liu, *JHEP* **12** (2014) 126, [1410.2883]. 13
[55] A. Deandrea and A. M. Iyer, 1710.01515. 13
[56] L. Basso, B. Fuks, M. E. Krauss, and W. Porod, *JHEP* **07** (2015) 147, [1503.08211]. 13
[57] J. Y. Araz, M. Frank, and B. Fuks, *Phys. Rev.* **D96** (2017), no. 1 015017, [1705.01063]. 13
[58] J. Y. Araz, G. Corcella, M. Frank, and B. Fuks, 1711.06302. 13

[59] D. Barducci and C. Delaunay, *JHEP* **02** (2016) 055, [1511.01101]. 13

[60] A. M. Sirunyan *et. al.*,, **CMS** Collaboration, *JHEP* **09** (2017) 053, [1703.06352]. 13, 18

[61] C. Biggio, M. Bordone, L. Di Luzio, and G. Ridolfi, *JHEP* **10** (2016) 002, [1607.07621]. 14

[62] E. Del Nobile, R. Franceschini, D. Pappadopulo, and A. Strumia, *Nucl. Phys.* **B826** (2010) 217–234, [0908.1567]. 14

[63] M. Cacciari, L. Del Debbio, J. R. Espinosa, A. D. Polosa, and M. Testa, *Phys. Lett.* **B753** (2016) 476–481, [1509.07853]. 15

[64] A. M. Sirunyan *et. al.*,, **CMS** Collaboration, *JHEP* **11** (2017) 085, [1706.03408]. 17, 60, 61

[65] F. del Aguila, M. Perez-Victoria, and J. Santiago, *JHEP* **09** (2000) 011, [hep-ph/0007316]. 17

[66] I. Doršner, S. Fajfer, A. Greljo, J. F. Kamenik, and N. Košnik, *Phys. Rept.* **641** (2016) 1–68, [1603.04993]. 18

[67] J. A. Aguilar-Saavedra, R. Benbrik, S. Heinemeyer, and M. Pèrez-Victoria, *Phys. Rev.* **D88** (2013), no. 9 094010, [1306.0572]. 18

[68] M. Buchkremer and A. Schmidt, *Adv. High Energy Phys.* **2013** (2013) 690254, [1210.6369]. 19

[69] L. Di Luzio, R. Gröber, J. F. Kamenik, and M. Nardecchia, *JHEP* **07** (2015) 074, [1504.00359]. 19

[70] J. Serra, *JHEP* **09** (2015) 176, [1506.05110]. 19, 21

[71] A. Anandakrishnan, J. H. Collins, M. Farina, E. Kuflik, and M. Perelstein, *Phys. Rev.* **D93** (2016), no. 7 075009, [1506.05130]. 19, 21

[72] G. Brooijmans *et. al.*, in *9th Les Houches Workshop on Physics at TeV Colliders (PhysTeV 2015) Les Houches, France, June 1-19, 2015*, 2016. 1605.02684. 19, 21, 164, 187, 191

[73] S. Banerjee, D. Barducci, G. Bélanger, and C. Delaunay, *JHEP* **11** (2016) 154, [1606.09013]. 19

[74] M. Chala, *Phys. Rev.* **D96** (2017), no. 1 015028, [1705.03013]. 19

[75] M. Chala, R. Gröber, and M. Spannowsky, 1801.06537. 19

[76] A. M. Sirunyan *et. al.*,, **CMS** Collaboration, 1802.01486. 21

[77] A. M. Sirunyan *et. al.*,, **CMS** Collaboration, *JHEP* **04** (2017) 136, [1612.05336]. 21

[78] A. M. Sirunyan *et. al.*,, **CMS** Collaboration, *Phys. Lett.* **B772** (2017) 634–656, [1701.08328]. 21

[79] **ATLAS** Collaboration,D. Biedermann, , in *Proceedings, 9th International Workshop on Top Quark Physics (TOP 2016): Olomouc, Czech Republic, September 19-23, 2016*, (Geneva), CERN, CERN, 2016. 21

[80] G. Aad *et. al.*,, **ATLAS** Collaboration, *Phys. Rev.* **D92** (2015), no. 11 112007, [1509.04261]. 21

[81] A. M. Sirunyan *et. al.*,, **CMS** Collaboration, 1708.02510. 21

[82] G. Brooijmans *et. al.*, 1405.1617. 21

[83] M. Buchkremer, G. Cacciapaglia, A. Deandrea, and L. Panizzi, *Nucl. Phys.* **B876** (2013)

376–417, [1305.4172]. 21, 22

[84] G. Cacciapaglia, A. Deandrea, D. Harada, and Y. Okada, *JHEP* **11** (2010) 159, [1007.2933]. 21

[85] G. Cacciapaglia, A. Deandrea, L. Panizzi, N. Gaur, D. Harada, and Y. Okada, *JHEP* **03** (2012) 070, [1108.6329]. 21, 22

[86] J. Fan, S. M. Koushiappas, and G. Landsberg, *JHEP* **01** (2016) 111, [1507.06993]. 21

[87] M. J. Dolan, J. L. Hewett, M. Krämer, and T. G. Rizzo, *JHEP* **07** (2016) 039, [1601.07208]. 21

[88] B. A. Dobrescu and F. Yu, 1612.01909. 21

[89] J. A. Aguilar-Saavedra, D. E. Lopez-Fogliani, and C. Muñoz, *JHEP* **06** (2017) 095, [1705.02526]. 21

[90] B. Fuks and H.-S. Shao, *Eur. Phys. J.* **C77** (2017), no. 2 135, [1610.04622]. 21, 22

[91] A. Alloul, N. D. Christensen, C. Degrande, C. Duhr, and B. Fuks, *Comput. Phys. Commun.* **185** (2014) 2250–2300, [1310.1921]. 21, 22, 53, 72, 90, 141

[92] G. Cacciapaglia, H. Cai, A. Carvalho, A. Deandrea, T. Flacke, B. Fuks, D. Majumder, and H.-S. Shao, *JHEP* **07** (2017), no. 7 005, [1703.10614]. 21

[93] C. Degrande, C. Duhr, B. Fuks, D. Grellscheid, O. Mattelaer, and T. Reiter, *Comput. Phys. Commun.* **183** (2012) 1201–1214, [1108.2040]. 22, 44, 90, 106, 118, 127, 158

[94] C. Degrande, *Comput. Phys. Commun.* **197** (2015) 239–262, [1406.3030]. 22

[95] J. Alwall, R. Frederix, S. Frixione, V. Hirschi, F. Maltoni, O. Mattelaer, H. S. Shao, T. Stelzer, P. Torrielli, and M. Zaro, *JHEP* **07** (2014) 079, [1405.0301]. 22, 30, 32, 44, 52, 72, 85, 90, 118, 119, 127, 141, 158, 166, 167, 172, 180

[96] R. D. Ball *et. al.*,, **NNPDF** Collaboration, *JHEP* **04** (2015) 040, [1410.8849]. 22, 53

[97] T. Sjöstrand, S. Ask, J. R. Christiansen, R. Corke, N. Desai, P. Ilten, S. Mrenna, S. Prestel, C. O. Rasmussen, and P. Z. Skands, *Comput. Phys. Commun.* **191** (2015) 159–177, [1410.3012]. 22, 30, 44, 53, 72, 98, 141, 167, 172, 174

[98] M. Cacciari, G. P. Salam, and G. Soyez, *JHEP* **04** (2008) 063, [0802.1189]. 22, 53, 167, 168

[99] M. Cacciari, G. P. Salam, and G. Soyez, *Eur. Phys. J.* **C72** (2012) 1896, [1111.6097]. 22, 53, 72, 141, 192

[100] G. Aad *et. al.*,, **ATLAS** Collaboration, *Phys. Rev.* **D90** (2014) 052008, [1407.0608]. 26

[101] **CMS Collaboration** Collaboration, Tech. Rep. CMS-PAS-SUS-13-009, CERN, Geneva, 2014. 26

[102] V. Khachatryan *et. al.*,, **CMS** Collaboration, *Phys. Lett.* **B736** (2014) 371–397, [1405.3886]. 26

[103] G. Aad *et. al.*,, **ATLAS** Collaboration, *Eur. Phys. J.* **C74** (2014) 2883, [1403.5222]. 26

[104] G. Aad *et. al.*,, **ATLAS** Collaboration, ATLAS-CONF-2012-104. 26

[105] G. Aad *et. al.*,, **ATLAS** Collaboration, *JHEP* **06** (2014) 124, [1403.4853]. 26

[106] V. Khachatryan *et. al.*,, **CMS** Collaboration, *Eur. Phys. J.* **C75** (2015), no. 5 235, [1408.3583]. 26

[107] J. McDonald, *Phys. Rev. Lett.* **88** (2002) 091304, [hep-ph/0106249]. 27

[108] L. J. Hall, K. Jedamzik, J. March-Russell, and S. M. West, *JHEP* **03** (2010) 080, [0911.1120]. 27, 28, 36

[109] R. T. Co, F. D'Eramo, L. J. Hall, and D. Pappadopulo, *JCAP* **1512** (2015), no. 12 024, [1506.07532]. 27, 36

[110] A. G. Hessler, A. Ibarra, E. Molinaro, and S. Vogl, *JHEP* **01** (2017) 100, [1611.09540]. 27, 36, 180

[111] A. Ghosh, T. Mondal, and B. Mukhopadhyaya, *JHEP* **12** (2017) 136, [1706.06815]. 27

[112] A. M. Baldini *et. al.*,, **MEG** Collaboration, *Eur. Phys. J.* **C76** (2016), no. 8 434, [1605.05081]. 27

[113] G. Belanger, F. Boudjema, A. Goudelis, A. Pukhov, and B. Zaldivar, 1801.03509. 28, 29

[114] M. Blennow, E. Fernandez-Martinez, and B. Zaldivar, *JCAP* **1401** (2014) 003, [1309.7348]. 28

[115] S. Chatrchyan *et. al.*,, **CMS** Collaboration, *Phys. Lett.* **B713** (2012) 408–433, [1205.0272]. 30

[116] G. Aad *et. al.*,, **ATLAS** Collaboration, *Phys. Lett.* **B720** (2013) 277–308, [1211.1597]. 30

[117] S. Chatrchyan *et. al.*,, **CMS** Collaboration, *JHEP* **07** (2013) 122, [1305.0491]. 30, 31

[118] G. Aad *et. al.*,, **ATLAS** Collaboration, *JHEP* **01** (2015) 068, [1411.6795]. 30

[119] M. Aaboud *et. al.*,, **ATLAS** Collaboration, *Phys. Rev.* **D93** (2016), no. 11 112015, [1604.04520]. 30

[120] V. Khachatryan *et. al.*,, **CMS** Collaboration, *CMS-PAS-EXO-16-036* (2016), no. CMS-PAS-EXO-16-036 CMS-PAS-EXO-16-036. 30, 171, 179, 180, 181, 182, 183, 184, 185

[121] V. Khachatryan *et. al.*,, **CMS** Collaboration, *Eur. Phys. J.* **C75** (2015) 325, [1502.02522]. 30, 31, 34, 180, 181, 182

[122] V. Khachatryan *et. al.*,, **CMS** Collaboration, *Phys. Rev. Lett.* **114** (2015), no. 6 061801, [1409.4789]. 31, 32

[123] V. Khachatryan *et. al.*,, **CMS** Collaboration,. 31

[124] W. Beenakker, M. Klasen, M. Krämer, T. Plehn, M. Spira, and P. M. Zerwas, *Phys. Rev. Lett.* **83** (1999) 3780–3783, [hep-ph/9906298]. 32

[125] V. Khachatryan *et. al.*,, **CMS** Collaboration, *Phys. Rev.* **D94** (2016) 112004, [1609.08382]. 33, 36

[126] J. Heisig, A. Lessa, and L. Quertenmont, *JHEP* **12** (2015) 087, [1509.00473]. 34, 180, 181, 182, 184

[127] M. Aaboud *et. al.*,, **ATLAS** Collaboration, 1712.02118. 36

[128] M. Aaboud *et. al.*,, **ATLAS** Collaboration, 1710.04901. 36

[129] A. M. Sirunyan *et. al.*,, **CMS** Collaboration, 1711.09120. 36, 38

[130] A. M. Sirunyan *et. al.*,, **CMS** Collaboration, 1801.00359. 36

[131] G. F. Giudice and R. Rattazzi, *Phys. Rept.* **322** (1999) 419–499, [hep-ph/9801271]. 36

[132] P. Meade, M. Reece, and D. Shih, *JHEP* **10** (2010) 067, [1006.4575]. 36

[133] A. Arvanitaki, N. Craig, S. Dimopoulos, and G. Villadoro, *JHEP* **02** (2013) 126, [1210.0555]. 36

[134] D. G. Cerdeño, V. Martín-Lozano, and O. Seto, *JHEP* **05** (2014) 035, [1311.7260]. 36

[135] G. Burdman, Z. Chacko, H.-S. Goh, and R. Harnik, *JHEP* **02** (2007) 009,

[hep-ph/0609152]. 36
[136] Z. Chacko, H.-S. Goh, and R. Harnik, *Phys. Rev. Lett.* **96** (2006) 231802, [hep-ph/0506256]. 36
[137] D. Tucker-Smith and N. Weiner, *Phys. Rev.* **D64** (2001) 043502, [hep-ph/0101138]. 36
[138] M. J. Strassler and K. M. Zurek, *Phys. Lett.* **B651** (2007) 374–379, [hep-ph/0604261]. 36
[139] M. J. Strassler and K. M. Zurek, *Phys. Lett.* **B661** (2008) 263–267, [hep-ph/0605193]. 36
[140] M. J. Strassler, hep-ph/0607160. 36
[141] Y. Cui and B. Shuve, *JHEP* **02** (2015) 049, [1409.6729]. 36
[142] S. Banerjee, G. Bélanger, B. Bhattacherjee, F. Boudjema, R. M. Godbole, and S. Mukherjee, 1706.07407. 36
[143] S. Asai, K. Hamaguchi, and S. Shirai, *Phys. Rev. Lett.* **103** (2009) 141803, [0902.3754]. 37
[144] S. Ambrosanio, B. Mele, A. Nisati, S. Petrarca, G. Polesello, A. Rimoldi, and G. Salvini, *Rend. Lincei Sci. Fis. Nat.* **12** (2001) 5–18, [hep-ph/0012192]. 37
[145] T. Sjostrand, S. Mrenna, and P. Skands, *JHEP* **05** (2006) 026, [hep-ph/0603175]. 37, 172, 180
[146] R. Brun and F. Rademakers, *Nucl. Instrum. Meth.* **A389** (1997) 81–86. 38, 187
[147] G. Aad *et. al.*,, **ATLAS** Collaboration, *Phys. Rev.* **D92** (2015), no. 7 072004, [1504.05162]. 38, 173
[148] https://twiki.cern.ch/twiki/bin/view/CMSPublic/DisplacedSusyParametrisationStudyForUser. 38
[149] P. Pani and G. Polesello, 1712.03874. 43, 44, 45, 46, 47, 53
[150] M. Bauer, M. Klassen, and V. Tenorth, 1712.06597. 43
[151] M. Bauer, U. Haisch, and F. Kahlhoefer, *JHEP* **05** (2017) 138, [1701.07427]. 43, 44, 45, 118
[152] D. Pinna, A. Zucchetta, M. R. Buckley, and F. Canelli, *Phys. Rev.* **D96** (2017), no. 3 035031, [1701.05195]. 43
[153] G. Arcadi, M. Lindner, F. S. Queiroz, W. Rodejohann, and S. Vogl, 1711.02110. 43
[154] T. Plehn, J. Thompson, and S. Westhoff, 1712.08065. 43
[155] D. Goncalves, P. A. N. Machado, and J. M. No, *Phys. Rev.* **D95** (2017), no. 5 055027, [1611.04593]. 44
[156] S. Banerjee, D. Barducci, G. Bélanger, B. Fuks, A. Goudelis, and B. Zaldivar, *JHEP* **07** (2017) 080, [1705.02327]. 44
[157] S. Alioli, P. Nason, C. Oleari, and E. Re, *JHEP* **06** (2010) 043, [1002.2581]. 44, 53
[158] C. Patrignani *et. al.*,, **Particle Data Group** Collaboration, *Chin. Phys.* **C40** (2016), no. 10 100001. 45, 106, 107, 115, 119, 124, 125
[159] C. G. Lester and D. J. Summers, *Phys. Lett.* **B463** (1999) 99–103, [hep-ph/9906349]. 45, 54
[160] A. Barr, C. Lester, and P. Stephens, *J. Phys.* **G29** (2003) 2343–2363, [hep-ph/0304226]. 45, 54
[161] P. Konar, K. Kong, K. T. Matchev, and M. Park, *JHEP* **04** (2010) 086, [0911.4126]. 45,

54

[162] C. G. Lester and B. Nachman, *JHEP* **03** (2015) 100, [1411.4312]. 45, 54

[163] M. Dimou, S. F. King, and C. Luhn, *JHEP* **02** (2016) 118, [1511.07886]. 49

[164] M. Dimou, S. F. King, and C. Luhn, *Phys. Rev.* **D93** (2016), no. 7 075026, [1512.09063]. 49

[165] K. De Causmaecker, B. Fuks, B. Herrmann, F. Mahmoudi, B. O'Leary, W. Porod, S. Sekmen, and N. Strobbe, *JHEP* **11** (2015) 125, [1509.05414]. 49, 50

[166] T. Hurth and W. Porod, *JHEP* **08** (2009) 087, [0904.4574]. 50

[167] M. Bruhnke, B. Herrmann, and W. Porod, *JHEP* **09** (2010) 006, [1007.2100]. 50

[168] A. Bartl, H. Eberl, B. Herrmann, K. Hidaka, W. Majerotto, and W. Porod, *Phys. Lett.* **B698** (2011) 380–388, [1007.5483]. [Erratum: Phys. Lett.B700,390(2011)]. 50, 51

[169] A. Bartl, H. Eberl, E. Ginina, B. Herrmann, K. Hidaka, W. Majerotto, and W. Porod, *Phys. Rev.* **D84** (2011) 115026, [1107.2775]. 50

[170] A. Bartl, H. Eberl, E. Ginina, B. Herrmann, K. Hidaka, W. Majerotto, and W. Porod, *Int. J. Mod. Phys.* **A29** (2014), no. 07 1450035, [1212.4688]. 50

[171] M. Backović, A. Mariotti, and M. Spannowsky, *JHEP* **06** (2015) 122, [1504.00927]. 50

[172] A. Crivellin, U. Haisch, and L. C. Tunstall, *JHEP* **09** (2016) 080, [1604.00440]. 50

[173] G. Aad *et. al.*,, **ATLAS** Collaboration, *Phys. Rev. Lett.* **114** (2015), no. 16 161801, [1501.01325]. 50, 51

[174] M. Aaboud *et. al.*,, **ATLAS** Collaboration, 1711.11520. 50, 51, 52

[175] A. M. Sirunyan *et. al.*,, **CMS** Collaboration, *JHEP* **10** (2017) 019, [1706.04402]. 50, 51

[176] A. M. Sirunyan *et. al.*,, **CMS** Collaboration, 1710.11188. 50, 51

[177] A. M. Sirunyan *et. al.*,, **CMS** Collaboration, 1711.00752. 50, 51

[178] A. M. Sirunyan *et. al.*,, **CMS** Collaboration, 1707.07274. 50, 51

[179] M. Aaboud *et. al.*,, **ATLAS** Collaboration, *JHEP* **12** (2017) 085, [1709.04183]. 50, 51

[180] M. Aaboud *et. al.*,, **ATLAS** Collaboration, 1712.02332. 51

[181] A. M. Sirunyan *et. al.*,, **CMS** Collaboration, *Phys. Rev.* **D96** (2017), no. 3 032003, [1704.07781]. 51

[182] C. Borschensky, M. Krämer, A. Kulesza, M. Mangano, S. Padhi, T. Plehn, and X. Portell, *Eur. Phys. J.* **C74** (2014), no. 12 3174, [1407.5066]. 53

[183] L. Lonnblad and S. Prestel, *JHEP* **03** (2012) 019, [1109.4829]. 53

[184] ATLAS Collaboration,, **ATLAS** Collaboration, *JINST* **3** (2008) S08003. 53

[185] **ATLAS** Collaboration,ATLAS Collaboration, ,, 2009. 53

[186] J. de Favereau, C. Delaere, P. Demin, A. Giammanco, V. Lemaître, A. Mertens, and M. Selvaggi,, **DELPHES 3** Collaboration, *JHEP* **02** (2014) 057, [1307.6346]. 53, 141

[187] ATLAS Collaboration,, "Expected performance of the ATLAS b-tagging algorithms in Run-2." ATL-PHYS-PUB-2015-022, 2015. 53

[188] A. L. Read, *J. Phys.* **G28** (2002) 2693–2704. [,11(2002)]. 55

[189] L. Moneta, K. Belasco, K. S. Cranmer, S. Kreiss, A. Lazzaro, D. Piparo, G. Schott, W. Verkerke, and M. Wolf, *PoS* **ACAT2010** (2010) 057, [1009.1003]. 55, 77, 79

[190] ATLAS Collaboration,, "Performance and Calibration of the JetFitterCharm Algorithm for c-Jet Identification." ATL-PHYS-PUB-2015-001, 2015. 56

[191] E. Katz, A. E. Nelson, and D. G. E. Walker, *JHEP* **08** (2005) 074, [hep-ph/0504252]. 58

[192] M. Park, A. E. Nelson, and D. G. E. Walker, to appear. 58

[193] G. Cacciapaglia, G. Ferretti, T. Flacke, and H. Serodio, 1710.11142. 59

[194] V. Khachatryan *et. al.*,, **CMS** Collaboration, *Phys. Rev.* **D93** (2016), no. 11 112009, [1507.07129]. 60

[195] R. Aaij *et. al.*,, **LHCb** Collaboration, *JHEP* **06** (2014) 133, [1403.8044]. 62, 65, 68

[196] R. Aaij *et. al.*,, **LHCb** Collaboration, *JHEP* **09** (2015) 179, [1506.08777]. 62

[197] R. Aaij *et. al.*,, **LHCb** Collaboration, *JHEP* **06** (2015) 115, [1503.07138]. 62

[198] W. Detmold and S. Meinel, *Phys. Rev.* **D93** (2016), no. 7 074501, [1602.01399]. 62

[199] R. Aaij *et. al.*,, **LHCb** Collaboration, *Phys. Rev. Lett.* **113** (2014) 151601, [1406.6482]. 62

[200] R. Aaij *et. al.*,, **LHCb** Collaboration, *JHEP* **08** (2017) 055, [1705.05802]. 62, 67

[201] M. Bordone, G. Isidori, and A. Pattori, *Eur. Phys. J.* **C76** (2016), no. 8 440, [1605.07633]. 62

[202] C. Bobeth, G. Hiller, and G. Piranishvili, *JHEP* **12** (2007) 040, [0709.4174]. 62

[203] C. Bouchard, G. P. Lepage, C. Monahan, H. Na, and J. Shigemitsu,, **HPQCD** Collaboration, *Phys. Rev. Lett.* **111** (2013), no. 16 162002, [1306.0434]. [Erratum: Phys. Rev. Lett.112,no.14,149902(2014)]. 62

[204] G. Hiller and F. Kruger, *Phys. Rev.* **D69** (2004) 074020, [hep-ph/0310219]. 62

[205] R. Aaij *et. al.*,, **LHCb** Collaboration, *JHEP* **02** (2013) 105, [1209.4284]. 62

[206] R. Aaij *et. al.*,, **LHCb** Collaboration, *JHEP* **11** (2016) 047, [1606.04731]. [Erratum: JHEP04,142(2017)]. 62

[207] R. Aaij *et. al.*,, **LHCb** Collaboration, *Phys. Rev. Lett.* **111** (2013) 191801, [1308.1707]. 62

[208] R. Aaij *et. al.*,, **LHCb** Collaboration, *JHEP* **02** (2016) 104, [1512.04442]. 62

[209] **Belle** Collaboration,A. Abdesselam *et. al.*, , in *Proceedings, LHCSki 2016 - A First Discussion of 13 TeV Results: Obergurgl, Austria, April 10-15, 2016*, 2016. 1604.04042. 62

[210] S. Wehle *et. al.*,, **Belle** Collaboration, 1612.05014. 62

[211] ATLAS Collaboration, *Angular analysis of $B_d^0 \to K^* \mu^+ \mu^-$ decays in pp collisions at $\sqrt{s} = 8$ TeV with the ATLAS detector*, Tech. Rep. ATLAS-CONF-2017-023, CERN, Geneva, 2017. 62

[212] CMS Collaboration, *Measurement of the P_1 and P_5' angular parameters of the decay $B^0 \to K^{*0} \mu^+ \mu^-$ in proton-proton collisions at $\sqrt{s} = 8$*, Tech. Rep. CMS-PAS-BPH-15-008, CERN, Geneva, 2017. 62

[213] S. Descotes-Genon, T. Hurth, J. Matias, and J. Virto, *JHEP* **05** (2013) 137, [1303.5794]. 62

[214] A. Khodjamirian, T. Mannel, A. A. Pivovarov, and Y. M. Wang, *JHEP* **09** (2010) 089, [1006.4945]. 63

[215] S. Descotes-Genon, J. Matias, and J. Virto, *Phys. Rev.* **D88** (2013) 074002, [1307.5683]. 63

[216] J. Lyon and R. Zwicky, 1406.0566. 63, 68

[217] S. Jager and J. Martin Camalich, *Phys. Rev.* **D93** (2016), no. 1 014028, [1412.3183]. 63
[218] M. Ciuchini, M. Fedele, E. Franco, S. Mishima, A. Paul, L. Silvestrini, and M. Valli, *JHEP* **06** (2016) 116, [1512.07157]. 63
[219] J. P. Lees *et. al.*,, **BaBar** Collaboration, *Phys. Rev. Lett.* **109** (2012) 101802, [1205.5442]. 63
[220] R. Aaij *et. al.*,, **LHCb** Collaboration, *Phys. Rev. Lett.* **115** (2015), no. 11 111803, [1506.08614]. [Addendum: Phys. Rev. Lett.115,no.15,159901(2015)]. 63
[221] M. Huschle *et. al.*,, **Belle** Collaboration, *Phys. Rev.* **D92** (2015), no. 7 072014, [1507.03233]. 63
[222] P. Goldenzweig, talk at the "Rencontres de Moriond, EW interactions and unified theories", 12-19 Mar, 2016. 63
[223] H. Na, C. M. Bouchard, G. P. Lepage, C. Monahan, and J. Shigemitsu,, **HPQCD** Collaboration, *Phys. Rev.* **D92** (2015), no. 5 054510, [1505.03925]. [Erratum: Phys. Rev.D93,no.11,119906(2016)]. 63
[224] J. A. Bailey *et. al.*,, **MILC** Collaboration, *Phys. Rev.* **D92** (2015), no. 3 034506, [1503.07237]. 63
[225] S. Fajfer, J. F. Kamenik, and I. Nisandzic, *Phys. Rev.* **D85** (2012) 094025, [1203.2654]. 63
[226] J. F. Kamenik and F. Mescia, *Phys. Rev.* **D78** (2008) 014003, [0802.3790]. 63
[227] Y. Amhis *et. al.*, 1612.07233. 63
[228] B. Bhattacharya, A. Datta, D. London, and S. Shivashankara, *Phys. Lett.* **B742** (2015) 370–374, [1412.7164]. 63, 65
[229] G. Hiller and M. Schmaltz, *Phys. Rev.* **D90** (2014) 054014, [1408.1627]. 63, 64
[230] D. Ghosh, M. Nardecchia, and S. A. Renner, *JHEP* **12** (2014) 131, [1408.4097]. 63
[231] S. L. Glashow, D. Guadagnoli, and K. Lane, *Phys. Rev. Lett.* **114** (2015) 091801, [1411.0565]. 63, 64, 65
[232] B. Gripaios, M. Nardecchia, and S. A. Renner, *JHEP* **05** (2015) 006, [1412.1791]. 63
[233] D. Guadagnoli and G. Isidori, *Phys. Lett.* **B724** (2013) 63–67, [1302.3909]. 64
[234] R. Aaij *et. al.*,, **LHCb** Collaboration, *Eur. Phys. J.* **C73** (2013), no. 4 2373, [1208.3355]. 64, 65
[235] D. Guadagnoli, *Mod. Phys. Lett.* **A32** (2017), no. 7 1730006, [1703.02804]. 64, 68
[236] D. Guadagnoli and K. Lane, *Phys. Lett.* **B751** (2015) 54–58, [1507.01412]. 65
[237] S. M. Boucenna, J. W. F. Valle, and A. Vicente, *Phys. Lett.* **B750** (2015) 367–371, [1503.07099]. 65
[238] D. Guadagnoli, D. Melikhov, and M. Reboud, *Phys. Lett.* **B760** (2016) 442–447, [1605.05718]. 65, 68
[239] R. Alonso, B. Grinstein, and J. Martin Camalich, *Phys. Rev. Lett.* **113** (2014) 241802, [1407.7044]. 65
[240] L. Calibbi, A. Crivellin, and T. Ota, *Phys. Rev. Lett.* **115** (2015) 181801, [1506.02661]. 65, 66
[241] F. Feruglio, P. Paradisi, and A. Pattori, *Phys. Rev. Lett.* **118** (2017), no. 1 011801, [1606.00524]. 65, 67
[242] A. Greljo, G. Isidori, and D. Marzocca, *JHEP* **07** (2015) 142, [1506.01705]. 66

[243] D. A. Faroughy, A. Greljo, and J. F. Kamenik, *Phys. Lett.* **B764** (2017) 126–134, [1609.07138]. 66

[244] S. M. Boucenna, A. Celis, J. Fuentes-Martin, A. Vicente, and J. Virto, *Phys. Lett.* **B760** (2016) 214–219, [1604.03088]. 66

[245] S. Davidson, D. C. Bailey, and B. A. Campbell, *Z. Phys.* **C61** (1994) 613–644, [hep-ph/9309310]. 66

[246] M. Bauer and M. Neubert, *Phys. Rev. Lett.* **116** (2016), no. 14 141802, [1511.01900]. 66

[247] D. Becirevic, N. Kosnik, O. Sumensari, and R. Zukanovich Funchal, *JHEP* **11** (2016) 035, [1608.07583]. 66

[248] S. Fajfer and N. Kosnik, *Phys. Lett.* **B755** (2016) 270–274, [1511.06024]. 66

[249] R. Barbieri, G. Isidori, A. Pattori, and F. Senia, *Eur. Phys. J.* **C76** (2016), no. 2 67, [1512.01560]. 66, 67

[250] R. Barbieri, C. W. Murphy, and F. Senia, *Eur. Phys. J.* **C77** (2017), no. 1 8, [1611.04930]. 67

[251] D. Becirevic, S. Fajfer, N. Kosnik, and O. Sumensari, *Phys. Rev.* **D94** (2016), no. 11 115021, [1608.08501]. 67

[252] G. Hiller and M. Schmaltz, *JHEP* **02** (2015) 055, [1411.4773]. 67

[253] F. Kruger and L. M. Sehgal, *Phys. Lett.* **B380** (1996) 199–204, [hep-ph/9603237]. 68

[254] D. Guadagnoli, M. Reboud, and R. Zwicky, *JHEP* **11** (2017) 184, [1708.02649]. 68

[255] R. Aaij *et. al.*,, **LHCb** Collaboration, 1612.06764. 68

[256] J. A. Bailey *et. al.*, *Phys. Rev.* **D93** (2016), no. 2 025026, [1509.06235]. 68

[257] Y. Dincer and L. M. Sehgal, *Phys. Lett.* **B521** (2001) 7–14, [hep-ph/0108144]. 68

[258] D. Melikhov and N. Nikitin, *Phys. Rev.* **D70** (2004) 114028, [hep-ph/0410146]. 68

[259] F. Dettori, D. Guadagnoli, and M. Reboud, 1610.00629. 68

[260] G. Aad *et. al.*,, **ATLAS** Collaboration, *Phys. Lett.* **B716** (2012) 1–29, [1207.7214]. 71, 103, 112

[261] S. Chatrchyan *et. al.*,, **CMS** Collaboration, *Phys. Lett.* **B716** (2012) 30–61, [1207.7235]. 71, 112

[262] G. Aad *et. al.*,, **ATLAS, CMS** Collaboration, *JHEP* **08** (2016) 045, [1606.02266]. 71, 112

[263] D. de Florian *et. al.*,, **LHC Higgs Cross Section Working Group** Collaboration, 1610.07922. 71, 75, 96

[264] M. Aaboud *et. al.*,, **ATLAS** Collaboration, *JHEP* **12** (2017) 024, [1708.03299]. 71, 79

[265] A. M. Sirunyan *et. al.*,, **CMS** Collaboration, 1709.07497. 71, 79

[266] G. F. Giudice, C. Grojean, A. Pomarol, and R. Rattazzi, *JHEP* **06** (2007) 045, [hep-ph/0703164]. 72, 88

[267] R. Contino, M. Ghezzi, C. Grojean, M. Muhlleitner, and M. Spira, *JHEP* **07** (2013) 035, [1303.3876]. 72, 88

[268] J. Ellis, V. Sanz, and T. You, *JHEP* **03** (2015) 157, [1410.7703]. 72, 88

[269] C. Degrande, B. Fuks, K. Mawatari, K. Mimasu, and V. Sanz, *Eur. Phys. J.* **C77** (2017), no. 4 262, [1609.04833].
UFO Model available at http://feynrules.irmp.ucl.ac.be/wiki/HELatNLO. 72

[270] T. A. collaboration,, **ATLAS** Collaboration,. 72

[271] A. Alloul, B. Fuks, and V. Sanz, *JHEP* **04** (2014) 110, [1310.5150]. 72, 90

[272] E. Conte, B. Fuks, and G. Serret, *Comput.Phys.Commun.* **184** (2013) 222–256, [1206.1599]. 72, 164, 165, 166

[273] A. M. Sirunyan *et. al.*,, **CMS** Collaboration, *JINST* **12** (2017), no. 10 P10003, [1706.04965]. 72

[274] A. M. Sirunyan *et. al.*,, **CMS** Collaboration, 1712.07158. 73, 141

[275] R. Contino, M. Ghezzi, C. Grojean, M. Mühlleitner, and M. Spira, *Comput.Phys.Commun.* **185** (2014) 3412–3423, [1403.3381]. 73

[276] A. Falkowski, B. Fuks, K. Mawatari, K. Mimasu, F. Riva, and V. Sanz, *Eur. Phys. J.* **C75** (2015), no. 12 583, [1508.05895]. 73, 88

[277] F. Pedregosa, G. Varoquaux, A. Gramfort, V. Michel, B. Thirion, O. Grisel, M. Blondel, P. Prettenhofer, R. Weiss, V. Dubourg, J. Vanderplas, A. Passos, D. Cournapeau, M. Brucher, M. Perrot, and E. Duchesnay, *Journal of Machine Learning Research* **12** (2011) 2825–2830. 74

[278] T. Chen and C. Guestrin, *CoRR* **abs/1603.02754** (2016) [1603.02754]. 74

[279] D. Liu, A. Pomarol, R. Rattazzi, and F. Riva, *JHEP* **11** (2016) 141, [1603.03064]. 82

[280] B. Bellazzini, F. Riva, J. Serra, and F. Sgarlata, *JHEP* **11** (2017) 020, [1706.03070]. 82

[281] **CLIC Physics Working Group** Collaboration,E. Accomando *et. al.*, , in *Proceedings, 11th International Conference on Hadron spectroscopy (Hadron 2005): Rio de Janeiro, Brazil, August 21-26, 2005*, 2004. hep-ph/0412251. 82, 85

[282] J. Ellis, P. Roloff, V. Sanz, and T. You, *JHEP* **05** (2017) 096, [1701.04804]. 82

[283] R. Rahaman and R. K. Singh, 1711.04551. 82

[284] A. Gutierrez-Rodriguez, M. A. Hernandez-Ruiz, O. A. Sampayo, A. Chubykalo, and A. Espinoza-Garrido, *J. Phys. Soc. Jap.* **77** (2008) 094101, [0807.0663]. 82

[285] A. Falkowski and F. Riva, *JHEP* **02** (2015) 039, [1411.0669]. 82, 88

[286] A. Azatov, R. Contino, C. S. Machado, and F. Riva, *Phys. Rev.* **D95** (2017), no. 6 065014, [1607.05236]. 82, 83

[287] G. Panico, F. Riva, and A. Wulzer, *Phys. Lett.* **B776** (2018) 473–480, [1708.07823]. 82, 83

[288] A. Helset and M. Trott, 1711.07954. 82

[289] K. Hagiwara, R. D. Peccei, D. Zeppenfeld, and K. Hikasa, *Nucl. Phys.* **B282** (1987) 253–307. 83

[290] M. Jacob and G. C. Wick, *Annals Phys.* **7** (1959) 404–428. [Annals Phys.281,774(2000)]. 83

[291] W. Kilian, T. Ohl, and J. Reuter, *Eur. Phys. J.* **C71** (2011) 1742, [0708.4233]. 87

[292] R. Franceschini, G. Panico, A. Pomarol, F. Riva, and A. Wulzer, *JHEP* **02** (2018) 111, [1712.01310]. 87

[293] N. Craig, J. Gu, Z. Liu, and K. Wang, *JHEP* **03** (2016) 050, [1512.06877]. 87

[294] J. Cohen, S. Bar-Shalom, and G. Eilam, *Phys. Rev.* **D94** (2016), no. 3 035030, [1602.01698]. 87

[295] M. Beneke, D. Boito, and Y.-M. Wang, *JHEP* **11** (2014) 028, [1406.1361]. 87

[296] G. Durieux, C. Grojean, J. Gu, and K. Wang, *JHEP* **09** (2017) 014, [1704.02333]. 87

[297] B. Grzadkowski, M. Iskrzynski, M. Misiak, and J. Rosiek, *JHEP* **10** (2010) 085, [1008.4884]. 88

[298] W. Buchmuller and D. Wyler, *Nucl. Phys.* **B268** (1986) 621–653. 88

[299] R. S. Gupta, A. Pomarol, and F. Riva, *Phys. Rev.* **D91** (2015), no. 3 035001, [1405.0181]. 88

[300] A. Efrati, A. Falkowski, and Y. Soreq, *JHEP* **07** (2015) 018, [1503.07872]. 88

[301] N. D. Christensen and C. Duhr, *Comput. Phys. Commun.* **180** (2009) 1614–1641, [0806.4194]. 90, 106

[302] R. Kleiss, W. J. Stirling, and S. D. Ellis, *Comput. Phys. Commun.* **40** (1986) 359. 90

[303] A. Denner, S. Dittmaier, M. Roth, and D. Wackeroth, *Nucl. Phys.* **B560** (1999) 33–65, [hep-ph/9904472]. 91, 92

[304] P. de Aquino, W. Link, F. Maltoni, O. Mattelaer, and T. Stelzer, *Comput. Phys. Commun.* **183** (2012) 2254–2263, [1108.2041]. 91

[305] N. D. Christensen, P. de Aquino, N. Deutschmann, C. Duhr, B. Fuks, C. Garcia-Cely, O. Mattelaer, K. Mawatari, B. Oexl, and Y. Takaesu, *Eur. Phys. J.* **C73** (2013), no. 10 2580, [1308.1668]. 91

[306] J. Alwall, C. Duhr, B. Fuks, O. Mattelaer, D. G. Öztürk, and C.-H. Shen, *Comput. Phys. Commun.* **197** (2015) 312–323, [1402.1178]. 91

[307] U. Baur, J. A. M. Vermaseren, and D. Zeppenfeld, *Nucl. Phys.* **B375** (1992) 3–44. 92

[308] U. Baur and D. Zeppenfeld, *Phys. Rev. Lett.* **75** (1995) 1002–1005, [hep-ph/9503344]. 92

[309] R. Gröber, M. Mühlleitner, E. Popenda, and A. Wlotzka, *Phys. Lett.* **B747** (2015) 144–151, [1502.05935]. 92

[310] I. Brivio and M. Trott, 1706.08945. 93

[311] A. David, A. Denner, M. Duehrssen, M. Grazzini, C. Grojean, G. Passarino, M. Schumacher, M. Spira, G. Weiglein, and M. Zanetti,, **LHC Higgs Cross Section Working Group** Collaboration, 1209.0040. 95

[312] J. R. Andersen *et. al.*,, **LHC Higgs Cross Section Working Group** Collaboration, 1307.1347. 95, 96, 97, 145

[313] F. Boudjema *et. al.*, 1307.5865. 95

[314] G. Aad *et. al.*,, **ATLAS** Collaboration, *JHEP* **09** (2014) 112, [1407.4222]. 96, 97, 99, 100, 159

[315] V. Khachatryan *et. al.*,, **CMS** Collaboration, *Eur. Phys. J.* **C76** (2016), no. 1 13, [1508.07819]. 96

[316] **CMS** Collaboration, Tech. Rep. CMS-PAS-HIG-17-015, CERN, Geneva, 2017. 96

[317] M. Aaboud *et. al.*,, **ATLAS** Collaboration, 1802.04146. 96, 101

[318] G. Aad *et. al.*,, **ATLAS** Collaboration, *Phys. Lett.* **B738** (2014) 234–253, [1408.3226]. 96, 97, 99, 100

[319] V. Khachatryan *et. al.*,, **CMS** Collaboration, *JHEP* **04** (2016) 005, [1512.08377]. 96

[320] M. Aaboud *et. al.*,, **ATLAS** Collaboration, *JHEP* **10** (2017) 132, [1708.02810]. 96, 101

[321] G. Aad *et. al.*,, **ATLAS** Collaboration, *JHEP* **08** (2016) 104, [1604.02997]. 96

[322] J. R. Andersen *et. al.*, in *9th Les Houches Workshop on Physics at TeV Colliders (PhysTeV 2015) Les Houches, France, June 1-19, 2015*, 2016. 1605.04692. 96

[323] https://hepdata.net/record/ins13066151. 96

[324] https://www.hepdata.net/record/ins13108351. 96

[325] A. Buckley, J. Butterworth, L. Lonnblad, D. Grellscheid, H. Hoeth, J. Monk, H. Schulz, and F. Siegert, *Comput. Phys. Commun.* **184** (2013) 2803–2819, [1003.0694]. 96, 106, 158, 164, 165, 166, 187

[326] M. Queitsch-Maitland,. https://rivet.hepforge.org/analyses/ATLAS_2014_I1306615.html. 96, 98

[327] https://www.hepforge.org/archive/rivet/contrib/ATLAS_2014_I1310835.tar.gz. 96, 98

[328] G. Aad *et. al.*,, **ATLAS** Collaboration, *Phys. Rev. Lett.* **115** (2015), no. 9 091801, [1504.05833]. 96, 101

[329] M. Grazzini and H. Sargsyan, *JHEP* **09** (2013) 129, [1306.4581]. 96

[330] I. W. Stewart, F. J. Tackmann, J. R. Walsh, and S. Zuberi, *Phys. Rev.* **D89** (2014), no. 5 054001, [1307.1808]. 96

[331] G. Aad *et. al.*,, **ATLAS** Collaboration, *Eur. Phys. J.* **C75** (2015), no. 5 208, [1501.07110]. 98

[332] V. Khachatryan *et. al.*,, **CMS** Collaboration, *Phys. Rev.* **D90** (2014), no. 9 092007, [1409.3168]. 98

[333] V. Khachatryan *et. al.*,, **CMS** Collaboration, *Eur. Phys. J.* **C74** (2014), no. 9 3036, [1405.7570]. 98

[334] https://twiki.cern.ch/twiki/bin/view/LHCPhysics/SUSYCrossSections. 98, 99

[335] A. M. Sirunyan *et. al.*,, **CMS** Collaboration, 1709.00384. 98, 99

[336] J. Duarte, C. Peña, A. Wang, M. Pierini, and M. Spiropulu, 1703.06544. 99

[337] **CMS** Collaboration, Tech. Rep. CMS-PAS-SUS-14-017, CERN, Geneva, 2015. 99

[338] K. Lane and L. Pritchett, 1701.07376. 102, 103, 106, 108

[339] A. Heister, 1610.06536. 102, 103, 104

[340] S. Chatrchyan *et. al.*,, **CMS** Collaboration, *Phys.Lett.* **B716** (2012) 30–61, [1207.7235]. 103

[341] G. C. Branco, P. M. Ferreira, L. Lavoura, M. N. Rebelo, M. Sher, and J. P. Silva, *Phys. Rept.* **516** (2012) 1–102, [1106.0034]. 103, 113

[342] M. Carena, I. Low, N. R. Shah, and C. E. M. Wagner, *JHEP* **04** (2014) 015, [1310.2248]. 104, 105

[343] G. Abbiendi *et. al.*,, **OPAL** Collaboration, *Eur. Phys. J.* **C32** (2004) 453–473, [hep-ex/0309014]. 105

[344] V. Khachatryan *et. al.*,, **CMS** Collaboration, *JHEP* **11** (2015) 018, [1508.07774]. 105

[345] M. Bahr *et. al.*, *Eur. Phys. J.* **C58** (2008) 639–707, [0803.0883]. 106, 158

[346] J. Bellm *et. al.*, *Eur. Phys. J.* **C76** (2016), no. 4 196, [1512.01178]. 106, 158

[347] J. M. Butterworth, D. Grellscheid, M. Kraemer, B. Sarrazin, and D. Yallup, *JHEP* **03** (2017) 078, [1606.05296]. 106, 107, 158

[348] J. Bellm *et. al.*, 1705.06919. 106

[349] E. Maguire, L. Heinrich, and G. Watt, *J. Phys. Conf. Ser.* **898** (2017), no. 10 102006, [1704.05473]. 106, 165

[350] G. Aad *et. al.*,, **ATLAS** Collaboration, *JHEP* **09** (2016) 029, [1603.01702]. 107

[351] V. Khachatryan *et. al.*,, **CMS** Collaboration, *JHEP* **03** (2017) 032, [1606.01522]. 107

[352] G. Aad *et. al.*,, **ATLAS** Collaboration, *JHEP* **06** (2014) 112, [1404.1212]. 107

[353] G. Aad *et. al.*,, **ATLAS** Collaboration, *JHEP* **03** (2013) 128, [1211.6096]. 107

[354] G. Aad *et. al.*,, **ATLAS** Collaboration, *Phys. Rev.* **D87** (2013), no. 11 112001, [1210.2979]. [Erratum: Phys. Rev.D88,no.7,079906(2013)]. 107

[355] G. Aad *et. al.*,, **ATLAS** Collaboration, *Phys. Lett.* **B753** (2016) 552–572, [1509.07844]. 107, 108

[356] **CMS Collaboration** Collaboration, Tech. Rep. CMS-PAS-HIG-16-007, CERN, Geneva, 2016. 112

[357] B. A. Dobrescu and K. T. Matchev, *JHEP* **09** (2000) 031, [hep-ph/0008192]. 112

[358] D. Curtin *et. al.*, *Phys. Rev.* **D90** (2014), no. 7 075004, [1312.4992]. 112

[359] B. A. Dobrescu, G. L. Landsberg, and K. T. Matchev, *Phys. Rev.* **D63** (2001) 075003, [hep-ph/0005308]. 112

[360] R. Dermisek and J. F. Gunion, *Phys. Rev. Lett.* **95** (2005) 041801, [hep-ph/0502105]. 112

[361] N. D. Christensen, T. Han, Z. Liu, and S. Su, *JHEP* **08** (2013) 019, [1303.2113]. 112

[362] M. Drees and K.-I. Hikasa, *Phys. Rev.* **D41** (1990) 1547. 112, 121, 123, 124, 125

[363] F. Domingo, U. Ellwanger, E. Fullana, C. Hugonie, and M.-A. Sanchis-Lozano, *JHEP* **01** (2009) 061, [0810.4736]. 112, 123

[364] F. Domingo, *JHEP* **04** (2011) 016, [1010.4701]. 112, 123

[365] F. Domingo and U. Ellwanger, *JHEP* **06** (2011) 067, [1105.1722]. 112, 123

[366] M. Baumgart and A. Katz, *JHEP* **08** (2012) 133, [1204.6032]. 112, 123, 124, 125

[367] U. Haisch and J. F. Kamenik, *Phys. Rev.* **D93** (2016), no. 5 055047, [1601.05110]. 112, 113, 117, 118, 119, 120, 123, 125

[368] F. Domingo, *JHEP* **03** (2017) 052, [1612.06538]. 112, 123

[369] V. Khachatryan *et. al.*,, **CMS** Collaboration, *Phys. Lett.* **B752** (2016) 146–168, [1506.00424]. 112, 113, 114, 116, 119, 120

[370] **CMS Collaboration** Collaboration, Tech. Rep. CMS-PAS-HIG-16-035, CERN, Geneva, 2016. 112, 119, 120

[371] V. Khachatryan *et. al.*,, **CMS** Collaboration, *JHEP* **01** (2016) 079, [1510.06534]. 112, 113, 114, 116, 119, 120

[372] V. Khachatryan *et. al.*,, **CMS** Collaboration, *JHEP* **10** (2017) 076, [1701.02032]. 112, 113, 114, 115, 116, 119, 120, 140

[373] G. Aad *et. al.*,, **ATLAS** Collaboration, *Phys. Rev.* **D92** (2015), no. 9 092001, [1505.07645]. 113, 115, 117, 119, 120

[374] M. Aaboud *et. al.*,, **ATLAS** Collaboration, 1802.03388. 113, 115, 116, 117, 119, 120

[375] **ATLAS Collaboration** Collaboration, Tech. Rep. ATLAS-CONF-2011-020, CERN, Geneva, Mar, 2011. 113, 116, 117, 119

[376] S. Chatrchyan *et. al.*,, **CMS** Collaboration, *Phys. Rev. Lett.* **109** (2012) 121801, [1206.6326]. 113, 116, 117, 118, 119, 120

[377] V. Khachatryan *et. al.*,, **CMS** Collaboration, *Phys. Lett.* **B758** (2016) 296–320, [1511.03610]. 113, 116, 117, 118, 119, 120

[378] A. M. Sirunyan *et. al.*,, **CMS** Collaboration, *JHEP* **11** (2017) 010, [1707.07283]. 113, 116, 117, 119

[379] **CMS Collaboration** Collaboration, Tech. Rep. CMS-PAS-HIG-17-013, CERN, Geneva, 2017. 113, 116, 117, 118, 119, 120, 128

[380] A. Mariotti, D. Redigolo, F. Sala, and K. Tobioka, 1710.01743. 113, 119, 120

[381] **CMS Collaboration** Collaboration, Tech. Rep. CMS-PAS-HIG-16-037, CERN, Geneva, 2016. 113, 116, 117, 118, 119, 120

[382] J. P. Lees *et. al.*,, **BaBar** Collaboration, *Phys. Rev. Lett.* **107** (2011) 221803, [1108.3549]. 113, 116, 117, 119

[383] J. P. Lees *et. al.*,, **BaBar** Collaboration, *Phys. Rev.* **D87** (2013), no. 3 031102, [1210.0287]. [Erratum: Phys. Rev. **D87**, 059903 (2013)]. 113, 116, 117, 118, 119, 120

[384] J. P. Lees *et. al.*,, **BaBar** Collaboration, *Phys. Rev.* **D88** (2013), no. 7 071102, [1210.5669]. 113, 116, 117, 119

[385] R. Aaij *et. al.*,, **LHCb** Collaboration, *JHEP* **11** (2015) 103, [1509.02372]. 113, 117, 118, 119, 120

[386] P. Ilten, Y. Soreq, J. Thaler, M. Williams, and W. Xue, *Phys. Rev. Lett.* **116** (2016), no. 25 251803, [1603.08926]. 113, 117, 119, 120

[387] R. Aaij *et. al.*,, **LHCb** Collaboration, 1710.02867. 113, 117, 118, 119, 120

[388] J. F. Gunion, H. E. Haber, G. L. Kane, and S. Dawson, *Front. Phys.* **80** (2000) 1–404. 113

[389] S. L. Glashow and S. Weinberg, *Phys. Rev.* **D15** (1977) 1958. 113

[390] E. A. Paschos, *Phys. Rev.* **D15** (1977) 1966. 113

[391] M. Spira, hep-ph/9510347. 118

[392] J. M. Cline, G. Dupuis, Z. Liu, and W. Xue, *JHEP* **08** (2014) 131, [1405.7691]. 119

[393] M. J. Dolan, F. Kahlhoefer, C. McCabe, and K. Schmidt-Hoberg, *JHEP* **03** (2015) 171, [1412.5174]. [Erratum: JHEP **07**, 103 (2015)]. 120, 125

[394] M. Spira, *Fortsch. Phys.* **46** (1998) 203–284, [hep-ph/9705337]. 121, 122, 134

[395] A. Djouadi, *Phys. Rept.* **457** (2008) 1–216, [hep-ph/0503172]. 121, 134

[396] A. Djouadi, *Phys. Rept.* **459** (2008) 1–241, [hep-ph/0503173]. 121, 134

[397] M. Spira, *Prog. Part. Nucl. Phys.* **95** (2017) 98–159, [1612.07651]. 121

[398] E. Braaten and J. P. Leveille, *Phys. Rev.* **D22** (1980) 715. 121

[399] N. Sakai, *Phys. Rev.* **D22** (1980) 2220. 121

[400] T. Inami and T. Kubota, *Nucl. Phys.* **B179** (1981) 171–188. 121

[401] S. G. Gorishnii, A. L. Kataev, and S. A. Larin, *Sov. J. Nucl. Phys.* **40** (1984) 329–334. [Yad. Fiz. **40**, 517 (1984)]. 121

[402] M. Drees and K.-I. Hikasa, *Phys. Lett.* **B240** (1990) 455. [Erratum: Phys. Lett. **B262**, 497 (1991)]. 121

[403] S. G. Gorishnii, A. L. Kataev, S. A. Larin, and L. R. Surguladze, *Mod. Phys. Lett.* **A5** (1990) 2703–2712. 121

[404] S. G. Gorishnii, A. L. Kataev, S. A. Larin, and L. R. Surguladze, *Phys. Rev.* **D43** (1991) 1633–1640. 121

[405] A. L. Kataev and V. T. Kim, *Mod. Phys. Lett.* **A9** (1994) 1309–1326. 121

[406] L. R. Surguladze, *Phys. Lett.* **B341** (1994) 60–72, [hep-ph/9405325]. 121

[407] K. Melnikov, *Phys. Rev.* **D53** (1996) 5020–5027, [hep-ph/9511310]. 121

[408] K. G. Chetyrkin, *Phys. Lett.* **B390** (1997) 309–317, [hep-ph/9608318]. 121

[409] K. G. Chetyrkin and A. Kwiatkowski, *Nucl. Phys.* **B461** (1996) 3–18, [hep-ph/9505358]. 121

[410] S. A. Larin, T. van Ritbergen, and J. A. M. Vermaseren, *Phys. Lett.* **B362** (1995) 134–140, [hep-ph/9506465]. 121

[411] A. Djouadi, J. Kalinowski, and M. Spira, *Comput. Phys. Commun.* **108** (1998) 56–74, [hep-ph/9704448]. 122

[412] A. Djouadi, J. Kalinowski, M. Muehlleitner, and M. Spira, 1801.09506. 122

[413] M. Spira, A. Djouadi, D. Graudenz, and P. M. Zerwas, *Nucl. Phys.* **B453** (1995) 17–82, [hep-ph/9504378]. 122, 123, 133

[414] R. Harlander and P. Kant, *JHEP* **12** (2005) 015, [hep-ph/0509189]. 122, 123, 133

[415] D. Maitre, *Comput. Phys. Commun.* **183** (2012) 846, [hep-ph/0703052]. 123

[416] U. Aglietti, R. Bonciani, G. Degrassi, and A. Vicini, *JHEP* **01** (2007) 021, [hep-ph/0611266]. 123, 133, 136

[417] E. Braaten, S. Fleming, and A. K. Leibovich, *Phys. Rev.* **D63** (2001) 094006, [hep-ph/0008091]. 124

[418] E. J. Eichten and C. Quigg, *Phys. Rev.* **D52** (1995) 1726–1728, [hep-ph/9503356]. 124

[419] D. McKeen, *Phys. Rev.* **D79** (2009) 015007, [0809.4787]. 125

[420] A. Rosca (for LEP Collaboration), *Nucl. Phys. Proc. Suppl.117,743(2003)* (2002) 743–745, [hep-ex/0212038]. 127, 129

[421] **CMS** Collaboration, , CMS-PAS-HIG-14-037. 127, 128, 129

[422] T. Gherghetta and A. Pomarol, *Nucl. Phys.* **B586** (2000) 141–162, [hep-ph/0003129]. 127

[423] L. Randall and R. Sundrum, *Phys. Rev. Lett.* **83** (1999) 3370–3373, [hep-ph/9905221]. 127

[424] S. Fichet and G. von Gersdorff, *JHEP* **03** (2014) 102, [1311.6815]. 128, 158

[425] S. Fichet, G. von Gersdorff, O. Kepka, B. Lenzi, C. Royon, and M. Saimpert, *Phys. Rev.* **D89** (2014) 114004, [1312.5153]. 128, 158

[426] C. Baldenegro, S. Fichet, G. von Gersdorff, and C. Royon, *JHEP* **06** (2017) 142, [1703.10600]. 128, 158

[427] A. Belyaev, G. Cacciapaglia, H. Cai, G. Ferretti, T. Flacke, A. Parolini, and H. Serodio, *JHEP* **01** (2017) 094, [1610.06591]. 128, 158

[428] S. Fichet, G. von Gersdorff, E. Ponton, and R. Rosenfeld, *JHEP* **09** (2016) 158, [1607.03125]. 128, 158

[429] G. Aad *et. al.*,, **ATLAS** Collaboration, *Phys. Rev. Lett.* **113** (Oct, 2014) 171801. 128

[430] G. Cacciapaglia, A. Deandrea, S. Gascon-Shotkin, S. Le Corre, M. Lethuillier, and J. Tao, *JHEP* **12** (2016) 068, [1607.08653]. 129, 157

[431] A. Angelescu, G. Moreau, and F. Richard, *Phys. Rev.* **D96** (2017), no. 1 015019, [1702.03984]. 130, 157

[432] A. Djouadi, M. Spira, and P. M. Zerwas, *Phys. Lett.* **B264** (1991) 440–446. 133

[433] S. Dawson, *Nucl. Phys.* **B359** (1991) 283–300. 133

[434] D. Graudenz, M. Spira, and P. M. Zerwas, *Phys. Rev. Lett.* **70** (1993) 1372–1375. 133

[435] C. Anastasiou, S. Bucherer, and Z. Kunszt, *JHEP* **10** (2009) 068, [0907.2362]. 133

[436] S. Catani, D. de Florian, and M. Grazzini, *JHEP* **05** (2001) 025, [hep-ph/0102227].

133

[437] R. V. Harlander and W. B. Kilgore, *Phys. Rev.* **D64** (2001) 013015, [hep-ph/0102241]. 133

[438] R. V. Harlander and W. B. Kilgore, *Phys. Rev. Lett.* **88** (2002) 201801, [hep-ph/0201206]. 133

[439] C. Anastasiou and K. Melnikov, *Nucl. Phys.* **B646** (2002) 220–256, [hep-ph/0207004]. 133

[440] V. Ravindran, J. Smith, and W. L. van Neerven, *Nucl. Phys.* **B665** (2003) 325–366, [hep-ph/0302135]. 133

[441] T. Gehrmann, M. Jaquier, E. W. N. Glover, and A. Koukoutsakis, *JHEP* **02** (2012) 056, [1112.3554]. 133

[442] C. Anastasiou, C. Duhr, F. Dulat, and B. Mistlberger, *JHEP* **07** (2013) 003, [1302.4379]. 133

[443] C. Anastasiou, C. Duhr, F. Dulat, F. Herzog, and B. Mistlberger, *JHEP* **12** (2013) 088, [1311.1425]. 133

[444] W. B. Kilgore, *Phys. Rev.* **D89** (2014), no. 7 073008, [1312.1296]. 133

[445] Y. Li, A. von Manteuffel, R. M. Schabinger, and H. X. Zhu, *Phys. Rev.* **D90** (2014), no. 5 053006, [1404.5839]. 133

[446] C. Anastasiou, C. Duhr, F. Dulat, E. Furlan, T. Gehrmann, F. Herzog, and B. Mistlberger, *JHEP* **03** (2015) 091, [1411.3584]. 133

[447] C. Anastasiou, C. Duhr, F. Dulat, F. Herzog, and B. Mistlberger, *Phys. Rev. Lett.* **114** (2015) 212001, [1503.06056]. 133

[448] C. Anastasiou, C. Duhr, F. Dulat, E. Furlan, F. Herzog, and B. Mistlberger, *JHEP* **08** (2015) 051, [1505.04110]. 133

[449] C. Anastasiou, C. Duhr, F. Dulat, E. Furlan, T. Gehrmann, F. Herzog, A. Lazopoulos, and B. Mistlberger, 1602.00695. 133

[450] B. Mistlberger, 1802.00833. 133

[451] A. Djouadi and P. Gambino, *Phys. Rev. Lett.* **73** (1994) 2528–2531, [hep-ph/9406432]. 133

[452] K. G. Chetyrkin, B. A. Kniehl, and M. Steinhauser, *Phys. Rev. Lett.* **78** (1997) 594–597, [hep-ph/9610456]. 133

[453] K. G. Chetyrkin, B. A. Kniehl, and M. Steinhauser, *Nucl. Phys.* **B490** (1997) 19–39, [hep-ph/9701277]. 133

[454] U. Aglietti, R. Bonciani, G. Degrassi, and A. Vicini, *Phys. Lett.* **B595** (2004) 432–441, [hep-ph/0404071]. 133

[455] G. Degrassi and F. Maltoni, *Phys. Lett.* **B600** (2004) 255–260, [hep-ph/0407249]. 133

[456] U. Aglietti, R. Bonciani, G. Degrassi, and A. Vicini, in *TeV4LHC Workshop: 2nd Meeting Brookhaven, Upton, New York, February 3-5, 2005*, 2006. hep-ph/0610033. 133

[457] S. Actis, G. Passarino, C. Sturm, and S. Uccirati, *Phys. Lett.* **B670** (2008) 12–17, [0809.1301]. 133

[458] S. Actis, G. Passarino, C. Sturm, and S. Uccirati, *Nucl. Phys.* **B811** (2009) 182–273, [0809.3667]. 133

[459] C. Anastasiou, R. Boughezal, and F. Petriello, *JHEP* **04** (2009) 003, [0811.3458]. 133

[460] M. Kramer, E. Laenen, and M. Spira, *Nucl. Phys.* **B511** (1998) 523–549, [hep-ph/9611272]. 133

[461] S. Catani, D. de Florian, M. Grazzini, and P. Nason, *JHEP* **07** (2003) 028, [hep-ph/0306211]. 133

[462] S. Moch and A. Vogt, *Phys. Lett.* **B631** (2005) 48–57, [hep-ph/0508265]. 133

[463] V. Ravindran, *Nucl. Phys.* **B746** (2006) 58–76, [hep-ph/0512249]. 133

[464] V. Ravindran, *Nucl. Phys.* **B752** (2006) 173–196, [hep-ph/0603041]. 133

[465] A. Idilbi, X.-d. Ji, J.-P. Ma, and F. Yuan, *Phys. Rev.* **D73** (2006) 077501, [hep-ph/0509294]. 133

[466] V. Ahrens, T. Becher, M. Neubert, and L. L. Yang, *Eur. Phys. J.* **C62** (2009) 333–353, [0809.4283]. 133

[467] D. de Florian and M. Grazzini, *Phys. Lett.* **B674** (2009) 291–294, [0901.2427]. 133

[468] D. de Florian and M. Grazzini, *Phys. Lett.* **B718** (2012) 117–120, [1206.4133]. 133

[469] D. de Florian, J. Mazzitelli, S. Moch, and A. Vogt, *JHEP* **10** (2014) 176, [1408.6277]. 133

[470] M. Bonvini and S. Marzani, *JHEP* **09** (2014) 007, [1405.3654]. 133

[471] M. Bonvini and L. Rottoli, *Phys. Rev.* **D91** (2015), no. 5 051301, [1412.3791]. 133

[472] S. Catani, L. Cieri, D. de Florian, G. Ferrera, and M. Grazzini, *Nucl. Phys.* **B888** (2014) 75–91, [1405.4827]. 133

[473] T. Schmidt and M. Spira, *Phys. Rev.* **D93** (2016), no. 1 014022, [1509.00195]. 133

[474] M. Muhlleitner and M. Spira, *Nucl. Phys.* **B790** (2008) 1–27, [hep-ph/0612254]. 133, 136

[475] C. Anastasiou, S. Beerli, S. Bucherer, A. Daleo, and Z. Kunszt, *JHEP* **01** (2007) 082, [hep-ph/0611236]. 133, 136

[476] R. Bonciani, G. Degrassi, and A. Vicini, *JHEP* **11** (2007) 095, [0709.4227]. 133, 136

[477] R. V. Harlander and M. Steinhauser, *Phys. Lett.* **B574** (2003) 258–268, [hep-ph/0307346]. 133

[478] R. Harlander and M. Steinhauser, *Phys. Rev.* **D68** (2003) 111701, [hep-ph/0308210]. 133

[479] R. V. Harlander and M. Steinhauser, *JHEP* **09** (2004) 066, [hep-ph/0409010]. 133

[480] R. V. Harlander and F. Hofmann, *JHEP* **03** (2006) 050, [hep-ph/0507041]. 133

[481] G. Degrassi and P. Slavich, *Nucl. Phys.* **B805** (2008) 267–286, [0806.1495]. 133

[482] C. Anastasiou, S. Beerli, and A. Daleo, *Phys. Rev. Lett.* **100** (2008) 241806, [0803.3065]. 133

[483] M. Muhlleitner, H. Rzehak, and M. Spira, *PoS* **RADCOR2009** (2010) 043, [1001.3214]. [,42(2010)]. 133

[484] M. Muhlleitner, H. Rzehak, and M. Spira, in *Physics at the LHC2010. Proceedings, 5th Conference, PLHC2010, Hamburg, Germany, June 7-12, 2010*, pp. 415–417, 2010. 133

[485] L. J. Hall, R. Rattazzi, and U. Sarid, *Phys. Rev.* **D50** (1994) 7048–7065, [hep-ph/9306309]. 134

[486] R. Hempfling, *Phys. Rev.* **D49** (1994) 6168–6172. 134

[487] M. Carena, M. Olechowski, S. Pokorski, and C. E. M. Wagner, *Nucl. Phys.* **B426** (1994) 269–300, [hep-ph/9402253]. 134

[488] D. M. Pierce, J. A. Bagger, K. T. Matchev, and R.-j. Zhang, *Nucl. Phys.* **B491** (1997) 3–67, [hep-ph/9606211]. 134

[489] J. Guasch, W. Hollik, and S. Penaranda, *Phys. Lett.* **B515** (2001) 367–374, [hep-ph/0106027]. 134

[490] G. D'Ambrosio, G. F. Giudice, G. Isidori, and A. Strumia, *Nucl. Phys.* **B645** (2002) 155–187, [hep-ph/0207036]. 134

[491] A. J. Buras, P. H. Chankowski, J. Rosiek, and L. Slawianowska, *Nucl. Phys.* **B659** (2003) 3, [hep-ph/0210145]. 134

[492] V. Barger, H. E. Logan, and G. Shaughnessy, *Phys. Rev.* **D79** (2009) 115018, [0902.0170]. 134

[493] N. D. Christensen, T. Han, and S. Su, *Phys. Rev.* **D85** (2012) 115018, [1203.3207]. 134

[494] M. S. Carena, D. Garcia, U. Nierste, and C. E. M. Wagner, *Nucl. Phys.* **B577** (2000) 88–120, [hep-ph/9912516]. 134

[495] J. Guasch, P. Hafliger, and M. Spira, *Phys. Rev.* **D68** (2003) 115001, [hep-ph/0305101]. 134

[496] D. Noth and M. Spira, *Phys. Rev. Lett.* **101** (2008) 181801, [0808.0087]. 134

[497] D. Noth and M. Spira, *JHEP* **06** (2011) 084, [1001.1935]. 134

[498] M. Ghezzi, S. Glaus, D. Müller, T. Schmidt, and M. Spira, 1711.02555. 134

[499] L. Mihaila and C. Reisser, *JHEP* **08** (2010) 021, [1007.0693]. 134

[500] A. Crivellin and C. Greub, *Phys. Rev.* **D87** (2013) 015013, [1210.7453]. [Erratum: Phys. Rev.D87,079901(2013)]. 134

[501] L. Mihaila and N. Zerf, *JHEP* **05** (2017) 019, [1612.06619]. 134

[502] H. M. Georgi, S. L. Glashow, M. E. Machacek, and D. V. Nanopoulos, *Phys. Rev. Lett.* **40** (1978) 692. 134

[503] E. Accomando, G. Chachamis, F. Fugel, M. Spira, and M. Walser, *Phys. Rev.* **D85** (2012) 015004, [1103.4283]. 136

[504] M. Carena, S. Heinemeyer, O. Stål, C. E. M. Wagner, and G. Weiglein, *Eur. Phys. J.* **C73** (2013), no. 9 2552, [1302.7033]. 137

[505] V. Khachatryan *et. al.*,, **CMS** Collaboration, *Phys. Lett.* **B749** (2015) 560–582, [1503.04114]. 139

[506] G. Aad *et. al.*,, **ATLAS** Collaboration, *Eur. Phys. J.* **C75** (2015), no. 9 412, [1506.00285]. 139, 154

[507] M. Aaboud *et. al.*,, **ATLAS** Collaboration, *Phys. Rev.* **D94** (2016), no. 5 052002, [1606.04782]. 139

[508] **CMS** Collaboration, , *CMS-PAS-HIG-17-009* (2017). 139, 140, 141, 142, 144

[509] **CMS** Collaboration, , *CMS-PAS-HIG-16-002* (2016). 139, 140, 141

[510] **CMS** Collaboration, , *CMS-PAS-HIG-16-011* (2016). 139

[511] G. Aad *et. al.*,, **ATLAS** Collaboration, *Phys. Rev.* **D92** (2015) 092004, [1509.04670]. 139, 154

[512] **CMS** Collaboration, , *CMS-PAS-HIG-16-029* (2016). 139

[513] A. M. Sirunyan *et. al.*,, **CMS** Collaboration, *Phys. Lett.* **B778** (2018) 101–127, [1707.02909]. 139, 154

[514] G. Aad *et. al.*,, **ATLAS** Collaboration, *Phys. Rev. Lett.* **114** (2015), no. 8 081802,

[1406.5053]. 139
[515] V. Khachatryan *et. al.*,, **CMS** Collaboration, *Phys. Rev.* **D94** (2016), no. 5 052012, [1603.06896]. 139
[516] **CMS** Collaboration, , *CMS-PAS-HIG-16-032* (2016). 139
[517] B. Coleppa, F. Kling, and S. Su, *JHEP* **09** (2014) 161, [1404.1922]. 139
[518] G. C. Dorsch, S. J. Huber, K. Mimasu, and J. M. No, *Phys. Rev. Lett.* **113** (2014), no. 21 211802, [1405.5537]. 139
[519] H. E. Haber and O. Stål, *Eur. Phys. J.* **C75** (2015), no. 10 491, [1507.04281]. [Erratum: Eur. Phys. J.C76,no.6,312(2016)]. 139
[520] V. Khachatryan *et. al.*,, **CMS** Collaboration, *Phys. Lett.* **B759** (2016) 369–394, [1603.02991]. 139
[521] **CMS** Collaboration, , *CMS-PAS-HIG-16-010* (2016). 139
[522] M. Gouzevitch, A. Oliveira, J. Rojo, R. Rosenfeld, G. P. Salam, and V. Sanz, *JHEP* **07** (2013) 148, [1303.6636]. 140
[523] M. L. Mangano, M. Moretti, F. Piccinini, and M. Treccani, *JHEP* **01** (2007) 013, [hep-ph/0611129]. 141
[524] D. A. Dicus and S. S. D. Willenbrock, *Phys. Rev.* **D37** (1988) 1801. 145
[525] L. J. Dixon and M. S. Siu, *Phys. Rev. Lett.* **90** (2003) 252001, [hep-ph/0302233]. 145
[526] K. J. F. Gaemers and F. Hoogeveen, *Phys. Lett.* **146B** (1984) 347–349. 145
[527] D. Dicus, A. Stange, and S. Willenbrock, *Phys. Lett.* **B333** (1994) 126–131, [hep-ph/9404359]. 145
[528] S. Moretti and D. A. Ross, *Phys. Lett.* **B712** (2012) 245–249, [1203.3746]. 145
[529] W. Bernreuther, M. Flesch, and P. Haberl, *Phys. Rev.* **D58** (1998) 114031, [hep-ph/9709284]. 146
[530] V. Barger, T. Han, and D. G. E. Walker, *Phys. Rev. Lett.* **100** (2008) 031801, [hep-ph/0612016]. 146
[531] R. Frederix and F. Maltoni, *JHEP* **01** (2009) 047, [0712.2355]. 146
[532] R. Barcelo and M. Masip, *Phys. Rev.* **D81** (2010) 075019, [1001.5456]. 146
[533] T. Figy and R. Zwicky, *JHEP* **10** (2011) 145, [1108.3765]. 146
[534] S. Jung, J. Song, and Y. W. Yoon, *Phys. Rev.* **D92** (2015), no. 5 055009, [1505.00291]. 146
[535] S. Gori, I.-W. Kim, N. R. Shah, and K. M. Zurek, *Phys. Rev.* **D93** (2016), no. 7 075038, [1602.02782]. 146
[536] A. Djouadi, J. Ellis, and J. Quevillon, *JHEP* **07** (2016) 105, [1605.00542]. 146
[537] M. Carena and Z. Liu, *JHEP* **11** (2016) 159, [1608.07282]. 146
[538] B. Hespel, F. Maltoni, and E. Vryonidou, *JHEP* **10** (2016) 016, [1606.04149]. 146
[539] D. Buarque Franzosi, E. Vryonidou, and C. Zhang, *JHEP* **10** (2017) 096, [1707.06760]. 146
[540] W. Bernreuther, P. Galler, C. Mellein, Z. G. Si, and P. Uwer, *Phys. Rev.* **D93** (2016), no. 3 034032, [1511.05584]. 146
[541] W. Bernreuther, P. Galler, Z.-G. Si, and P. Uwer, *Phys. Rev.* **D95** (2017), no. 9 095012, [1702.06063]. 146
[542] M. Aaboud *et. al.*,, **ATLAS** Collaboration, *Phys. Rev. Lett.* **119** (2017), no. 19 191803,

[1707.06025]. 146, 154
[543] S. P. Martin, *Phys. Rev.* **D94** (2016), no. 3 035003, [1606.03026]. 146
[544] E. Maina, *JHEP* **06** (2015) 004, [1501.02139]. 146
[545] N. Kauer and C. O'Brien, *Eur. Phys. J.* **C75** (2015) 374, [1502.04113]. 146
[546] A. Ballestrero and E. Maina, *JHEP* **01** (2016) 045, [1506.02257]. 146
[547] N. Kauer, C. O'Brien, and E. Vryonidou, *JHEP* **10** (2015) 074, [1506.01694]. 146
[548] S. Jung, Y. W. Yoon, and J. Song, *Phys. Rev.* **D93** (2016), no. 5 055035, [1510.03450]. 146
[549] N. Greiner, S. Liebler, and G. Weiglein, *Eur. Phys. J.* **C76** (2016), no. 3 118, [1512.07232]. 146
[550] B. Hespel, D. Lopez-Val, and E. Vryonidou, *JHEP* **09** (2014) 124, [1407.0281]. 146
[551] M. Carena, Z. Liu, and M. Riembau, 1801.00794. 146
[552] S. Dawson and I. M. Lewis, *Phys. Rev.* **D92** (2015), no. 9 094023, [1508.05397]. 146, 148
[553] R. V. Harlander, S. Liebler, and T. Zirke, *JHEP* **02** (2014) 023, [1307.8122]. 146, 148
[554] R. Harlander, J. Klappert, S. Liebler, and L. Simon,. 146
[555] E. Fuchs, S. Thewes, and G. Weiglein, *Eur. Phys. J.* **C75** (2015) 254, [1411.4652]. 146
[556] E. Fuchs and G. Weiglein, 1705.05757. 146
[557] S. Patel, E. Fuchs, S. Liebler, and G. Weiglein, in *The Final HiggsTools Meeting Durham, UK, September 11-15, 2017*, 2018. 1801.05331. 146
[558] A. Djouadi, W. Kilian, M. Muhlleitner, and P. M. Zerwas, *Eur. Phys. J.* **C10** (1999) 45–49, [hep-ph/9904287]. 146
[559] J. Baglio, A. Djouadi, R. Gröber, M. M. Mühlleitner, J. Quevillon, and M. Spira, *JHEP* **04** (2013) 151, [1212.5581]. 146
[560] M. J. Dolan, C. Englert, and M. Spannowsky, *JHEP* **10** (2012) 112, [1206.5001]. 146
[561] L. Di Luzio, R. Gröber, and M. Spannowsky, *Eur. Phys. J.* **C77** (2017), no. 11 788, [1704.02311]. 146
[562] C. O. Dib, R. Rosenfeld, and A. Zerwekh, *JHEP* **05** (2006) 074, [hep-ph/0509179]. 146
[563] R. Gröber and M. Mühlleitner, *JHEP* **06** (2011) 020, [1012.1562]. 146
[564] R. Contino, M. Ghezzi, M. Moretti, G. Panico, F. Piccinini, and A. Wulzer, *JHEP* **08** (2012) 154, [1205.5444]. 146
[565] A. Carvalho, F. Goertz, K. Mimasu, M. Gouzevitch, and A. Aggarwal, 1710.08261. 146
[566] B. Hespel, F. Maltoni, and E. Vryonidou, *JHEP* **06** (2015) 065, [1503.01656]. 146
[567] C. Englert, R. Rosenfeld, M. Spannowsky, and A. Tonero, *EPL* **114** (2016), no. 3 31001, [1603.05304]. 146
[568] for HPAIR see M. Spira's website,. 148
[569] O. Brein, R. V. Harlander, and T. J. E. Zirke, *Comput. Phys. Commun.* **184** (2013) 998–1003, [1210.5347]. 148
[570] R. Gröber, M. Mühlleitner, M. Spira, and J. Streicher, *JHEP* **09** (2015) 092, [1504.06577]. 148
[571] D. de Florian, I. Fabre, and J. Mazzitelli, *JHEP* **10** (2017) 215, [1704.05700]. 148

[572] R. Gröber, M. Mühlleitner, and M. Spira, *Nucl. Phys.* **B925** (2017) 1–27, [1705.05314]. 148

[573] V. Khachatryan *et. al.*,, **CMS** Collaboration, *Phys. Lett.* **B748** (2015) 221–243, [1504.04710]. 154

[574] Tech. Rep. ATLAS-CONF-2016-004, CERN, Geneva, Mar, 2016. 154

[575] **CMS Collaboration** Collaboration, Tech. Rep. CMS-PAS-HIG-16-032, CERN, Geneva, 2016. 154

[576] S. Fichet and G. von Gersdorff, *JHEP* **12** (2015) 089, [1508.04814]. 157

[577] G. Aad *et. al.*,, **ATLAS** Collaboration, *JHEP* **01** (2013) 086, [1211.1913]. 159

[578] G. Aad *et. al.*,, **ATLAS** Collaboration, *Phys. Rev.* **D89** (2014), no. 5 052004, [1311.1440]. 159

[579] G. Aad *et. al.*,, **ATLAS** Collaboration, *JHEP* **08** (2016) 005, [1605.03495]. 159

[580] S. Chatrchyan *et. al.*,, **CMS** Collaboration, *JHEP* **06** (2014) 009, [1311.6141]. 159

[581] G. Aad *et. al.*,, **ATLAS** Collaboration, *Nucl. Phys.* **B875** (2013) 483–535, [1307.6795]. 159

[582] G. Aad *et. al.*,, **ATLAS** Collaboration, *Phys. Rev.* **D85** (2012) 092014, [1203.3161]. 159

[583] G. Aad *et. al.*,, **ATLAS** Collaboration, *Phys. Rev.* **D87** (2013), no. 11 112003, [1302.1283]. [Erratum: Phys. Rev.D91,no.11,119901(2015)]. 159

[584] G. Aad *et. al.*,, **ATLAS** Collaboration, *Phys. Rev.* **D93** (2016), no. 11 112002, [1604.05232]. 159

[585] Forum on the Interpretation of the LHC Results for BSM studies, https://twiki.cern.ch/twiki/bin/view/LHCPhysics/InterpretingLHCresults. 164

[586] G. Brooijmans *et. al.*, in *Proceedings, 7th Les Houches Workshop on Physics at TeV Colliders: Les Houches, France, May 30-June 17, 2011*, pp. 221–463, 2012. 1203.1488. 164

[587] S. Kraml *et. al.*, *Eur. Phys. J.* **C72** (2012) 1976, [1203.2489]. 164, 187

[588] M. Drees, H. Dreiner, D. Schmeier, J. Tattersall, and J. S. Kim, *Comput. Phys. Commun.* **187** (2015) 227–265, [1312.2591]. 164, 165, 166

[589] M. Cacciari and G. P. Salam, *Phys. Lett.* **B641** (2006) 57–61, [hep-ph/0512210]. 164, 165, 166

[590] E. Conte, B. Dumont, B. Fuks, and C. Wymant, *Eur. Phys. J.* **C74** (2014), no. 10 3103, [1405.3982]. 164, 165, 166

[591] B. Dumont, B. Fuks, S. Kraml, S. Bein, G. Chalons, E. Conte, S. Kulkarni, D. Sengupta, and C. Wymant, *Eur. Phys. J.* **C75** (2015), no. 2 56, [1407.3278]. 164, 165, 166

[592] B. M. Waugh, H. Jung, A. Buckley, L. Lonnblad, J. M. Butterworth, and E. Nurse, in *15th International Conference on Computing in High Energy and Nuclear Physics (CHEP 2006) Mumbai, Maharashtra, India, February 13-17, 2006*, 2006. hep-ph/0605034. 164, 165, 166

[593] T. Sjostrand, S. Mrenna, and P. Z. Skands, *Comput. Phys. Commun.* **178** (2008) 852–867, [0710.3820]. 166

[594] M. Aaboud *et. al.*,, **ATLAS** Collaboration, *Eur. Phys. J.* **C76** (2016), no. 7 392, [1605.03814]. 167, 168, 188

[595] B. Fuks, S. Banerjee, and B. Zaldivar,. DOI: 10.7484/INSPIREHEP.DATA.GTF5.RN03.

167
[596] A. Buckley,. http://rivet.hepforge.org/analyses/ATLAS_2016_I1458270.html. 167
[597] S. Baek and T. H. Jung,. DOI: 10.7484/INSPIREHEP.DATA.88NC.0FER.1. 168
[598] **ATLAS** Collaboration,T. A. collaboration, „ "Search for long-lived, massive particles in events with displaced vertices and missing transverse momentum in 13 TeV pp collisions with the ATLAS detector." 2017. 171, 172, 173, 174, 175, 176
[599] V. Khachatryan *et. al.*„ **CMS** Collaboration, *Phys. Rev. Lett.* **114** (2015), no. 6 061801, [1409.4789]. 171, 179
[600] B. C. Allanach, M. Badziak, G. Cottin, N. Desai, C. Hugonie, and R. Ziegler, *Eur. Phys. J.* **C76** (2016), no. 9 482, [1606.03099]. 175
[601] Z. Liu and B. Tweedie, *JHEP* **06** (2015) 042, [1503.05923]. 175
[602] J. A. Evans and J. Shelton, *JHEP* **04** (2016) 056, [1601.01326]. 180
[603] E. Bagnaschi *et. al.*, *Eur. Phys. J.* **C77** (2017), no. 2 104, [1610.10084]. 180
[604] J. Heisig, J. Kersten, N. Murphy, and I. Strümke, *JHEP* **05** (2017) 003, [1701.02313]. 180
[605] M. Garny, J. Heisig, B. Lülf, and S. Vogl, 1705.09292. 180
[606] F. Feroz, M. P. Hobson, and M. Bridges, *Mon. Not. Roy. Astron. Soc.* **398** (2009) 1601–1614, [0809.3437]. 182
[607] F. Feroz, M. P. Hobson, E. Cameron, and A. N. Pettitt, 1306.2144. 182
[608] S. Sekmen and G. Unel, 1801.05727. 187
[609] C. Collaboration,, **CMS** Collaboration,. 188
[610] tech. rep., The version these proceedings refers to is tagged Houches2017Proceedings. 188
[611] International Organization for Standardization, *ISO/IEC 14977* **1996** (1996). 188
[612] Wikipedia contributors,, 2018. [Online; accessed 5-February-2018]. 188
[613] International Organization for Standardization, *ISO/IEC 14882* **2017** (2017). 189
[614] M. Dobbs and J. B. Hansen, *Comput. Phys. Commun.* **134** (2001) 41–46. 191